Thin-Film Synthesis of Metal Halide Perovskites for Optoelectronics

A DISSERTATION
SUBMITTED TO THE FACULTY OF THE GRADUATE SCHOOL
OF THE UNIVERSITY OF MINNESOTA
BY

Catherine Paige Gaburo Clark

IN PARTIAL FULFILLMENT OF THE REQUIREMENTS
FOR THE DEGREE OF
DOCTOR OF PHILOSOPHY

Eray S. Aydil, Advisor
Russell J. Holmes, Advisor

August, 2020

Acknowledgements

First of all, I want to express my deep gratitude to my graduate advisors, Professor Eray Aydil and Professor Russell Holmes, for their unwavering guidance and support over the last five years. Your steadfast enthusiasm, attention to detail, and dedication to high-quality science has helped me become a better researcher. Thank you for digging into the wild world of metal-halide perovskites with me.

Thank you to all of my Holmes group colleagues for supporting me day-in and day-out throughout graduate school. To Nathan, Tom, Ian, Kyle, Tao, and Deepesh, John, Kaicheng, Nolan, Robert, Wan-Ju, and Jenya, thank you for your guidance, wisdom, and community. Special thanks to John for unmeasurable technical and emotional support throughout our graduate school journey.

I have also had the privileged of collaborating with and learning from many researchers in the broader UMN community: Bryan Voigt, Debmalya Ray, Hung Pham, Professor Laura Gagliardi, Rebecca Combs, Ellen Monzo, Kamilah Amen, Dr. Tom Weber, Professor Lee Penn, Professor Matthew Aro, Professor Patrick Schoff, Elisah VandenBussche, Dr. Javier Garcia Barriocanal, Dr. Greg Haughstad, Dr. Seema Thakral, and Bill Voje, thank you for your stimulating conversations, productive partnerships, and consistent tutelage. Thank you to our brilliant colleagues at Physical Electronics Dr. John Newman, Dr. Kateryna Artyushkova, Dr. Ben Schmidt and especially Dr. Jenny Mann, for your expertise, guidance, enthusiasm, and time. Thank you to my undergraduate mentees Nic Rothbacher, Kyle Miller, Katherine Gramling, and Carly Reller for your time, energy, and excellent questions.

My time in graduate school was greatly enriched by the CEMS staff, especially Teresa Bredahl, Julie Prince, and Gayle Gabrielski - I am forever indebted for all that you do to make CEMS a stellar and welcoming place. Thank you also to everyone on all of the graduate student groups that helped keep me balanced - roundtable committee, GSC, the Boreas Leadership

Team, and the CEMS anti-racist student group.

To my family and chosen-family: Jordan, Beth, Kirk, Julia, Willy, Steve, Caryl, Kit, Steve, June, Dani, John, Anna, Ryan, Elisah, Rebecca, Julia, Amelia, Nick, Aaron, Sarah, Etonde, Elizabeth, Priscilla, Dylan, and Sabrina, thank you for your continued and constant love and support, you have made everything worth it.

Finally, I also want to acknowledge my many funding sources, without which this work would not have been possible in the slightest. My deepest appreciation goes to the National Science Foundation (NSF) through an iSuperseed grant to MRSEC (DMR-1420013), the University of Minnesota Institute on the Environment, the University of Minnesota Industrial Partnership for Research in Interfacial and Materials Engineering (IPRIME), Ronald L. and Janet A. Christenson, 3M through the 3M Science and Technology Fellowship, and the UMII MnDRIVE Graduate Assistantship.

Dedication

To **Jordan K. Casomar (Thomas)**, for seeing me better than I see myself, for refusing to understate my brightness and my goodness, and for keeping me laughing in the dark times.

To my parents, **Beth Clark** and **Kirk Gaburo**, to my sister **Julia Clark**, and to my basically-family **Amelia van Iwaarden** and **Julia Lurie**, for loving me since forever and for making me never think twice about whether I belonged in the world of math and science and engineering.

To my grad school friends, **John** and **Anna Myers-Bangsund**, **Ryan Gnabasik**, and **Elisah VandenBussche**, for being there through every twist and turn and for becoming so much more than just my grad school friends.

To my **Headwaters** community, for showing me the kind of world I want to live in and for teaching me how to build it.

Abstract

Metal halide perovskites (MHPs), like the archetypal methylammonium lead iodide ($MAPbI_3$), have emerged in the last decade as promising materials for efficient, low-cost optoelectronics. MHP solar cells have already reached efficiencies $>25\%$, rivaling established technologies like single-crystal Si. Yet several challenges prevent the widespread commercialization of MHPs, including their instability in ambient conditions, their toxicity, and the need for scaleable fabrication techniques. Fundamentally, the origins of important material properties relating to carrier transport and recombination are still not well understood. Thin film deposition techniques that enable detailed study of process-structure-property relationships and are commercially relevant are consequently becoming increasingly essential.

This thesis seeks to address these challenges through the design, implementation, and utilization of a carrier-gas assisted vapor deposition (CGAVD) method that can grow MHP films with highly tunable stoichiometries and morphologies. Alongside the design of a CGAVD system with six independently controllable experimental parameters, an analytical model is developed and experimentally validated that allows the determination of robust and repeatable growth regimes and the prediction of material deposition rates.

Harnessing this technique, we demonstrate the ability to deposit $MASnI_3$ and $MASnBr_3$ films and to systematically vary their compositions across a wide range, and realize corresponding changes in film microstructures (grain size, coverage) and electronic properties (resistivity, carrier concentration, mobility). Control of grain size and film texturing is also achieved independent of stoichiometry *via* modulation of chamber pressure and substrate temperature.

The benefits of CGAVD are further highlighted by the successful growth of novel all-MHP heterojunctions. Two stable pairings are identified: $MAPbBr_3$/$MASnBr_3$ and $CsPbBr_3$/$MASnBr_3$. Design rules to control the mixing of heterojunctions are developed by exploring the dependence of mixing rate on MHP layer composition and grain size. Finally, through a collaboration with Physical Electronics, we optimize the use of XPS depth-profiling for MHPs and investigate which ions are diffusing in a layered structure that exhibits mixing.

Moving forward, the incorporation of CGAVD-grown heterojunctions and Pb MHPs into optoelectronic devices will harness the tunability of this system towards a deeper understanding of process-structure-property relationships in MHP thin films and novel layered structures.

Contents

List of Tables

List of Figures

List of Abbreviations

Acronyms

AFM Atomic force microscopy

CAD Computer aided design

CGAVD Carrier gas assisted vapor deposition

COMSOL Finite element analysis software

CVD Chemical vapor deposition

DSSC Dye-sensitized solar cell

EL Electroluminescence, light emission after electrical excitation

ETL Electron-transport layer

EQE External quantum efficiency

FA Formamidinium

FEA Finite element analysis

FF Fill factor

GCIB Gas cluster ion beam

HTL Hole-transport layer

J$_{SC}$ Short circuit current

LED Light-emitting device

LPM Liters per minute

LP-OVPD Low-pressure organic vapor phase deposition

MA	Methylammonium
MHP	Metal halide perovskite
OLED	Organic light-emitting device
OPV	Organic photovoltaic
PeLED	Perovskite light emitting device
PCE	Power conversion efficiency
PL	Photoluminescence, light emission after excitation by light
PLQE/Y	Photoluminescence quantum efficiency/yield
PV	Photovoltaic
PVD	Physical vapor deposition
QCM	Quartz crystal microbalance/monitor
QD	Quantum dot
RBS	Rutherford backscattering
sccm	Standard cubic centimeters per minute
SEM	Scanning electron microscopy
TEM	Transmission electron microscopy
Tof-SIMS	Time-of-flight secondary ion mass spectrometry
UEM	Ultrafast transmission electron microscopy
$\mathbf{V}_{OC}$	Open circuit voltage
VTE	Vacuum thermal evaporation
XPS	X-ray photoelectron spectroscopy
XRD	X-ray diffraction

Materials

Metal halide perovskite precursor materials

MAI Methylammonium iodide

FAI Formamidinium iodide

PEAI Phenethylammonium iodide

CsI Cesium iodide

MABr Methylammonium bromide

FABr Formamidinium bromide

CsBr Formamidinium bromide

PbI_2 Lead iodide

$PbBr_2$ Lead bromide

SnI_2 Tin iodide

$SnBr_2$ Tin bromide

ABX_3 Metal halide perovskites

$MAPbI_3$ Methylammonium lead iodide

$FAPbI_3$ Formamidinium lead iodide

$CsPbI_3$ Cesium lead iodide

$MAPbBr_3$ Methylammonium lead bromide

$FAPbBr_3$ Formamidinium lead bromide

$CsPbBr_3$ Cesium lead bromide

$MASnI_3$ Methylammonium tin iodide

$MASnBr_3$ Methylammonium tin bromide

Transport layers, electrodes, and misc.

Spiro-OMeTAD	2,2',7,7'-Tetrakis[N,N-di(4-methoxyphenyl)amino]-9,9'-spirobifluorene
TiO_2	Titanium oxide
ITO	Indium doped tin oxide
FTO	Flourine doped tin oxide
Al_2O_3	Aluminum oxide
Alq_3	Tris-(8-hydroxyquinoline)aluminum
DCM2	4-(Dicyanomethylene)-2-methyl-6-(4-dimethylaminostyryl)-4H-pyran
α-NPD	2,2'-Dimethyl-N,N'-di-[(1-naphthyl)-N,N'-diphenyl]-1,1'-biphenyl-4,4'-diamine
TCTA	Tris(4-carbazoyl-9-ylphenyl)amine
PTCDA	Perylene-3,4,9,10-tetracarboxylic dianhydride
PEDOT:PSS	Poly(3,4-ethylenedioxythiophene)-poly(styrenesulfonate)
$CaTiO_3$	Calcium titanate
CIGS	Copper indium gallium selenide
CdTE	Cadmium telluride
TOPO	Trioctylphosphine oxide
DMF	N,N-Dimethylformamide
DMSO	Dimethyl sulfoxide

Variables

μ	Coordination factor or carrier mobility
t	Goldschmidt's tolerance factor
r_A, r_B, r_X	Radii of A, X, B site cations
α	Absorption coefficient
m_e^*	Electron effective mass
m_h^*	Hole effective mass

m_0	Electron rest mass
τ	Carrier lifetime
L	Carrier diffusion length
D	Diffusivity
q	Electron charge
k_B	Boltzmann constant
η	Power conversion efficiency
$\dot{V}_{CG,i}$	Carrier gas flow rate for material i
$\dot{V}_{DIL}$	Dilution gas flow rate
T_i	Temperature of source material i
T_g	Gas temperature
T_s	Substrate temperature
P	Pressure
ΔH_i^s	Sublimation enthalpy for species i
Re	Reynolds number
r_i	Deposition rate for species i
$r_{A,B}$	Normalized excess precursor ratio, r-ratio
ρ	Resistivity
$TC_{h_i k_i l_i}$	Texture coefficient
$I_{h_i k_i l_i}$	Intensity of the $(h_i k_i l_i)$ diffraction peak
E_K	Photoelectron kinetic energy
$h\nu$	Photon energy
E_B	Photoelectron ionization (binding) energy
$t_{crossover}$	Crossover time
FT	Film thickness

$r_{sputter}$	Sputter rate
$L_{tail,i}$	Tail length
$t_{i@10\%ofmax}$	Tail length time
d_{sub}	Distance from the substrate

Chapter 1

Introduction to Metal Halide Perovskites

1.1 Motivation

As the climate crisis looms and global energy consumption increases, technologies that produce and consume electricity efficiently with minimal fossil fuel input are becoming increasingly vital. Renewable energy technologies that use sunlight are particularly promising as the quantity of solar energy reaching the earth's surface is thousands of times larger than our global energy consumption [1]. Furthermore, sunlight-to-electricity conversion using photovoltaics (PVs) can produce useful electricity in off-grid locations, enabling electrification without the need for expansive and expensive transmission and distribution infrastructure. While PV technologies are currently the fastest growing energy source worldwide, they contribute less than 3% to global electricity production, highlighting the need and opportunities for continued technological development [2]. Minimizing the power consumption of ubiquitous devices, such as televisions, cell-phones, and laptops, is also necessary to maintain our desired quality of life while avoiding catastrophic climate change. Optoelectronic materials science and engineering sits at the forefront of this challenge to create devices that manage our electricity generation and consumption efficiently and with a low-carbon footprint.

In the last decade, there has been a revolution in the field of optoelectronic materials with the emergence of metal halide perovskites (MHPs) like the archetypal methylammonium lead iodide ($CH_3NH_3PbI_3$ or $MAPbI_3$). This materials system has enormous potential to enable

low cost, high efficiency, flexible optoelectronic devices. Within this context, the motivation of my PhD research has been to contribute to the field of MHPs in order to make possible cheap, efficient, and commercially viable technologies that can improve our quality of life while averting the climate crisis. My efforts have focused on developing methods to fabricate and study thin film metal-halide perovskites towards the eventual goal of enabling their incorporation into commercially viable devices.

This Chapter seeks to provide a high-level history of the field of MHPs as well as an explanation of common nomenclature in order to contextualize my thesis work. A brief overview of the structure of this thesis is also included for reference.

1.2 A Brief History of Metal Halide Perovskites

While reports of organic–inorganic halide perovskites date back to the late 1800s [3], detailed optical and electrical characterization of these materials did not begin until the 1990s [4–9]. The majority of these reports focused on layered or 2D MHPs and their potential for incorporation into transistors and electroluminescent devices like light-emitting diodes (LEDs) [7, 8, 10–13]. Widespread interest in MHPs arguably did not start until their success as an active material in photovoltaics (PVs). The first reports of MHPs for use in solar cells was by Miyasaka *et al.* in 2006, reporting a 2.2% efficient PV by using $MAPbBr_3$ as a sensitizer in a dye-sensitized solar cell (DSSC) configuration [14]. Use of MHPs in this DSSC configuration, where they served primarily as a light absorber on a porous TiO_2 electrode, continued until 2011 and culminated in the realization of a 6.5% efficient $MAPbI_3$ solar cell [15, 16]. Unfortunately, these DSSCs degraded rapidly due in part to the liquid electrolyte. Use of a solid electrolyte in 2012 culminated in solar cells with 9.7% power conversion efficiency (PCE) [17]. Interestingly, this first solid electrolyte employed, spiro-MeOTAD (2,2',7,7'-tetrakis(N,N-di-p-methoxyphenylamine)-9,9'-spirobifluorene), remains one of the most widely-used hole transport layers in MHP PV devices to-date.

One of the most important discoveries that laid the foundation for the rapid advancement of MHP devices was the demonstration by Snaith *et al.* in 2012 that MHPs exhibit excellent electron and hole transport properties. By showing that the PCE of MHP PVs could be improved by replacing the standard TiO_2 electrode with an insulating Al_2O_3 scaffold, the ability of MHPs to both absorb light and effectively transport carriers was revealed, and enabled the fabrication

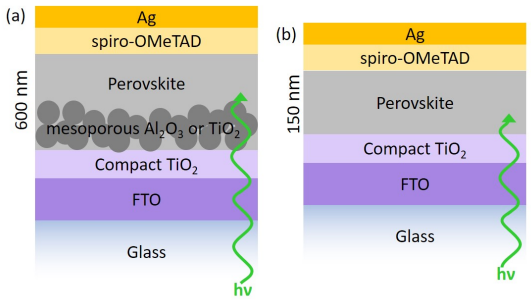

Figure 1.1. Schematic of MHP PV architectures reported in the seminal work by Lee *et al.*, which demonstrated the ability of MHPs to both absorb light and transport charges efficiently. (a) Mesoporous architecture, where the photoactive layer is comprised of MHP on a mesoporous TiO_2 or Al_2O_3 scaffold. (b) Planar device architecture, which was the first of its kind reported in the literature. Adapted from [18].

of a planar MHP solar cell for the first time [18]. Along with achieving over 10% PCE, this discovery proved that MHPs could be utilized more broadly than just as light sensitizers in a DSSC configuration.

Since 2012, the power conversion efficiency for MHP-based solar cells has increased at an unprecedented rate, as shown in Figure 1.2. The current single junction record efficiency of 25.2% has surpassed other thin-film technologies such as CIGS and CdTe and is approaching that of single crystal silicon (with a record efficiency of 26.1%) [19]. Note that the Schockley-Queisser limit for a single junction PV device with a direct bandgap of 1.34 eV is $\sim$33.7%, denoted by the grey dashed line in Figure 1.2.

This fast-paced improvement in PV efficiency is the result of the work of hundreds if not thousands of research groups and includes a wide array of technical advancements. Figure 1.3 shows the increase in MHP papers and citations over time, highlighting the explosion of research in this field since 2012 [20]. Major categories of improvement over the last decade have included (1) the incorporation of multiple A- and X- site cations to improve optoelectronic properties and stability ($e.g.$, in high-performing perovskites like $Cs_{0.05}FA_{0.85}MA_{0.10}Pb(I_{0.97}Br_{0.03})_3$) [21–23], (2) the exploration of transport layers for improved band alignments, carrier extraction, and stability [24–27], and (3) the tuning of deposition conditions to optimize film morphology and chemistry and thereby minimize physical and electronic defects [28–32]. A detailed review of important material properties related to these advancements will be discussed in Chapter 2.

Alongside the developments in single-junction PV devices, MHPs have also been implemented in tandem configurations, both with existing Si cells [33–36] and, excitingly, in all-perovskite tandem configurations [37–39]. Implementing perovskites in a tandem architecture

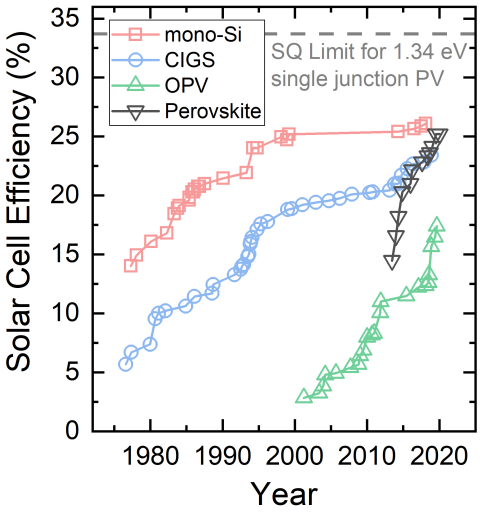

Figure 1.2. Highest confirmed power conversion efficiencies for selected photovoltaic technologies adapted from [19], including single crystal Si (mono-Si), copper indium gallium selenide (CIGS), organic (OPV), and perovskite photovoltaics. The horizontal line at 33.7% power conversion efficiency represents the Shockley–Queisser limit for a single junction solar cell with an ideal 1.34 eV bandgap.

may provide an opportunity to realize very high efficiency devices as well as a pathway towards commercialization for MHP PVs given the dominance of Si solar cells commercially.

While MHPs have been studied most extensively in relation to their application in photovoltaic devices, their ideal and tunable material properties have enabled their successful incorporation into a much wider array of devices, including photodetectors [40–42], light emitting diodes [43], lasers [44, 45], transistors [46, 47], and resistive memory devices [48, 49]. Aside from PVs, MHPs have been most widely studied for their use in LEDs (often called PeLEDs) due to their narrow emission linewidths and highly tunable bandgaps [50–55]. Recent achievements in the field of PeLEDS include $>$20% external quantum efficiency (EQE) for green and red LEDs [43, 56].

Despite the enormous progress and high efficiency of MHP devices, several challenges remain before this technology can be widely commercialized, including the toxicity of high-performance MHPs containing lead [57, 58] and the degradation of these materials in ambient conditions due to light, heat, moisture, and oxygen [59]. While MHPs are compatible with high-throughput processes and can be successfully fabricated with a variety of techniques, further optimization of large-scale fabrication methods is still required.

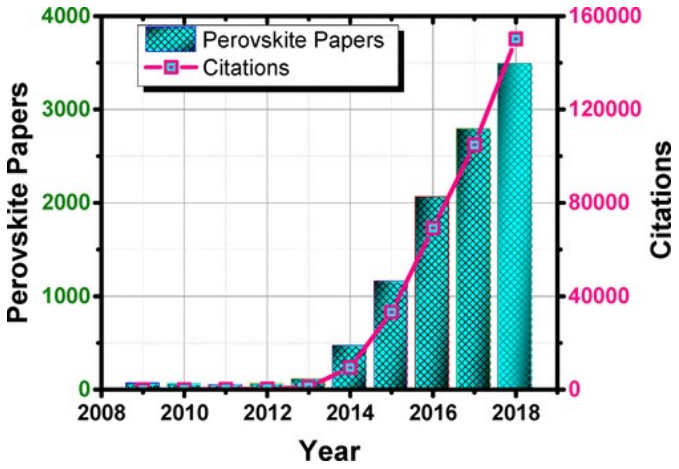

Figure 1.3. Growth in MHP research from 2009-2018, show through a rapidly increasing number of publications and citations in this field. Reprinted with permission from F. De Angelis. "Celebrating 10 years of perovskite photovoltaics". In: ACS Energy Letters 4.4 (2019), pp. 853-854. DOI: 10.1021/acsenergylett.9b00500 [20]. Copyright 2019 American Chemical Society.

1.3 Perovskite Nomenclature

As the field of metal halide perovskites has grown rapidly over the last decade, the nomenclature has evolved somewhat haphazardly. In this section, I will outline typically used nomenclature in the literature as well as the specific naming conventions that will be used throughout the rest of this text.

The term "perovskite" traditionally refers to a class of materials that have crystal structures similar to calcium titanate ($CaTiO_3$), with an ABX_3 stoichiometry where A and B are large and small cations, respectively, and X is an anion. This is the structure of the most commonly studed MHP, methylammonium lead iodide ($CH_3NH_3PbI_3$), and is shown in Figure 1.4a. Here, the A-site cation sits in the 3-dimensional cuboctahedral cavity formed by a network of corner-sharing BX_6 octahedra. In MHP literature, common A-sites include methlyammonium ($CH_3NH_3^+$ or MA), formamidinium ($NH_2CH{=}NH_2^+$ or FA), and cesium, B-sites are typically Pb or Sn, and X-sites are halogens including iodine, bromine, and chlorine.

In the metal-halide perovskite literature, however, the term "perovskite" is applied to a much broader set of stoichiometries and crystal structures [60]. For example, 2D perovskites (Figure 1.4e) are typically described as $R_2A_{n-1}B_nX_{3n+1}$, where R is a large organic cation and "n" denotes the number of $[BX_6]^{4-}$ layers separated by R cations. 2D perovskites have shown promise to increase the stability and hydrophobicity of MHPs [61, 62], as well as improve device performance in LEDs [63, 64] and PVs [65]. Other common structures categorized as

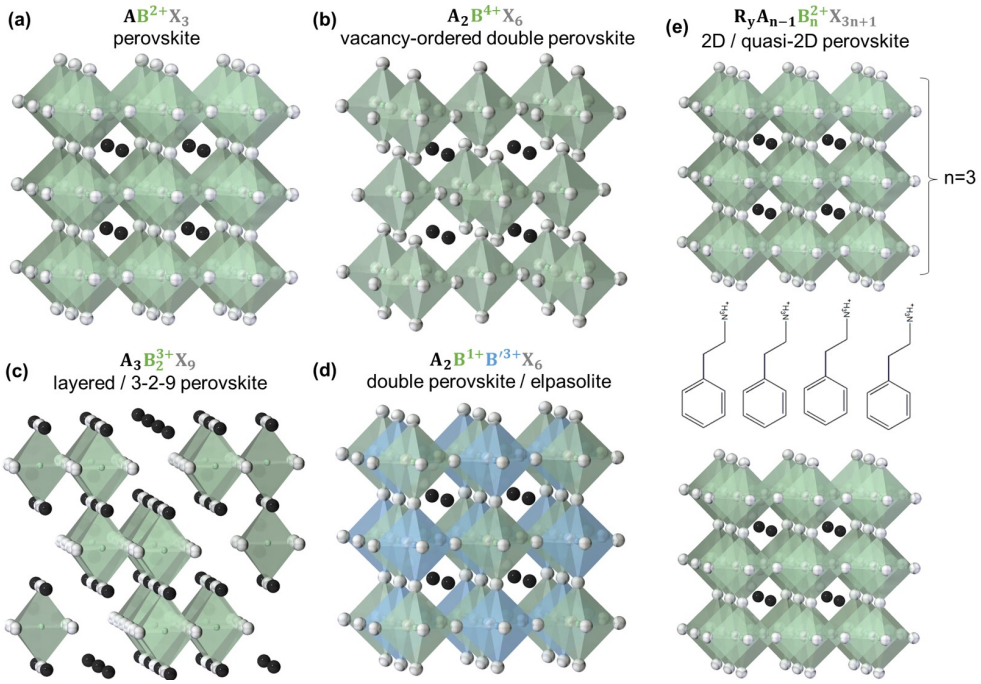

Figure 1.4. Examples of various MHP crystal structures and stoichiometries. (a) Idealized $AB^{2+}X_3$ perovskite, where A (black) and B (green) are large and small cations, respectively, and X (grey) is an anion. (b) Structure of the $A_2B^{4+}X_6$ vacancy-ordered double perovskite, like the structure in (a) but with every other B cation removed. (c) Structure of the $A_3B_2^{3+}X_9$ layered perovskite, like the structure in (a) but with every third B cation removed. (d) Structure of the $A_2B^{1+}B^{3+}X_6$ elpasolite perovskite, where every other B-site alternates between two different cation species. (e) Example of a 2D perovskite structure, typically described as $R_2A_{n-1}B_nX_{3n+1}$, where R is a large organic cation and "n" denotes the number of $[BX6]^{4-}$ layers separated by R cations. In this example, R is phenethylammonium and n=3.

"perovskites" in the field of MHPs are shown in Figure 1.4b-d, and include vacancy ordered, 3-2-9, and double-perovskite types. In this work, the terms "perovskite" and "MHP" will be used to denote metal-halide perovskite materials with an ABX_3 stoichiometry and a type of crystal structure shown in Figure 1.4a unless otherwise noted. As is common in the literature, organic A-sites will also be abbreviated in this text, including MA for methlyammonium ($CH_3NH_3^+$) and FA for formamidinium ($NH_2CH{=}NH_2^+$).

1.4 Overview of Thesis

As noted in the beginning of this chapter, my PhD research has sought to contribute to the realization of cheap, efficient, and commercially viable technologies based on MHPs. Specifically, the main focus of my work has been to develop and utilize a solvent-free deposition technique that enables the detailed study of process-structure-property relationships in MHP thin films and the fabrication of novel MHP layered structures.

To provide further background for these efforts, this thesis begins with an introduction of the properties (Chapter 2) and standard processing techniques for MHPs (Chapter 3) that form the foundation off of which my efforts build. I then present the design and development of the deposition technique (CGAVD) that is employed throughout this work, focusing on the critical elements that enable the success of this method (Chapter 4). In Chapters 5 and 6, I demonstrate the unique capabilities of CGAVD to realize tunable stoichiometry and morphology in MHP thin films and to enable the growth of all-perovskite heterojunctions for the first time. Finally, Chapter 7 focuses on our detailed exploration of depth-profiled X-ray photoelectron spectroscopy (XPS) as a tool to characterize MHP films and heterojunctions in collaboration with Physical Electronics, Inc. Chapter 8 provides a high-level summary of my thesis work including major achievements, as well as ideas for future work and a broad outlook on the future of MHP materials.

Additional data corresponding to the above chapters, as well as descriptions and data for smaller side projects are included in the Appendices. Smaller side projects include: the attempted synthesis of alkaline earth metal halide perovskites in collaboration with the Gagliardi group (Appendix C), investigations of beam damage on $MAPbI_3$ in TEM (Section 8.2.3), and preliminary explorations of photoluminescence (PL) degradation in MHPs (Section 8.2.2).

Chapter 2

Fundamental Material Properties of Metal Halide Perovskites

The rapid advancement of MHPs to achieve high-performing optoelectronic devices is due in large part to their ideal and highly tunable properties. This chapter presents a summary of material properties for MHPs focusing on those that are relevant to this thesis and that are critical for their application in optoelectronic devices.

2.1 Crystal Structure

As shown in Figure 1.4a, 3D ABX_3 MHPs form a network of corner sharing BX_6 octahedra, where the A-site sits in the octahedral cavity. The sizes of the A, B, and X ions determine whether this structure can be formed, and when it does they determine the symmetry, space group, and lattice parameters of the resulting MHP. Two common metrics used to assess whether a particular combination of A, B, and X ions will form a perovskite structure are the coordination factor (μ)

$$\mu = r_B/r_X \tag{2.1}$$

and Goldschmidt's tolerance factor (t)

$$t = \frac{(r_A + r_X)}{\sqrt{2}(r_B + r_X)}. \tag{2.2}$$

In both equations, r_A, r_B and r_X are the radii of the ions at sites A, B and X, respectively.

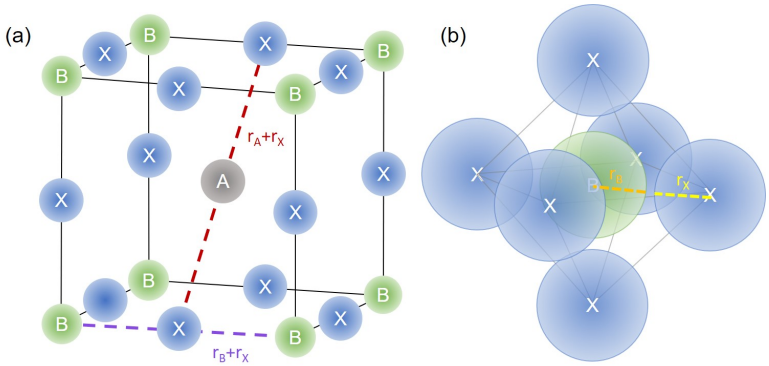

Figure 2.1. Schematic (not to scale) showing relevant geometry for (a) Goldschmidt's tolerance and (b) coordination factors, including r_B+r_X, r_A+r_X, r_B, and r_X.

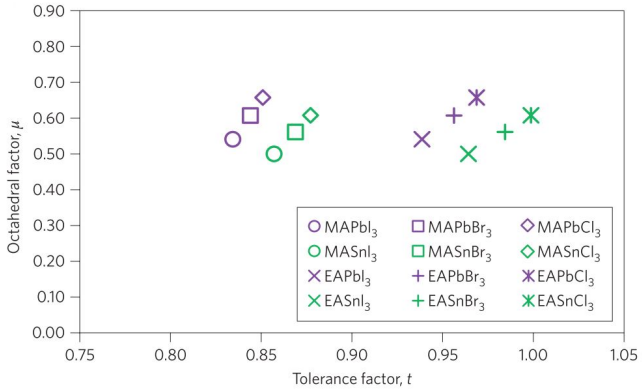

Figure 2.2. Octahedral factors (μ) and Goldschmidt's tolerance factors (t) for common MHP materials, where MA = methylammonium, FA = formamidinium, and EA = ethylammonium. Reprinted by permission from Springer Nature: Nature Photonics, "The emergence of perovskite solar cells", M.A. Green, A. Ho-Baillie, and H.J. Snaith. Copyright 2014 [6].

Whereas μ corresponds to the ability of the six X-site halogens to form an octahedron by packing around the B-site cation, the tolerance factor (t) determines if the A-site cation will fit in the cavity formed by these octahedra. Relevant geometrical quantities for these relations are shown in Figure 2.1. For halide perovskites, Li *et al.* find that the vast majority of experimentally synthesizable MHPs satisfy $0.442 < \mu < 0.895$ and $0.813 < t < 1.107$ [66]. Octahedral and tolerance factors for common MHP materials are shown in Figure 2.2. This range of viable μ and t values informed my own attempts to synthesize MHPs from alkaline earth metals Mg, Ca, Sr, and Ba as potential replacements for lead, which was a substantial portion of my preliminary thesis work [67]. These studies, which were performed alongside computational work by the Gagliardi group,[1] are described in detail in Appendix C and ref [67].

[1] Debmalya Ray, myself, Hung Q Pham, Joshua Borycz, Russell J Holmes, Eray S Aydil, and Laura Gagliardi

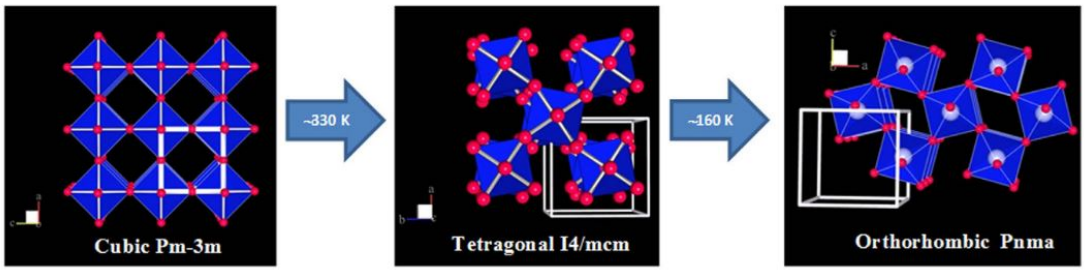

Figure 2.3. $MAPbI_3$ phases as a function of temperature, where lower symmetry phases result from octahedral tilting. Reproduced with permission from [69].

Material	RT Crystal Structure	Space Group	Lattice Parameter (Å)	Source
$MAPbI_3$	tetragonal	I4/mcm	a* = b* = 6.26, c* = 6.22	[70]
$MASnI_3$	tetragonal	P4mm	a = b = 6.24, c = 6.23	[71]
$MAPbBr_3$	cubic	$Pm\bar{3}m$	a = b = c = 5.9	[68]
$MASnBr_3$	cubic	$Pm\bar{3}m$	a = b = c = 5.9	[72]
$FAPbBr_3$	cubic	$Pm\bar{3}m$	a = b = c = 5.99	[73]
$FAPbI_3$	cubic	$Pm\bar{3}m$	a = b = c = 6.36	[74]
$CsPbBr_3$	orthorhombic	Pbnm	a = 8.2, b = 8.24, c = 11.74	[75]

Table 2.1: Room temperature crystal structures, space groups, and lattice parameters for common MHP materials. *Lattice parameters for pseudocubic tetragonal structure presented to enable easier comparison between material, calculated as a* = b* = a/$\sqrt{2}$, c* = c/2, where a and c are the tetragonal lattice parameters.

Most ABX_3 MHPs adopt cubic, tetragonal, or orthorhombic structures depending on temperature and μ and t. For example, $MAPbI_3$ has been shown to undergo a transition from a low temperature orthorhombic phase (Pnma) to a tetragonal I4/mcm phase at 160 K to a high-temperature cubic $Pm\bar{3}m$ phase above 330 K [68]. These phase transitions are associated with a tilting of the PbI_6 octahedra, as shown in Figure 2.3 [69]. Examples of common MHP crystal structures, lattice parameters, and space groups are presented in Table 2.1

One interesting challenge with structural characterization of organic-inorganic halide perovskites is the rotational disorder of the organic cations. Due to the non-spherically symmetric nature of these cations (*e.g.*, MA) they can orient in different directions within the cuboctahedral cavity, and have also been shown to rapidly re-orient on timescales of 10s of picoseconds at room temperature [76]. Variations in A-site ion alignment, and the dynamic nature of these ions, could impact electronic and magnetic properties [69, 76, 77].

2.2 Optoelectronic Properties

2.2.1 Light Absorption, Emission, and Bandgap

Of utmost importance to their application in photovoltaic devices, archetypal MHP materials are semiconductors that have direct bandgaps and strong absorption coefficients in the visible spectrum. $MAPbI_3$, for instance, has a direct optical bandgap of ≈1.5 eV, and a large absorption coefficient (α) in the visible range (α ≈5x10^4 cm^{-1} at 730 nm/1.7 eV) [6, 78–80]. This absorption coefficient is on par with other thin-film semiconductors such as CdTe and InP, as shown in Figure 2.4.

In ABX_3 MHPs like $MAPbI_3$, the conduction band is comprised primarily of metal p orbitals, whereas the valence band has both metal s and halogen p orbital character [67, 82]. In addition to resulting in large absorption coefficients, this orbital configuration means that the bandgap of MHPs can be easily tuned by changing the B-site and X-site ions [83, 84]. Figure 2.5 shows how changing the X-site cation in $MAPbX_3$ from Cl to Br to I results in a shift in optical bandgap of close to 400 nm (∼1.6 eV) [81], arising from a combination of different orbital energy levels of each halogen as well changes in orbital overlap between B- and X- ions [85]. This enormous tunability means that perovskite materials can be easily customized for a specific application by changing their halide ions, as demonstrated in optimized-bandgap MHPs for tandem solar cells [34, 37, 38, 86]. It should be noted that the bandgap of MHPs can also be tuned by other (more indirect) methods such as octahedral tilting and lattice contractions [87], however these effects are typically smaller than changes in bandgap from halide substitution.

Figure 2.5b also alludes to another property common to MHPs - their high luminescence

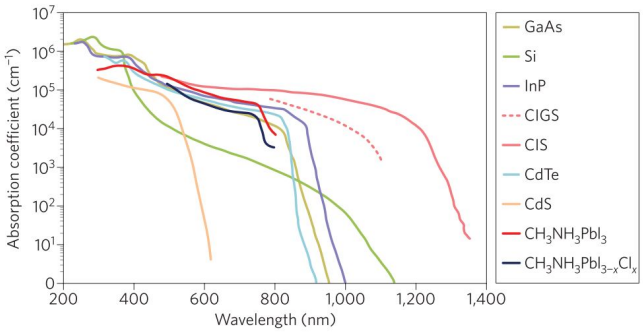

Figure 2.4. Absorption coefficients (α) for common semiconducting materials, including $MAPbI_3$, which has a high absoption coefficient across the visible range. Reprinted by permission from Springer Nature: Nature Photonics, "The emergence of perovskite solar cells", M.A. Green, A. Ho-Baillie, and H.J. Snaith. Copyright 2014 [6].

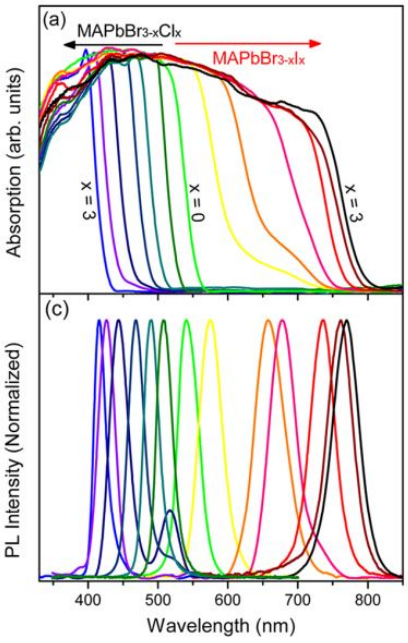

Figure 2.5. Example of facile tunability of MHP bandgap, shown by changing the halogen in $MAPbX_3$ from Cl to Br to I. This results in a shift in optical bandgap of close to 400 nm, visible in both absorbance (a) and PL (b) measurements. Reprinted with permission from D. M. Jang *et al.* "Reversible Halide Exchange Reaction of Organometal Trihalide Perovskite Colloidal Nanocrystals for Full-Range Band Gap Tuning". In: NanoLetters 15.8 (2015), pp. 5191-5199. DOI: 10.1021/acs.nanolett.5b01430 [81]. Copyright 2015 American Chemical Society.

efficiency and color purity. Photoluminescence quantum efficiencies (PLQEs) >90% [88, 89] and very narrow PL emission peaks of ∼20 nm full with at half maximum (FWHM) have been achieved in MHPs [88, 90–92]. These properties make them ideal candidates for light-emitting devices as well as photovoltaics. Fundamentally, the mechanisms of low non-radiative recombination rates are currently not well understood, and have been ascribed to indirect band gaps arising from the Rashba effect, the low density of deep-gap defects, and low energy phononic states in MHPs [93].

2.2.2 Carrier Generation and Transport

Like many inorganic semiconductors, MHPs exhibit large static dielectric constants (∼30) [94, 95], and as a result photo-generated excitons in $MAPbI_3$ have small binding energies (<16 meV), which means readily dissociate into free charge carriers at room temperature [79, 96, 97].[2] Importantly, this means MHP devices do not necessarily require interfaces with energetic offsets in order to separate charge carriers efficiently, as is typically the case in organic

[2]However, many light-emitting devices engineer excitons in MHPs *via* spatial confinement to improve photoluminescence efficiency [98, 99].

semiconducting devices [100–102]. This is beneficial because it allows flexibility in device architectures, as shown by the seminal work of Lee *et al.* who fabricate both mesoporous and planar MHP solar cells [18]. Interestingly, the details of how charges are separated and transported towards the proper contacts in MHP devices (*i.e.*, the details of band structure and the resulting roles of drift and diffusion) are still under scrutiny [103]. Consensus in this area is difficult in part because it has been shown that in MHP devices the balance between drift and diffusion depends strongly not only on the energetics of the MHP and transport layers, but also on the concentration of ionic defects [104].

Electron and hole effective masses (m_e* and m_h*, respectively) are small and similar, typically on the order of $\sim$0.1m_0 - 0.3m_0, where m_0 is the rest mass of an electron (9.11x10^{-31} kg) [97, 105, 106]. The ability of MHPs to transport both holes and electrons efficiently limits the need for spatially intimate contact between the MHP and charge transport layers (*e.g.*, a bulk heterojunction configuration) and enables the realization of efficient planar solar cells with hundreds-of-nm thick MHP layers. Carrier mobilities (μ), which are inversely proportional to effective masses, can be quite large, in some cases exceeding 1000 cm^2/Vs. However, more typical reports range between 1 - 100 cm^2/Vs [60, 105, 107–110], and the origin of these "relatively low" carrier mobilities is still under intense debate [95, 105]. Indeed, the discrepancy between the observed mobilities for MHPs and the mobilities expected based on their small effective masses is one fundamental area of research that requires further understanding [93] - as discussed in more detail in Section 8.2.3.

Charge carriers in MHPs have also exhibited very long lifetimes (τ), on the order of $>1\mu$s for single crystal and polycrystalline films [105, 107, 111, 112]. Combined with high mobilities, these long carrier lifetimes result in very long carrier diffusion lengths ($L = \sqrt{D\tau}$, where $D = q\mu/k_BT$, q is the electron charge, k_B is the Boltzmann constant, and T is the absolute temperature) [108, 113]. In $MAPbI_3$, for example, carrier diffusion lengths have been reported as high as 175 μm in solution-grown single crystals [113].

2.2.3 Defect Tolerance and Doping

One of the key properties that has enabled the meteoric rise of MHPs is their defect tolerance, or their ability to maintain excellent optical and electrical performance even when substantial defects are present. The defect tolerance of MHPs like $MAPbI_3$ is often attributed to the nature of low formation energy defects such as vacancies, substitutions, and interstitials, which create

shallow transition levels instead of deep-gap states, and thus do not act as non-radiative recombination centers or traps [114, 115]. While some types of defects can create deep-gap states, these typically have larger formation energies and thus are unlikely to exist in high concentrations at room temperature. Energy levels for common intrinsic defects in $MAPbI_3$ are shown in Figure 2.6. Thus, even in the presence of substantial defect densities, MHPs have displayed high performance (*e.g.*, high open-circuit voltages) and maintained important properties such as long electron and hole diffusion lengths [82, 115, 116]. An important consequence of this defect tolerance is that high-performance MHPs can be fabricated with a variety of techniques (as discussed in Chapter 3), allowing widespread access to research and development of these materials without the requirement of highly specialized and expensive fabrication equipment. However, the fundamental reason behind these electronically benign defects is still not well understood fundamentally [93, 117].

Because the existence of easily-forming MHP defects do not render MHP materials unusable for optoelectronic applications, these defects can be used to dope these materials. Computational and experimental studies indicate that the "self-doped" majority carrier (electrons or holes) and carrier density of MHPs can be controlled by varying the synthesis conditions [82, 112, 115]. Wang *et al.*, for example, synthesized $MAPbI_3$ as p-type or n-type depending on

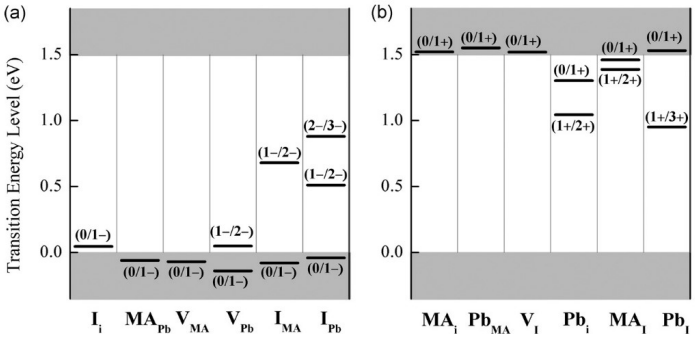

Figure 2.6. Schematic showing energy levels of defects in $MAPbI_3$ from (a) intrinsic acceptors and (b) intrinsic donors. Note that defects shown here with deep-gap states (I_{MA}, I_{Pb}, Pb_i, Pb_i) all have large formation energies ($<$1.5 eV). Reprinted from W.-J. Yin, T. Shi, and Y. Yan. "Unusual defect physics in $CH_3NH_3PbI_3$ perovskite solar cell absorber". In: Applied Physics Letters 104.6 (2014), with the permission of AIP Publishing [115].

the ratio of MAI/PbI_2 precursors [118]. They found that MAI-rich synthesis conditions result in p-type behavior, whereas excess PbI_2 precursor results in an n-type film. This property has enabled the realization of a perovskite p-n homojunction to improve carrier transport and minimize recombination losses [119], although this type of homojunction is rarely reported in the MHP literature and is not required to realize high performance solar cells.

It should be noted, however, that the term "doping" in MHP literature is typically used to describe the addition of extrinsic "dopants" such as K, Rb, Mn, Sr, etc., at concentrations that are much higher (*e.g.*, 50%) than is typical in inorganic semiconductors [82, 120]. These "dopants" can have a variety of impacts, from changing how crystallization occurs to impacting the optoelectronic properties to improving environmental stability of the MHP material [120–123]. The incorporation of rubidium in multi-cation MHPs like (MAFACs)$Pb(IBr)_3$, for example, has been shown to increase V_{OC} and FF in a PV device, potentially by passivating defects at the perovskite/ETL interface [124].

2.3 Ion Migration and Hysteresis

One of the unusual characteristics of MHPs that was observed early in their development was the hysteresis in current-voltage (IV) measurements, epitomized by large differences in forward and reverse IV scans [125–127]. An example of this type of hysteresis is shown in Figure 2.7.

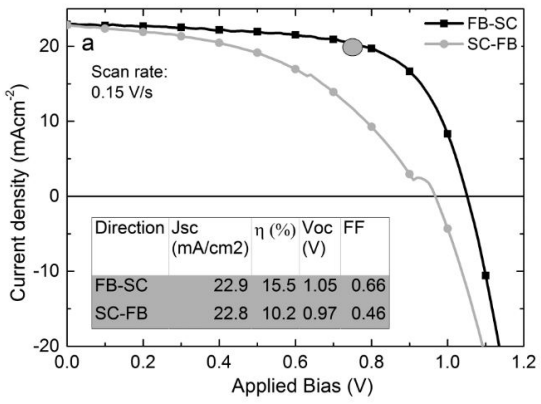

Figure 2.7. Example of current-voltage (IV) hysteresis in a mesoporous $MAPbI_{3-x}Cl_x$ PV, showing forward bias to short circuit (FB-SC) and short circuit to forward bias (SC-FB) current-voltage curves and a table with extracted performance parameters. Here, J_{SC} = short circuit current, V_{OC} = open circuit voltage, $\eta\%$ = power conversion efficiency, and FF = fill factor. Reprinted with permission from H.J. Snaith *et al.* "Anomalous hysteresis in perovskite solar cells". In: Journal of Physical Chemistry Letters 5.9 (2014), pp. 1511–1515. Copyright 2014 American Chemical Society [125].

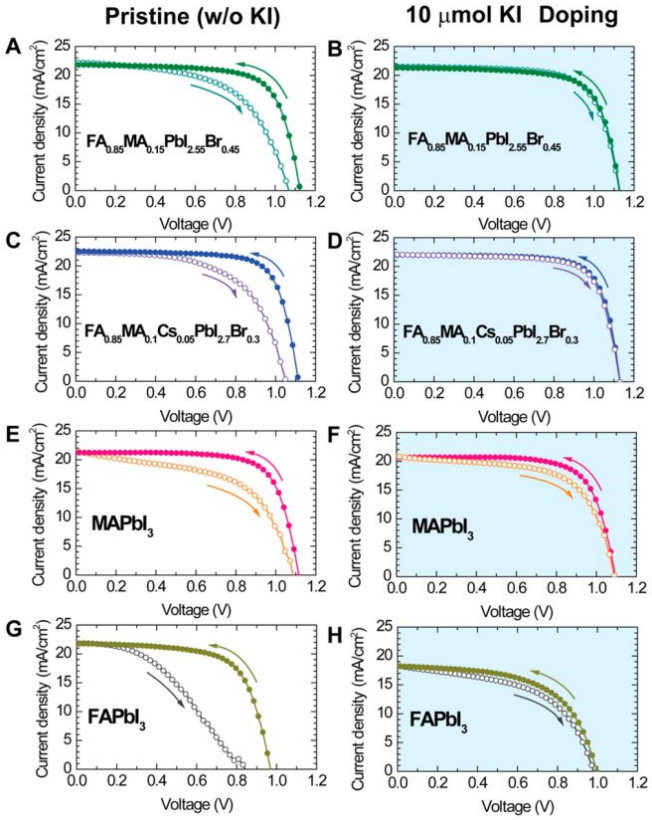

Figure 2.8. Examples of current-voltage (I-V) hysteresis for several MHP PVs (A, C, E, G), highlighting the difference in IV curve as a function of sweep direction. Hysteresis is minimized with the addition of KI doping (B, D, F, H). Reprinted with permission from D. Y. Son *et al.* "Universal Approach toward Hysteresis-Free Perovskite Solar Cell via Defect Engineering". In: Journal of the American Chemical Society 140.4 (2018), pp. 1358-1364. Copyright 2018 American Chemical Society [128].

Initial hypotheses for this behavior included ferroeletric polarization, ion migration, electronic trapping/detrapping, and/or some combination of these factors [125, 128, 129]. While the origins of this IV hysteresis are not universally agreed upon, several studies have suggested that both ion migration and electronic traps play important roles in I-V hysteresis [126, 129–133]. For example, van Reenen *et al.* use a numerical drift-diffusion model to predict I-V curves as a function of ion migration and electronic traps, and find that the inclusion of both is required to adequately model experimental results [130]. Consequently, they hypothesize that hysteresis can be reduced by minimizing the density of mobile ionic species and/or interfacial electronic

traps. Work by Dr. Yunlong Zou, a previous member of the Holmes group, provide evidence for the contribution of mobile ions to hysteresis by demonstrating its strong temperature dependence [134].

Indeed, defect engineering has proven to be a promising route to address hysteresis in PVs. For example, Son *et al.* use potassium iodide (KI) doping to nearly eliminate hysteresis in solar cells based on $FA_{0.85}MA_{0.15}PbI_{2.55}Br_{0.45}$, $FA_{0.85}MA_{0.1}Cs_{0.05}PbI_{2.7}Br_{0.3}$, $MAPbI_3$ and $FAPbI_3$, as seen in Figure 2.8 [128]. They find that this reduction in hysteresis arises from the prevention of Frenkel defects and associated reduction in trap densities due to KI doping.

2.4 Degradation and Stability

One of the major challenges impeding the widespread commercialization of MHPs is their facile degradation when exposed to common environmental factors like oxygen, light, water, and/or heat [59, 135–137]. While some MHP devices have achieved impressive milestones in stability, maintaining 94% PCE over 1000 hours of unencapsulated operation in ambient conditions [138], the typical degradation rate of perovskite solar cells is much faster than commercially acceptable (module lifetime of 20-25 years) [59]. One review finds that the average degradation rate of MHP PV modules is well over 50%/year, compared to $\sim$0.5%/yr for crystalline Si [59]. In addition to having ramifications for maintaining long-term efficiency, this lack of stability is problematic due to the toxicity and water-solubility of common degradation products like PbI_2.

While the precise chemical mechanisms of degradation depend on the specific MHP and the combination of intrinsic and extrinsic stressors, it is widely observed that the composition of the MHP has a substantial impact on stability [135, 137]. Inclusion of organic components, and MA specifically, increases the environmental instability of MHPs, likely due to the myriad of degradation mechanisms involving these organic species [29, 135, 139]. It is also widely observed that tin MHPs are much less stable than Pb-MHPs, which is attributed to the favorable oxidation of Sn^{2+} to Sn^{4+} [140–143]. This mechanism is thought to arise from a thermally activated "cooperative" oxidation process in which multiple adjacent Sn ions are required to simultaneously form the reaction products SnO_2 and SnI_4 [144]. In light of these chemical degradation mechanisms, one of the main routes to improve chemical stability of ABX_3 MHPs has been to avoid Sn and replace MA with more stable cations. For instance, Turren-Cruz *et al.* replace MA with a combination of FA, Cs, and Rb in $Rb_{0.05}Cs_{0.1}FA_{0.85}PbI_3$ to achieve a very

low degradation rate of 0.236% per year (calculated over 1000 hrs at maximum power point operation) [145].

Additionally, most degradation processes occur more quickly at defects such as grain boundaries and at the MHP surface [135, 146]. As such, another common route to improve stability has been the passivation of surfaces and grain boundaries, and/or the use of protective interfacial or encapsulation layers [147, 148]. Passivation has been achieved with a variety of methods, including the addition of ammonium salts, Lewis Acids, Lewis bases, and ionic liquids [135]. 2D/3D perovskites, which often incorporate a large hydrophobic cation, have also been successful to improve the stability of MHPs [29, 61, 62, 149]. Grancini *et al.* achieve a MHP PV with zero loss in performance for $>$10,000 hours by engineering a 2D/3D $(HOOC(CH_2)_4NH_3)_2PbI_4$/$MAPbI_3$ perovskite junction [150].

In addition to the degradation that can happen within an isolated MHP layer, further stability issues arise when these materials are incorporated into multi-layer devices like PVs and PeLEDs. One major challenge is that common transport layers like Spiro-OMeTAD are unstable, and have been shown to degrade even more rapidly than MHPs in some cases [151]. As such, substantial effort has been made to investigate transport layers that are highly stable when implemented in MHP devices [24, 152–156]. For instance, Jin *et al.* replace the problematic Spiro-OMeTAD with inorganic $Cu_{2-x}GeS_3$ to improve device stability [157]. Corrosion of the metal electrodes, often associated with the migration of metal and ionic species between layers, has also been a major source of PV device degradation [158, 159]. Additionally, the operation conditions of the device (*i.e.*, applied electric field) can accelerate degradation by contributing to the movement of ionic species; this is especially important in devices that operate at higher biases such as PeLEDs [137].

Due to the intrinsically fragile nature of MHP materials, it seems likely that a combination of techniques (including optimizing MHP chemistry, film morphology, and barrier layers) will be required if they are to reach commercial viability. And, due to the toxic nature of Pb- and Sn-based MHPs, careful thought must be taken to minimize the potential leakage of these compounds into the surroundings. Interesting approaches to this challenge are already underway, like the development of ”on-device” Pb sequestration strategies to retain any potential leakage in the case of catastrophic damage [160].

Chapter 3

Thin Film Fabrication Techniques

One of the reasons that MHP research has increased so quickly over the last decade is likely due to the ability to synthesize MHPs with a wide variety of relatively facile, low temperature techniques. All conformations of MHP materials, including thin films, nanocrystals/quantum dots, and larger single crystals have multiple methods which have proven viable to create high-performing materials [161]; common techniques are shown schematically in Figure 3.1. In this Chapter, I briefly review the most common synthesis techniques for thin-film MHPs, with a focus on vapor-based methods, which hold promise for industrial applications and form the basis of my thesis work.

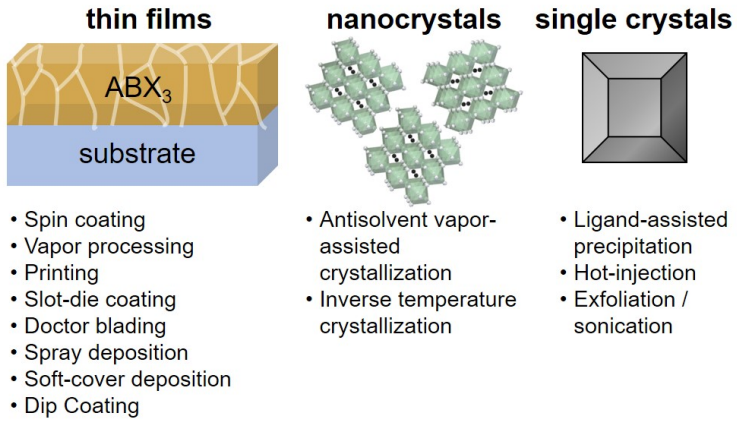

Figure 3.1. Examples of common synthesis techniques for MHP thin films, nanocrystals, and large single crystals. Adapted from ref [161].

3.1 Solution-Based Methods

The vast majority of thin film MHPs are made using solvent based techniques, likely due to their simplicity, low cost, and low barrier of entry for research [162, 163]. Among this class of techniques, spin-coating is by far the most common; and even within this spin-coating method there are a myriad of variations that have been explored in the literature. Broadly, spin-coating methods are typically classified into "one-step" [164, 165] and "two-step" [166–171] categories. Schematics of these methods are shown in Figure 3.2. In one-step methods, all precursor powders (e.g. MAI and PbI_2 for $MAPbI_3$) are dissolved in a single solution, which is applied to the substrate. On the other hand, two-step methods involve first depositing only the metal halide onto the film *via* spin-coating, and then introducing the organic halide in either solution or vapor phase. For Pb perovskites, annealing steps are required after spin coating in order for the AX and BX_2 species to react (as well as to drive any remaining solvent out of the film). For Sn ABX_3 perovskites, this reaction happens spontaneously at room temperature.

While both one-step and two-step methods are still employed, the general trend of the field seems to be favoring one-step methods where AX and BX_2 precursors are all dissolved in the same solution, as generating controllable crystallization and conversion to the perovskite is more challenging in the two step method, especially for mixed A-, B- and/or X-site MHP formulations [172]. Indeed, high efficiency mixed A- and X- site PV devices are fabricated using the one-step method [21, 173, 174].

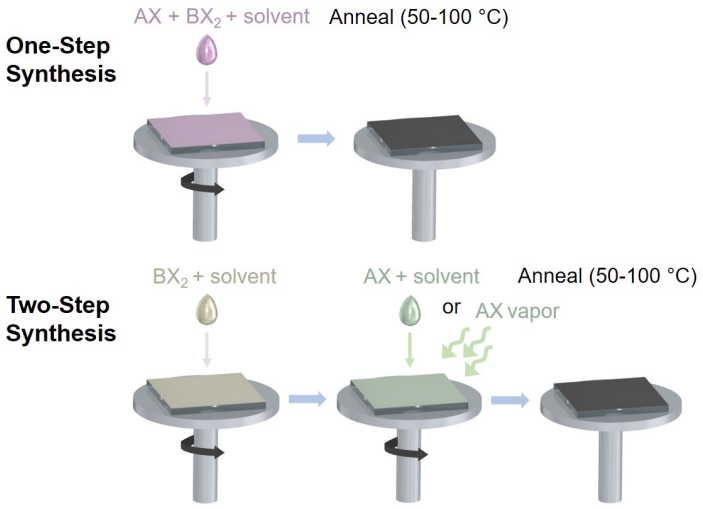

Figure 3.2. Examples of one step (top) and two-step (bottom) spin-coating synthesis methods. In the two-step method, reaction with AX can be accomplished either through a secondary spin-coating step or by vapor treatment. Colors are used for clarity and do not necessarily represent film colors.

Within these broad categories of spin-coating, many additional techniques have been employed to improve film quality and resulting device performance: nearly every high efficiency devices uses a procedure more complicated than the simplistic ones shown in Figure 3.2. One of the most common additions is the use of an antisolvent to accelerate crystallization during spin-coating [21, 173–175]. This method applies a solvent in which the MHP has low solubility, like chlorobenzene, as a secondary step after the MHP solution has already been deposited on the substrate. By reducing the solubility of the MHP precursors, this method tends to increase nucleation density (compared to films without antisolvent addition), resulting in flat, uniform, pinhole free films. For example, Zhu *et al.* use a one-step spincoating plus antisolvent method, combined with a bulky ligand additive (4-tert-butyl-benzylammonium iodide), to achieve a MHP PV with 23.5% power conversion efficiency [21]. An example of the result of employing an antisolvent treatment on a $MAPbBr_3$ film can be seen in Figure 3.3. Here, my application of 200 μL of chlorobenzene 15s into the spincoating cycle had a dramatic impact on grain size and surface coverage.

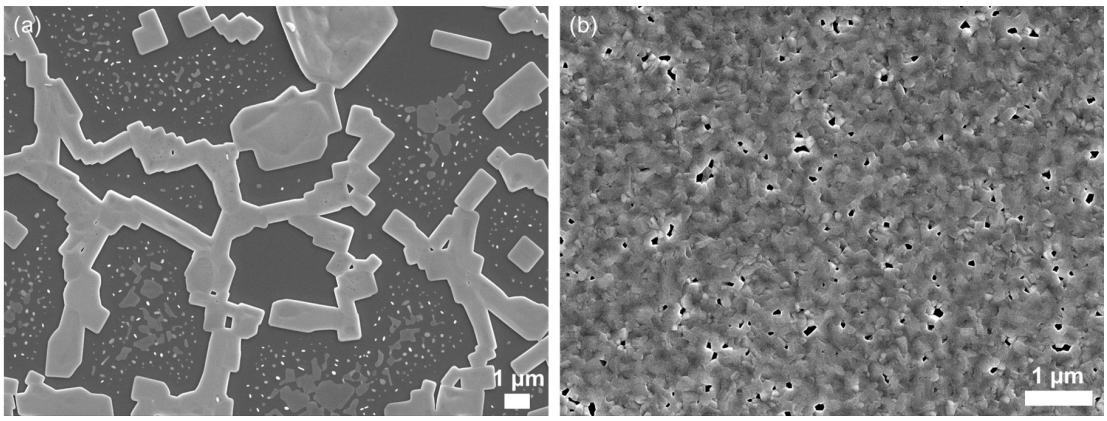

Figure 3.3. Impact of anti-solvent drip during spin coating for $MAPbBr_3$. MABr + $SnBr_2$ in 1:4 vol% DMF:DMSO solution was static spun on Si wafers at 3000 rpm. In (a), the film was allowed to spin for 2 minutes until dry, whereas in (b) 200 μL of chlorobenzene was dropped onto the film 15 seconds into the spinning cycle.

As shown in Figure 3.1, there are many other solution-based synthesis techniques to deposit MHP thin films. These include but are not limited to printing [176, 177], slot-die coating [178, 179], blade coating [180, 181], spray deposition [182, 183], soft-cover deposition [184], and dip coating [185, 186]. While the development of most of these methods is still in early stages, they

are becoming increasingly important as a means to fabricate large area devices [163]. As the field moves towards commercialization, it will be interesting to see which of these techniques become the most viable for high-throughput, cost effective fabrication that can result in high quality films and high efficiency devices.

3.2 Vapor-Based Methods

Compared to solution-based methods, vapor deposition techniques have several advantages. They can be used with a wide array of MHP precursors without the need to substantially tune the synthesis method, and similarly accommodate multiple precursor materials which may not have compatible solubilities. They also allow incremental tuning of film morphologies (*e.g.* grain size) across a wide range without changes in chemistry. The purity of MHP materials can also be tightly controlled with vapor-based methods, which is critical for their efficiency and long-term stability in devices. Vapor techniques also typically allow for precise thickness control. Importantly, vapor deposition also enables the fabrication of multi-layer stacks, like all-perovskite heterojunctions, which are inaccessible with standard solution-based methods because of the common solubility of neighboring layers. Finally, vapor based methods have been proven to be industrially relevant as they are currently commercialized for organic light-emitting devices.

Currently, the body of research using vapor-phase deposition for MHPs is relatively small compared to solution based methods. Figure 3.4 highlights this, showing the power conversion efficiency vs. active area for MHP solar cells $<$10 cm^2, in which only two reports use a fully vapor deposited MHP (one denoted ”CVD” and one denoted ”co-evaporation”; the other vapor methods also have a solution processed step) [187]. Despite this, the nascent body of work on vapor-deposited metal halide perovskites has already demonstrated deposition on large-area flexible substrates and fine control over film composition and morphology [188–227]. Vapor deposition has also been used to fabricate an interlayer-free 2-terminal perovskite-Si tandem cell, thus providing a practical route to tandem and multi-layer perovskite solar cells [228].

However, the efficiencies of vapor-based MHP devices are still significantly lower than those of their solution-based counterparts. Since 2016, the highest efficiency for a fully vacuum deposited MHP solar cell has hovered between 20 and 21%, compared to the over 25% achieved using solution methods [19, 187, 190, 227, 229]. As such, significant work must be done to

harness the power of this technique to achieve parity with solution processed device efficiencies, as well as for fabricating novel HP films and layered structures.

In general, vapor-based methods for MHPs have fallen under two categories: high-vacuum thermal evaporation (VTE) and low- to medium-vacuum CVD-type methods. Schematics for these two broad categories are shown in Figure 3.5. In high-vacuum thermal evaporation, also commonly referred to as physical vapor deposition (PVD) in the MHP literature, source material is resistively heated in a chamber operating in the range of 10^{-5}-10^{-7} Torr, and sublimes in a plume-like geometry. Typically, the substrate and walls are relatively cold compared to the material sublimation temperatures, and as such the vapor condenses when it encounters these surfaces. Deposition rate is often monitored *via* the use of quartz crystal microbalances, or QCMs. CVD-type techniques, as depicted in Figure 3.5b, operate at higher pressures, generally above 10^{-2} Torr, and in a hot-walled reactor. Here, the sublimed material vapor is transported *via* carrier gas to the substrate surface where it selectively condenses. In both of these methods, materials can either be deposited at the same time (co-deposition) or sequentially, and films can be annealed during and/or after deposition.

Among these two configurations, the most commonly employed vapor deposition method

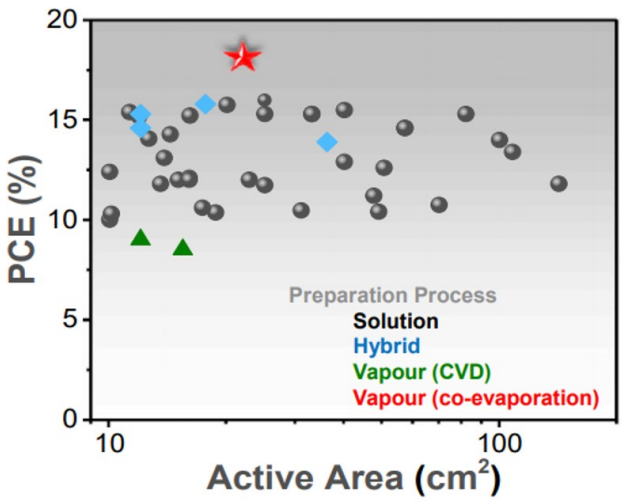

Figure 3.4. Power conversion efficiency (PCE) vs. active area for MHP solar cells, separated by processing technique. Among these reports, only two use a fully-vapor deposited MHP layer (one denoted "CVD" and one denoted "co-evaporation"; the other vapor methods also have a solution processed step). Reprinted from Joule, 5, J. Li *et al.*, "Highly Efficient Thermally Co-evaporated Perovskite Solar Cells and Mini-modules", 1035-1053, Copyright 2020, with permission from Elsevier [187].

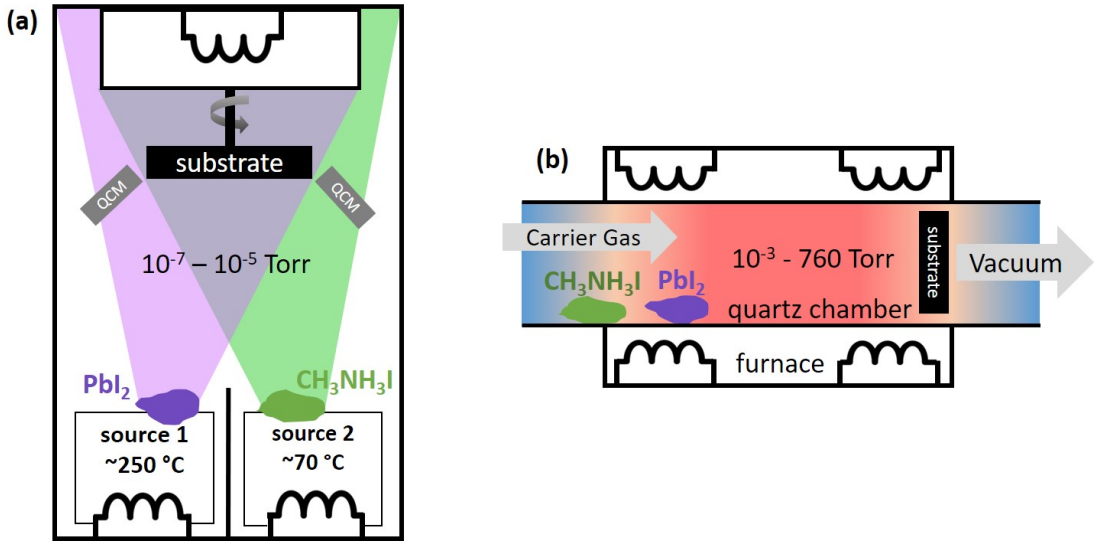

Figure 3.5. Schematics of vapor deposition systems for MHPs. (a) High-vacuum thermal evaporation (VTE), showing sublimation of two precursor materials under resistive heating. Deposition rate and the resulting film thickness is typically monitored *via* QCMs. (b) CVD-type, low-to medium-vacuum system, where a carrier gas transports sublimed vapors through a hot-walled reactor to the substrate, where they selectively condense.

by far is the VTE approach, either with co-evaporation or sequential evaporation of the precursor materials [188–203]. VTE techniques typically excel at very fine levels of stoichiometric and thickness control, and can result in high-purity films. Indeed, all of the fully vacuum processed MHP PVs that have achieved >20% efficiency used the VTE method [187, 190, 227, 229]. Early works for high-efficiency VTE devices include a 20% PCE fully vacuum deposited[1] $MAPbI_3$ perovskite *via* co-evaporation of MAI and PbI_2 by Mombolona *et al.* in 2016 [227]. Shortly thereafter, Zhu *et al.*, realized a >20% efficient planar solar cell using a $MA_{0.77}Cs_{0.23}PbI_3$ absorber deposited *via* co-evaporation of $PbCl_2$ and CsCl, followed by an MAI treatment at atmospheric pressure [190]. Very recently in May 2020, Li *et al.* achieved a record efficiency of 18.13% for a large area, 21 cm^2 device using VTE with co-deposition of MAI and PbI_2 [187]. Although not resulting in a device with >20% PCE, recent experiments using VTE co-evaporation have also shown impressive capabilities to tune grain size of $MAPbI_3$ film from hundreds of nm to microns by changing substrate temperature [230].

[1] including all transport layers

Despite these promising reports, VTE deposition is not without its limitations. One of the challenges commonly observed with VTE of hybrid MHPs is the high background pressure resulting from the large volatility of organic halides like MAI [187]. Instead of subliming in a plume-like geometry as depicted in Figure 3.5a, the MAI vapor will fill the chamber, thereby making deposition rate monitoring using standard QCM configurations nearly impossible [187, 204]. For instance, MAI has been observed to deposit on the *back* side of the QCM, which has no line-of-sight to the MAI source [193]. To circumvent this issue, creative solutions have been implemented whereby the QCMs are situated facing opposite of the MAI source or are placed behind a permanently closed shutter, thereby improving the accuracy of deposition rate sensing by measuring the overall MAI pressure in the chamber [192, 193]. Furthermore, it has been demonstrated that the deposition rate of MAI depends strongly on MAH_2PO_x impurities in the starting material, which often vary from batch to batch, therefore making consistent deposition of MAI even more challenging [231]. While these impurities can be reduced by improved washing techniques [231], precursor purification is not widely reported in the literature.

An alternative but understudied approach is the CVD-type carrier-gas assisted vapor deposition method shown in Figure 3.5b. While this type of technique is commonly referred to as "CVD" in the MHP literature, I will use the term CGAVD here to emphasize the use of a carrier gas and the lack of gas-phase reactions. CGAVD methods typically provide a large parameter space to tune film composition and microstructure (as we show in detail in Chapter 5), and have been employed widely in the context of organic semiconductors to realize exquisite control of composition and morphology in planar and bulk heterojunction devices [232–237]. For metal halide perovskites, however, CGAVD has been only sporadically used, appearing in less than $\sim$ 50 papers in total. Most implementations have used a "hybrid" approach, where the metal halide (*e.g.* PbI_2) film is first deposited using a solution or high-vacuum process, and then CGAVD is used to expose that film to the organic halide (*e.g.* MAI). This method was pioneered by the Qi group at Okinawa Institute of Science and Technology [206, 238–242], with the Cui groups (University of Minnesota) [224, 225] and Lu groups (Hefei University of Technology) [208, 222, 223] also making notable contributions. Using this hybrid approach to synthesize $Cs_{0.1}FA_{0.9}PbI_{2.9}Br_{0.1}$, Qiu *et al.* achieve an impressive 10% PCE for a relatively large area (91.8 cm^2) solar module [240]. For smaller area devices, power conversion efficiencies using this hybrid technique have achieved just over 15% [206, 207, 241].

For MHP films where both metal-halide and organic-halide are deposited at the same time

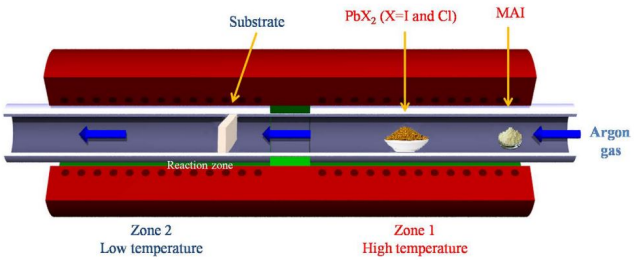

Figure 3.6. Schematic of CGAVD setup from Tavakoli *et al.*, which they use to co-evaporate PbX_2 and MAI to fabricate 11.1% efficient photovoltaic cells. Reproduced with permission from [205].

using CGAVD, there are even fewer reports. In fact, we are aware of only *one* report where the full perovskite film is deposited using CGAVD [243]. In this work, large $\sim$1 μm grained, pinhole free $MAPbI_{3-x}Cl_x$ films were formed *via* codeposition in CGAVD and incorporated into 11.1% efficient photovoltaic cells [205]. While this efficiency value is relatively low compared to other vapor and solution based methods, this is expected given the limited exploration of this technique. A schematic of the setup presented by Tavakoli *et al.* is shown in Figure 3.6, where the MAI and PbX_2 powders appear to be situated in crucibles sitting directly inside of the reaction chamber. Given this schematic, it appears that there is only one carrier gas flow, no substrate cooling, and no additional control for chamber pressure. While this work provides a validation that both PbX_2 and MAI can be deposited within the same CGAVD chamber, additional control and tunability will likely be required for optimization of this method.

In addition to the overall limited reports, none of the works published utilizing CGAVD for MHPs provide an in-depth or comprehensive exploration of how deposition conditions impact morphologies, or what range of stoichiometries and morphologies are even accessible with this technique. Furthermore, no papers report the deposition of Sn-based or other non-Pb MHPs using CGAVD. Consequently, there is substantial room for further exploration and development of this powerful technique that has already resulted in relatively high efficiencies, can allow facile tuning of morphologies and stoichiometries as well as the deposition of multi-layer MHPs, and has commercial relevance for deposition of large-area MHP films. As such, the majority of my PhD work focused on implementing, developing, and applying this promising technique towards a deeper and richer understanding of its capabilities.

Chapter 4

Design and Development of Carrier-Gas Assisted Vapor Deposition System

As discussed in Chapter 3, carrier-gas assisted vapor deposition (CGAVD) techniques are not well established for metal halide perovskites. A main goal of my research was to carefully develop and apply this technique to MHPs: I sought to investigate the growth behavior of perovskite films in detail in order to build a foundation of knowledge for this technique that would enable myself and others to systematically grow perovskite films. This work was guided by the success criteria presented in Section 4.1 and accomplished in three major phases. The first (Section 4.2) involved building and testing a relatively simple proof-of-concept setup in order to demonstrate that a CGAVD system would indeed work to grow MHP thin films. After verifying this method, we then focussed on the detailed design of a 4-source CGAVD chamber with cooled substrate (Section 4.3). To validate and test this design, an analytical model was developed to understand material transport and deposition as a function of operating conditions, and experiments were done to assess the overall system performance against the success criteria (Section 4.4). The development of a detailed understanding of the operation of this CGAVD setup enabled us to later grow and investigate of a variety of MHP films and heterostructures (Chapters 5–7).

4.1 Design Goals and Success Criteria

In order to build a system that allows a detailed understanding of how system pressures, temperatures, and flow rates impact film growth rates, stoichiometries, and microstructure, and to enable the growth of films that would be relevant for eventual incorporation into optoelectronic devices, I came up with the following success criteria to guide our system design:

(1) **Enable the deposition of common precursor materials** for MHPs including but not limited to: SnI_2, $SnBr_2$, PbI_2, $PbBr_2$, MAI, and MABr. This is a basic requirement that is necessary to grow a variety of MHP films with this technique.

(2) Allow these materials to be either **sequentially deposited or co-deposited** to enable the study of how this impacts film properties and performance.

(3) Enable **control of the flux ratio** of the materials being deposited. This is required in order to tune film stoichiometry and deposition rate, which are expected to impact film morphology.

(4) Provide **sufficient experimental parameter space** to enable films to be deposited with a wide range of stoichiometries and morphologies (including grain size, roughness, orientation), in order to study how these impact film properties and device performance.

(5) Yield films with **lateral (in-plane) uniformity** in thickness, stoichiometry, and morphology across a length-scale relevant for studying optoelectronic devices ($\sim$cm).

(6) Minimize growth-to-growth variation for **experimental repeatability**.

4.2 Prototype

In order to test if a CGAVD technique could achieve the first goal outlined in Section 4.1, I first built a simplified, one-source prototype depicted in Figure 4.1. Here, my aim was simple: to test if I could form a tin perovskite (e.g. $MASnI_3$) by depositing both precursors using carrier-gas assisted vapor deposition.

This system was comprised mainly of components that already existed in our lab, including a 3-zone tube furnace, a 1.5” OD quartz tube to act as the deposition chamber, a custom quartz ampoule to hold the source material, an aluminum substrate holder (with bolts to secure the substrate) attached to a linear feed-through, rough vacuum and purge gas connections, and KF

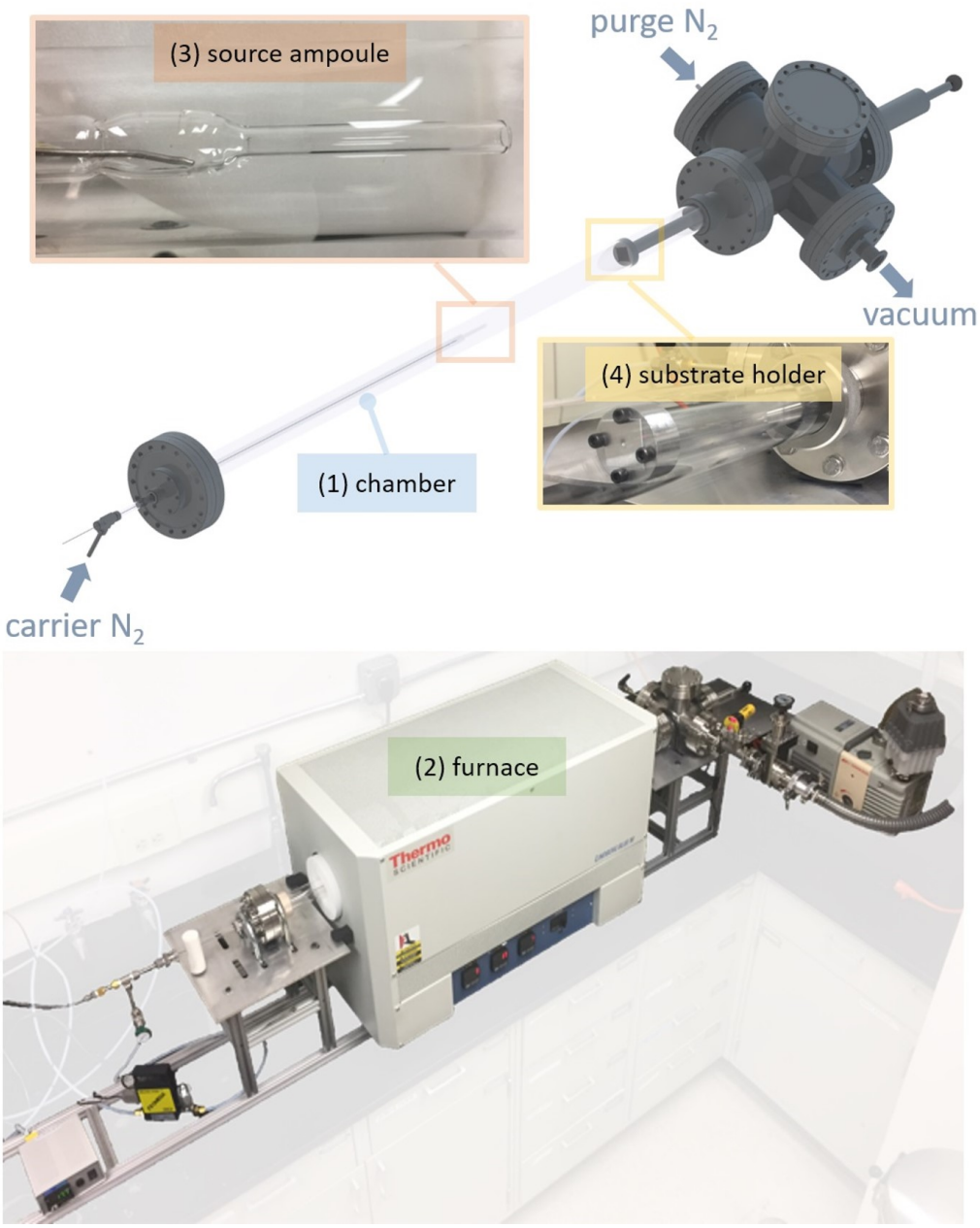

Figure 4.1. Schematic (top) and picture (bottom) showing prototype vapor deposition setup, including the quartz chamber (1), furnace (2), source ampoule (3), and substrate holder on linear feedthrough (4).

and ultra-torr fittings to connect and seal these components. With this setup, I was able to tune four different experimental variables:

1. **carrier gas flow-rate ($\dot{\mathbf{V}}$)** - using a mass flow controller
2. **chamber pressure (P)** - a function of both the carrier gas flow rate and the position of a gate valve prior to the rough pump
3. **substrate temperature ($\mathbf{T}_{sub}$)** - by moving the substrate axial position
4. **source temperature ($\mathbf{T}_{source}$)** - by moving the source ampoule axial position

Prior to depositing precursor materials, I first mapped out the temperature profile in the quartz chamber using thermocouples inserted into the source ampoule and the substrate holder. This was required in order to understand what temperature ranges were accessible for both the source and substrate, how steep temperature gradients were, and how these temperatures depended on the oven temperature and chamber pressure. Measuring at a variety of furnace temperatures and carrier gas flow rates, I constructed the temperature profiles shown in Figure 4.2. As expected, the temperatures rises from room temperature outside the chamber to the furnace setpoint at 10-15 inches into the chamber. These temperature profiles were also confirmed using finite element analysis (FEA) in COMSOL, which matched well with the experimental results found in Figure 4.2. Details for these FEA simulations can be found in Figure D.1.

Using these temperature profiles to inform the axial placement of source material, I then

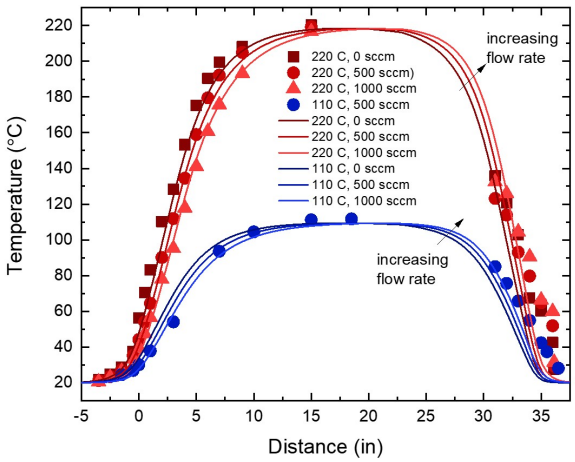

Figure 4.2. Experimentally measured (symbols) and FEA simulated (lines) chamber temperature profiles as a function of axial distance into the chamber at various oven temperatures (110 °C and 220 °C) and carrier gas flow rates (0 - 1000 sccm). Oven temperature has a much larger impact on the temperature profile than carrier gas flow rate.

demonstrated the successful deposition of two MHP precursors: MAI and SnI_2. These materials were deposited separately on a variety of substrates, including glass, ITO, and c-TiO_2. Importantly, both MAI and SnI_2 depositions were done using the same oven temperature, suggesting that it would be possible to co-deposit these materials given the space for multiple source ampoules. Examples of these initial depositions can be seen in Figure 4.3, showing XRD patterns and absorption spectra for typical films. This result proved that CGAVD could enable the deposition of both organic and metal halide powders necessary for perovskite formation without requiring substantially different furnace setpoint temperatures.

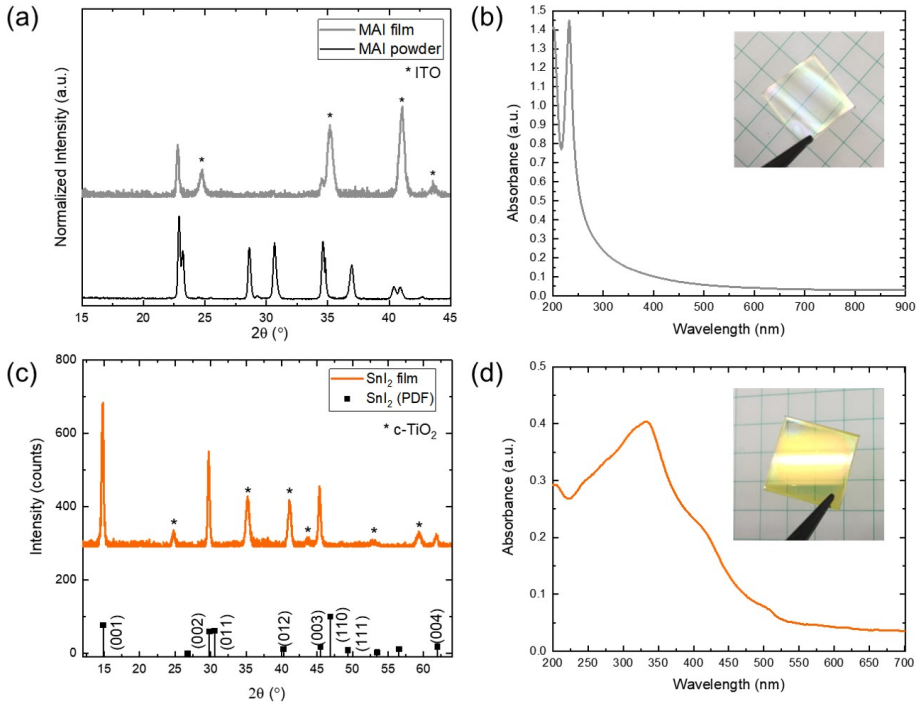

Figure 4.3. Examples of typical MAI (a and b) and SnI_2 (c and d) depositions using the prototype CGAVD system. (a) and (c) show XRD patterns and (b) and (d) show absorption spectra for these films; insets show typical colors of MAI (white/clear) and SnI_2 (yellow) films deposited on 1x1 cm ITO substrates. X-ray diffraction was collected using a Bruker D8 2D diffractometer with Co Kα radiation (λ=1.7889 Å). Deposition conditions for these films were T_{oven} = 220 °C, $\dot{V}$ = 200 sccm, P = 0.5 Torr, T_{SnI_2} = 220 °C, T_{MAI} = 110 °C, T_{sub} = 55 - 170 °C.

While this prototype system only had one source ampoule, and thus could only enable sequential deposition, I wanted to test the possibility to form full perovskites in CGAVD prior to constructing the next generation system. To do that, I made a slight modification to the substrate holder by attaching an aluminum rail to the existing puck, thereby changing the orientation of the substrates with respect to the impinging gas flow (parallel instead of perpendicular) as well as allowing multiple substrates to be loaded at the same time. This modified substrate holder loaded with three glass slides can be seen in Figure 4.4a, which also shows the result of sequential SnI_2 and MAI depositions.

These sequential depositions highlight several important results. The first is the successful formation of phase-pure $MASnI_3$ perovskite using this technique, which corresponds to the black film at location 1 in Figure 4.4a. Absorbance, PL, and XRD data for this location can be seen in Figure 4.4b-c and align well with literature reports [140]. Additionally, the axial

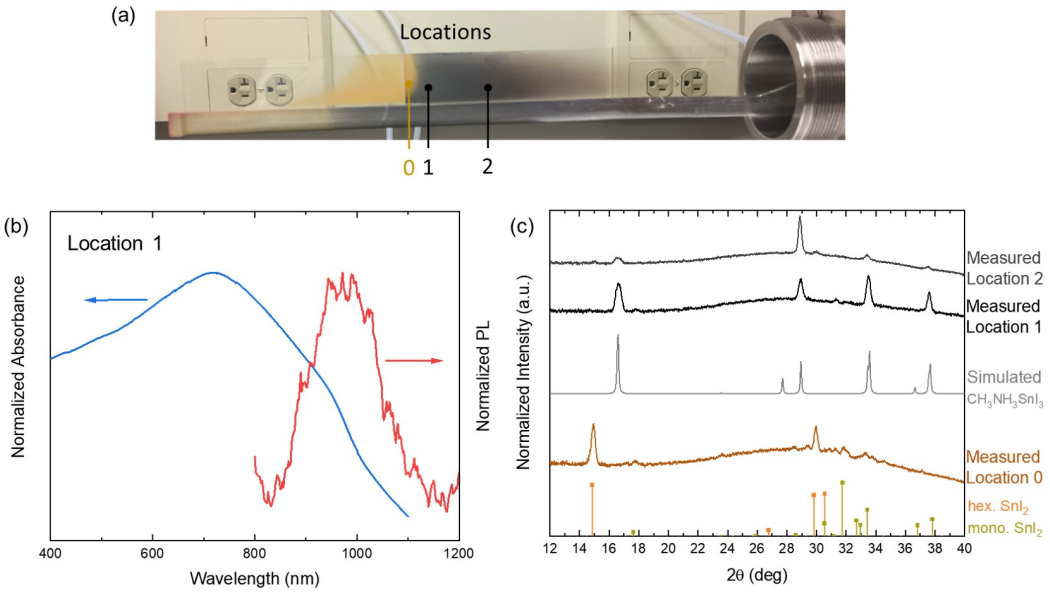

Figure 4.4. First successful deposition of MHP in the CGAVD prototype system *via* sequential deposition of SnI_2 and MAI on glass. (a) Picture of modified substrate holder as well as results of sequential deposition of SnI_2 and MAI. (b) Absorbance and PL spectra for location 1. (c) XRD patterns for locations 0, 1, and 2. X-ray diffraction was collected using a Bruker D8 2D diffractometer with Co Kα radiation (λ=1.7889 Å). Deposition conditions for these films were T_{oven} = 220 °C, $\dot{V}$ = 200 sccm, P = 0.5 Torr, T_{SnI_2} = 220 °C, T_{MAI} = 110 °C.

locations of condensation of SnI_2 and MAI on the substrates appear to be visually different. In Figure 4.4a, it is clear that there is an area of yellow film prior to the onset of the black film. XRD (Figure 4.4c) confirms that the yellow film in location 0 corresponds to SnI_2, implying that the SnI_2 vapor began to condense on these substrates earlier (*i.e.* at higher temperatures) than MAI. While this finding aligns with our expectations given the higher sublimation enthalpy of SnI_2 compared to MAI, it also highlights a limitation of this type of substrate holder design. While our prototype design allowed us to linearly actuate the substrate to reach different substrate temperatures, Figure 4.4a makes clear that the location/temperature of the substrate is inextricably coupled with if, and how much, material would end up depositing on the substrate. Thus, our ability to get material to deposit at significantly different substrate temperatures was limited with this design. This motivated the design of an actively cooled substrate holder as discussed in Section 4.3.3.

Another obvious issue with our prototype design is the limitation of having only one source material loaded at a time due to the singular ampoule—making it impossible to test co-deposition of materials in this configuration. This was addressed in the next design iteration by the incorporation of four separate sources (Section 4.3.2).

In summary, our CGAVD prototype design allowed us to successfully deposit both organic and inorganic precursors at the same oven temperature, and form a full MHP from sequential deposition. We also demonstrated *via* our finite-element modeling (Appendix D) that we understood the thermal behavior and dominant mechanisms driving the temperature profiles in this system. These results addressed goal 1 outlined in Section 4.1, which was to enable the deposition of common precursor materials. It also partially addressed goal 2, which was to enable both sequential and/or co-deposition of these precursors. In order to address the remaining goals (2–6), we needed to significantly improve and alter the design, which is presented in the following section.

4.3 Detailed Final Design

The details of our final CGAVD system design resulted from the consideration of many factors, including lessons learned during our prototype development, restrictions associated with the use of existing equipment (*e.g.* the tube furnace), and by the design of similar systems in the literature. This section discusses the overall system design as well as detailed designs for the

4-source manifold, cooled substrate holder, and system enclosure. Note that many of the components discussed in this section were custom designed; detailed drawings of these components can be found in Appendix D.

4.3.1 Overall System Design

A substantial portion of the overall/conceptual design for our final CGAVD setup was based off of the low-pressure organic vapor phase deposition (LP-OVPD) system developed by Shtein *et al.* and described in detail in ref [234]. A schematic of this system is shown in Figure 4.5. Major components include a 3-zone tube furnace and tubular chamber, multiple source ampoules/barrels fitted with their own material holders and thermocouples, separate carrier gas and sheath (purge) gas sources, and a rotating, linearly actuatable water-cooled substrate holder outfitted with a shutter and thickness monitor. Using this system, Shtein *et al.* have studied the mechanisms of material transport in carrier-gas assisted vapor deposition for materials like Alq_3, DCM2, and α-NPD in detail [234]. Due to the extensive tunability of this setup, the detailed understanding of how this deposition system behaves for organic materials, and the similarities between our furnace configurations, we modeled our overall system design on that presented by Shtein *et al.* [234].

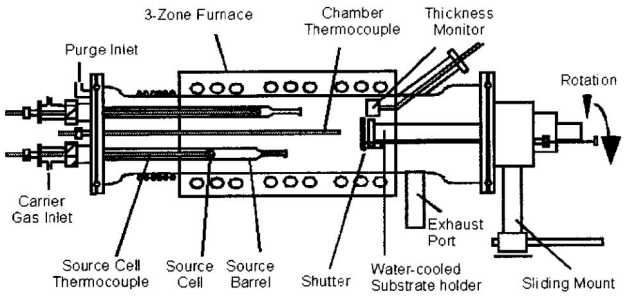

Figure 4.5. Schematic of low-pressure organic vapor phase deposition (LP-OVPD) system, reproduced from [234], that formed the basis for our conceptual design. Reprinted from M. Shtein *et al.* "Material transport regimes and mechanisms for growth of molecular organic thin films using low-pressure organic vapor phase deposition". In: Journal of Applied Physics 89.2 (2001), pp.1470-1476, with the permission of AIP Publishing.

As such, our system contains many similar components to the design in Figure 4.5. A simplified 3D model and schematic is shown in Figure 4.6, and consists of a 3" diameter quartz

tube inside a three-zone cylindrical furnace.[1] The axial temperature profile within the tube is controlled by the furnace temperature set points. Four 0.5" diameter quartz tubes are positioned eccentrically inside the larger 3" tube. Within each 0.5" tube, source material powder (*e.g.*, MABr, MAI, $SnBr_2$, or SnI_2) is packed in a fritted gas dispersion tube[2] and attached to a linear feedthrough with embedded thermocouples for real-time temperature monitoring. These linear feedthroughs are used to translate the sources axially (*via* an ultra-torr fitting) to vary source material temperature. For more details see Section 4.3.2.

Nitrogen, the carrier gas, flows through each source tube and over the source material, carrying sublimed vapor towards a cooled substrate as depicted in Figure 4.6b. The tubes-within-tubes arrangement with independent carrier gas flows for each source minimizes back flow and source material contamination, and allows independent control of material flux for each source

[1]The outer dimension of the quartz chamber was limited to ∼3" by the inner diameter of the tube furnace.

[2]This was later changed to a custom-made quartz powder holder in order to reduce the deposition and sticking of powder to the linear feedthroughs. Schematics for this holder are shown in Section D.2.

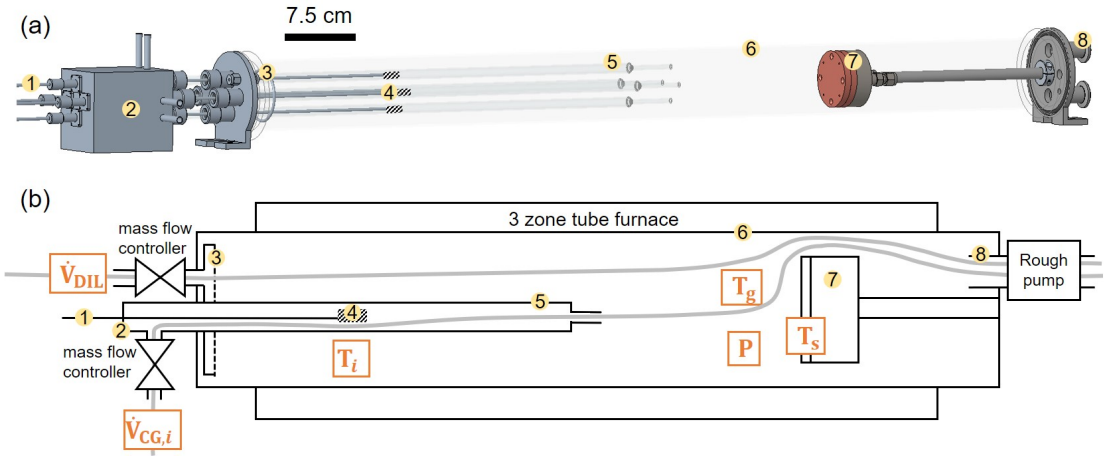

Figure 4.6. (a) CAD model (to scale) of final CGAVD system design. (b) Schematic highlighting the six independent experimental parameters in CGAVD (orange boxes): the carrier gas flow rate $\dot{V}_{CG,i}$; the dilution gas flow rate $\dot{V}_{DIL}$; the source material temperature T_i; the gas temperature T_g; the substrate temperature T_s; and the deposition pressure P. Part numbers are defined as follows: (1) linear actuator with embedded thermocouple; (2) N_2 carrier gas manifold; (3) showerhead for dilution gas delivery; (4) source material attached to linear actuator; (5) source material ampoule; (6) 3" diameter quartz chamber; (7) water-cooled substrate holder; (8) ports for rough pump. Note that the schematic in (b) only shows one source material ampoule instead of four for clarity.

(discussed further in Sections 4.3.2 and 4.4). Additional N_2 is fed into the annular region around the source material tubes (item 3 in Figure 4.6). This flow dilutes the vapors emerging from the source tubes, providing additional control over the species fluxes independent from the source material evaporation rate and chamber pressure; it also reduces backwards diffusion and condensation of sublimed vapor which serves to keep the chamber clean. After exiting the source tube, the vapors impinge, condense, and/or react on the cooled substrate to form films.

Using this configuration, we address two of the major issues identified in our prototype design: the lack of separate material ampoules and the coupling between substrate temperature and amount of material condensation. Furthermore, we have two additional experimental parameters we can adjust to tune deposition conditions. In total, then, our final CGAVD design has six experimental parameters that can be varied *independently* to alter the deposition of a source material i:

1. the carrier gas flow rate, $\mathbf{V}_{CG,i}$,
2. the chamber dilution gas flow rate, $\mathbf{V}_{DIL}$,
3. the source material temperature, $\mathbf{T}_i$,
4. the chamber gas temperature, $\mathbf{T}_g$,
5. the substrate temperature, $\mathbf{T}_s$,
6. and the total chamber pressure, $\mathbf{P}$.

These six independent parameters are highlighted in orange in Figure 4.6b. All gas flow rates are set and maintained constant during deposition by mass flow controllers, with the exception of $\dot{\mathrm{V}}_{DIL}$ which is controlled by a needle valve and recorded as a change in total chamber pressure using a pressure gauge. The substrate temperature, T_s, is adjusted by changing cooling water temperature and/or flow rate. The total pressure, P, is controlled by a combination of dilution gas and a gate valve aft of the rough pump. A detailed treatment of how these parameters impact deposition rate is presented in Section 4.4.1.

Compared to the LP-OVPD system used by Shtein *et al.* and presented in Figure 4.5, our system has a few major differences. The first is the lack of chamber thermocouple in our system; instead of measuring the temperature *in-situ*, we find that our chamber temperature is relatively stable and constant for a given oven temperature as seen in Figure 4.2. Thus, in setting the oven temperature, we can accurately know the temperature of the gas prior to the substrate, with an accuracy of less than 10 °C. Second, our substrate holder is not rotating nor on a linear actuator.

Due to the expense of these types of components (especially when combined with water cooling), we chose to implement them only in stages if deemed necessary. Interestingly, we find that rotation is not necessary to achieve films that are laterally uniform,[3] as described in detail in Section 4.4.2. Furthermore, we designed the axial location of our substrate holder in order to maximize material deposition on the substrate, and coupled with active water cooling, determined that linear actuation was not necessary to control deposition and substrate temperature. While we have not measured our materials utilization efficiency rigorously, visually-obvious regions of deposition are confined to the front surface of the substrate holder for typical operating conditions.[4] Finally, our system does not have a way to monitor film thickness *in-situ*. This is due largely to the geometric limitations imposed by our furnace. Given the 3" OD of our deposition chamber, we were not able to fit a quartz-crystal microbalance (QCM) type monitoring system without blocking our substrate substantially. Using an ellipsometric-type thickness monitoring system was also considered, but would have required substantial modifications to the oven and chamber, which were deemed unfeasible for this design. As discussed in Section 8.2.4, the addition of thickness monitoring is something to be considered if this system undergoes future design iterations.

4.3.2 Four Source Assembly

In order to enable the co-deposition of multiple precursor materials, our final CGAVD system required a design containing multiple sources. Building off of our prototype and the configuration outlined by Shtein *et al.* [234], we chose to implement a tubes-in-tubes arrangement whereby each source material would be situated inside of an individual quartz ampoule with an independently controllable carrier gas flow. The space limitations imposed by our furnace and chamber size limited the number of possible sources to four; where each source ampoule was 0.5" in diameter. As typical MHP materials require two precursor materials, having four sources was deemed sufficient as it would enable us to deposit two different MHPs without re-loading sources, as well as to make more complicated mixed A, B, and/or X site MHPs.

In order to supply separate carrier gas flows to each source, we designed a custom N_2 manifold as depicted in Figure 4.7. Here, a system of Swagelok-connected tubes would feed separate

[3] over an area of at least 4 cm^2

[4] However, materials utilization efficiency, which can be qualitatively observed by visually noting the regions of deposition in the chamber, is significantly reduced at high substrate temperatures and very low chamber pressures.

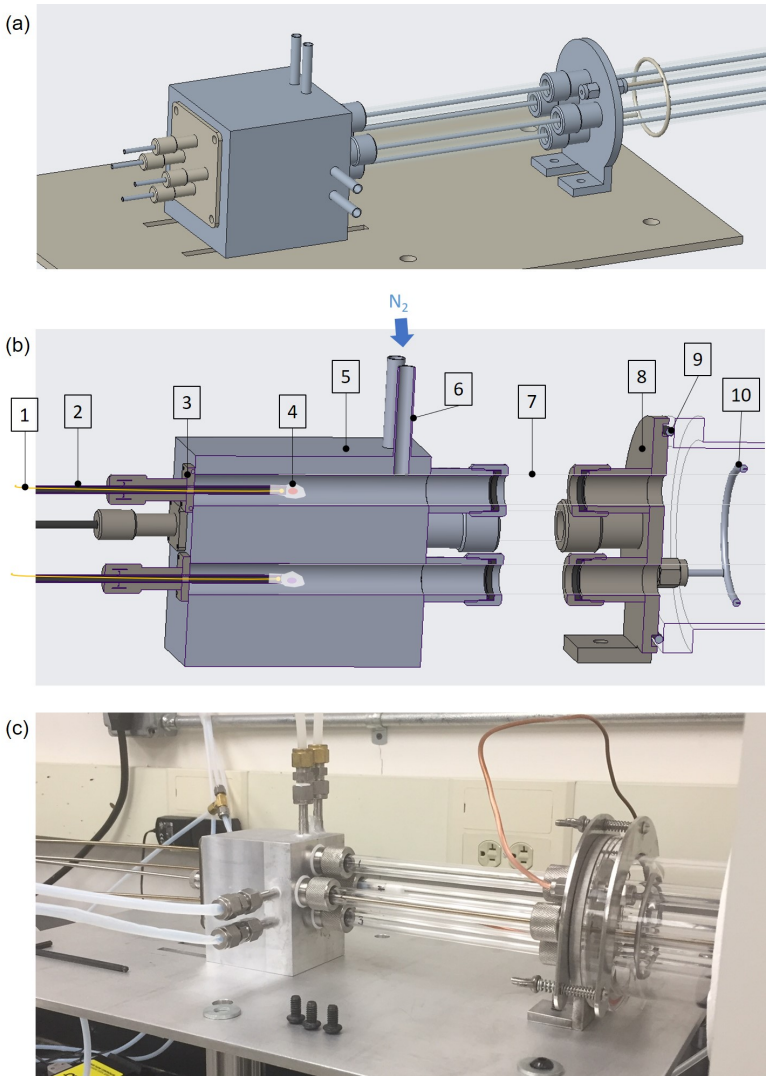

Figure 4.7. Four Source Assembly Design. (a) 3D CAD model of the overall design. (b) Cross-sectional model, showing the flow of N_2 into the manifold and how the thermocouples and source holders interface with the SS linear feedthroughs. (c) Picture of the implemented design. Part numbers are as follows: (1) Thermocouples for *in-situ* source material temperature monitoring, (2) SS feedthrough, constructed of a 1/8" hollow SS rod welded shut at one end. (3) Ultra-torr fittings welded to a flate plate to interface with N_2 manifold *via* o-ring. (4) Source material holder; either a fritted gas dispersion tube or a custom quartz boat. (5) Aluminum N_2 manifold, with welded ultra-torr fittings to interface with quartz source ampoules. (6) Tubes for N_2 input for each source. (7) Quartz source ampoules, which terminate just aft (to the right in the orientation pictured here) of the N_2 inputs. (8) Flange interface with chamber, with welded ultra-torr fittings to interface with quartz source ampoules. (9) O-ring for sealing between flange and chamber. (10) Showerhead for N_2 dilution gas flow.

cavities in an aluminum manifold block, which was connected to the source ampoules *via* ultra-torr quick connects.[5] Each of the four source material holders is inserted into the manifold by a SS linear feedthrough with an embedded thermocouple, connected *via* ultra-torr quick connects welded to a plate and sealed to the manifold using an o-ring. With this arrangement, source material can be moved axially within the chamber before, during, and after deposition by loosening the ultra-torr fittings, sliding the SS feedthrough to the desired location, and re-tightening the fittings. As described in Section 4.3.1, we also included a showerhead-type dilution gas flow mechanism (item 10 in Figure 4.7). This dilution gas flow serves to minimize backflow and acts as another way to change chamber pressure (see Section 4.4). Detailed drawings for these components can be found in Appendix D.

An important design consideration for the source-end of this system is the geometry of the source material ampoules. Specifically, their length and nozzle geometry can significantly impact the flow behavior in the overall system, as a constriction of flow will result in an increase in velocity,[6] thus minimizing the potential for backwards diffusion. Shtein *et al.* discuss this explicitly, and use a 0.6 cm diameter, 10 cm long nozzle on the end of their 2.5 cm diameter source barrels [234]. The smaller diameter of our deposition chamber necessitated a smaller overall source ampoule diameter of 0.5" ($\sim$1.3 cm), but we incorporated a similar $\sim$0.6 cm ID nozzle geometry in order to prevent backflow. When depositing metal halide materials like SnI_2 or $SnBr_2$, evidence of backflow can be easily seen *via* the deposition of highly visible yellow material on the (cold) source side of the chamber walls. I have generally observed no appreciable material deposition/backflow for total chamber pressures above $\sim$200 mTorr. However, for deposition pressures below this, it is not uncommon to observe backflow indicated by material accumulation on the walls of the chamber prior to the source material axial position.

In regards to determining the optimal total length of the ampoule, there were three main factors we considered. The first was that they should be long enough such that the source material can be set at a wide range of temperatures. Based on the temperature profiles shown in Figure 4.2, it is thus ideal for the source ampoules to reach at least 15" into the furnace. Second, the longer the source material ampoules, the less likely there will be cross-contamination between the sources and/or substantial backwards source material diffusion and condensation. Third, there must be sufficient distance between the exit of the ampoules and the substrate to allow

[5]The desired carrier-gas flow rate for each source is separately controlled by massflow controllers.

[6]This is true for subsonic flows, which is this case for this system.

for flow collimation in order to prevent deposition non-uniformities on the substrate. Shtein *et al.* show that given their geometry, a distance larger than 4 cm is required to achieve flow collimation [234]. Due to the different geometry of our design as well as the desire to explore a wide range of operating conditions, we designed the source ampoule-to-substrate distance to be variable between 0" and 15" by ajusting the distance between the chamber and the N_2 manifold as seen in Figure 4.7. This distance was initially set to $\sim$6 inches, which was later determined sufficient to achieve collimated flow based on subsequent experiments (see Section 4.4).

4.3.3 Water-Cooled Substrate Holder

As discussed in Section 4.2, our initial prototype motivated the design of an improved substrate holder concept for the final CGAVD system. Specifically, the goal of the updated substrate holder is to enable temperature control of the substrate during and/or after deposition, and to have this temperature de-coupled from the axial position of the substrate holder within the furnace. This requirement motivated the design of the actively cooled system depicted in Figure 4.8. This system consists of a removable copper plate (item 1), equipped with clips to secure the substrate, which is bolted into the water-cooled Cu/SS cylinder. This cylinder is held in place *via* pipe clamps and a cantilevered SS rod. Water flows through tubes connected with SS Swagelok fittings, and this assembly is attached to a SS flange coupled to the chamber with an o-ring. This SS flange also has attachments for a thermocouple to monitor substrate temperature as well as two ports for rough pump attachment. Detailed drawings for these components can be found in Appendix D.

While this system can accommodate several types of cooling liquids and sources (*e.g.* building-supplied chilled water mixture or standalone circulating bath), we incorporated an existing water circulator (NESLAB EX-250HT) that was capable of pumping water at $\sim$0.4 LPM. As this circulator does not have chilling capabilities, substrate temperature is controlled by changing the temperature of the water in the bath using ice and/or modulating the water flow rate.

An important detail of this design was determining how far the substrate should be inserted into the furnace/chamber. Based on our experience with the prototype design, it was clear that the axial location of the substrate could impact both the temperature of the gas impinging on the substrate as well as how much sublimed material vapor would have already begun condensing on the walls of the chamber. In order to maximize our material utilization efficiency and keep

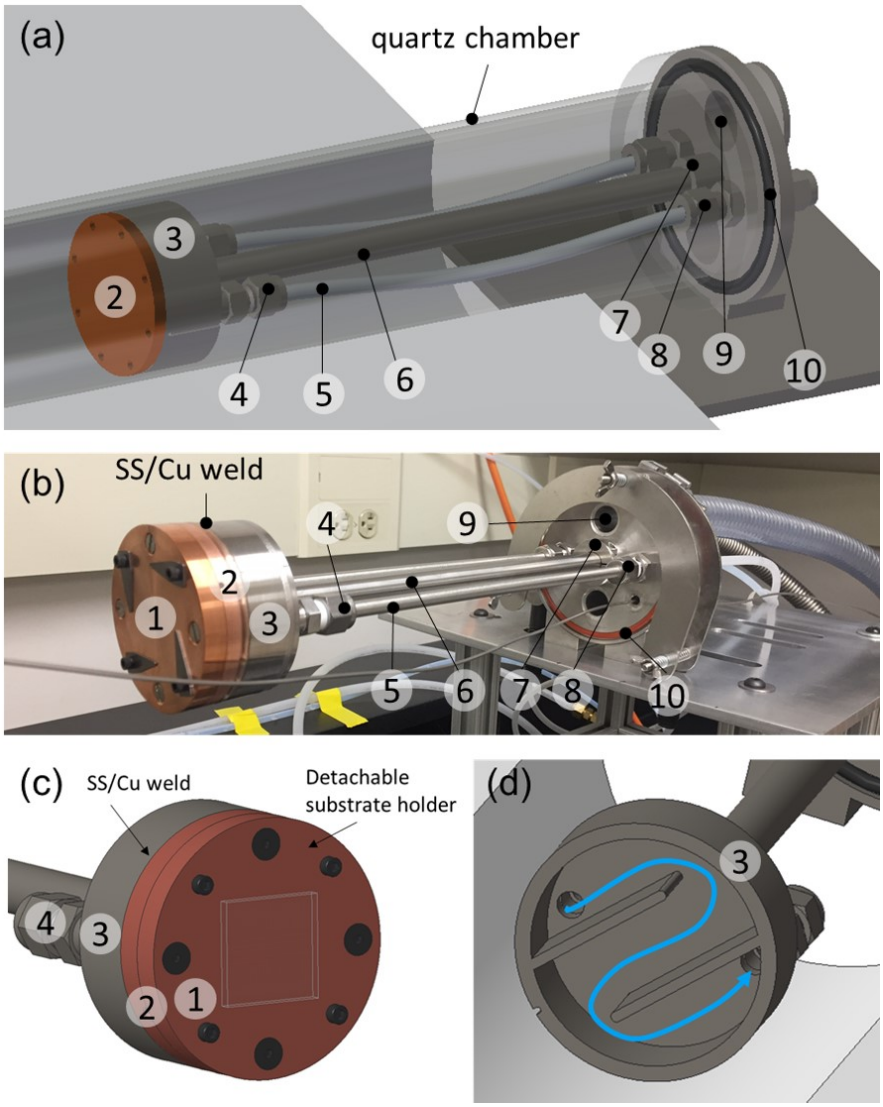

Figure 4.8. Design for water-cooled substrate holder. (a) 3D CAD model showing substrate holder situated inside of quartz furnace. (b) Picture of substrate holder with substrate clips visible. (c) 3D model close-up highlighting detachable Cu substrate plate and SS/Cu weld on SS/Cu cylinder. (d) 3D model of inner cooling channels and schematic of water flow (blue line) inside of SS/Cu cylinder. Part numbers are as follows: (1) detachable Cu plate with clips to hold substrate in place, (2) interfacing welded Cu plate for improved heat transfer, (3) SS cylinder with internal cooling channels, (4 and 8) 1/4" SS Swagelok couplings, (5) flexible PTFE tubing for water inlet and outlet, (6) SS support rod, (7) welded pipe clamp to hold SS rod, (9) rough vacuum attachment ports, (10) SS flange with o-ring to seal to quartz chamber.

the chamber as clean as possible, we sought to promote preferential deposition on the substrate as opposed to the chamber walls. As such, our aim was to locate the substrate holder far enough into the chamber that minimal material would condense prior to reaching the substrate.

Based on the observed correlations between substrate temperatures and deposition regions for SnI_2 and MAI shown in Figure 4.4, as well as the axial temperature profile of the CGAVD system, the graph shown in Figure 4.9a was constructed. Using this graph, we can see that for an oven temperature of 220 °C,[7] SnI_2 and MAI deposition occur after about ∼31 inches.[8] To be conservative, we chose to position the surface of the substrate at 27.5" aft of the furnace inlet, which is equivalent to 1.5" prior to the end of the heated zone of the furnace, denoted by the dashed purple line in Figure 4.9.

Using this geometric positioning, we then modeled the temperature of the substrate holder inside the furnace operating at 220 °C using COMSOL. Figure 4.9b shows the result of this

[7] 220 °C was used as the furnace setpoint temperature for this design decision because it is the lowest and thus most conservative operating condition. At higher furnace set point temperatures, materials would begin to condense at an axial position even farther past the substrate holder.

[8] Zero inches corresponds to the location of the furnace inlet.

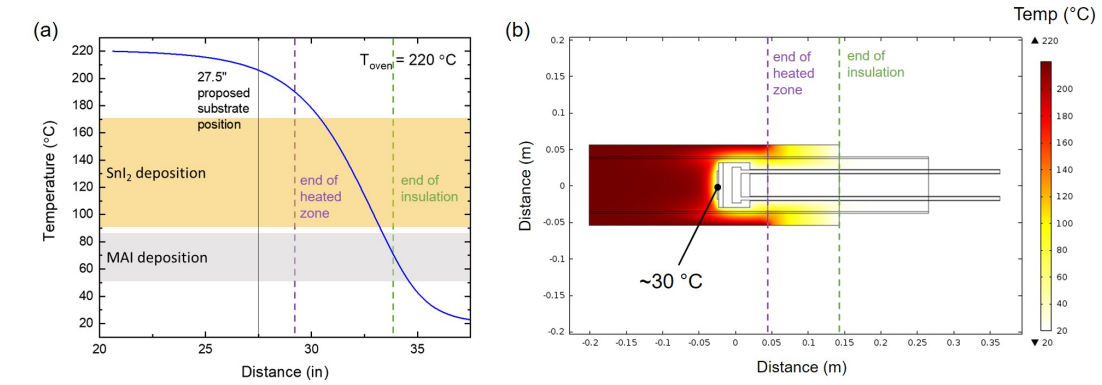

Figure 4.9. Determination of axial position of water-cooled substrate holder. (a) Graph showing the axial temperature profile in the chamber as well as the spatial regions of SnI_2 and MAI deposition for a furnace temperature of 220 °C. 27.5" was chosen for the axial position of the surface of the substrate holder in order to minimize material deposition prior to this position. This is equivalent to 1.5" prior to the end of the heated zone of the furnace, denoted by the dashed purple line. (b) FEA analysis confirming effective cooling of this design, where the surface of the substrate holder is ∼30 °C for ∼0.4 LPM, 25 °C cooling water flow and 220 °C oven temperature.

calculation, where the furnace temperature, cooling water flow rate (∼0.4 LPM), and cooling water temperature (25 °C) were used as boundary conditions. Based on these results, it appears that this design would achieve substantial cooling, with the surface of the substrate holder reaching ∼30 °C.

The cooling efficacy of this design was also tested experimentally. Figure 4.10 shows the measured temperature on the surface of the substrate holder as a function of time at various furnace temperatures. Initially, the room temperature furnace heats to a setpoint of 100 °C over about 30 minutes. Without cooling water flowing, the surface of the substrate holder also increases to ∼100 °C and plateaus. Then, when the cooling water is turned on, the temperature of the substrate holder surface drops quickly (in ∼5 minutes) to ∼15 °C (the temperature of the cooling water). Subsequent increases in furnace temperature to ∼300 °C and then ∼400 °C result in only minor increases in substrate temperature, confirming that this design allows us to effectively cool substrates even at hotter-than typical operating temperatures.[9]

Another important design goal for this substrate holder was to minimize temperature gradients across the surface in order to promote even deposition across the substrate and thus minimize lateral thickness and compositional gradients in our films. Figure 4.8d shows the cooling channel design inside of the SS/Cu cylinder, which is configured to promote even water

[9]These tests were performed with chamber pressures at 760 Torr to be conservative. Typical deposition pressures will be substantially lower than room pressure, and thus the convective heat transfer between the hot chamber gas flow and the susbtrate will be much lower than in this test.

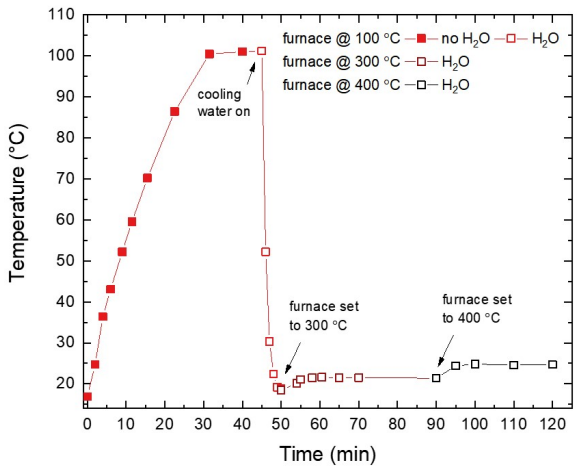

Figure 4.10. Experimental test of cooled substrate holder efficacy, performed at 760 Torr. The room temperature furnace and substrate holder heat to a setpoint of 100 °C over about 30 minutes. When the ∼15 °C cooling water is turned on, the temperature of the substrate holder surface drops quickly; subsequent increases in furnace temperature up to 400 °C result in only minor increases in substrate temperature.

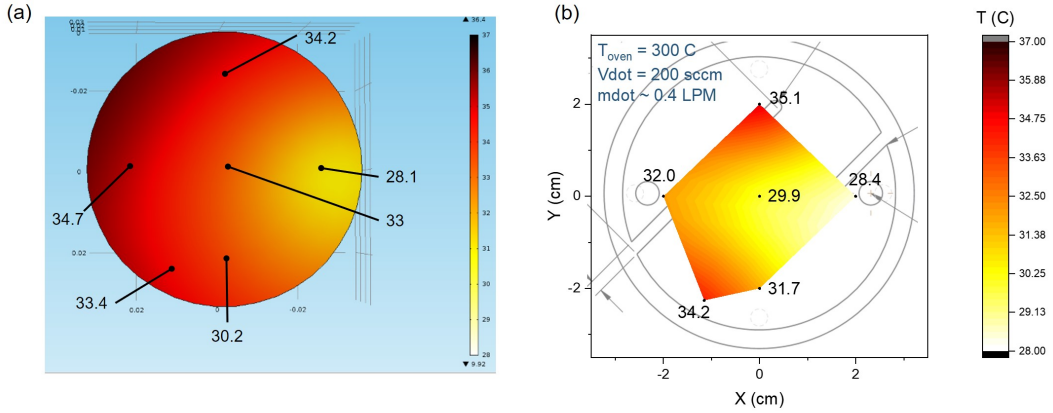

Figure 4.11. (a) Simulated and (b) experimental temperature variations across the substrate holder surface, showing good agreement between experiment and simulation and less than ∼7 °C variation in the central region that would be in contact with substrates.

circulating and cooling across the entire substrate holder. In order to assess the effectiveness of this channel design, I also performed FEA analysis on this component. Using the cooling channel geometry shown in Figure 4.8d and applying the thermal boundary conditions based on previous studies of the oven temperature, we arrive at the FEA simulated variation in surface temperature depicted in Figure 4.11a. We observe a less than 10 °C variation in temperature across the entire substrate holder surface, and less than ∼7 °C in the central region that would be in contact with substrates. This result was validated with experimental measurements, shown in Figure 4.11b, which demonstrate similar absolute temperature values as well as variation across the surface of the substrate holder.[10]

4.3.4 Enclosure

One challenge identified early-on in the validation of the CGAVD system was the limitations imposed by having to load and unload source powders and thin films in ambient conditions. Especially during humid months, water would visibly condense on films that were being unloaded from the chamber, which would immediately ruin them due to the water-solubility of typical MHPs. To protect our films and powders from degradation due to moisture and oxygen,

[10]The lateral variation of substrate temperature as a function of flow rates/chamber pressures was not explored, and additional simulations and/or experimental measurements would need to be performed to assess this.

as well as to improve lab safety by providing a physical barrier between people and toxic MHP materials, we built an N_2 enclosure for the CGAVD system. Many iterations of this design were considered, but the final design functions very similarly to a nitrogen glove box.

Figure 4.12 shows the design of this enclosure, which is comprised of aluminum x-track framing and clear acrylic panels. For ease of cleaning and maintenance, several of these panels (shown in green in Figure 4.12) are easily removable. Both source and substrate sides have small doors and gloves ports for loading and unloading items, and the chamber is sealed with a series of foam gaskets and caulking. House nitrogen supplies the atmosphere and the enclosure is connected to the building exhaust. Detailed drawings for custom components can be found in Appendix D.

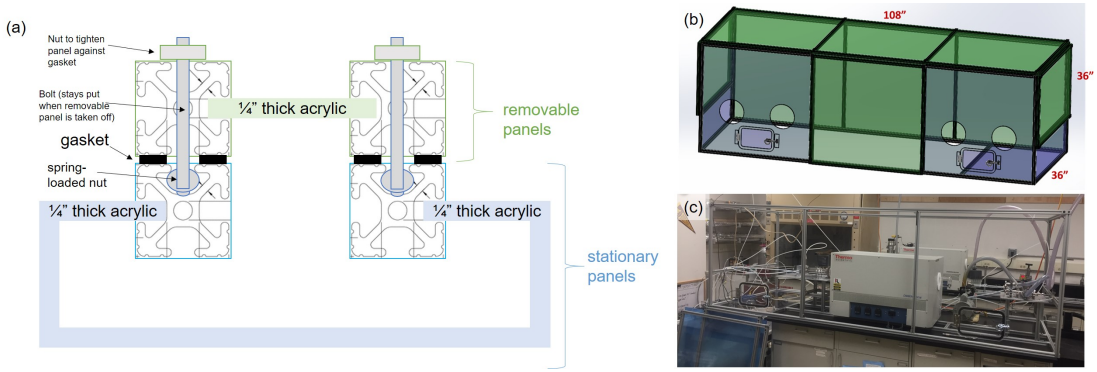

Figure 4.12. Design of N_2 enclosure design for CGAVD system to prevent water and oxygen contamination and protect users from toxic MHP materials. (a) Conceptual design, showing major structural components including x-track framing and acrylic panels, as well as the sealing and attachment mechanisms between panels. Green panels denote those that can be removed easily for cleaning and/or maintenance, and blue panels are those that are fixed in place. This color scheme is also shown in (b), which shows the overall system design and dimensions. Circular ports in (b) correspond to the location for glove attachment. (c) Picture showing enclosure (before glove assembly).

4.4 Validation and Verification

After designing and building the 4-source CGAVD with water cooled substrate, we sought to validate its performance against the success criteria outlined in Section 4.1. This validation occurred in two major steps. The first (Section 4.4.1) was the development of an analytical

model to describe the transport mechanisms in our system, which is necessary to understand how different experimental variables will impact deposition rates. This systematic and informed approach is particularly important for our system given its vast parameter space. For instance, as we will show in the following sections, a combination of low T_i and high $\dot{V}_{CG,i}$ during deposition can cause deposition rates to depend on the source material surface area, which is difficult to control and thus can introduce significant run-to-run variation. The second phase of validation (Section 4.4.2) involved experiments to validate this analytical model and explore how well it performed against the success criteria.

4.4.1 Derivation of Analytical Deposition Rate

In order to harness the full potential of CGAVD, a detailed understanding is needed of how changes in system pressures, temperatures, and flow rates impact film deposition rates. Following Shtein *et al.* [234], we develop in this section an analytical model of mass transport in CGAVD for the unique case of co-deposition of MHP precursors. We then discuss simplifications relevant to our system and identify specific operating regimes that will lead to robust and repeatable film growth. Note that all derivations here assume steady-state operation.

Table 4.1 contains the important variables required for the derivation of material deposition rate, as well as typical values for these quantities for the depositions described in this thesis. These variables are sorted into four categories for ease of understanding: the independently controllable experimental parameters, fit parameters, known and/or fixed quantities, and calculated/intermediate quantities.

Variable	Description	Typical Values	Unit
	Six independently controllable experimental parameters		
T_i	source material temperature for species i	375–600	K
T_g	temperature of gas in chamber at substrate	500–600	K
T_s	substrate temperature	5 - 80	°C
$\dot{V}_{CG,i}$	carrier gas flow rate for species i measured @ mass flow controller [11]	3E-8–2E-7	m^3/s
$\dot{V}_{DIL}$	dilution gas flow rate measured @ mass flow controller	0–4E-6	m^3/s

[11] *i.e.* ambient pressure measurement

P	chamber pressure during deposition	40–1400	Pa
	Fit parameters		
ΔH_i^s	sublimation enthalpy of source material i	8E4 – 2E5	J/mol
$C_{1,i}$	material specific constant from integrating the Clausius-Clapeyron equation to calculate equilibrium vapor pressure	10 – 1000	Pa
$C_{2,i}$	constant from integrating the Clausius-Clapeyron equation to calculate equilibrium vapor pressure	400 – 700	K
$C_{3,i}$	constant relating boundary layer thickness and Reynolds number	$\sim$0	m
	Known and or Fixed Parameters		
R	universal gas constant	8.314	J/mol*K
A_{SH}	cross-sectional area of substrate holder	0.0032	m^2
A_{chamb}	cross-sectional area of chamber	0.0046	m^2
M_i	molar mass of source material i	0.1–0.4	kg/mol
M_{N_2}	molar mass of nitrogen gas	28.014E-3	kg/mol
ρ_i	source material density	variable	kg/m^3
P_0	standard pressure	101325	Pa
T_0	standard temperature	293.15	K
γ	empirical constant from Chapman-Enskog theory	50.7	$\frac{Pa*m^2}{K^{3/2}*s}$
$\sigma i2^2$	average collision diameter	$\sim$5	Å
Ω_i	temperature dependent collision integral	$\sim$1 [244]	unitless
	Calculated and/or Intermediate Quantities		
$r_{dep,i}$	deposition rate of material i	0.05–5	Å/s
$r_{conv,i}$	rate at which the source material is convectively transported from the source	$\sim r_{dep,i}$	mol/s
$r_{diff,i}$	rate at which the source material diffuses through the boundary layer of thickness δ at the surface of the substrate	$\rightarrow \infty$	mol/s

r_i	flux rate of species i at the surface of the substrate	1E-6–1E-8	mol/s
D_i	diffusivity of vapor in carrier gas	1E-4	m^2/s
δ	velocity boundary layer thickness [12]	$\rightarrow \infty$	m
$Conc_{BL,i}$	concentration of sublimed source material vapor in carrier gas at boundary layer interface	variable	mol/m^3
$\dot{V}_{CG,i,ch}$	carrier gas flow for species i at deposition pressure	1E-4–2E-3	m^3/s
$\dot{V}_{DIL,ch}$	dilution gas flow rate at deposition pressure	0–3E-2	m^3/s
$\dot{V}_{total,ch}$	Total gas flow rate [13]at deposition pressure	1E-4–4E-2	m^3/s
$\dot{V}_{total}$	Total gas flow rate [14] at ambient pressure	3E-8–5E-6	m^3/s
$P_{i,eq}$	source material equilibrium pressure @ source material temperature	variable	Pa
P_i	source material vapor pressure in ampoule	variable	Pa
P_{BL}	source material partial pressure @ velocity boundary layer [15]	$P<P_{BL}<P + 0.5\rho v^2$	Pa
T_{BL}	gas temperature of the boundary layer relevant for diffusion across the boundary layer	$T_s<T_{BL}<T_g$	K
Re	Reynolds number	0.1–10	unitless
v	flow velocity	0.01–0.5	m/s

Table 4.1: Variables used in deposition rate derivation along with typical values for the experiments reported herein.

Single Material Deposition Rate Derivation

The deposition rate of material i ($r_{dep,i}$) on the substrate will depend both on the flux of material that reaches the surface of the substrate (r_i) and the rate that molecules stick and unstick to the substrate (often referred to as the "sticking coefficient"). The sticking coefficient is quite

[12]of normal, columnated flow impinging on substrate

[13]$\Sigma\dot{V}_{CG,i,ch} + \dot{V}_{DIL,ch}$

[14]$\Sigma\dot{V}_{CG,i} + \dot{V}_{DIL}$

[15]relevant for the diffusion across the velocity boundary layer driven by the source material concentration gradient

challenging to parametrize analytically, as it depends on T_s and the surface properties of the film, including any reactions with other species. To capture the most general case, we can write

$$r_{dep,i} = r_i * f(T_s, \text{film surface properties, rxns}) \tag{4.1}$$

For the purposes of this derivation, we will assume $r_{dep,i} \approx r_i$, *i.e.* that the sticking coefficient is near unity. We have found through subsequent experiments that this assumption is true for cold substrate temperatures (less than ~25 °C). Thus, the following derivation will focus on determining an analytical expression for r_i.

The rate that source material molecules reach the surface of the substrate (r_i) depends on the rate at which the source material is convectively transported[16] from the source ($r_{conv,i}$) and the rate at which the source material diffuses through the boundary layer of thickness δ at the surface of the substrate ($r_{diff,i}$). Figure 4.13 depicts schematically these transport regions. As these processes of convective and diffusive transport occur in series, we can thus write

$$\frac{1}{r_i} = \frac{1}{r_{conv,i}} + \frac{1}{r_{diff,i}} \tag{4.2}$$

or, rearranging,

$$r_i = \frac{r_{conv,i}}{1 + \frac{r_{conv,i}}{r_{diff,i}}} \tag{4.3}$$

We will treat each of these quantities ($r_{diff,i}$ and $r_{conv,i}$) separately, starting with $r_{conv,i}$. Assuming steady state operation and conservation of mass in the chamber, $r_{conv,i}$ is equal to the rate of source material flux out of the source material ampoule. For ideal gas behavior

[16] *i.e.* carried along with the bulk gas flow through the chamber

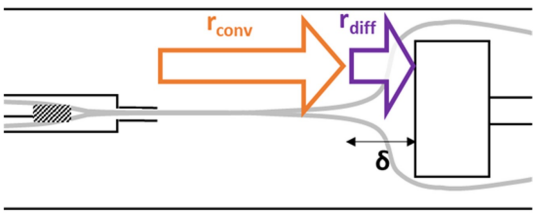

Figure 4.13. Regions of convective and diffusive transport of sublimed material vapor in CGAVD where the substrate is perpendicular to the gas flow. Convective transport carries the vapor from the source to the substrate boundary layer, diffusive transport occurs across the boundary layer (thickness δ).

relevant for these temperatures and pressures, this quantity depends on the source material vapor pressure in the ampoule (P_i), the temperature (T_i), and the carrier-gas flow rate in the ampoule ($\dot{V}_{CG,i,ch}$):

$$r_{conv,i} = \dot{V}_{CG,i,ch} * \frac{P_i}{RT_i} \tag{4.4}$$

Here, $\dot{V}_{CG,i,ch}$ is the volumetric carrier gas flow rate at the chamber pressure P; it is related to the measured volumetric carrier gas flowrate controlled by the mass flow controllers [17] by:

$$\dot{V}_{CG,i,ch} = \dot{V}_{CG,i} * \frac{P_0}{P} * \frac{T_g}{T_0} \tag{4.5}$$

Within the source material ampoule at steady state, the convective rate of transport of material out of the ampoule ($r_{conv,i}$) must be in balance with the relative rates of source material evaporation ($r_{evap,i}$) and condensation ($r_{cond,i}$):

$$r_{conv,i} = r_{evap,i} - r_{cond,i} \tag{4.6}$$

where $r_{evap,i}$ depends on the equilibrium vapor pressure ($P_{i,eq}$), and a kinetic factor of evaporation ($k_{evap,i}$):

$$r_{evap,i} = k_{evap,i} * P_{i,eq} \tag{4.7}$$

Similarly, $r_{cond,i}$ depends on the *actual* vapor pressure in the ampoule (P_i), and a kinetic factor of condensation ($k_{cond,i}$):

$$r_{cond,i} = k_{cond,i} * P_i \tag{4.8}$$

Combining Equations 4.4 and 4.6-4.8, we get

$$P_i = P_{i,eq} * \frac{k_{evap,i}}{\frac{\dot{V}_{CG,i,ch}}{RT_i} + k_{cond,i}} \tag{4.9}$$

Equation 4.9 describes the relationship between the equilibrium vapor pressure of source material i and the actual vapor pressure in the source material ampoule. The higher the source

[17] *i.e.* the flow rate measured outside of the chamber @ ambient temperature and pressure

material temperature, the closer these two quantities will be.

Integrating the Clausius-Clapeyron relation,[18] we can describe the equilibrium pressure of the source material i as

$$P_{i,eq} = C_{1,i} e^{\frac{\Delta H_i^s}{R}(\frac{1}{T_i} - \frac{1}{C_{2,i}})} \tag{4.10}$$

where $C_{1,i}$, $C_{2,i}$, and ΔH_i^s are material-specific constants. Combining Equations 4.4, 4.5, 4.9, and 4.10, we arrive at a final analytical expression for the rate of material convection out of the source ampoule for a given material i:

$$r_{conv,i} = \frac{P_0}{RT_0} \frac{\dot{V}_{CG,i}}{T_i} \frac{T_g}{P} C_{1,i} e^{\frac{\Delta H_i^s}{R}(\frac{1}{T_i} - \frac{1}{C_{2,i}})} \frac{k_{evap,i}}{\frac{\dot{V}_{CG,i} P_0 T_g}{PRT_i T_0} + k_{cond,i}} \tag{4.11}$$

In this equation, we can observe that there are four of the six experimentally controllable parameters: $\dot{V}_{CG,i}$, T_g, P, and T_i. Additionally, as $\dot{V}_{DIL}$ and be used to impact the chamber pressure P, this variable is also implicitly contained in Equation 4.11.

Now we turn our attention to deriving an expression for $r_{diff,i}$. The diffusive flux of material i across a boundary layer of thickness δ will be driven by the concentration gradient across the boundary layer ($\Delta C/\delta$) according to 1D Fick's law at steady state:

$$Flux_i = -D_i \frac{\Delta C_i}{\delta} \tag{4.12}$$

If we assume a sticking coefficient of $\sim$1 (reasonable for cold substrate temperatures), we implicitly assume that the concentration of source material vapor at the substrate surface is zero, so $\Delta C_i \rightarrow Conc_{BL,i}$. Thus the rate of diffusion of species i across the substrate holder surface area (A_{SH}) can be written as

$$r_{diff,i} = Flux_i * A_{SH} = D_i \frac{Conc_{BL,i}}{\delta} * A_{SH} \tag{4.13}$$

The source material concentration at the boundary layer ($Conc_{BL,i}$), is equal to the concentration of source material leaving the ampoule (P_i/RT_i), multiplied by the flow dilution ratio (ratio of carrier-gas to total N_2 flow):

[18] and assuming that the sublimation enthalpy is independent of temperature

$$Conc_{BL,i} = \frac{P_i}{RT_i}\frac{\dot{V}_{CG,i}}{\dot{V}_{total}} \tag{4.14}$$

We can express the diffusion coefficient D_i using Chapman-Enskog theory [244][19] (variables defined in Table 4.1):

$$D_i = \frac{\gamma T_{BL}^{3/2}\sqrt{1/M_i + 1/M_{N_2}}}{P_{BL}(\sigma i 2)^2\Omega_i} \tag{4.15}$$

Note that the temperature (T_{BL}) and pressure (P_{BL}) in Equation 4.15 are the temperatures and pressures relevant for diffusion across the boundary layer. T_{BL} is bounded by the chamber temperature (T_g) and the substrate temperature (T_s): $T_s < T_{BL} < T_g$, and P_{BL} is bounded by the deposition pressure and the stagnation pressure given by the Bernoulli eqn: $P < P_{BL} < P + \frac{1}{2}\rho v^2$ where v = flow velocity = $\frac{\dot{V}_{total}}{A_{chamb}}\frac{P_0}{P}\frac{T_g}{T_0}$ and ρ = density of chamber gas = $\frac{P}{T_g}\frac{MM_{N_2}}{R}$. For stagnation flow, the boundary layer thickness (δ) typically has a dependence such as [245]:

$$\delta \approx \frac{C_3}{\sqrt{Re}} \tag{4.16}$$

Where Re = Reynolds number = $\frac{\rho v L}{\mu}$, L = relevant length scale, *e.g.* $2r_{chamb}$, and μ = dynamic viscosity. Thus,

$$\delta \approx \frac{C_3}{\sqrt{\frac{\rho v L}{\mu}}} = \frac{C_3\sqrt{\mu}}{\sqrt{\frac{\dot{V}_{total}}{A_{chamb}}\frac{P_0}{T_0}\frac{MM_{N_2}}{R}2r_{chamb}}} \tag{4.17}$$

The viscosity of gasses at these pressures is relatively independent of pressure but depends strongly on temperature as described by the Sutherland formula:

$$\mu = \mu_0\frac{T_0 + \beta}{T + \beta}\left(\frac{T}{T_0}\right)^{3/2} \tag{4.18}$$

Here μ_0, T_0, and β are constants tabulated for a specific gas. Rearranging and consolidating, we get

[19] Hirschfelder *et al.* apply Chapman-Enskog theory to binary mixtures of gases to determine this first-order approximation for diffusion rate [244]. Notably, while this approximation may vary as a function of the molecular weights, mole fractions, and viscosities of the mixture components, we find that these approximations have no impact on the accuracy of our analytical model as we later show that the diffusion across the boundary layer is not rate-limiting.

$$\mu = \mu_0 \frac{T_0 + \beta}{T_0^{3/2}} \frac{T_g^{3/2}}{T_g + \beta} \tag{4.19}$$

Combining Equations 4.13-4.15 and 4.17-4.19 and isolating relevant experimental parameters:

$$r_{diff,i}(mol/s) = \frac{\alpha_i}{C_{3,i}} \frac{T_{BL}^{3/2}}{P_{BL}} \frac{P_i}{T_i} \frac{\dot{V}_{CG,i}}{\sqrt{\dot{V}_{total} \frac{T_g^{3/2}}{T_g + \beta}}} \tag{4.20}$$

where α_i contains only known quantities:

$$\alpha_i = \frac{A_{SH} \frac{\gamma \sqrt{1/M_i + 1/M_{N_2}}}{(\sigma i 2)^2 \Omega_i}}{R \sqrt{\mu_0 \frac{T_0 + \beta}{T_0^{3/2}} \frac{\pi r_{chamb} R T_0}{2 M M_{N_2} P_0}}} \tag{4.21}$$

Now that we have expressions for both $r_{conv,i}$ (Equation 4.11) and $r_{diff,i}$ (Equation 4.20), plugging these into Equation 4.3 will yield a full description of the flux of a species i onto the surface of the substrate (r_i). If the sticking coefficient is unity, this will correspond to the deposition rate in mol/s, which we can convert to Å/s:

$$r_{dep,i}(\text{Å}/s) = r_i(mol/s) \frac{10^{10} M_i}{\rho_i A_{chamb}} \tag{4.22}$$

Co-deposition Rate Derivation

For co-deposition, where two precursors A (*e.g.*, MABr) and B (*e.g.*, $SnBr_2$) are deposited simultaneously and react to form a perovskite on the substrate,[20] the flux rates for each precursor can be converted to a deposition rate for the perovskite. If the flux rates are equal, then the number of moles of perovskite reaching the surface of the film are the same as the flux of the precursor:

$$r_A(mol/s) = r_B(mol/s) = r_{perov}(mol/s) \tag{4.23}$$

[20] for the tin perovskites discussed in this work, the precursors react when co-deposited without the need for an extra annealing step, even at cold substrate temperatures of ∼5 °C.

If we assume a sticking coefficient of 1 and a 100% reaction rate, we can convert this to Å/s based on the density and molar mass of the perovskite material:

$$r_{dep,perov}(\text{Å}/s) = r_{perov}(mol/s)\frac{10^{10}M_{perov}}{\rho_{perov}A_{chamb}} \tag{4.24}$$

However, if the molar fluxes are not equal (*i.e.*, $r_A \neq r_B$), we can envision two limiting cases for the total film deposition rate:

1. Minimum Flux Limited

   In this case, the excess precursor is rejected from the film, and the molar deposition rate of the perovskite is equivalent to the minimum molar flux of the two precursors:

   $$r_{perov}(mol/s) = min(r_A, r_B) \tag{4.25}$$

   and

   $$r_{dep,perov}(\text{Å}/s) = min(r_A, r_B)\frac{10^{10}M_{perov}}{\rho_{perov}A_{chamb}} \tag{4.26}$$

2. Total Flux

   If the excess precursor is not rejected, the total deposition rate will be the sum of the perovskite deposition plus the deposition of the excess precursor phase:

   $$r_{dep,perov}(\text{Å}/s) = min(r_A, r_B)\frac{10^{10}M_{perov}}{\rho_{perov}A_{chamb}} + |r_A - r_B|\frac{10^{10}M_{max(A,B)}}{\rho_{max(A,B)}A_{chamb}} \tag{4.27}$$

Interestingly, we observed both of these cases using CGAVD and found that whether the deposition was minimum flux limited or included the total flux depended on the substrate temperature (See Section 4.4.2).

Simplifications for Depositions Reported Herein

There are two major simplifications that apply to the depositions reported herein, which are based on both theoretical and experimental observations, and that greatly simplify the overall analytical expression for deposition rate used throughout this thesis:

1. Diffusion across boundary layer is not rate limiting (*i.e.* $r_i \approx r_{conv,i}$)

   For laminar, large Reynolds number (Re) flows ($500 << Re << 2000$), diffusion through the momentum boundary layer can be a rate limiting factor, and must be taken into account to accurately model deposition rates [245]. At the pressures and flow rates used in this study, however, $Re << 500$ (see Figure D.2), and the momentum boundary layer does not have a significant impact on the overall deposition rate. In other words, $r_i \approx r_{conv,i}$.

   This relative unimportance of diffusive transport in this technique is quite convenient because it means that the radial nonuniformities in boundary layer thickness—that exist for typical stagnation flow normal to a flat plate—will not result in a significant variation of deposition rate across the substrate. This relaxes the need for a rotating substrate holder to achieve uniform film thickness.

   Indeed, later experiments confirm this simplification in two ways. First, fitting our data including the diffusion term, we found that $C_{3,i} \rightarrow 0$ and consequently $r_{diff,i} \rightarrow \infty$ for all i reported herein. Second, this is corroborated experimentally by the remarkable thickness uniformity we observe across our substrates (Section 4.4.2).

2. Operating in "equilibrium regime" (*i.e.* $P_i \approx P_{i,eq}$)

   Equation 4.9 implies two limiting regimes of deposition, as described in detail by Shtein *et al.* [234]. In the "equilibrium" regime, source temperatures are high and carrier gas flow rates are low, and the vapor pressure in the ampoule is close to equilibrium. In this case, $\dot{V}_{CG,i,chamb}/RT_i \rightarrow 0$ and $k_{evap,i} \approx k_{cond,i}$. In the "kinetic regime," sublimed source material is carried out at a rate high enough that equilibrium cannot be established. In an extreme case, sublimation is so slow that every sublimed molecule is immediately swept out of the ampoule, and $P_i \rightarrow 0$. In this kinetic regime the deposition rate then depends on the surface area of source material in the ampoule *via* $k_{evap,i}$ and $k_{cond,i}$. A schematic depiction of these two regimes can be seen in Figure 4.14. As the surface area of source material powder is difficult to control, it is desirable to avoid the kinetic regime all together, such that $P_i \approx P_{i,eq}$.

Using these two simplifying assumptions, we can re-write Equations 4.3 and 4.11 to describe the expected deposition rate of a material i in our CGAVD system:

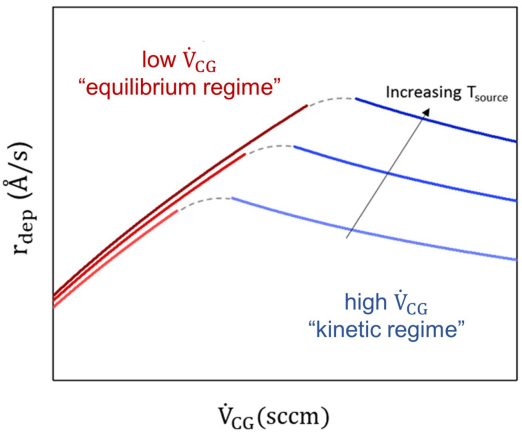

Figure 4.14. Deposition rate as a function of carrier gas flow rate and source temperature for equilibrium and kinetic regimes. Operation in the equilibrium regime (*i.e.*, high source material temperature, low carrier gas flow rate) is desirable as the deposition rate is independent of source material surface area. In the kinetic regime, the source material vapor pressure is far below its equilibrium pressure, and as such depends on the surface area of the source material.

$$r_i(\text{Å}/s) = C_{1,i}\frac{P_0 T_g}{RT_0}\frac{\dot{V}_{CG,i}}{PT_i}e^{\frac{\Delta H_i^s}{R}(\frac{1}{T_i}-\frac{1}{C_{2,i}})}\frac{10^{10}M_i}{\rho_i A_{chamb}} \tag{4.28}$$

4.4.2 Experimental Validation

Validation of Analytical Deposition Rate Model

Individual Precursor Materials

To validate and calibrate the model in Equation 4.28, neat films of MABr, MAI, $SnBr_2$, and SnI_2 were deposited at a variety of source material temperatures (T_i) and carrier gas flow rates ($\dot{V}_{CG,i}$), while keeping the pressure, furnace temperature, and substrate temperature constant (P = 2.6 Torr, T_g = 220 °C, T_s = 15 °C).

The first thing we needed to understand was what temperatures and flow rates corresponded to equilibrium and kinetic regimes for each source material. As discussed in Section 4.4.1, this is important because operating in the equilibrium regime is likely to result in better ability to control deposition rate and more repeatability between growths. An example of the deposition data collected as a function of carrier gas flow rates and source material temperatures can be seen in Figure 4.15 for $SnBr_2$. Here, we can see that the behavior of deposition rate with increasing carrier gas flow rate is drastically different for two different source material temperatures (T_{SnBr_2} = 241 °C and 221 °C). For T_{SnBr_2} = 221 °C, r_{SnBr_2} stays relatively constant (or perhaps slightly decreases) with increasing carrier gas flow rates between 5 sccm and 200 sccm. This would imply that these depositions occurred in the kinetically limited regime, as

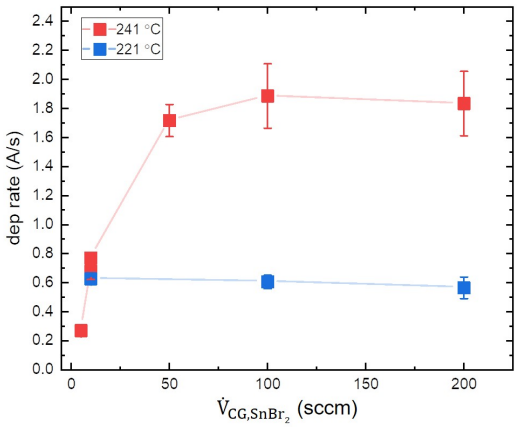

Figure 4.15. Experimental deposition rates[a] for $SnBr_2$ taken at two source temperatures T_{SnBr_2} = 241 °C and 221 °C, and various carrier gas flow rates 5 sccm $< \dot{V}_{CG,SnBr_2} <$ 200 sccm. The deposition rate for T_{SnBr_2} = 241 °C increases until 100 sccm, indicative of equilibrium regime operation. Conversely, the deposition rate only decreases with increasing carrier gas flowrate for T_{SnBr_2} = 221 °C, indicative of the kinetic regime.

[a] calculated by taking measured film thickness / deposition time

shown schematically in Figure 4.14. However, for T_{SnBr_2} = 241 °C, the deposition rate increases with increasing carrier gas flow rate until 100 sccm, thus implying that these datapoints are in the equilibrium regime. The rollover in deposition rates after 100 sccm for T_{SnBr_2} = 241 °C denotes transition into the kinetic regime.

After determining the equilibrium regime for each material, we can then repeat this type of experiment to can map out a 3D space of r_i vs. $\dot{V}_{CG,i}$ vs. T_i. These data were used fit Equation 4.28. Experimental data and fit surfaces are shown in Figure 4.16 for MABr, MAI, $SnBr_2$, and SnI_2.[21] With this fit, we are able to extract the enthalpy of sublimation, ΔH_i^s. Shown in Table 4.2, these fit values agree well with available reported values, providing evidence that our analytical deposistion rate model describes the physical behavior of our system. Given this validation, we can then continue to use this analytical model to help predict deposition rates inside the equilibrium regime to inform our experimental plans.

Co-deposition

In addition to mapping out how individual precursor deposition aligns with our analytical model, we also wanted to probe the behavior of co-deposition of multiple precursor materials. Indeed, a fundamental difference between the use of CGAVD for organic molecules and its use for metal halide perovskite materials is the possibility that the perovskite precursor materials will react with each other at the surface of the film. Section 4.4.1 outlines two potential cases

[21] It should be noted that 3D surface fitting was used because it produced more unique fit results than individually fitting r_i vs. $\dot{V}_{CG,i}$ and r_i vs. T_i.

i	ΔH_i^s **FIT** (kj/mol)	ΔH_i^s **LIT** (kj/mol)	Source
MABr	83 [79, 85]	78 - 105	[246]
MAI	104 [91, 115]	105	[247]
$SnBr_2$	140 [126, 155]	135	[246]
SnI_2	180 [175, 186]	140 - 172	[246, 248]

Table 4.2: Enthalpies of sublimation for MABr, MAI, $SnBr_2$, and SnI_2 extracted from fitting experimentally measured deposition rates to Equation 4.28. Square brackets correspond to 95% confidence intervals. No value for ΔH^s_{MABr} could be found in the literature; this range corresponds to ΔH^s_{MAI} and ΔH^s_{MACl}, which bound the value for MABr.

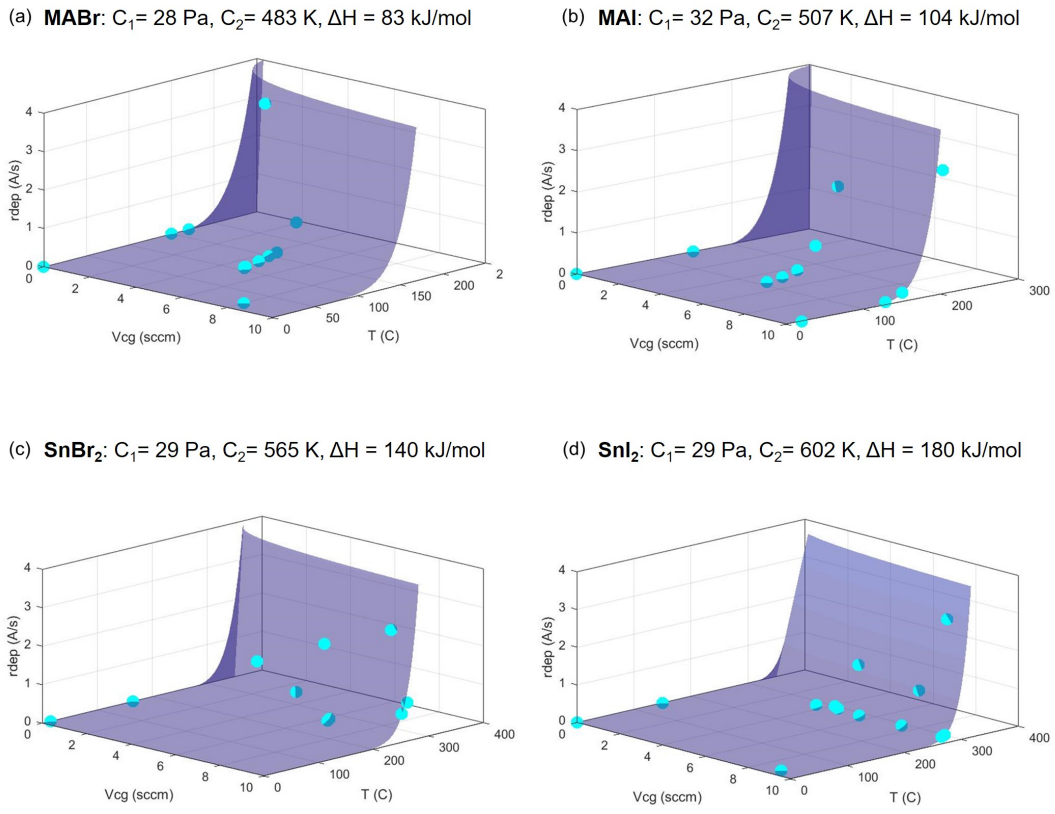

Figure 4.16. Deposition rate data and fits of Equation 4.28 with corresponding fit parameters and 95% confidence intervals [in brackets] for (a) MABr; (b) MAI; (c) $SnBr_2$; and (d) SnI_2. Deposition rate was measured experimentally using ellipsometry. Fits were done with a non-linear least-square fit of Equation 4.28 in Matlab. Data shown here is for P = 2.6 Torr.

that can occur during co-deposition. The first is that only material that is incorporated into the MHP lattice will stick the the substrate. In this "minimum flux limited" case, the rate of MHP deposition will then depend solely on the precursor with lower flux at the substrate surface. Further increasing the component with excess flux would then have no impact on the total MHP deposition rate. In the other case, 100% of the precursor vapor reaching the substrate will stick. For imbalanced flux rates, this implies that there may be multiple phases present in the film: MHP and excess precursor.

For co-depositions involving two materials (denoted A and B), the ratio r_A/r_B represents the ratio of precursor species available to react and form the perovskite at the substrate/film surface. This ratio can be computed by dividing Equation 4.28 for species A and B:

$$\frac{r_A}{r_B} = \frac{C_{1,A}}{C_{1,B}} \frac{T_B}{T_A} \frac{\dot{V}_{CG,A}}{\dot{V}_{CG,B}} e^{\left[\frac{\Delta H_A^s}{R}\left(\frac{1}{T_A}-\frac{1}{C_{2,A}}\right)-\frac{\Delta H_B^s}{R}\left(\frac{1}{T_B}-\frac{1}{C_{2,B}}\right)\right]} \tag{4.29}$$

Equation 4.29 implies that changes in film stoichiometry during co-deposition of components A and B can be realized through changes in $\dot{V}_{CG,A}$, $\dot{V}_{CG,B}$ T_A and/or T_B. To simplify our analysis, we can also define the normalized precursor excess ratio, or "r-ratio", $r_{A,B}$:

$$r_{A,B} = (r_A - r_B)/min(r_A, r_B) \tag{4.30}$$

where $r_{A,B} = 0$ indicates equal molar fluxes of species A and B, a negative value indicates excess metal halide (*e.g.*, $SnBr_2$) and a positive value indicates excess organic halide (*e.g.*, MABr).

Following Equation 4.30, we performed a series of experiments to tune the excess precursor ratio between MABr and $SnBr_2$ by changing $\dot{V}_{CG,i}$ and T_i (i = MABr, $SnBr_2$). Deposition conditions for these films and XRD patterns are shown in Figure D.3. The phase purity of the films is calculated using the diffraction peak intensity of three different components: $MASnBr_3$ (perovskite), MABr, and $SnBr_2$. The XRD peak intensity ratios I_{MABr}/I_{MASnBr_3} and I_{SnBr_2}/I_{MASnBr_3} are calculated by dividing the largest excess precursor (*i.e.*, MABr or $SnBr_2$) XRD peak intensity with that of the $MASnBr_3$ (100) peak (at 2θ=17.5°). Films are deemed "stoichiometric" if there are no observable diffraction peaks from MABr or $SnBr_2$.

Initial experiments were carried out at cold substrate temperatures (T_s ∼15 °C) in order to promote a high sticking coefficient. Interestingly, during these growths it was observed that there was a small window of non-zero $r_{MABr,SnBr_2}$ which resulted in stochiometric films; *i.e.*

even without perfectly balanced precursor fluxes, no excess precursor peaks were observed in the XRD patterns. At larger values of of $r_{MABr,SnBr_2}$, however, visible diffraction peaks from MABr or $SnBr_2$ were observed. This result would indicate that there are some deposition conditions in which the deposition could be minimum flux limited, but perhaps other conditions in which excess material flux would indeed stick to the substrate and become incorporated into the films.

To investigate this further, $MASnBr_3$ depositions were carried out at a variety of substrate temperatures T_s. Figure 4.17 shows that the range of $r_{MABr,SnBr_2}$ which results in stoichiometric films depends strongly on T_s. For low T_s of 15–20 °C, an imbalance of precursor fluxes results in stoichiometric films for -0.3 $< r_{MABr,SnBr_2} <$ 0.3. This window increases for warmer T_s of 25–30 °C, where stoichiometric films are formed up to flux imbalances of -0.7 $< r_{MABr,SnBr_2} <$ 0.7. For $T_s >$ 35 °C, this range extends further, such that a flux imbalance of -1 $< r_{MABr,SnBr_2} <$ 1 still results in a stoichiometric film. This result suggests that $MASnBr_3$ films grown using CGAVD have a self-correcting window in the sense that the surface adsorption and reaction probabilities of MABr and/or $SnBr_2$ adjust to balance their net incorporation rates into the film. This relaxes the need to balance the precursor fluxes exactly in order to deposit phase-pure $MASnBr_3$ films. An example of the XRD patterns for T_s = 15 °C films can be seen in Figure D.3.

To further confirm this result, we can compare the measured deposition rates for phase-pure films in the "min flux limited" regime with deposition rates predicted using Equation 4.27. Figure 4.18 shows these calculated and measured deposition rates. Interestingly, deposition

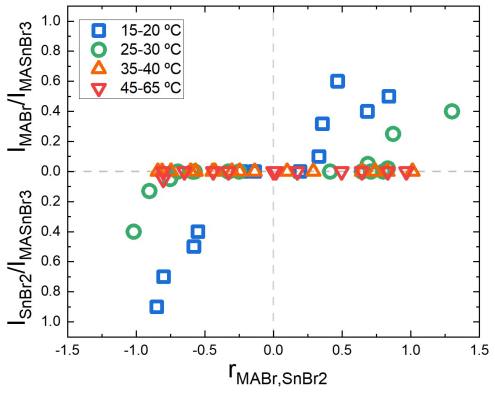

Figure 4.17. Impact of T_s on stoichiometrically "self-correcting" window for $MASnBr_3$ films on quartz. For low T_s of 15–20 °C, an imbalance of precursor fluxes results in non-stoichiometric films for $|r_{MABr,SnBr_2}| > 0.3$. This window increases for warmer T_s of 25–30 °C where stoichiometric films are formed for $|r_{MABr,SnBr_2}| < 0.7$. For $T_s >$ 35 °C, this range extends further, such that a flux imbalance of 100% for either $SnBr_2$ or MABr still results in a stoichiometric film.

rates calculated including total precursor fluxes (Equation 4.27) greatly overestimate the measured values, whereas excluding excess precursor flux (Equation 4.26) results in a calculated deposition rate that agrees well with experiment. This good agreement is further evidence of the stoichiometrically self-correcting behavior of $MASnBr_3$ deposited using CGAVD. Furthermore, Figure 4.18 shows that substrate temperatures between 30 and 70 °C have a minimal effect on deposition rate, allowing the us to independent tuning T_s and r_i.

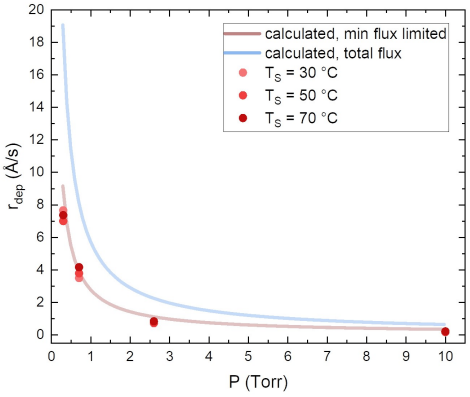

Figure 4.18. Measured and calculated deposition rates corresponding to stoichiometric $MASnBr_3$ fimls. Measured deposition rates agree well with calculated values when excess precursor flux is excluded (Equation 4.26). Calculated deposition rates that include total flux of both precursors significantly overestimates deposition rate—indicating that excess precursor flux is rejected during $MASnBr_3$ film formation using CGAVD.

CGAVD System Performance Relative to Success Criteria

In addition to validation our analytical model using our final CGAVD setup, we also wanted to assess its performance against the success criteria outlined in Section 4.1. Here, we briefly discuss the achievements we have made relative to these criteria, highlighting successes in green and ongoing tasks in orange.

✓ **Enable the deposition of common organic- and metal-halide MHP precursors**

Throughout this thesis, we have demonstrated the successful deposition of SnI_2, $SnBr_2$, MAI, and MABr. We have also used this system to deposit other materials like phenethylammonium iodide (PEAI), tris(4-carbazoyl-9-ylphenyl)amine (TCTA), and perylene-3,4,9,10-tetracarboxylic dianhydride (PTCDA). While have only recently begun depositing lead-halide precursors with the help of another graduate student in the Holmes group, Wan-Ju Hsu, these preliminary experiments are promising and have shown the successful

deposition of PbI_2 films. Overall, our extensive depositions have shown that this technique is capable of succesfully depositing a wide range of organic, organic halide, and metal halide precursor materials.

✓ **Allow sequential or co-deposition**

This is enabled by the 4-source setup described in Section 4.7. While we have used sequential-deposition in limited cases, the majority of the depositions in this thesis work were done with co-deposition.

✓ **Enable fine control of the flux ratio**

The ability to independently tune the source material temperature T_i and source material carrier gas flow rate $\dot{V}_{CG,i}$ resulted in effective tuning of flux ratios across a wide range. This enabled the tuning of r-ratio depicted in Figure 4.18, as well as the tuning of film stoichiometry and morphology discussed in detail in Chapter 5.

✓ **Allow access to a wide range of film stoichiometries and morphologies**

Substantial ranges in film stoichiometries and morphologies were achieved using this system, as described in detail in Chapter 5. For example, we successfully tuned the average grain area of $MASnBr_3$ films from ~ 0.001 to > 0.7 μm^2.

✓ **Yield films with lateral uniformity in thickness, stoichiometry, and morphology**

Given that our design does not include substrate rotation, we initially thought there may be substantial lateral variations in our films. As such, over the course of this thesis work, many checks were made to measure the lateral uniformity of our films (over $\sim$1 cm length scales) using techniques like XRD, AFM, SEM, XPS, ellipsometry, optical microscopy, and absorption. Excluding growths where a specific issue occurred, like a substrate lifting off of the substrate holder during deposition, we found remarkable lateral uniformity in stoichiometry, thickness, and morphology, for our films across $\sim$cm length scales. Figure 4.19 shows typical examples of these measurements. In Figure 4.19a, lateral stoichiometric consistency of $MASnI_3$ is demonstrated for a film deposited on a patterned ITO

substrate, where each location corresponds to a separate 1mm ITO contact. Nearly identical XRD patterns on these four locations suggests compositional uniformity across this film. Figure 4.19b shows the thickness of a $MASnBr_3$ film measured across a 2x2 cm area using ellipsometry. In this 2x2 cm square, which is the largest substrate our system can accomodate, thickness varies by less than 10%. Figure 4.19c shows an example SEM image for a $MASnBr_3$ film, where the morphology pictured here is representative across the cm-scale substrate. Overall, our extensive measurements have confirmed that we can achieve a high degree of laterial uniformity in MHP film stoichiometry, thickness, and morphology across cm length scales using our CGAVD system.

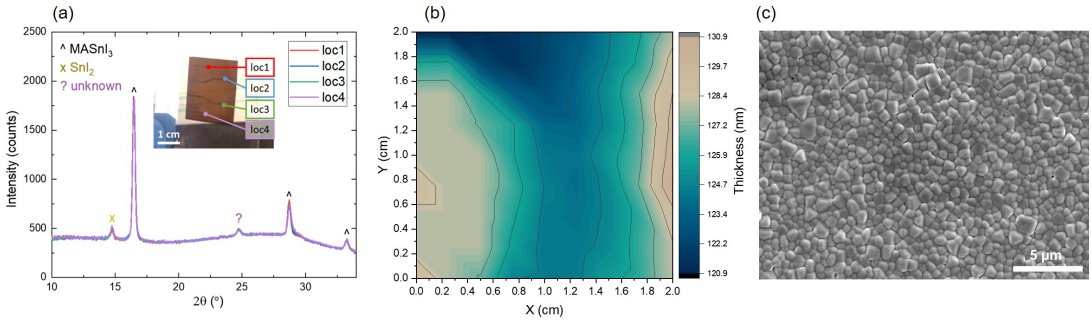

Figure 4.19. Examples of data showing lateral uniformity for MHP films grown in CGAVD. (a) XRD measurement taken at 4 different locations on a $MASnI_3$ film, showing nearly identical diffraction patterns. Each location corresponds to a 1 mm wide ITO contact. X-ray diffraction was collected using a Bruker D8 2D diffractometer with Co Kα radiation (λ=1.7889 Å). (b) Thickness measurements across a 2x2 cm $MASnBr_3$ film on Si using ellipsometry. (c) SEM image of $MASnBr_3$ showing morphological uniformity that is representative of the morphology observed across cm length scales by translating the substrate.

? Minimize growth-to-growth variation

One of the biggest challenges I've had throughout my thesis work is associated with growth-to-growth variations using this CGAVD system. As described in Section 4.3.1, our setup does not include active thickness monitoring, and instead relies on predicted deposition rates using Equations 4.28 and 4.26. While these equations are useful to predicting ball-park deposition rates, we have found that our experimental deposition rates tend to vary significantly between depositions with identical deposition parameters (see Figure 4.20), making it challenging to get reproducible results.

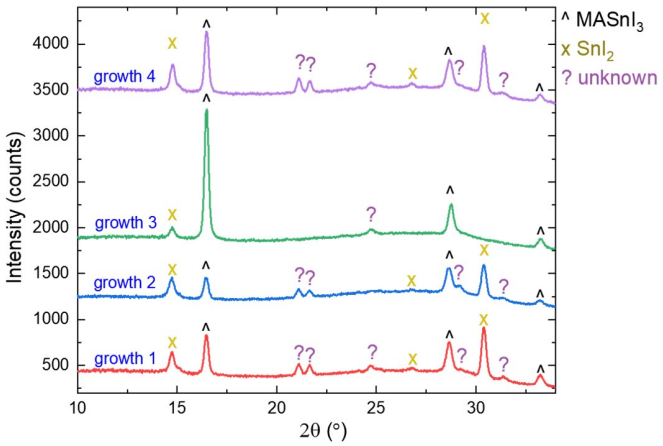

Figure 4.20. Growth-to-growth stoichimetric variations for $MASnI_3$ films on glass using the exact same deposition pressures, temperatures, and flow rates. Note that all four growths were performed in the same week and using the same source material. X-ray diffraction was collected using a Bruker D8 2D diffractometer with Co Kα radiation (λ=1.7889 Å).

We hypothesize that these inconsistencies are due to a variety of factors. The first is chamber fouling/contamination due to material being deposited on the chamber walls from previous growths: we have seen cases where a deep chamber clean reduces the stoichiometric variation between growths. As such, deep cleans were done on a routine basis in order to minimize this issue. It is recommended going forward that growths for devices are done immediately after a deep chamber clean.[22] The second potential source of variations between growths is differences in source material mass/morphology. While we have attempted to perform all depositions in the equilibrium regime where source material surface area does not dictate the equilibrium vapor pressure in the ampoule, we have observed that substantial differences in the starting mass of source material (*e.g.* 100 mg vs. 50 mg) have a significant impact on deposition rate. It is possible that there is a lower limit to acceptable source mass below which an equilibrium vapor pressure cannot be established, so care should be taken to ensure there is sufficient and relatively consistent source material mass between runs. Furthermore, it has been observed that for some materials like $SnBr_2$, the visual color and appearance of the powder changes after a deposition. It is unknown how much this morphology impacts deposition rate, and therefore whether the use of one source for multiple runs will impact the deposition of that material. Finally, due to the non-linear temperature gradient established by the furnace, different source material holders (*e.g.* MAI and SnI_2) experience different temperature

[22]Chamber cleaning procedures are documented in the CGAVD SOP stored on the Holmes Group Drive.

gradients across their $\sim$1 cm length. As such, the material at the end of the source material holder may see a significantly different temperature than the material at the beginning of the source material holder, which could have a substantial impact on deposition rate depending on how full the source material holder is. To solve the issues with source material area, morphology, and temperature, I recommend to design and implement an actively heated source material holder, as described in Section 8.2.4.

Chapter 5

Controlling MHP Film Morphology and Stoichiometry Using CGAVD

It is widely acknowledged that MHP film quality and morphology strongly impact device performance, as film microstructure can influence charge recombination and collection, shunting pathways, and ion migration kinetics [6, 140, 188, 211, 215, 246, 249–252]. However, there is still much to understand regarding the interplay between synthesis conditions, film microstructure, and the resulting optoelectronic properties. For example, the impact of grain boundaries on non-radiative recombination rates is still an area of debate [198, 214, 253, 254]. The ability to grow films with a wide range of morphologies can enable new insight into these process-property-performance relationships. In this chapter, we take advantage of the high tunability of the CGAVD system described in Chapter 4 to grow films of widely varying stoichiometries and morphologies.[1] We also demonstrate our ability to grow MHP films on a variety of substrates and explore how stoichiometry can impact the resistivity, carrier density, and mobility of $MASnI_3$ films.[2]

[1] Additional experimental details found in Appendix E.

[2] This chapter summarizes work published in ref [255] and authored by myself, Bryan Voigt, Eray S Aydil, and Russell J Holmes.

5.1 Stoichiometric Impact on Morphology

Figure 4.17 in Chapter 4 shows that at sufficiently high substrate temperatures (T_s), there is a range of precursor fluxes that can result in a stoichiometric film, even when the ratios of precursor fluxes are different than stoichiometric. In characterizing films used to construct Figure 4.17, we observed a substantial change in film morphology associated with changing r-ratios according to Equation 4.30. As a reminder, r-ratio ($r_{A,B}$) denotes the normalized excess precursor flux ratio of precursors A and B: $r_{A,B} = (r_A - r_B)/\min(r_A, r_B)$,[3] and thus is a measure of how stoichiometrically balanced the precursor fluxes are at the surface of the substrate. An example of the XRD patterns showing these excess precursor phases for the films grown at T_s = 15 °C can be found in Figure 5.1. The corresponding morphologies we observed are shown in Figure 5.2a-f, where films in a-c contain excess MABr, film d is stoichiometric, and films in e-f contain excess $SnBr_2$. Qualitatively, films containing excess MABr or excess $SnBr_2$ phases exhibit non-ideal microstructures: MABr-rich films (a-c) have large grains but also incomplete coverage with domains that appear to be perovskite grains surrounded by excess MABr. $SnBr_2$-rich films exhibit small grains, pinholes, cracks, and ill-defined grain boundaries (e, f). In contrast, stoichiometric films exhibit large, well-defined grains and dense substrate coverage (d).

[3]Where r_A is the flux of precursor A and r_B is the flux of precursor B at the substrate. $r_{A,B} = 0$ indicates equal molar fluxes of species A and B, a negative value indicates excess metal halide (*e.g.*, $SnBr_2$) and a positive value indicates excess organic halide (*e.g.*, MABr).

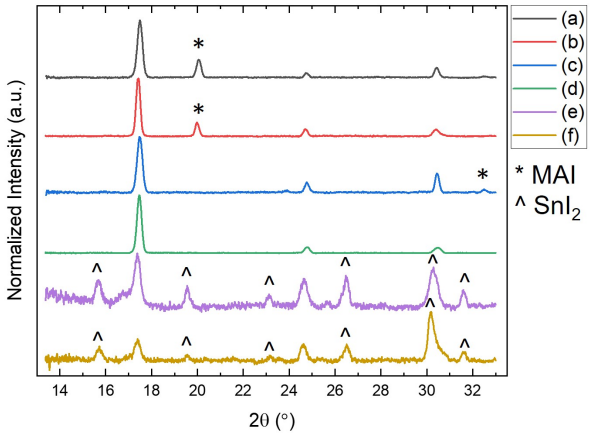

Figure 5.1. X-ray diffraction patterns corresponding to films shown in Figure 5.2. Asterisks and hats denote diffraction peaks corresponding MAI and SnI_2 phases, respectively; the remaining peaks are $MASnBr_3$. X-ray diffraction was collected using a Bruker D8 2D diffractometer with Co Kα radiation (λ=1.7889 Å).

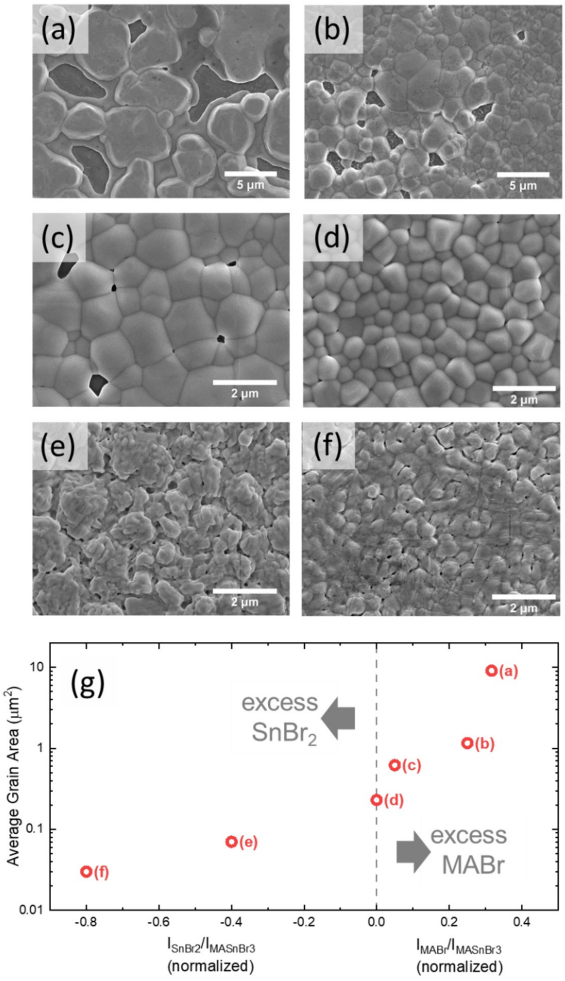

Figure 5.2. Impact of unbalanced precursor fluxes on morphology. (a)-(f) SEM micrographs and (g) corresponding grain sizes of films with varying amounts of excess MABr or $SnBr_2$. Excess MABr results in large grain areas of >1 μm^2, but films have significant pinholes/voids. Excess $SnBr_2$ results in morphologies that have significant non-uniformities, have smaller grain sizes <0.1 μm^2, and less distinct grain boundaries. For these depositions, $\dot{V}_{CG,SnBr_2}$ = 3-5 sccm, $\dot{V}_{CG,MABr}$ = 3-4 sccm, $\dot{V}_{DIL}$ $\approx$ 190 sccm, T_{MABr} $\approx$ 150 °C, T_{SnBr_2} $\approx$ 250 °C, T_g = 280 °C, T_s = 15 °C, and P = 2.6 Torr.

In order to quantify the differences in grain sizes, we calculated the average grain area and peak intensity ratios from the grain size images in Figure E.2 and the XRD patterns in Figure 5.1, respectively. XRD intensity ratios I_{MABr}/I_{MASnBr_3} and I_{SnBr_2}/I_{MASnBr_3} are calculated by dividing the most intense excess precursor peak with that of the $MASnBr_3$ (100) peak (at 2θ = 17.5°). Films are deemed "stoichiometric" if there are no observable diffractions from MABr or $SnBr_2$. Average grain area is calculated by applying the Weka Trainable Segmentation tool in ImageJ to several SEM images taken from different locations on each substrate (Figure E.2). Figure 5.2g shows average grain size as a function of film stoichiometry. As described qualitatively, the stoichiometry of these films has a substantial impact on grain area, increasing

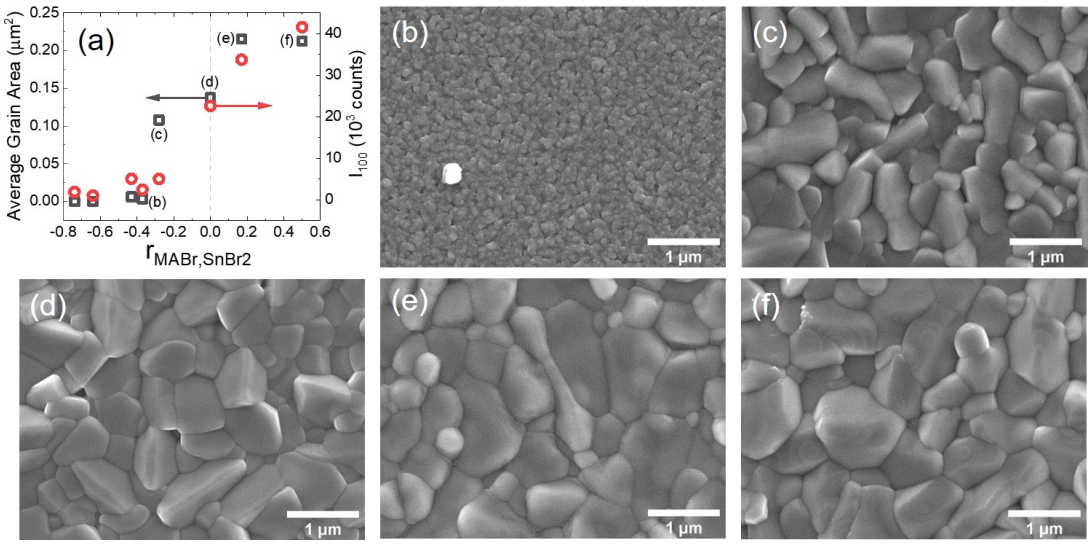

Figure 5.3. (a) Grain size (black squares) and crystallinity (red circles) for $MASnBr_3$ on quartz within the stoichiometric region but at different MABr:$SnBr_2$ flux ratios. Here, the flux ratio was controlled by changing T_{SnBr2}, and $r_{MABr,SnBr_2}$ corresponding to each image in (b)-(f) is labeled in (a). All other variables remained constant for these depositions: $\dot{V}_{CG,SnBr_2}$ = 6 sccm, $\dot{V}_{CG,MABr}$ = 3 sccm, $\dot{V}_{DIL}$ = 191 sccm, T_{MABr} = 136 °C, T_g = 300 °C, T_s = 30 °C, and P = 2.6 Torr.

from 0.03 μm^2 for an r-ratio of -0.8 (excess $SnBr_2$) to 10 μm^2 for an r-ratio of 0.3 (excess MABr).

While Figure 5.2 provides evidence that film stoichiometry can be used to change film morphology, it is unlikely that the non-stoichiometric films here would be relevant for incorporation into devices due to their non-ideal microstructures. Stoichiometric films, on the other hand, exhibit microstructures suitable for devices. We therefore explored if tuning r-ratios *within* the stoichiometric region could be a method for decoupling morphological control from compositional control, while at the same time resulting in films with complete surface coverage. Specifically, we grew $MASnBr_3$ films while tuning the r-ratio within the stoichiometric window as shown in Figure 5.3. In this case, $r_{MABr,SnBr_2}$ was tuned by adjusting the $SnBr_2$ source temperature while keeping all other experimental variables constant. XRD patterns for these films are shown in Figure E.1. Using these diffraction patterns, we can calculate the intensity of the (100) diffraction as a proxy for film crystallinity. Figure 5.3a shows that this diffraction intensity changes dramatically with changes in $r_{MABr,SnBr_2}$, increasing by an order of magnitude from

$r_{MABr,SnBr_2}$ = -0.27 to $r_{MABr,SnBr_2}$ = 0.5. Average grain size has a similar trend, increasing from 0.003 μm^2 to over 0.2 μm^2 for -0.75 $< r_{MABr,SnBr_2} <$ 0.5.

5.2 Electrical Properties vs. Stoichiometry

In addition to using stoichiometry to tune film morphology, we also hypothesized that modifying r-ratio using our CGAVD technique might result in films with different electronic properties. As described in Section 2.2.3, first-principle calculations and experimental results using solution processing have shown that carrier type and concentration can be modified by changing the ratio of MHP precursors during synthesis (*e.g.*, MAI and SnI_2) [82, 115, 118, 119]. To probe how electronic properties varied with stoichiometry using our CGAVD technique, we deposited $MASnX_3$ films with varying MAX:SnX_2 ratios (X = Br, I). All electronic characterization was performed by Bryan Voigt; details can be found in Section E.1.

Four-terminal resistivity measurements for $MASnBr_3$ and $MASnI_3$ films at 280 K resulted in resistivity values of 7x10^4 Ω cm and 3 Ω cm, respectively. These values, as well as the substantially larger resistivity for $MASnBr_3$ compared to $MASnI_3$, are consistent with previous reports [60, 256, 257]. For $MASnI_3$, the lower resistivity enabled Hall effect measurements to be made as a function of excess precursor species (MAI, characterized by I_{MAI}/I_{MASnI_3}, or SnI_2, characterized by I_{SnI_2}/I_{MASnI_3}). Figure 5.4 shows the resulting resistivity, hole concentration, and Hall mobility of $MASnI_3$ films at 280 K as a function of excess precursor species.[4] The resistivity (ρ) is between 0.04 – 3 Ω cm, within the range typically reported for $MASnI_3$ [60, 256]. Resistivity appears to decrease from SnI_2 excess to MAI excess, with a wide range of ρ values scattered around the stoichiometric point.

Interestingly, all $MASnI_3$ films exhibited holes as majority carriers in Hall effect measurements, with an increase in hole concentration of nearly one order of magnitude upon moving from SnI_2 excess, through stoichiometric, and to MAI excess. Hole-dominated conduction is typically associated with the oxidation of Sn^{2+} to Sn^{4+} [107, 258, 259], and the relatively high hole concentrations here may be due to the lack of a reducing agent such as SnF_2, as well as air exposure of the source material and films as they are loaded and unloaded from the CGAVD

[4] XRD patterns for these films are shown in Figure E.3, and representative Hall resistance vs. magnetic field data is shown in Figure E.4.

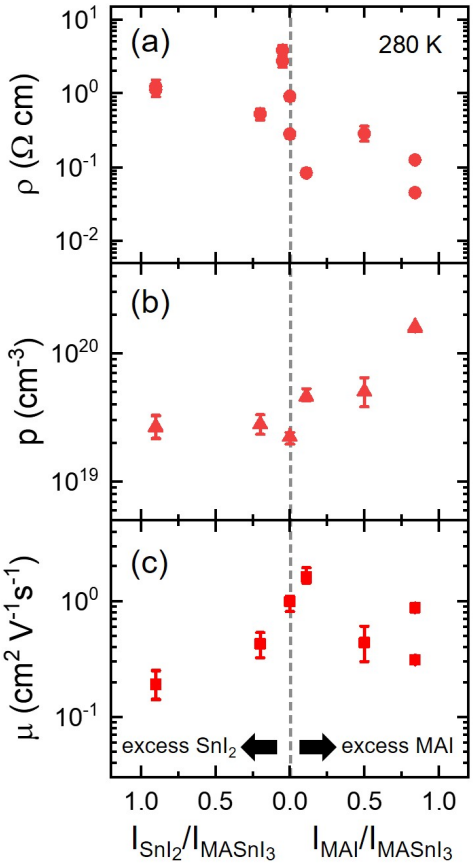

Figure 5.4. Resistivity (ρ), hole concentration (p), and Hall mobility (μ) of $MASnI_3$ films as a function of stoichiometry. Error bars on p and μ include random uncertainty from the linear regression of the field dependence of the Hall resistance and uncertainty in film thickness. In nearly all cases, uncertainty from thickness dominated. For these depositions, $\dot{V}_{CG,SnI_2}$ = 3 sccm, $\dot{V}_{CG,MAI}$ = 3 sccm, $\dot{V}_{DIL}$ = 44 sccm, P = 0.65 Torr, T_{SnI_2} = 270-275 °C, T_{MAI} = 154-161 °C, and T_g = 300 °C.

chamber and prepared for electronic transport measurements.[5] Consequently, mobilities calculated assuming the Drude model (*i.e.*, $\rho = 1/ep\mu$ where e is the electric charge) are relatively low for these films, ranging from 0.2 to 1.5 cm^2/Vs.

While the carrier concentrations and mobilities reported herein are not optimized, and represent a relatively narrow range of experimental parameter space, these initial studies show that CGAVD can be used to tune the electronic properties of MHP films, which is crucial for their eventual optimization for optoelectronic devices.

[5] At the time of these depositions, the enclosure had not been completed, and so loading and unloading of films and substrates was done in ambient conditions.

5.3 Controlling grain size using P and T_s

Given the demonstrated impact of film stoichiometry on electronic properties (Section 5.2) in addition to film microstructure (Section 5.1), it would be desirable to tune film morphology by means other than the precursor flux ratio. This would allow the decoupling and independent modulation both of the film morphology and the electronic properties. Importantly, the vast parameter space afforded by the CGAVD technique provides the means to accomplish this. Here, we show that for a given precursor flux ratio $r_{MABr,SnBr_2}$, the morphology of metal halide perovskite films can be tuned using the total chamber pressure, P, and the substrate temperature, T_s.

In order to probe how film microstructure changes as a function of P and T_s, we deposited a series of $MASnBr_3$ films at various chamber pressures and substrate temperatures. SEM images resulting from these depositions are shown in Figure 5.5. From these SEM images we can observe that grain size appears to increase with increasing pressure and increasing temperature. At P = 10 Torr and T_s = 80 °C, very large $MASnBr_3$ grains of up to $\sim 2\ \mu m$ diameter are achieved. As far as we are aware, these are the largest grains for a contiguous $MASnBr_3$ film (*i.e.*, no pinholes) reported in the literature.

To assess these trends more quantitatively, we calculated the grain areas by using the Weka Trainable Segmentation tool in ImageJ. In addition to grain area, we can also assess film orientation using the XRD patterns for these films by calculating a texture coefficient $TC_{h_ik_il_i}$ [260]:

$$TC_{h_ik_il_i} = \frac{I_{h_ik_il_i}}{I_{0,h_ik_il_i}} \left[\frac{1}{N} \Sigma_1^N \frac{I_{h_ik_il_i}}{I_{0,h_ik_il_i}} \right]^{-1} \tag{5.1}$$

where $I_{h_ik_il_i}$ is the intensity of the measured $(h_ik_il_i)$ diffraction peak, $I_{0,h_ik_il_i}$ is the intensity of the calculated $(h_ik_il_i)$ peak for a powdered crystalline sample, and N = 5 is the number of peaks considered. For a polycrystalline sample, $TC_{h_ik_il_i}$ = 1, whereas $TC_{h_ik_il_i} < 1$ indicates suppressed $(h_ik_il_i)$ peaks and $TC_{h_ik_il_i} > 1$ indicates orientation in the $(h_ik_il_i)$ direction.

Figure 5.6 shows the impact of deposition pressure P and substrate temperature T_s on grain size and texture coefficients for the phase-pure $MASnBr_3$ films show in Figure 5.5. Grain area distributions are shown in Figure E.5. As suggested by Figure 5.5, Figure 5.6a shows that increasing T_s results in larger grains, with grain size increasing from T_s = 30 °C to T_s = 70 °C for all pressures. Interestingly, the degree to which deposition pressure impacts grain size

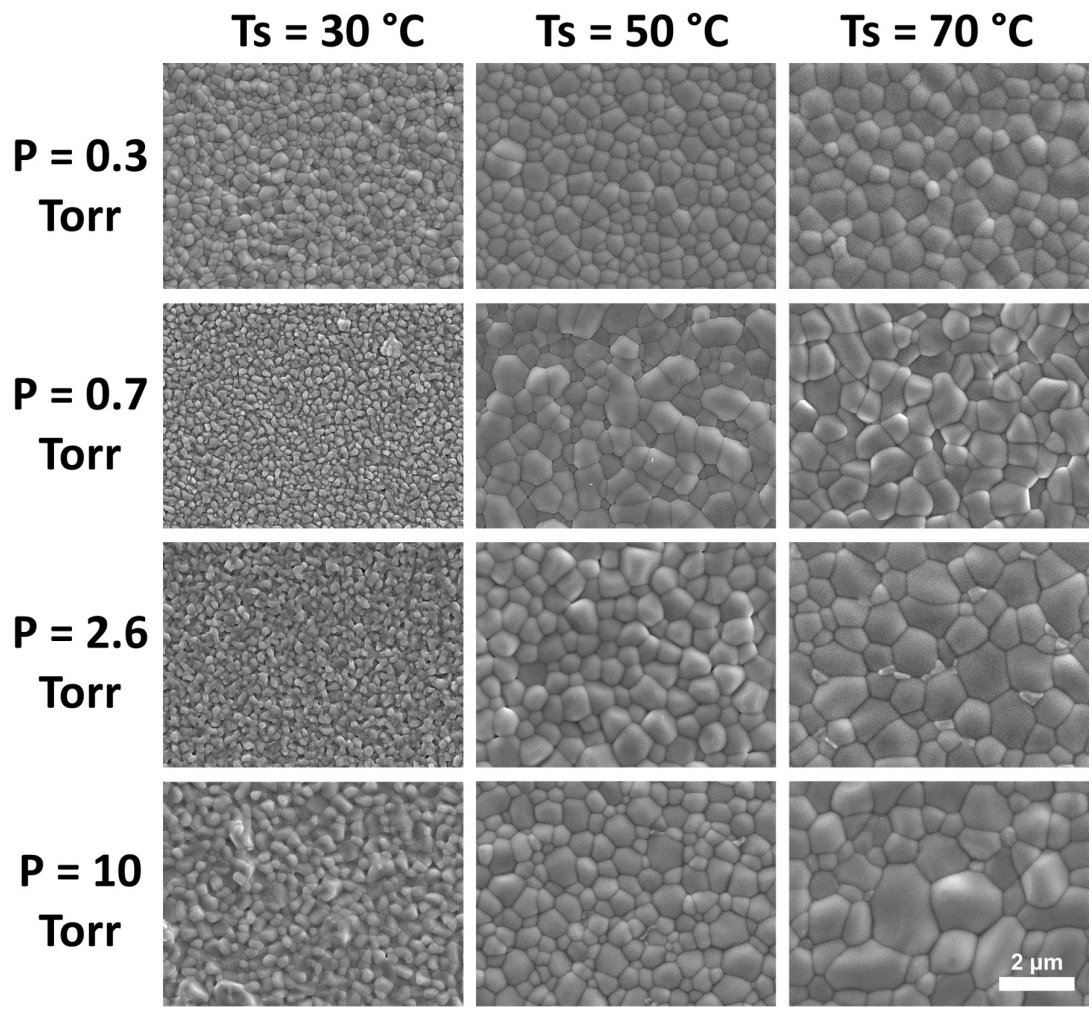

Figure 5.5. SEM images showing how grain size changes for $MASnBr_3$ films on quartz as a function of P and T_s. All other variables remained constant for these depositions: $\dot{V}_{CG,SnBr_2}$ = 4 sccm, $\dot{V}_{CG,MABr}$ = 3 sccm, $\dot{V}_{DIL}$ = 20 sccm (for P $<$ 2.6 Torr) or $\dot{V}_{DIL}$ = 200 sccm (for P $\geq$ 2.6 Torr), T_{SnBr_2} = 233 °C, T_{MABr} = 142 °C, and T_g = 300 °C. For all depositions, $r_{MABr,SnBr_2} \approx 1$.

appears to increase with increasing T_s. For T_s = 30 °C, changing the deposition pressure from 0.3 to 10 Torr has relatively little impact on average grain size. For T_s = 50 °C, however, the same change in pressure results in an approximate doubling of grain size. For T_s = 70 °C this effect is even more dramatic, as grain size triples from P = 0.3 Torr to P = 10 Torr. Grain size

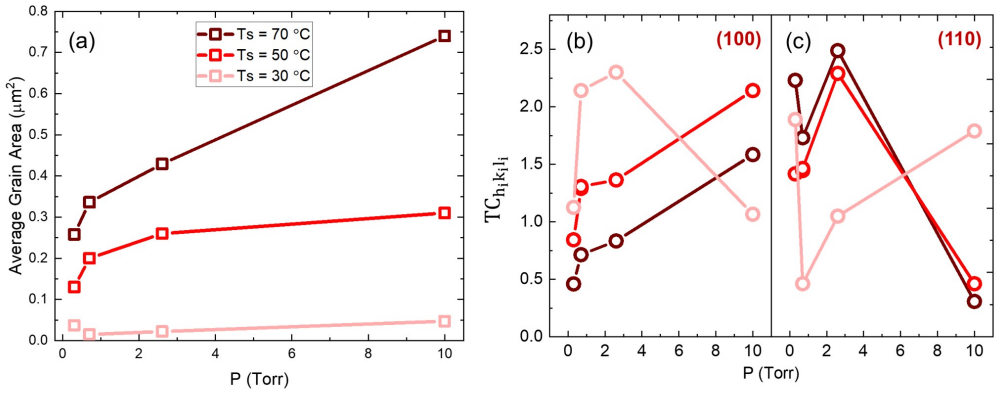

Figure 5.6. Film grain size (a) and texture coefficient $TC_{h_i k_i l_i}$ (b,c) as a function of P and T_s for $MASnBr_3$ films shown in Figure 5.5.

distributions (Figure E.5) have a similar dependence on P and T_s; at low substrate temperatures (T_s = 30 °C), deposition pressure has little impact on grain size distributions, but for T_s > 30 °C, the range of grain areas increases with both P and T_s. The grain sizes in this work span a range that has been reported for solution processed Sn MHPs [261], however the ability to incrementally tune grain size while maintaining uniform and complete coverage (and phase purity) is difficult to achieve with common spin-coating methods.

Film texturing can also be tuned using P and T_s. Figures 5.6b and 5.6c show the texture coefficient for (100) and (110) peaks calculated using Equation 5.1, demonstrating the ability to preferentially orient or suppress these peaks. $TC_{h_i k_i l_i}$ for additional peaks are shown in Figure E.6. As with grain size, the dependence of $TC_{h_i k_i l_i}$ on P varies with substrate temperature. Whereas the orientation of the (100) peak increases monotonically with increasing pressure for $T_s \geq$ 50 °C, this trend is not monotonic for T_s = 30 °C. For the $T_s \geq$ 50 °C, the (110) peak can be nearly completely suppressed at P = 10 Torr, but it is slightly oriented for T_s = 30 °C and P = 10 Torr.

5.4 Deposition on Various Substrates

One of the advantages of vapor processing techniques is that it can allow facile deposition onto a variety of substrates or on other films. As discussed in Chapter 6, this can enable the

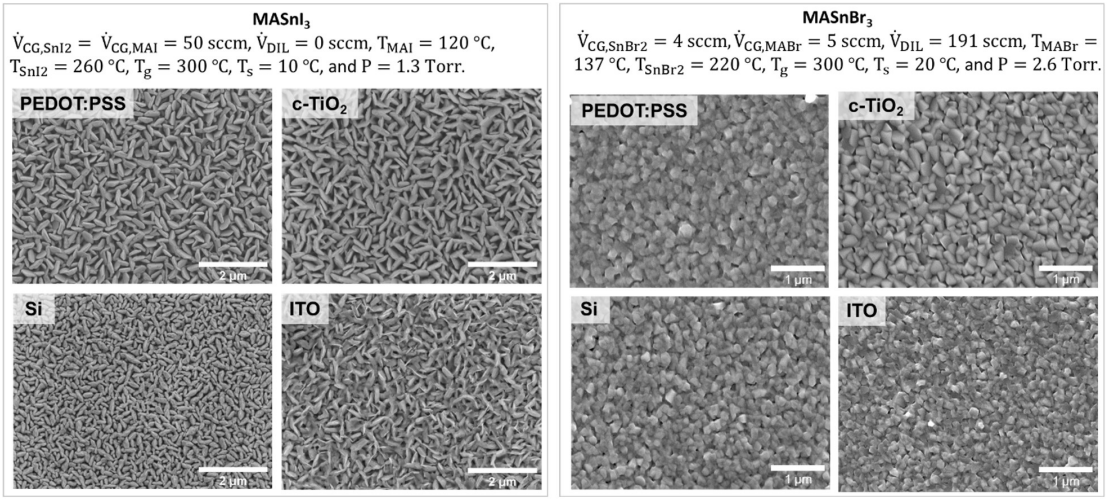

Figure 5.7. $MASnX_3$ morphological consistency across various substrate types for stated deposition conditions. Not all morphologies pictured are ideal for solar cells, however the morphology of these films appears to vary more as a function of deposition conditions than substrate type.

creation of novel multi-layer films like all-perovskite heterojunctions, as well as deposition on flexible substrate materials that can be challenging with common spin-coating techniques. Given that this was a critical part of our long-term goals, we wanted to confirm that we could indeed grow our films on a variety of substrates/underlayers. Figure 5.7 shows the morphology of $MASnI_3$ and $MASnBr_3$ films grown on four different substrates (PEDOT:PSS, c-TiO_2, Si, and indium-tin-oxide (ITO)-coated glass) under identical deposition conditions. Interestingly, there is relatively little variation in apparent microstructure between these different underlayers. While these particular films are not optimized for incorporation into optoelectronic devices, the ability to deposit films with similar morphology on different surfaces provides an opportunity to conduct meaningful studies with a variety of electron- and hole-transport layers.

Furthermore, we were able to succesfully deposit $MASnI_3$ films on a flexible Kapton film (Figure 5.8), opening the door for potential future fabrication of flexible devices using this system.

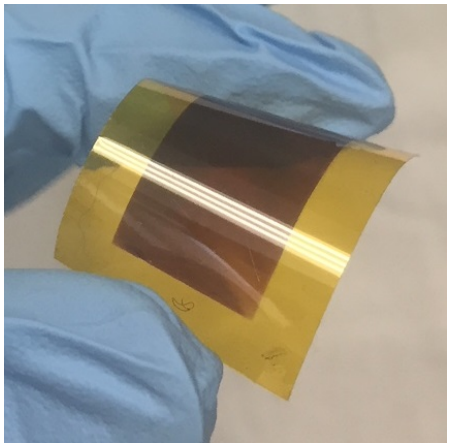

Figure 5.8. Successful deposition of $MASnI_3$ on flexible Kapton film using CGAVD. Approximate film dimensions are 1 cm x 2 cm.

5.5 Summary

This chapter demonstrates our ability to harness the CGAVD technique to carefully and intentionally tune the stoichiometry and morphology of MHP films. By systematically tuning experimental parameters such as the source material temperatures and carrier gas flow rates, we can tune film stoichiometry across a wide range, and observe corresponding changes in film morphologies and electronic properties. To change grain area and film orientation independently of stoichiometry, we modulate chamber pressure and substrate temperature. With this method we can easily tune the grain area from $\sim$0.001 to $>$0.7 μm^2 for $MASnBr_3$ thin films. Finally, we show the ability to deposit MHP films on flexible substrates and that the morphology of our $MASnX_3$ films using CGAVD is relatively independent of substrate/underlayer, enabling film growth on a variety of relevant electron and hole transport layers. The work in this chapter not only highlights the power of the CGAVD technique to access morphologies that can be used to optimize film properties and device performance, but it also lays the groundwork for our heterojunction work in Chapter 6.

Chapter 6

Formation and Stability of Perovskite-Perovskite Heterojunctions

6.1 Background

As with classical inorganic semiconductors, heterojunctions play a crucial role in dictating the energetic landscape and operation of MHP devices [262]. Optimization of these energetics can directly impact device performance by improving carrier transport and minimizing optical and voltage losses [263–267]. Because the ability to effectively engineer interfaces between multiple MHPs (*e.g.* between adjacent layers with different A, B, and/or X site ions) has been elusive, current state-of-the-art devices rely on heterojunctions between the active MHP layer and adjacent metal oxide or organic semiconductor layers [154, 268]. While these structures have already achieved high efficiencies, challenges associated with the use of organic and metal oxide transport layers remain. For example, poor stability is commonly observed for typical organic transport layers, and in some cases these organics have been shown to be the limiting factor for the overall stability of MHP devices [269, 270]. On the other hand, high-temperatures are required to synthesize common inorganic transport layers like TiO_2 and ZnO, which limits the ease of fabrication and the choice of substrate [271, 272]. Synthesis of all-perovskite heterojunctions could address these challenges by enabling the replacement of these problematic transport layers with MHP materials while also providing an opportunity to further optimize transport layer properties towards more efficient devices [273].

Furthermore, the realization of perovskite-perovskite heterojunctions would enable a broader

swath of electronic and optoelectronic devices in analogy to conventional semiconductors (*e.g.*, III-V), permitting a more effective application of the outstanding properties and tunability of the MHP material system. For example, all-perovskite heterojunctions could accelerate the development of high-speed electronics based on resonant tunneling heterostructures [274, 275], low-power multivalued logic applications[275], or next-generation integrated optoelectronic and photonic circuits [276, 277].

In addition to the promise of new applications and improved performance, all-perovskite heterojunctions also provide an ideal platform to study mass transport in MHP materials [278]. Ionic transport in MHPs gives rise to important materials engineering challenges including current-voltage hysteresis in solar cells [125, 279] and light-induced phase instability in mixed-halide MHPs [280], but can also be exploited for new applications like resistive switching devices [48].

Despite their promise, all-perovskite heterojunctions are a relatively unexplored frontier, likely due to challenges with fabricating multi-layer perovskite structures and the diffusion of ionic species between layers [277]. As such, successful reports of all-perovskite heterojunctions are limited to those with at least one perovskite with reduced dimensionality (0D, 1D, 2D). Heterostructures with 0D perovskites (*e.g.* quantum dots) have been shown to improve photoluminescence quantum yield (PLQY) [89, 281] and MHP phase stability [282]. Yang *et*

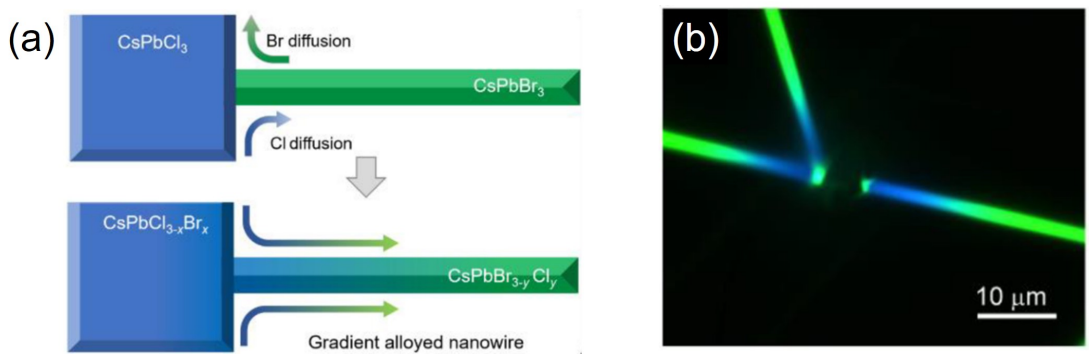

Figure 6.1. (a) $CsPbBr_3$/$CsPbCl_3$ nanowire heterojunction geometry to study ion diffusion. (b) Optical image of the nanowires under 400nm laser excitation. Adapted with permission from D. Pan *et al*. "Visualization and Studies of Ion-Diffusion Kinetics in Cesium Lead Bromide Perovskite Nanowires". In: Nano Letters 18.3 (2018), pp. 1807–1813. Copyright 2018 American Chemical Society.

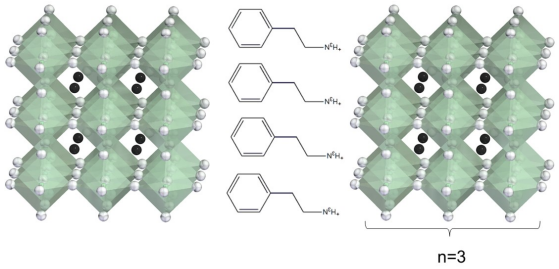

Figure 6.2. Example of a 2D perovskite structure, typically described as $R_2A_{n-1}B_nX_{3n+1}$, where R is a large organic cation and "n" denotes the number of $[BX6]^{4-}$ layers separated by R cations. In this example, R is phenethylammonium and n=3.

al. employ a 0D/3D ($CsPbBr_3$ QD)/($MAPbI_{3-x}Cl_x$) perovskite heterostructure in a photodetector to improve transport of carriers and the corresponding response time and detectivity [42]. All-perovskite heterojunctions have also been successfully formed in 1D nanowires [276, 278, 283]. An example of these nanowire heterostructures is shown in Figure 6.1, where this geometry is used to study halide diffusion. Dou *et al.* use anion-exchange chemistry to fabricate $CsPbBr_3$/$CsPbCl_3$ and $CsPbBr_3$/$CsPbI_3$ perovskite nanowires with sharp optical and electronic interfaces [276]. Recently, $CsPbI_3$/$CsPbBr_3$ nanowire heterojunctions have enabled flexible and self-powered lateral photodetector arrays [283].

The vast majority of reported all-perovskite heterojunctions are 2D/3D or "quasi-2D" heterostructures, where a bulky organic cation separates one or more MHP layers with reduced-dimensionality [284]. 2D perovskites are typically described by the formula $R_2A_{n-1}B_nX_{3n+1}$, where R is a large organic cation and "n" denotes the number of $[BX_6]^{4-}$ layers separated by R cations as shown in Figure 6.2 [62]. Many reports focus on the enhanced stability 2D/3D heterostructures provide (relative to their 3D counterparts) due to the hydrophobicity of the R-site cation [61, 62], but quasi-2D heterostructures have also been employed to modify the energetic landscape of MHP devices [63, 65, 285]. It has been widely shown that reducing 2D layer thickness results in widening of the bandgap and an increase in exciton binding energies [286–288]. By layering smaller bandgap 3D and larger bandgap 2D perovskites, quantum wells can be created to spatially confine excitons and improve PL efficiency [63]. Wang *et al.*, for example, show the spontaneous formation of multiple quantum wells in $NMA_2(FAPbI_3)_{n-1}PbI_4$ (NMA = 1-naphthylmethylamine, FA = formamidinium) quasi-2D perovskites, which result in efficient energy transfer and radiative recombination of excitions [64]. A schematic of the proposed band diagram for these multiple-quantum well structures are shown in Figure 6.3,

The successes of all-perovskite heterojunctions based on reduced dimensionality MHPs highlights the wide applicability of these structures and motivates continued exploration. While

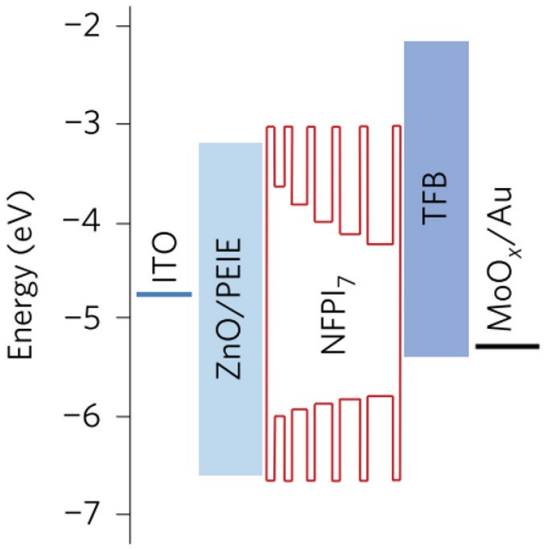

Figure 6.3. Schematic of proposed energy band diagram for the multiple quantum well MHP films from ref [64]. Here, $NFPI_7$ denotes a quasi-2D MHP formed from 1-naphthylmethylamine iodide (NMAI), formamidinium iodide (FAI) and PbI_2 precursors in a molar ratio of 2:1:2, which result in a film with majority n = 2 quantum wells (*i.e.*, NMA_2FAPbI_3). Adapted by permission from Springer Nature: Nature Photonics, "Perovskite light-emitting diodes based on solution-processed self-organized multiple quantum wells", N. Wang *et al.*, Copyright 2016.

promising, exclusive reliance on self-assembled and low-dimensional (0D, 1D, 2D) structures limits the possibilities for interfacial engineering and optimization of layer properties: an example of such a limitation in quasi-2D MHPs is the trade-off between high stability and low charge carrier mobility due to the insulating nature of the organic R cations [289]. As such, the ability to synthesize all-perovskite heterojunctions from an array of 3D perovskites would allow more intentional engineering and optimization of these interfaces.

In this chapter we demonstrate for the first time the formation of perovskite-perovskite heterojunctions between thin films of 3D ABX_3 MHPs and identify two pairings with stability $>$1500 hours. We also identify which species are diffusing across the interface and the impact of grain size on mixing rate for a case where multiple cations are varied across the interface. Thus, in addition to demonstrating an approach to realizing stable perovskite-perovskite heterojunctions, we offer design rules for maximizing interface stability.

6.2 Experimental Methods

In order to successfully form perovskite-perovskite heterojunctions, a multi-step process is employed that utilizes both solution and vapor deposition methods as shown in Figure 6.4. Briefly, a solution-processed layer of $APbX_3$ is deposited on glass or Si substrates followed by a layer of $MASnX_3$ deposited using the CGAVD system described in Chapter 4 [255]. This multi-step

process circumvents the need for solvent orthogonality and/or a chemically robust interlayer for sequential solution processing, thus enabling the formation and study of all-perovskite heterojunctions with intimate contact between the MHP layers. Additional synthesis details can be found in Appendix F.

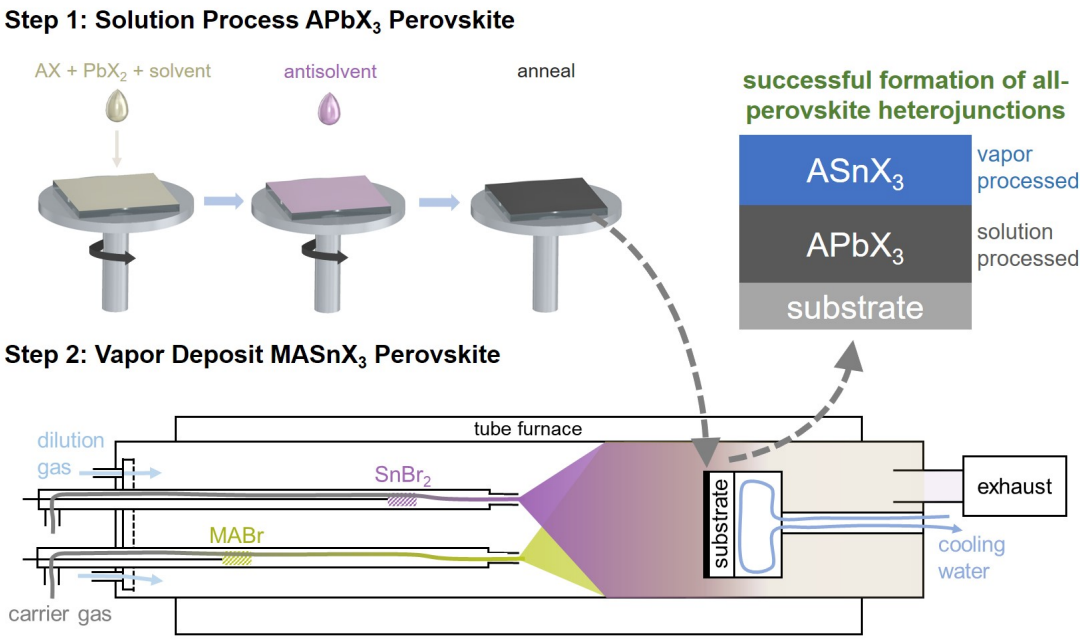

Figure 6.4. Schematic representation of heterojunction formation by sequential deposition of $APbX_3$ and $MASnX_3$ perovskite layers. First, $APbX_3$ films are deposited *via* spin-coating. These films are then transferred to a vapor deposition chamber where MAX and SnX_2 are co-deposited to form a $MASnX_3$ perovskite layer.

6.3 Successful formation of heterojunctions

The propensity of ionic species to diffuse in perovskites and the resulting possibilities for stable MHP heterojunctions depends on many factors including the identity of the diffusing species and the type, quantities, and energetics of diffusion pathways associated with that species. For instance, many first-principles calculations indicate that the halide ion (X^-) is the most mobile species in the perovskite lattice [290, 291]. This high rate of mass transport has been used to synthesize mixed halide perovskites *via* solid-solid or liquid-solid "ion-exchange" techniques [292]. As such, it seems likely that the formation of a stable all-perovskite MHP where the

halogen is varied across the interface may be difficult. Liquid-solid ion-exchange has also been used to mix A-site (FA/MA) [293] and B-site (Pb/Sn) [294] cations, with evidence of fully-mixed, homogenous films. Despite this evidence of mobile A- and B-site species, there have been many fewer reports of their transport in 3D MHP structures across solid-solid interfaces, and the potential for long-term stability of MHP interfaces with varying A- and B-sites remains unknown.

Our first goal was therefore to test the dependence of heterojunction formation on the ions occupying the A, B, and/or X sites. We did this by fabricating three different structures using the method outlined in Section 6.2: $MAPbBr_3$/$MASnBr_3$ (varying only the B site), $FAPbBr_3$/$MASnBr_3$ (varying both A and B sites), and $FAPbI_3$/$MASnBr_3$ (varying ions on all sites). We then probed in detail whether we were able to form these heterojunctions at all - *i.e.,* whether the layers stayed separated long enough to measure or if they mixed too rapidly to be characterized. Practically, heterojunction formation is considered "successful" if the two layers remain unmixed long enough to be observed using absorption and XRD measurements, taken $\sim$30 minutes and 1-2 hours after growth, respectively.

Figure 6.5 shows the successful formation of $MAPbBr_3$/$MASnBr_3$ and $FAPbBr_3$/$MASnBr_3$ heterojunctions, and evidence of partial mixing for $FAPbI_3$/$MASnBr_3$. In each case, absorbance spectra show two distinct onset features that correspond to the band gaps of the constituent layers of the heterojunction. The contribution of each layer to the total absorbance is highlighted in Figures 6.5a - 6.5c, with $MASnBr_3$ exhibiting an onset at $\lambda \sim 580$ nm, $MAPbBr_3$ at $\lambda \sim 540$ nm, $FAPbBr_3$ at $\lambda \sim 550$ nm, and $FAPbI_3$ at $\lambda \sim 825$ nm. Shading for the smaller bandgap layer corresponds to the measured absorption of those individual films ($MASnBr_3$ in orange for Figure 6.5a and 6.5b, $FAPbI_3$ in green for Figure 6.5c), and shading for the larger bandgap layer corresponds to the remaining absorption for the heterojunction. The thin orange shoulder in Figure 6.5c near 825 nm is likely due to differences in background subtraction for the heterojunction and $FAPbI_3$ film arising from the high-intensity scattering background of $FAPbI_3$ (see Figure F.6). The total absorption of the heterojunction is nearly a superposition of the absorptions of the individual isolated films as shown in Figure 6.6. This is in contrast to the well-documented single-onset absorption spectra typical of mixed A, B, and/or X-site MHPs [295, 296], which would be expected if ion diffusion across the interface led to alloy formation. All absorbance spectra have backgrounds subtracted for clarity.

Heterojunction formation is also examined using X-ray photoelectron spectroscopy (XPS)

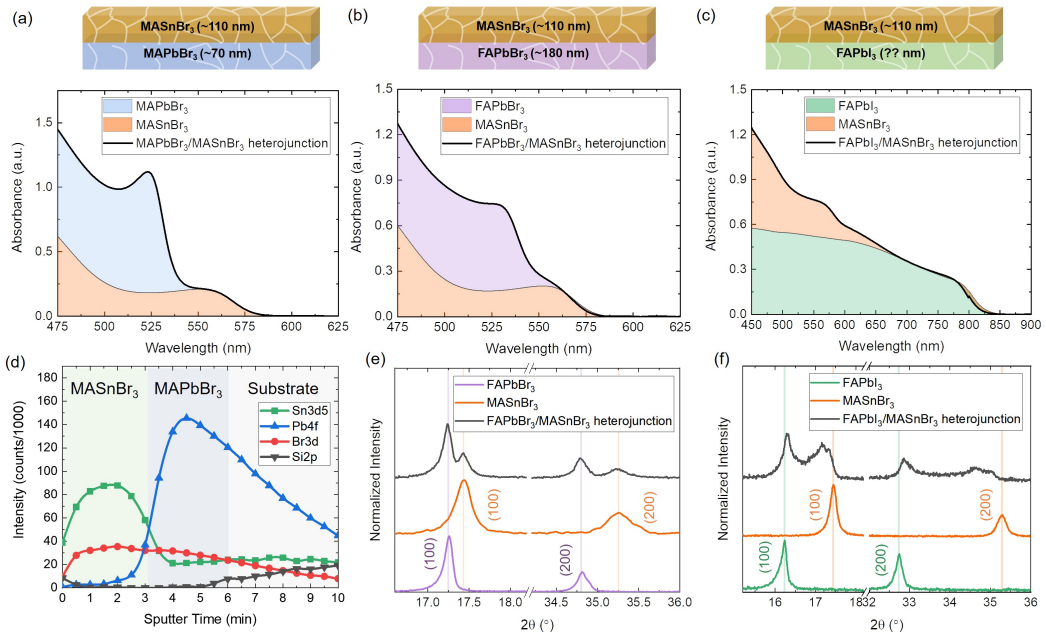

Figure 6.5. Formation of three different perovskite heterojunctions: (a) and (d) $MAPbBr_3/MASnBr_3$, (b) and (e) $FAPbBr_3/MASnBr_3$, and (c) and (f) $FAPbI_3/MASnBr_3$. Absorbance data (a) – (c) shows distinct features that correspond to the absorption of the individual perovskite layers: the measured absorption of the heterojunction is very close to the superposition of the individual layer absorptions. (d) XPS depth profile of $MAPbBr_3/MASnBr_3$ shows a clear transition from an Sn-only $MASnBr_3$ perovskite layer to a majority Pb $MAPbBr_3$ layer; persistence of Sn and Pb signals into the substrate are attributed to inefficient sputtering of metallic species. Shaded layers corresponding to approximate interfaces are for visualization only. XPS was performed by Dr. Jenny Mann of Physical Electronics. XRD of (e) $FAPbBr_3/MASnBr_3$ and (f) $FAPbI_3/MASnBr_3$ heterojunctions show peaks that correspond to both perovskite layers; slight peak shifts in the $FAPbI_3/MASnBr_3$ may indicate partial mixing of the two layers. X-ray diffraction was collected using a PANalytical X'pert PRO diffractometer with Co Kα radiation (λ=1.7889 Å).

sputter depth profiles (performed by Dr. Jenny Mann of Physical Electronics) or X-ray diffraction (XRD). For the $MAPbBr_3/MASnBr_3$ heterojunction, the constituent layers have the same room temperature crystal structure ($Pm\bar{3}m$) and similar lattice parameters (a=5.901 Å for $MAPbBr_3$ and a=5.905 Å for $MASnBr_3$) [68, 72], rendering their X-ray diffraction patterns indistinguishable within the diffractometer resolution limits.[1] In this case, XPS sputter depth

[1]It should be noted, however, that the XRD pattern of the heterojunction is consistent with presence of these films on the substrate as seen in Figure F.2a.

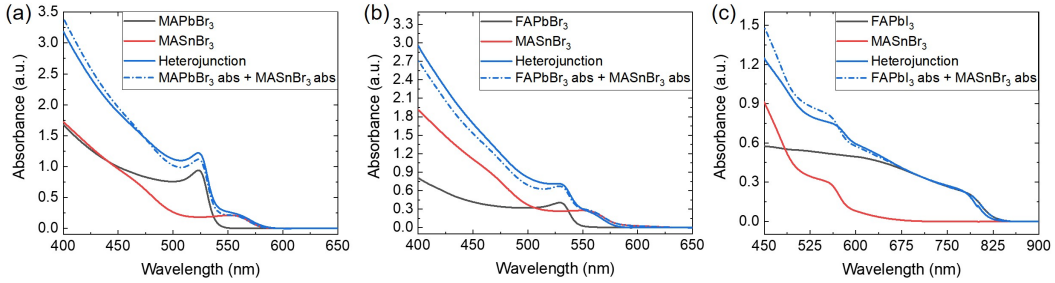

Figure 6.6. Absorption data (a) – (c) for individual films and heterojunctions depicted in Figure 6.5a – c (backgrounds subtracted for clarity). The linear superposition of the individual perovskite films (dashed blue line) aligns well with the measured absorption spectra of the corresponding heterojunction as one would expect for a multi-layer film where the layers are segregated.

profiling of the $MAPbBr_3$/$MASnBr_3$ heterojunction using a C_{60}^+ sputtering source is more informative. For additional experimental details, see Appendix F and Chapter 7. As a function of sputter time, Figure 6.5d shows a transition from high Sn 3d5/2 photoelectron intensity, originating from the top $MASnBr_3$ layer ($\sim$110 nm thick), to the Pb 4f photoelectrons originating from the bottom $MAPbBr_3$ layer ($\sim$70 nm thick). After 5 minutes of sputtering, the Si 2p signal from the glass substrate is observed. Residual Sn and Pb counts which persist after reaching the substrate are attributed to inefficient removal of metallic species and differences in sputtering rates between organic, metallic, and halogen species, both of which have been observed in the literature [297, 298]. Furthermore, a majority of Sn 3d5/2 and Pb 4f signals after 3.5 and 8 minutes, respectively, are at lower binding energies which we ascribe to metallic damage (discussed in detail in Chapter 7). If this damage signal is excluded, the interface between the layers appears sharper and the persistence of Sn 3d5/2 and Pb 4f signals into the substrate is diminished as can be seen in Figure 7.9b.

For MHPs with sufficiently different lattice parameters, such as $FAPbBr_3$/$MASnBr_3$ and $FAPbI_3$/$MASnBr_3$, XRD can be used to probe the crystal structure in each layer and whether the two layers have alloyed.[2] For a heterojunction, the overall XRD pattern should contain peaks corresponding to both crystalline layers. If ion diffusion leads to substantial intermixing, an alloy would form, characterized by XRD peaks shifted from the neat materials. As shown in Figure 6.5e, (100) peaks corresponding to both $MASnBr_3$ (2θ=17.45°) and $FAPbBr_3$

[2]XRD was collected using a PANalytical X'pert PRO diffractometer with Co Kα radiation (λ=1.7889 Å).

(2θ=17.25°) are visible, confirming the formation of a $FAPbBr_3$/$MASnBr_3$ heterojunction. It is interesting to note that this separation is less pronounced for the $FAPbI_3$/$MASnBr_3$ heterojunction in which the halogen is also varied across the interface (Figure 6.5f). Although the diffraction pattern for $FAPbI_3$/$MASnBr_3$ shows two distinct low-angle peaks (2θ=16.31° and 17.25°), they do not align with the neat (100) $FAPbI_3$ (2θ=16.25°) and (100) $MASnBr_3$ peaks (2θ=17.45°). Moreover, there is significant diffraction intensity between the two peaks. We attribute this to mixing across the interface during the time elapsed between absorbance and XRD measurements (1-2 hours). Additional data for these three heterojunctions can be found in Figure F.3.[3]

Taken together, the data in Figure 6.5 confirmed our ability to form all-perovskite heterojunctions using our multi-step solution and vapor processing method, as well as to verify their formation using absorption, depth-profiled XPS, and XRD measurements. This success fulfilled one of the ultimate goals of my PhD work, and proved that all-MHP heterojunctions formed from 3D films are indeed possible, motivating additional studies on the stability and mixing of these heterojunctions.

6.4 Heterojunction stability over time

Our observation of mixing in structures with a variation in the halogen ion ($FAPbI_3$/$MASnBr_3$), but not for those with the same halogen ($MAPbBr_3$/$MASnBr_3$ and $FAPbBr_3$/$MASnBr_3$), is consistent with first-principles calculations which reveal that the X-site species are the most mobile in the ABX_3 MHP lattice [290, 291]. To further probe the interfacial stability of all-perovskite heterojunctions, we examined the time evolution of seven heterostructures in detail. To do this, we fabricated these structures as outlined in Section 6.2 and then performed periodic absorption and XRD measurements to track the location of absorption and diffraction peaks over time. We then extract a "mixing time" by calculating the time (since deposition) at which XRD peaks corresponding to different layers merge into single peaks and/or the absorbance spectrum evolves to show a single onset feature; this is equivalent to the time at which these data are stable and no longer change with time. Mixing time is thus considered the time when

[3] A small diffraction peak corresponding to excess PbI_2 (Figure F.2f) observed in the neat $FAPbI_3$ film is not present in the heterojunction film; it is possible that this slight non-stoichiometry of the $FAPbI_3$ film could contribute to faster mixing by altering the defect concentration in the bottom layer.

films are fully mixed, and not when evidence for diffusion is first observed.[4] This is in part due to the practical challenges of determining mixing time from the first observation of mixing, as films that mixed rapidly were difficult to observed in an unmixed form. In general, however, the samples/structures in which mixing was observed quickest were also the samples to have the shortest fully-mixed mixing time.

An example of this mixing time calculation is shown in Figure 6.7 using absorption and XRD data for a $FAPbBr_3$/$MASnBr_3$ heterojunction. For the absorption data in Figure 6.7a, time points up to 190 hr show two absoprtion onsets indicating the existence of two phases.[5] At 314 hr, however, only one clear absorption onset is visible. Measurements after 314 hrs do not change, further supporting the notion that the diffusing species has fully mixed between the two layers. Because of the timespan between measurements, it is not clear when between the 190 hr and 314 hr measurements the films were fully mixed. As such, we calculate mixing time as the average of these two time points (*i.e.* (314 hr+190 hr)/2=252 hr, as shown in Figure 6.7c),

[4]Absorption and XRD measurements for mixing time calculations are performed on the same sample, and that these samples are stored in an N_2 glovebox between measurements.

[5]Note these are the same absorption onsets as seen in Figure 6.5b.

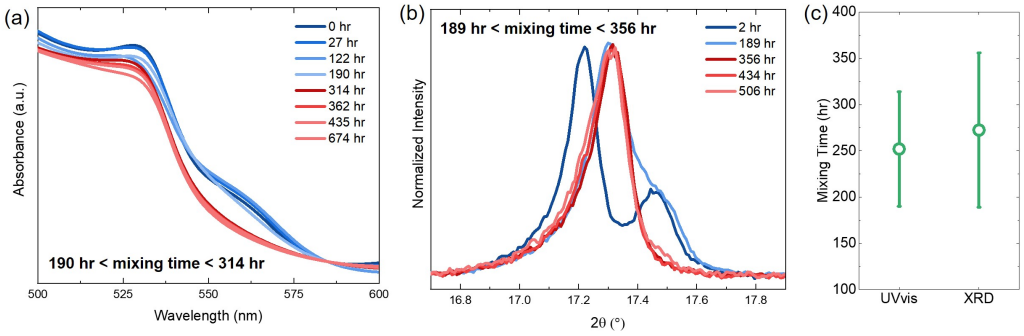

Figure 6.7. Example of mixing over time for a $FAPbBr_3$/$MASnBr_3$ heterojunction. (a) Absorption data over time, showing the transition from two absorption features to a single unchanging onset after 314 hr. (b) XRD data, where the initially distinct diffraction peaks show mixing behavior and eventually form one peak after 356 hr. (c) Mixing time calculated from (a) and (b) by taking the average of the last timepoint before the sample is fully mixed and the first time point after the sample is fully mixed; error bars correspond to the time range of these two datapoints. X-ray diffraction was collected using a PANalytical X'pert PRO diffractometer with Co Kα radiation (λ=1.7889 Å).

and consider the two measurement timepoints to be the error bars.

Similarly, the XRD data in Figure 6.7b show two diffraction peaks corresponding to $FAPbBr_3$ and $MASnBr_3$ at t = 2 hr. At t = 189 hr, substantial mixing is observed, as the peak locations have shifted and there is substantial diffraction intensity between them. However, this spectra continues to change until the 356 hr measurement, where only one clear peak is observed. After this timepoint, no further changes are seen. Thus, in this case we would calculate the "mixing time" to be 272.5 hr, with error bars spanning from 189 hr to 356 hr, as seen in Figure 6.7c. Good agreement between mixing time calculated using absorption and XRD data provide confidence that these two measurement techniques are capturing the same mixing behavior in these samples.

Employing this procedure, we construct and measure the seven different $APbX_3/MASnX_3$ structures shown in Figure 6.8a. Here, the x-axis corresponds to approximate mixing time, where heterojunctions are assigned to three broad categories: 0 - 100 hrs, 100 - 1000 hrs, and no mixing observed. These coarsely grained categories were chosen as a result of the variation in mixing time error bars between samples, which are shown approximately in Figure 6.9. Ideally, XRD and absorption measurements could be taken at short and consistent intervals for all films (*e.g.* every two hours) in order to minimize the uncertainty in mixing time calculations and variation between samples. However, due to practical limitations such as shared instrument scheduling, not all heterojunction samples could be measured at the same time intervals. Furthermore, the need for more or less frequent measurements is also dictated by how quickly the heterojunctions mix, with faster mixing samples requiring shorter times between measurements in order to capture their mixing behavior. As such, the x-axis scale in Figure 6.8a reflects a conservative assessment of the uncertainty in our mixing time calculations. Additional data for these heterojunctions can be found in Figures F.2 - F.7.

Interestingly, Figure 6.8a shows that both $MAPbBr_3/MASnBr_3$ and $CsPbBr_3/MASnBr_3$ heterojunctions appear stable for $>$1500 hours, as evidenced by their unchanging absorbance spectra in Figures 6.8b and 6.8c.[6] $MAPbBr_3/MASnBr_3$ samples heated at 60 °C for 7 hours in an N_2 atmosphere also showed no observable mixing (Figure 6.10), further indicating the robustness of this interface. The mixing time of the remaining heterojunctions decreases dramatically when the halogen is varied between the layers, as expected based on our previous

[6] 1500 hrs was the longest time measured for these samples and that is why mixing time is cited as $>$1500 hours. It does not mean that any mixing was observed after 1500 hours: in fact no mixing was observed for any $MAPbBr_3/MASnBr_3$ or $CsPbBr_3/MASnBr_3$ samples.

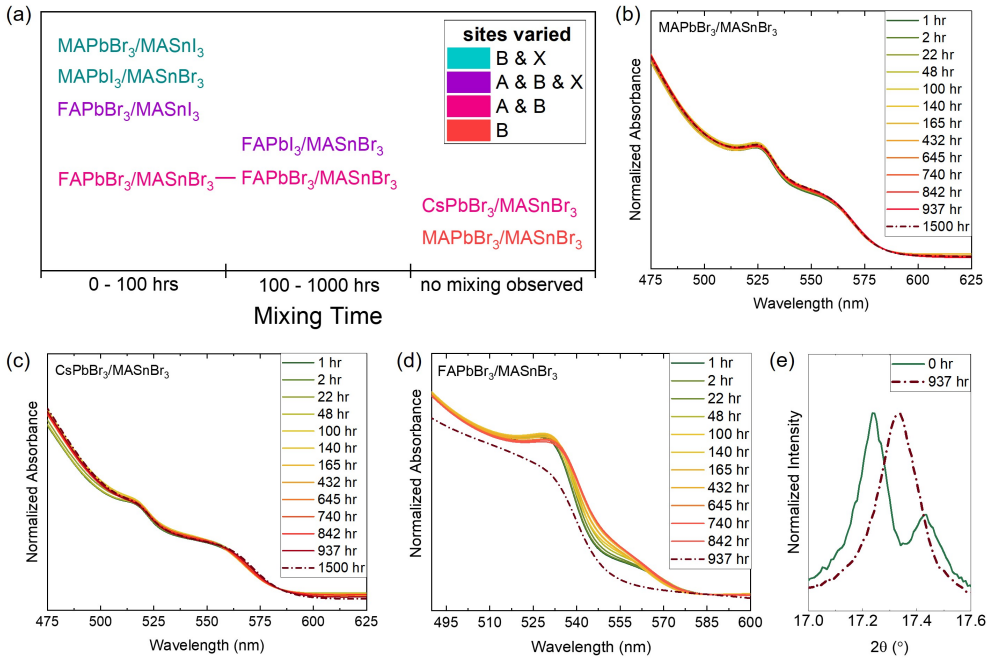

Figure 6.8. (a) Mixing time for various perovskite heterojunctions. Time-dependent absorbance of stable $MAPbBr_3/MASnBr_3$ (b) and $CsPbBr_3/MASnBr_3$ (c) heterojunctions, where no mixing is observed. Time-dependent absorbance spectra (d) and XRD pattern (e) for the $FAPbBr_3/MASnBr_3$ heterojunction with the longest observed mixing time. The single absorption onset and (100) XRD peak at 937 hours indicate interdiffusion of at least one species in the originally layered film. Times are rounded to the nearest hour and all absorbance data are normalized to their value at a wavelength of λ = 585 nm for clarity. X-ray diffraction was collected using a PANalytical X'pert PRO diffractometer with Co Kα radiation (λ=1.7889 Å).

discussion.

On the other extreme, some pairings mixed so rapidly (<1 hour) that characterization prior to substantial mixing was not possible due to transfer-time limitations for characterization (*e.g.* $MAPbBr_3/MASnI_3$ in Figure F.3). A detailed study of one of these rapidly mixing cases was performed on fully vapor-deposited $MASnI_3/MASnBr_3$ films. For this study, phase pure $MASnBr_3$ and $MASnI_3$ thin films were deposited *via* one-step co-deposition by manipulating $\dot{V}_{CG,i}$ and T_i according to Equation 4.29 such that $r_{MABr}/r_{SnBr_2} \sim 1$ and $r_{MAI}/r_{SnI_2} \sim 1$, respectively. Due to the rapid mixing of these sequentially deposited MHPs, the stoichiometry of the resulting $MASnBr_xI_{3-x}$ ($0 < x < 3$) films could be tuned using the relative thickness

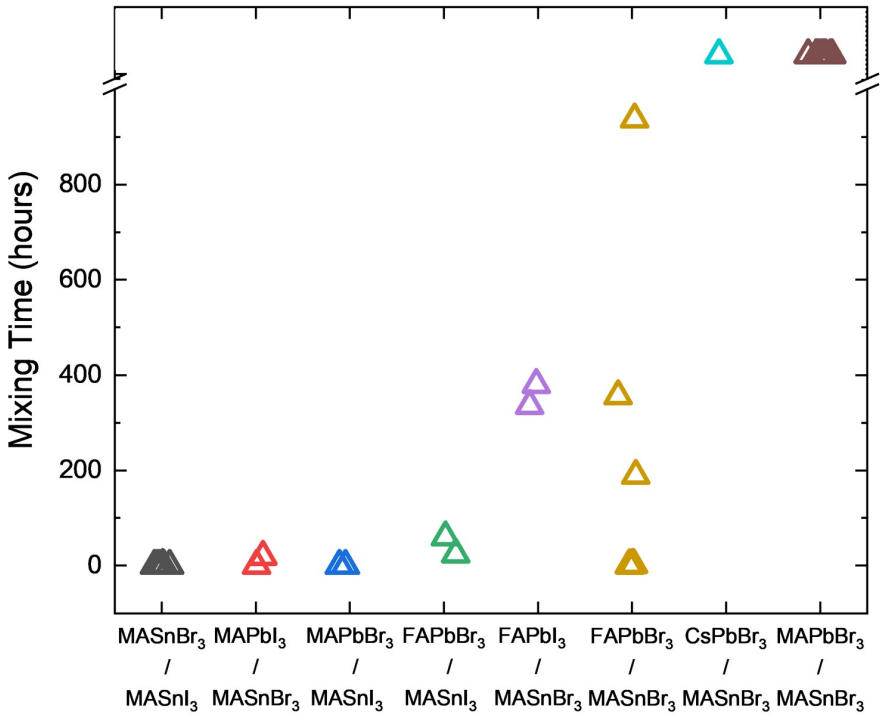

Figure 6.9. Approximate mixing times for samples used to determine the ranges in mixing times depicted in Figure 6.8a. Mixing times are assigned based on the time elapsed between fabrication and when absorbance spectra or XRD pattern show a single onset feature or set of diffraction peaks. The data points here are the average of the last timepoint before the sample is fully mixed and the first time point after the sample is fully mixed, as described in detail in Figure 6.7. Each datapoint corresponds to a single layered structure, and multiple datapoints denote different samples. Note that the deposition conditions and resulting morphology of the layers was kept as consistent as possible between samples with the exception of the $FAPbBr_3$/$MASnBr_3$ and $MAPbBr_3$/$MASnBr_3$ heterojunctions, where the bottom Pb film morphology was intentionally varied as discussed in Section 6.5.

of each layer. Figure 6.11 shows X-ray diffraction (XRD), optical absorption, and photoluminescence (PL) from films with x = 0, 1.5, 2 and 3. These data are consistent with previous reports on $MASnBr_xI_{3-x}$ synthesized using other techniques [140, 214, 299]. XRD peaks shift monotonically to larger 2θ values with increasing Br content, from 16.5° (x = 0) to 17.5° (x = 3), implying a smooth phase-transition from tetragonal $MASnI_3$ to pseudocubic $MASnBr_3$ as

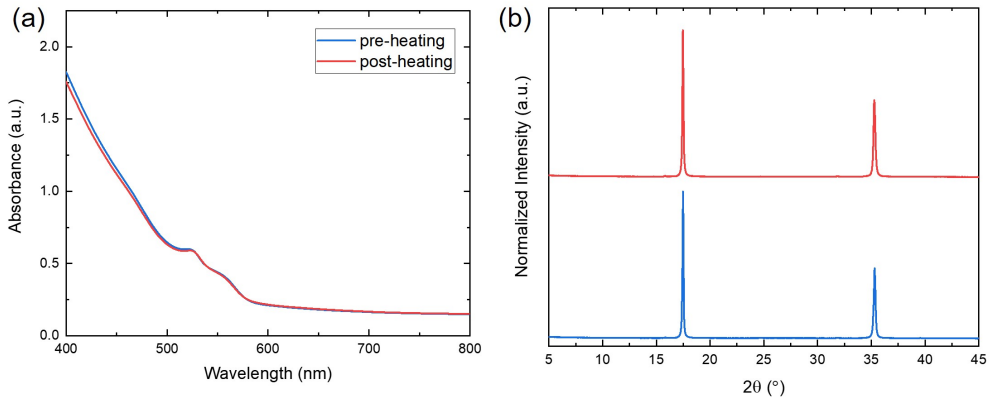

Figure 6.10. Absorbance spectra (a) and XRD patterns (b) of a $MAPbBr_3$/$MASnBr_3$ heterojunction before and after heating at 60 °C for 7 hours in an N_2 atmosphere. No appreciable change in XRD pattern or absorption features is observed after heating, indicating a lack of substantial B-site cation diffusion across the interface. XRD was collected using a PANalytical X'pert PRO diffractometer with Co Kα radiation (λ=1.7889 Å).

described elsewhere [299]. Strong texturing along (001) is evident for x = 0, 1.5, and 2. While texturing can be substantially tuned independent of stoichiometry using CGAVD (see Section 5.3), strong texturing is observed more readily for $MASnI_3$ films than $MASnBr_3$ films.

The measured optical absorption spectra (Figure 6.11b) show onsets decreasing from a wavelength of 880 nm for x = 0 to 575 nm for x = 3. Photoluminescence is observed at a wavelength of 730 nm for x = 1.5 and 960 nm for x = 0, with no significant PL from films with $x \geq 2$. This is consistent with previous reports, where the PL efficiency was negligible ($< 0.1\%$) and no electroluminescence was observed from $MASnBr_xI_{3-x}$ films with $x > 1.5$ [299]. Interestingly, the sequentially deposited $MASnBr_3$ and $MASnI_3$ films mix spontaneously even at substrate temperatures as low as 15 °C. To our knowledge, this is the first synthesis of $MASnBr_xI_{3-x}$ by sequential deposition of single-halide perovskite films. This rapid and spontaneous mixing implies high I^- and Br^- diffusion rates within the perovskite crystal structure. Based on this observation, $MASnBr_xI_{3-x}$ appears to be energetically favourable and stable at room temperature.

Notably, despite having different halogens, the $FAPbI_3$/$MASnBr_3$ heterostructure (Figure F.6) is substantially more stable than the others. This could be due to differences in grain size and defects [52, 300], the impact of the A-site on halogen diffusion [52, 301], and/or the

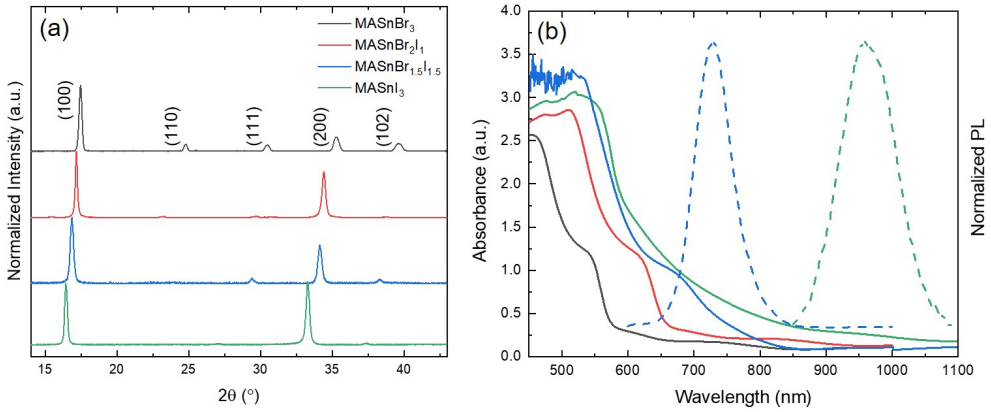

Figure 6.11. (a) X-ray diffraction patterns of $MASnBr_3$, $MASnI_3$, and $MASnBr_xI_{3-x}$ films deposited on quartz using CGAVD. $MASnI_3$ and $MASnBr_xI_{3-x}$ films are highly oriented along [001], with small (111) and (102) peaks visible for $MASnBr_2I_1$. (b) Corresponding absorbance (solid lines) and photoluminescence (dashed lines) spectra. No significant photoluminescence is observed for x $>$ 1.5, which is consistent with previous reports. Film thicknesses are 450 nm, 310 nm, 130 nm, and 410 nm for x = 3, 2, 1.5, and 0, respectively. See Figure F.10 for deposition parameters for these films. X-ray diffraction was collected using a Bruker D8 2D diffractometer with Co Kα radiation (λ=1.7889 Å).

substantially different lattice parameters of these two MHPs [72, 74]. Additional studies are needed to determine the impact of these parameters on the larger mixing time observed for $FAPbI_3$/$MASnBr_3$.

Among the pairings containing a single halogen type, only $FAPbBr_3$/$MASnBr_3$ exhibits mixing. Figures 6.8d – 6.8e show absorption and XRD data for the $FAPbBr_3$/$MASnBr_3$ that exhibited the longest mixing time. Similar to previous data presented in Figure 6.7, the initial (t=1 hr) absorbance spectra and XRD patterns have distinct onsets and peaks, respectively, that correspond to the individual $FAPbBr_3$ ($\sim$180 nm thick) and $MASnBr_3$ ($\sim$190 nm thick) layers. Over time, these distinct onsets and peaks merge, and at t=937 hr the absorbance has one clear onset and the XRD pattern has a single peak, indicating mixing. Furthermore, the location of the XRD peak (2θ=17.34°) after 937 hours is approximately halfway between the (100) peaks of the two constituent films (2θ=17.25° for $FAPbBr_3$ and 2θ=17.45° for $MASnBr_3$) as expected for a 50% FA and 50% MA composition predicted based on the individual film thicknesses before mixing.

It is interesting to note the difference in stability between $FAPbBr_3$/$MASnBr_3$ and $CsPbBr_3$/$MASnBr_3$ heterojunctions, as both have variations in the A- and B- sites. This difference in mixing behavior could reflect a variety of factors, including differences in lattice parameter, defect density, and/or the impact of the A-site on defect migration. While mechanisms of ion migration in $CsPbBr_3$ are not fully understood [302], first-principle calculations suggest that the energy barriers for A-site defect migration are larger for $FAPbBr_3$ than $CsPbBr_3$ [303]. This result would imply, everything else (*e.g.* defect densities) being equal, that a $FAPbBr_3$/$MASnBr_3$ heterostructure should mix more slowly than $CsPbBr_3$/$MASnBr_3$. Since this is not what we observe, it suggests that either the energy barriers for A-site defect migration are different in our $FAPbBr_3$ and $CsPbBr_3$ films than calculated in ref [303], and/or that there are other factors dominating the difference in mixing rate. Furhtermore, Figure 6.8a clearly demonstrates that the $FAPbBr_3$/$MASnBr_3$ heterojunctions explored in this work exhibit the largest range in mixing time, spanning both the 0 - 100 hr and 100 - 1000 hr domains. Since no other heterojunctions tested had this large of a range in mixing time, we set out to understand this further by exploring mixing rate vs. grain size (in Section 6.5).

6.5 Heterojunction Mixing vs. Grain Size

The diffusion of ionic species across perovskite-perovskite interfaces likely depends on several factors, including bulk and interfacial defect type and density, as well as the morphology (*e.g.*, grain size, orientation, roughness) and crystal structure of each layer. While ion transport may occur both in the bulk and along the grain boundaries [300, 304], grain boundary diffusion likely dominates in polycrystalline films [304–306]. To understand how much film morphology and grain size could impact diffusion, mixing times in $MAPbBr_3$/$MASnBr_3$ and $FAPbBr_3$/$MASnBr_3$ heterostructures were studied as a function of $APbBr_3$ (bottom film) morphology. To capture extremes, two types of $MAPbBr_3$ and $FAPbBr_3$ films were fabricated, one with very small ($<0.005\ \mu m^2$) tightly packed grains and another with very large ($>3\ \mu m^2$) island domains. In an attempt to only change one variable (in this case the bottom Pb film morphology), the top $MASnBr_3$ layer was deposited on $MAPbBr_3$ and $FAPbBr_3$ films in a single growth to minimize morphological variations in the top layer. SEM images of these bottom Pb films can be seen in Figure 6.12.

Despite these very different morphologies, no mixing was observed for any $MAPbBr_3$/

$MASnBr_3$ heterojunctions, as demonstrated by the unchanging absorbance spectra in Figure 6.13. This data further suggests minimal diffusion of the B-site across the $MAPbBr_3$/$MASnBr_3$ interface regardless of grain boundary density, making this heterojunction a promising candidate for incorporation into optoelectronic devices.

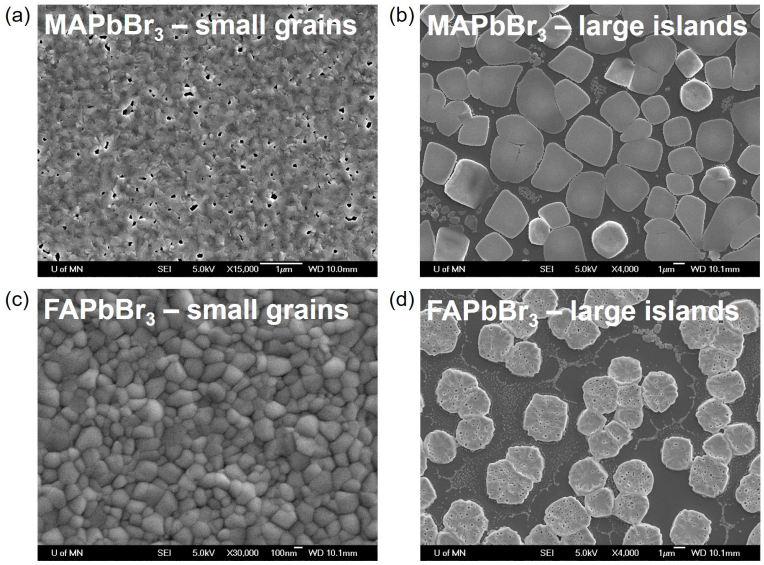

Figure 6.12. SEM images for small-grained (a) and large-island (b) $MAPbBr_3$ and small-grained (c) and large-island (d) $FAPbBr_3$. Small-grained and large-island films were fabricated with a 200 μL chlorobenzene application at 10s and 40s into the spin-coating process, respectively. Scalebars are 1 μm (a), (b) and (d) and 100 nm (c).

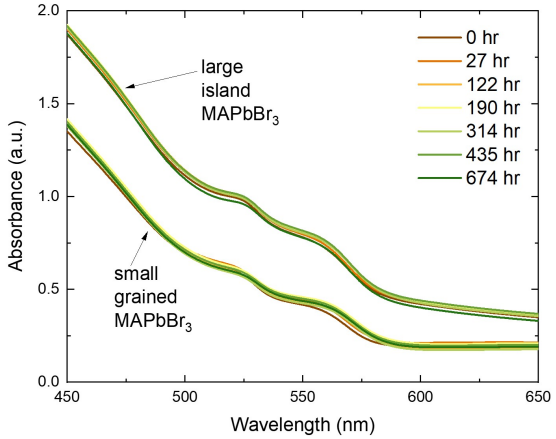

Figure 6.13. Absorbance spectra of $MAPbBr_3$/$MASnBr_3$ heterojunction as a function of $MAPbBr_3$ grain size and time. No mixing was observed for either morphology for >600 hours.

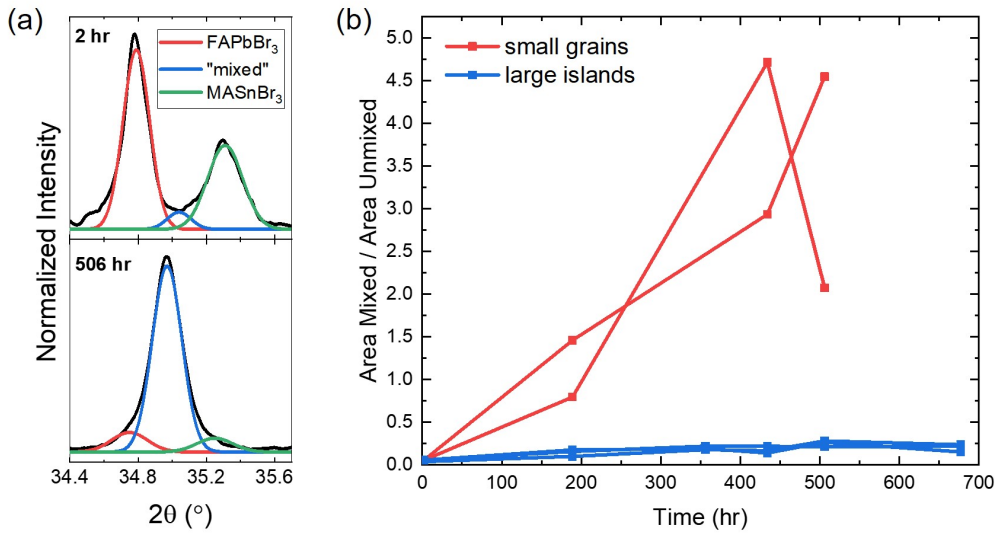

Figure 6.14. Mixing behavior of $FAPbBr_3$/$MASnBr_3$ heterojunctions as a function of $FAPbBr_3$ grain size. (a) Example of XRD peak fitting for a small grained $FAPbBr_3$/$MASnBr_3$ heterojunction at t = 2 hr and t = 506 hr. XRD data was fit using three Gaussian peaks centered at 2θ=34.8°, 35.0°, and 35.3°. (b) Ratio of "mixed" to "unmixed" XRD peak area as a function of time. The vertical-axis corresponds to the ratio of XRD peak areas corresponding to "mixed" and "unmixed" components of the film, where 0 would indicate a completely unmixed heterojunction. Heterojunctions with small-grained $FAPbBr_3$ films mix at a substantially faster rate than large-grained films. X-ray diffraction was collected using a PANalytical X'pert PRO diffractometer with Co Kα radiation (λ=1.7889 Å).

In contrast, for $FAPbBr_3$/$MASnBr_3$ heterostructures, the rate of mixing can be actively varied by controlling the morphology of $FAPbBr_3$. Figure 6.14 shows the mixing behavior of $FAPbBr_3$/$MASnBr_3$ heterojunctions for "small grained" and "large island" $FAPbBr_3$ films over a period of 500 hours. To quantify the difference in mixing rate, XRD peaks between 2θ=34.4° and 35.7° were fit using three Gaussian peaks corresponding to $FAPbBr_3$ (2θ=34.8°), $MASnBr_3$ (2θ=35.3°), and an alloy (2θ=35.0°). Figure 6.14a shows an example of this fitting for a "small grained" film, where the XRD pattern prior to mixing (t = 2 hr) can be fit primarily with peaks corresponding to $FAPbBr_3$ and $MASnBr_3$ and, after mixing (t = 506 hr), with a single peak corresponding to the alloy. The fit was constrained to include three peaks centered at the locations above to avoid missing small contributions from different components. For all morphologies,

the X-ray beam size ($>$1 mm^2) is several orders of magnitude larger than the domain sizes in $APbBr_3$ films. Fitting XRD patterns over time, we observe a substantial difference in rate of mixing (Figure 6.14b). In Figure 6.14b, the vertical axis is the area of the mixed (i.e., alloy) peak (at 2θ=35°) divided by the sum of the areas of the unmixed peaks (at 2θ=34.8° and 35.3°). The heterojunctions with large island $FAPbBr_3$ films show minimal mixing over 500 hours, while small grained films are nearly completely mixed (Figure F.9). This result supports the hypothesis that grain boundaries assist ion migration across the interface and demonstrates the dramatic impact of morphology on the stability of all-perovskite heterojunctions.

6.6 Ion difussion in $FAPbBr_3$/$MASnBr_3$ heterojunctions

Another interesting feature of the $FAPbBr_3$/$MASnBr_3$ heterostructure is that both the A-site (FA^+, MA^+) and the B-site (Sn^{2+}, Pb^{2+}) could potentially be mixing. To investigate which species are diffusing across the interface, an XPS depth profile was performed on "mixed" (measured $>$1500 hrs after deposition) and "unmixed" (measured $<$100 hrs after deposition) films. A detailed treatment of the measurement and results is presented in Chapter 7; a brief summary of the data is included here for completeness. All XPS measurements were performed by Dr. Jenny Mann of Physical Electronics.

As seen in Figures 6.15a and 6.15b, the sharpness of the transition between Sn 3d5/2 and Pb 4f photoelectron intensity profiles appears unchanged for the two cases. This unchanging Pb/Sn interface sharpness supports the hypothesis that minimal diffusion of the B-site cations (Sn^{2+}, Pb^{2+}) is occuring, as was also observed for $MAPbBr_3$/$MASnBr_3$ heterojunctions (Figure 7.10). In contrast, the N 1s and C 1s depth profiles vary significantly between the mixed and the unmixed samples. The N 1s chemical states for the unmixed case (Figure 6.15c) show an MA^+ contribution only in the top layer of the heterojunction, whereas the mixed case (Figure 6.15d) has both MA^+ and FA^+ contributions throughout. The presence of the FA^+ species at the surface of the "mixed" $FAPbBr_3$/$MASnBr_3$ heterojunction confirms the diffusion of the A-site species from the bottom layer through the entirety of the top layer, thus suggesting that A-site diffusion is responsible for the mixing inferred from absorption and XRD measurements on this heterostructure.

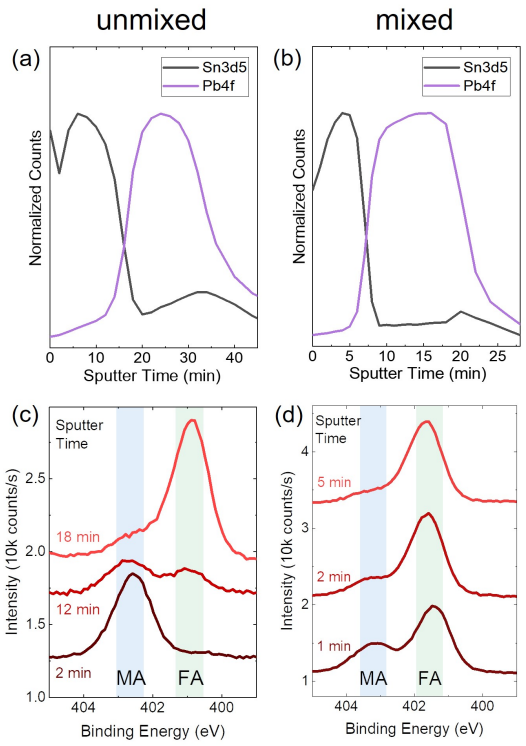

Figure 6.15. XPS depth profiles for unmixed (a), (c) and mixed (b), (d) $FAPbBr_3/MASnBr_3$ heterojunctions, showing Sn 3d5/2 and Pb 4f photoelectron intensities in (a) and (b) and the N 1s chemical states in (c) and (d). Different sputtering time scales for the two cases reflect differences in film thicknesses: $MASnBr_3$ layers are $\sim$110 nm thick for the mixed case and $\sim$190 nm thick for the unmixed case, $FAPbBr_3$ is fixed at $\sim$180 nm. Whereas the sharpness of the interface between Sn and Pb appear similar for the two cases, the distribution of MA^+ and FA^+ as evidenced by the N 1s signals in (c) and (d) differ significantly, suggesting that A-site diffusion is responsible for the mixing observed in this heterostructure. XPS measurements performed by Dr. Jenny Mann of Physical Electronics.

6.7 Conclusion

This chapter highlights our successful formation and characterization of all-perovskite heterojunctions based on thin layers of 3-dimensional ABX_3 perovskites. Using a combination of solution and vapor processing, we synthesize seven $APbX_3/MASnX_3$ (A=Cs, MA, FA; X=Br, I) layered structures and identify two with stability >1500 hours: $MAPbBr_3/MASnBr_3$ and $CsPbBr_3/MASnBr_3$. Consistent with the literature, we find rapid mixing in structures when the halogen is different on either side of the heterojunction interface. Control of mixing rate is achieved through reducing grain boundary density of the bottom layer, providing insight into methods for controlling ion diffusion in MHP heterostructures. We further probe the mixing behavior of $FAPbBr_3/MASnBr_3$ heterojunctions in detail and find that while A-site species diffusion is substantial over hundreds of hours, B-site diffusion is negligible. By enabling the controllable formation of a variety of 3D all-perovskite heterojunctions for the first time, this work provides a pathway to advance the understanding of ion transport in MHPs and explore the potential of all-perovskite heterostructures for advanced electronic applications. Furthermore,

we identify two ideal candidates ($MAPbBr_3$/$MASnBr_3$ and $CsPbBr_3$/$MASnBr_3$) for incorporation into optoelectronic devices.

Chapter 7

Probing MHP Compositions using Depth-profiled XPS

7.1 Background

X-ray photoelectron spectroscopy (XPS), is a powerful surface-sensitive spectroscopic technique that can be used to quantify chemical species (*e.g.* Sn or Pb) and chemical states (*e.g.* double vs. single carbon bonds). A schematic for an XPS measurement can be seen in Figure 7.1, where a sample is irradiated with photons (typically Mg Kα or Al Kα X-rays) and emits photoelectrons. Quantification is achieved by measuring the number and kinetic energy E_K of the elastically scattered photoelectrons, given by

$$E_K = h\nu - E_B \tag{7.1}$$

where $h\nu$ is the photon energy and E_B is the ionization (binding) energy of the photoelectron [307]. The value of E_B depends on the element, which electron has been ejected from the atom (*e.g.* 4s or 4p), and the bonding environment of the atom. Coupled with the intensity of the photoelectron signal, E_B can be used to determine elemental species, chemical state, and for materials with more than one species, stoichiometry. Figure 7.1 shows example XPS spectra for several metals, where labels correspond to specific core electronic transitions. Due to the small inelastic mean free path of ejected photoelectrons, analysis depths are typically $<$10 nm [307], although this depth can be altered by changing the photon energy [308].

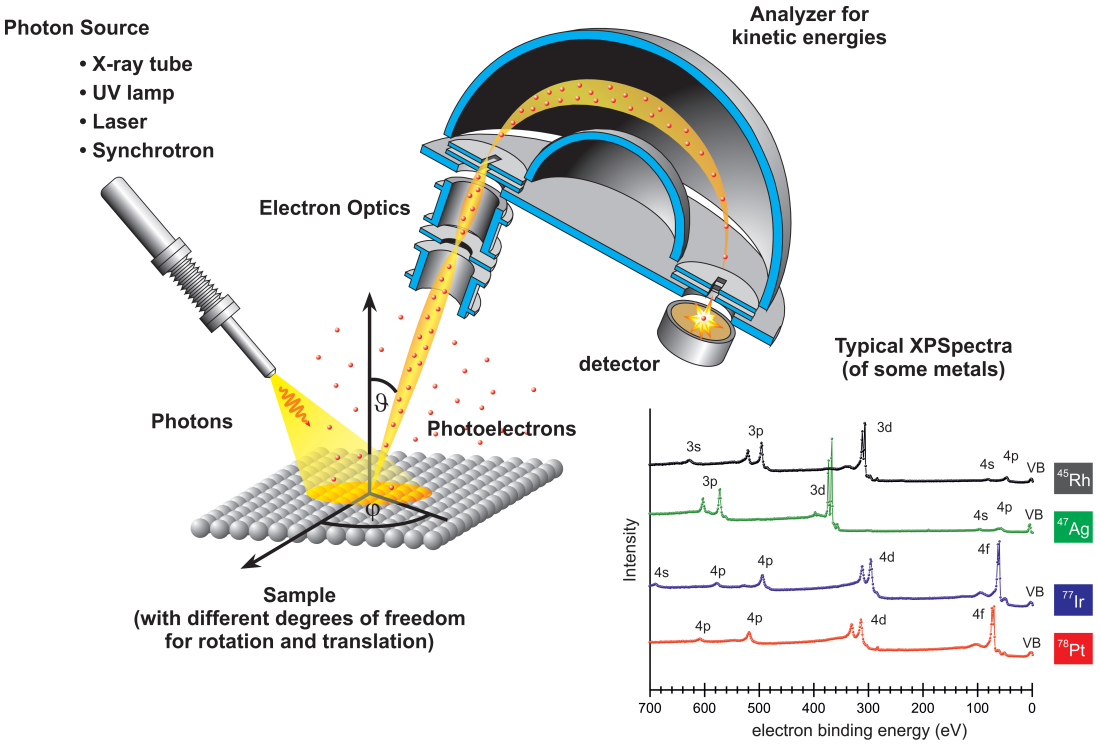

Figure 7.1. Schematic for XPS measurement, where high energy photons strike a sample which emits photoelectrons. Example XPS spectra with labeled transitions for several metals. Reproduced with permission from Frank Müller, Epitaktisches Wachstum von Graphen und Boronitren auf Übergangsmetallen, Habilitation Thesis, Saarland University (2014) [309].

In the field of MHPs, XPS has been used extensively to probe composition and binding states at the surface of films or full device structures. Several studies have shown the migration of halide ions through Ag electrodes by tracking the Ag 3d signal and differentiating between binding energies for elemental Ag and AgI [158, 310–312]. Kato *et al.*, for example, used XPS to show that iodine migrates to the surface of an Ag electrode for glass/FTO/TiO_2/$MAPbI_3$/spiro-MeOTAD/Ag solar cells when stored in air with 50% RH [310]. XPS has also been used to monitor the reaction between PbI_2 and MAI to form $MAPbI_3$ [313], to observe changes in MHP chemistry with different aging conditions [314], to compare surface composition for samples fabricated using different procedures [308], and to measure the change in valence band energy as a function of Br in $MAPb(I_{1-x}Br_x)_3(Cl)_y$ [315]. For a detailed discussion of the application of surface photoelectron measurements in MHPs see ref [307].

To quantify species, composition, and chemical states as a function of depth into a sample, XPS is often combined with ion milling to sequentially remove and measure layers of material. Typical sputtering sources range from monatomic ions like Ar^+ or Cs^+ to gas cluster ion beams (GCIBs) like ${Ar_{2500}}^+$ or ${C_{60}}^+$. Whereas monotomic sources are commonly used for inorganic samples [316], it has been widely shown that large clusters, with lower energy per atom (E/n), tend to perform better at removing organic materials with minimal damage and contamination [317–321].

For samples that contain both organic and inorganic components, achieving uniform sputtering of all components can be quite challenging, as these species tend to have substantially different sputtering rates for the same source [322]. These differential sputtering rates, along with damage accumulation and beam-induced species migration within films, can result in significant measurement artifacts. For example, Noël *et al.* find that the sharpness of the interface between metallic (Au or Cr) and organic (Tyrosine) layers depends substantially on the order of the layers. When tyrosine is the top layer, and therefore sputtered first, the interface appears relatively sharp, and little organic signal persists into the metal layer. When the metal layer is on top, however, the Cs^+ ion beam induces substantial migration of the metal into the organic, which persists throughout the entire depth of the organic layer [323]. Differential etching rates have even been observed for all-inorganic materials such as tantalum pentoxide, where preferential sputtering of oxygen is larger for monotomic ions compared to an argon cluster source, and thus the ratio of Ta to O appears different depending on the sputtering source [324]. As such, great care must be taken in order to separate such measurement artifacts from real sample properties.

Due to the multi-component nature of MHP materials (often with several A-site and X-site species), as well the intrinsic hybrid (organic-inorganic) nature of common MHPs, it is no surprise that depth-profiling techniques reliant on ion sputtering would encounter similar challenges. Indeed, Harvey *et al.* have recently shown that gradients in A-site organic cations observed in depth-profiled ToF-SIMS are measurement artifacts due to beam damage from the primary ion beam, and not real compositional gradients through the MHP film [321]. In addition to this organic A-site gradient artifact, many reports show the existence of substantial elemental Pb (Pb^0) in addition to Pb^{2+} in $APbX_3$ films [297, 325–327]; it is unclear whether Pb^0 exists in the film prior to sputtering or if it is a measurement artifact. Another challenge is the non-stoichiometric halogen/metal ratio that is documented for nearly all MHP depth-profiled

XPS measurements. Whereas this ratio would be 3 for a phase-pure MHP like $MAPbI_3$, the reported experimental value is consistently lower [262, 297, 326–329]. While often attributed to the existence of excess precursor domains, the ubiquity of this smaller-than-stoichiometric halogen/metal ratio may suggest some contribution from the measurement technique.

Despite these challenges, only a few reports have provided an in-depth investigation of ion sputtering in MHPs. The first is a detailed study on the effects of different sputtering conditions on a state-of-the-art triple cation $(FA_xCs_{1-x}PbI_3)_{0.85}(MAPbBr_3)_{0.15}$ MHP [297]. Here, Noël *et al.* employ five different ion sources including monatomic beams (Ar^+ and Cs^+) and Ar_n^+ clusters (n=500, 1000, 4000) as well as a wide energy-per-atom range (2.5 eV to 1 keV). Compared to Ar^+, they find that 500 eV Cs^+ results in nearly material-independent sputtering rates, sharp interfaces, and stable ToF-SIMS molecular profiles. Large, low energy GCIB sources ($n > 500$, $E < 10$ keV) preferentially sputter the organic A-site cation and show ineffective removal of metallic species like Pb. By optimizing the GCIB parameters to higher-energy, medium-size clusters ($300 < n < 500$, $E/n > 20$ eV), they are able to minimize the damage accumulation and achieve more consistent etching rates. Similarly, Harvey *et al.* explore sputtering conditions for ToF-SIMS to minimize damage accumulation from the high-energy bismuth primary ion beam (30 keV) [321]. Damage reduction is achieved by increasing the sputtering time between analysis cycles and by switching to a high-energy ($\sim$40 eV/atom) GCIB source. These investigations highlight the importance of optimizing sputtering conditions to minimize artifacts and sample damage for MHP materials, yet leave many unanswered questions like the origins of Pb^0 signals and non-stoichiometric halogen/metal ratios.

The continued development of depth-profiled techniques to investigate MHP materials is highly valuable as it can help answer increasingly important questions relating to the distribution and segregation of ionic species in MHPs, the nature of interfaces, the environmental stability of MHP materials, and how stoichiometry and processing conditions impact these properties. In the following sections, we combine depth-profiling measurements and other characterization techniques to investigate the impact of measurement conditions on a variety of MHP materials and the causes of non-stoichiometric observations in XPS measurements. We then apply these techniques to probe novel MHP-MHP heterojunctions described in Chapter 6.

7.2 Experimental Methods

All XPS measurements were performed by Dr. Jennifer Mann at Physical Electronics, inc. using a Physical Electronics VersaProbe III Scanning XPS Microprobe with monochromatic Al Kα (1486.6 eV) X-rays. Sputter sources, energies, currents, raster size, sample rotation, and pass energies varied by sample; details for all experiments can be seen in Table G.1. The binding energy scale of all spectra was charge corrected by taking the location of the adventitious carbon C 1s peak observed in the first cycle (before any sputtering has occurred) and shifting it to 284.8 eV. Samples were mounted on a sample carrier with non-conductive double-sided adhesive tape. Dual beam charge neutralization, consisting of a beam of low energy ($\sim$1 eV) electrons and low energy ($\sim$8 eV) Ar^+ ions was used during all data acquisitions. All data were processed using Physical Electronics' MultiPak data reduction software (version 9.9.1.1). For additional experimental details and descriptions, see Appendix G.

7.3 Probing differential etching rates in organic MHPs

As mentioned in Section 7.1, minimal studies have systematically investigated how sputtering conditions impact XPS profiles for MHP materials. Furthermore, no studies have applied this technique to Sn-based MHPs, which tend to be more environmentally unstable than their lead-based counterparts. To investigate the impact of sputter source on tin MHPs, we performed XPS depth profiles using four different sputtering sources as seen in Figure 7.2: C_{60}^+ (20 kV/20 nA), Ar_{620}^+ (20 kV/10 nA), Ar_{2500}^+ (20 kV/40 nA), and Ar^+ (500 eV/500 nA). Additional experimental details can be found in Appendix G.

As seen in Figure 7.2, the choice of sputtering source has a substantial impact on several aspects of the XPS sputter depth profiles. By tracking signals corresponding to the perovskite (C 1s, N 1s, Br 3d, Sn 3d5) and the substrate (Si 2p, O 1s), we can observe that the time required to sputter through the MHP material changes significantly between the four sputtering conditions. Whereas 20 kV/40 nA Ar_{2500}^+ (Figure 7.2c) rapidly removes the MHP material (on the order of $\sim$100 nm in 5 minutes), this same film thickness takes over twice as long to be removed when using 500 eV/500 nA monatomic Ar^+ (Figure 7.2d). The rate of MHP removal with 20 kV/20 nA C_{60}^+ (Figure 7.2a) and 20 kV/10 nA Ar_{620}^+ (Figure 7.2b) fall between these extremes.

We can also use the profiles in Figure 7.2 to evaluate differential sputtering by assessing

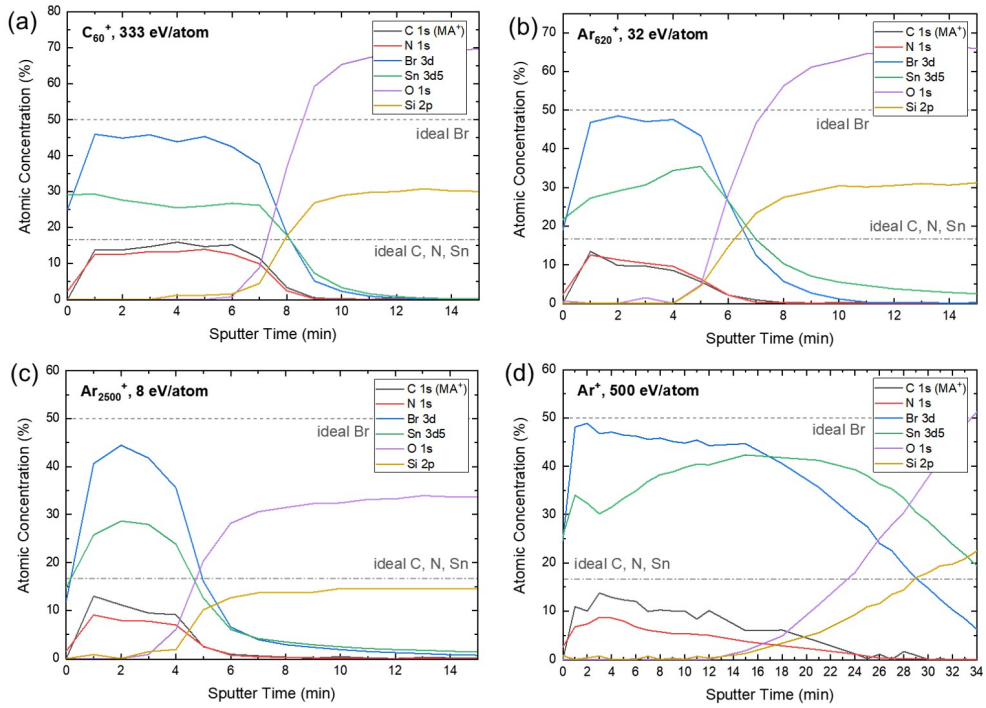

Figure 7.2. XPS depth profiles for ∼100 nm thick $MASnBr_3$ films as a function of sputter source: (a) 20 kV C_{60}^+ (333 eV/atom), (b) 20 kV Ar_{620}^+ (32 eV/atom), (c) 20 kV Ar_{2500}^+ (8 eV/atom) and (d) 500 eV Ar^+ (500 eV/atom). Adventitious carbon signal is not included in C 1s trace. All $MASnBr_3$ films were prepared identically in a single CGAVD growth.

relative concentrations of elements and how consistent those concentrations are over time. As observed in the literature, the ratio of halogen/metal in our case is lower than the stoichiometric condition (Br/Sn=3) for all sputter sources: whereas the Br 3d signal is lower than the stoichiometric condition (50 at%), the Sn concentration is higher than stoichiometric (16.7 at%) as seen in Figure 7.2.

Both of these metrics, sputter rate and Br/Sn ratio, can be explored in more detail by calculating quantitative metrics. To determine sputter rates for different sputtering source conditions, we first define the portions of the sputter profile corresponding to the film and the substrate. While the exact location of the interface between the substrate and film is hard to pinpoint due to differential sputtering discussed in Section 7.1 as well as film roughness, we can define the crossover time, $t_{crossover}$, as the time at which the substrate contribution to the total signal is

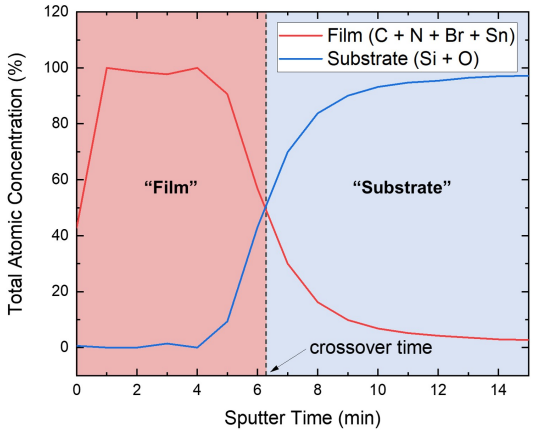

Figure 7.3. Depiction of "crossover time" calculation for the data presented in Figure 7.2b (Ar^+_{620}), where the signals from elements in the film (C, N, Br, Sn) and elements in the substrate (Si, O) are summed to calculate their respective total atomic concentrations (red and blue traces). The "crossover time" is the time at which these traces cross (in this case, ∼6.4 minutes); the XPS spectra prior to this point are denoted as the "film" and after this point as the "substrate."

larger than the contribution from the MHP film (in at%). This is equivalent to the time at which the total concentration of signals from elements in the film (C, N, Br, Sn) drop below 50% and the total concentration of signals from the substrate (Si, O) increase above 50%:

$$\mathrm{t}_{crossover}\ (\mathrm{min}) = \text{time at which Si + O} > 50\ \text{at\%} \tag{7.2}$$

This determination of crossover time and the resulting definition of which XPS sputter times corrsespond to the "film" and the "substrate" are presented in Figure 7.3 using the Ar^+_{620} data from Figure 7.2b. Here, the red and blue traces correspond to the total atomic concentration of the MHP film and substrate, respectively. The "crossover time" is the time at which these traces cross (in this case, ∼6.4 minutes). Based on this crossover time, the XPS spectra prior to this time point are denoted as the "film" and after this point as the "substrate."

An approximate sputtering rate ($\mathrm{r}_{sputter}$) for the MHP, based on this determination of the interface between the film and the substrate and the film thickness (FT), is then given by:

$$\mathrm{r}_{sputter}\ (\mathrm{nm/min}) \sim \frac{\mathrm{FT\ (nm)}}{\mathrm{t}_{crossover}\ (\mathrm{min})} \tag{7.3}$$

Performing this calculation for each profile in Figure 7.2 results in the sputter rates shown in Figure 7.4a. It can be see that the three cluster sources tested (C^+_{60}, Ar^+_{620}, Ar^+_{2500}) remove MHP material at a similar rate (12-17 nm/min), but the monatomic Ar^+ is substantially slower (∼4 nm/min). While these sputter rates can provide guidance on the conditions needed for XPS

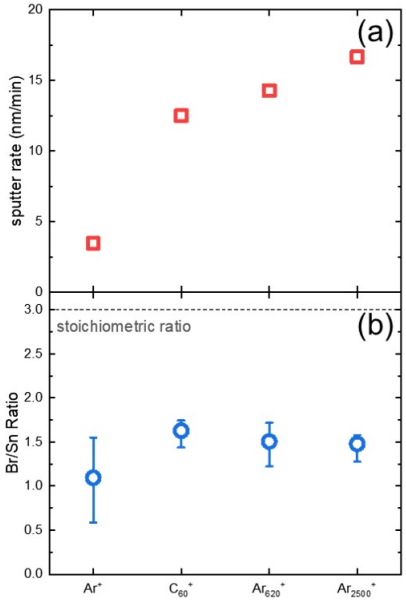

Figure 7.4. Approximate sputtering rate (a) and Br/Sn ratio (b) for the $MASnBr_3$ XPS sputter profiles depicted in Figure 7.2 as a function of sputter source at the given conditions. Sputter rate is calculation according to Equation 7.3 and Br/Sn ratio is the average ratio of Br 3d/Sn 3d5 throughout the film (not including the first sputter cycle); error bars are min and max values in this range.

depth profiling, *e.g.* which sputter conditions give the best depth resolution, it should be noted that there are other means to control sputtering rate including the ion beam raster area, energy, and current. Noel *et al.*, for instance, achieve more than a doubling of sputtering rate when increasing from 500 eV to 1 keV Cs^+ sputtering source [297].

Similarly, the Br/Sn ratio can be calculated by taking the average of Br 3d (at%)/Sn 3d5(at%) signals for the sputter times that correspond to the MHP film, as shown in Figure 7.4b. In this case, error bars correspond to min and max values during this time, and the initial time point (where signals are attenuated due to surface contamination) is excluded for clarity. All sources result in a Br/Sn ratio ranging between 1 and 1.7, which are far below the ideal value of 3 that would be expected for a perfectly stoichiometric film in the absence of differential sputtering. As discussed in Section 7.1, this lower-than-expected halogen/metal ratio is ubiquitous to XPS sputter profile measurements on MHPs, and is often ascribed to excess precursor phases and/or metallic clusters within the film [262, 297, 326–329]. It should be noted that the $MASnBr_3$ films used for these profiles had no observed excess crystalline precursor phases as measured by XRD (Figure G.2). Despite the low absolute Br/Sn values for all sputter sources, Figure 7.4b shows that C_{60}^+ and Ar_{620}^+ have the most stable halogen/metal ratios (*i.e.* smallest error bars),

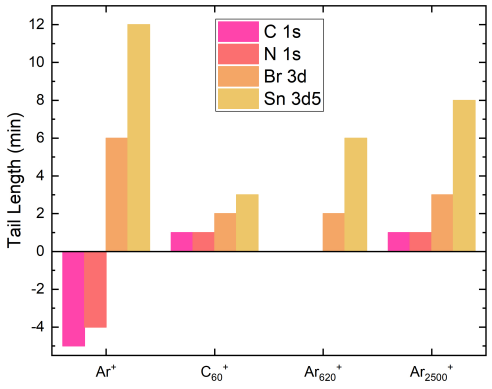

Figure 7.5. Persistence of C, N, Br, and Sn signals after the substrate has been reached for the $MASnBr_3$ XPS sputter profiles depicted in Figure 7.2. Tail length is calculated as the time at which each signal is less than 10% of its max counts minus $t_{crossover}$; a tail length of 0 means that signal drops below of 10% of its max signal at the same time that the substrate accounts for $>$50 % of the total at%. Whereas each species is removed at a similar time with C_{60}^+, Sn species persists for a long time after MA is removed for Ar_{2500}^+.

and Ar^+ appears to have the least stable as well as lowest value. This data indicates that C_{60}^+ and Ar_{620}^+ may minimize differential sputtering of halogen and metal components and thus could be the best choices for MHP materials.

To further understand the differences in differential sputtering between C_{60}^+, Ar_{620}^+, Ar_{2500}^+ and monatomic Ar^+, we can look at how long different elements in the MHP material persist in the XPS sputter profiles. For signals corresponding to each element in the MHP (C 1s, N 1s, Br 3d, Sn 3d5), we define "tail length" $L_{tail,i}$ of species 'i' as the time at which the species signal drops below 10% of its maximum (*i.e.* the tail length time $t_{i@10\%ofmax}$), minus $t_{crossover}$:

$$L_{tail,i}(min) = t_{i@10\%ofmax}(min) - t_{crossover}(min) \tag{7.4}$$

Again using the Ar_{620}^+ data in Figure 7.2b as an example, we see that the Br 3d trace has a maximum value of 48.5 at%, and it drops below 10% of this value (4.85 at%) at a sputter time of $\sim$9 minutes. From Figure 7.3, we know $t_{crossover}\sim$6.4 minutes, and thus $L_{tail,i}$ $\sim$2.6 minutes for this example. As such, a positive tail length means the species signal persists after $t_{crossover}$, and a negative tail indicates the signal disappears prior to $t_{crossover}$.

Repeating for each species and sputter source, we construct Figure 7.5. For a condition with no preferential sputtering between the elements that make up the MHP (in this case C, N, Br, Sn), we would expect the tail length for these species to be exactly equal; the larger the difference in tail length between two elements, the larger the degree of differential sputtering exists between these elements. As such, Figure 7.5 clearly demonstrates that the C_{60}^+ sputtering source results in the lowest amount of differential sputtering for $MASnBr_3$ films, followed by

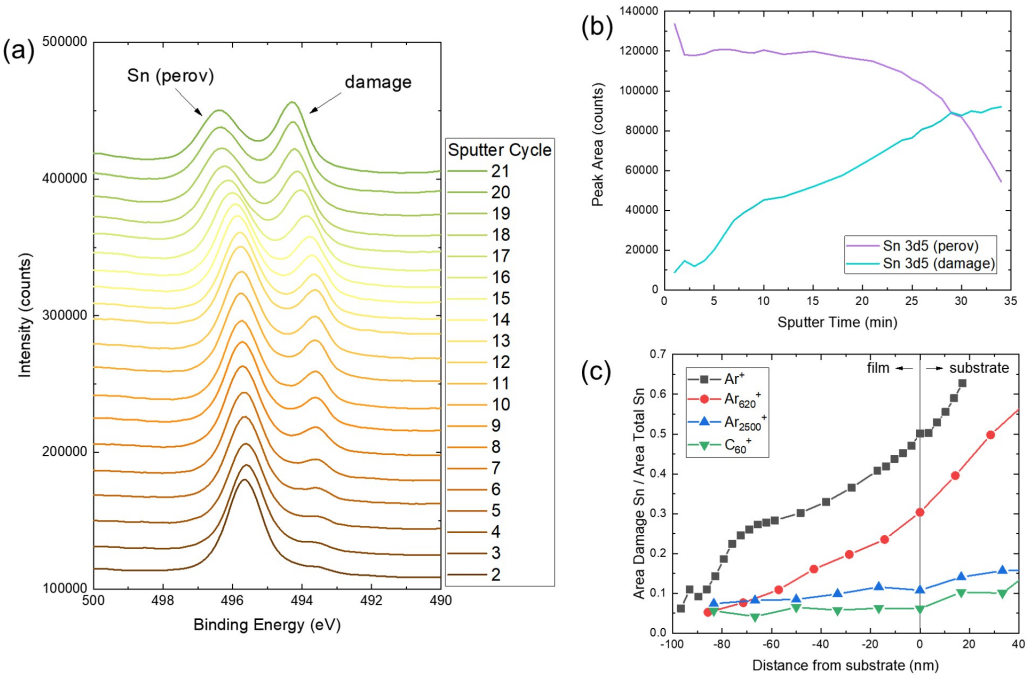

Figure 7.6. Comparison of metallic species damage vs. sputter source in XPS depth profiles. (a) Sn 3d5 peaks corresponding to the data in Figure 7.2d as a function of sputter cycle, where the damage presents as a low binding energy peak that grows in time. (b) Relative areas of Sn signal attributed to perovskite peak (purple) and damage peak (blue), calculated by fitting and integrating the peaks in (a) using MultiPak. (c) Ratio of damage peak area / total Sn peak area for all four depth profiles shown in Figure 7.2.

Ar^{+}_{620}. In contrast, Ar^{+} has substantially different tail lengths: whereas the organics are removed efficiently (dissapearing before $t_{crossover}$), metallic and halogen species persist for a long time after the substrate is reached.[1].

In addition to, and potentially coupled with, the observed preferential sputtering in MHP films is the issue of metallic species damage during ion milling. When MHP films are sputtered, metallic species damage often presents as a secondary, lower binding energy peak. As seen in Figure 7.6a, this lower energy peak (located in this case at ∼493.5 eV for Sn damage in a $MASnBr_3$ MHP) is quite small for initial sputter cycles, and grows in intensity as ion milling

[1]Note that tail lengths for Ar^{+} had to be extrapolated as they never dropped below 10% of their maximum signal within the measurement window, as shown in Figure 7.2

continues. While this damage peak is often ascribed to elemental metal (in this case, Sn^0), additional calibration would be needed to verify this assignment, and as such we will denote it simply as a damage peak going forward.

To quantitatively compare the amount of Sn signal originating from this damage peak, we calculate the area of the Sn peak associated with the perovskite as well as the area of the damage peak using MultiPak software. This results in the curves shown in Figure 7.6b, highlighting the increase in damage as a function of sputter time. To compare different source conditions, we convert sputter time to distance from the substrate (d_{sub}) using the film thickness and crossover time:

$$d_{sub}\text{ (nm)} = r_{sputter}\text{ (nm/min) x sputter time (min) - FT (nm)} \tag{7.5}$$

Taking the ratio of the damage area to the total Sn peak area for all sputter sources and plotting vs. d_{sub} results in the 7.6c. Here, we observe clearly that Ar^+ results in the most metallic species damage, followed by Ar^+_{620}. Both C^+_{60} and Ar^+_{2500} cause relatively little Sn damage in $MASnBr_3$ films.

Taken together, these analyses point to C^+_{60} as an ideal sputtering source for MHP materials, as it results in the good halogen/metal stability, the smallest amount of differential sputtering, and minimal Sn damage.

7.4 Investigation of low halogen/metal ratios

As shown in Section 7.3, our XPS sputter profiles show a halogen/metal ratio that is substantially lower than 3, the value that would be expected as the films appear stoichiometric in X-ray diffraction measurements. In order to determine if this is due to a measurement artifact or if there is indeed excess precursor or metallic regions in the films (as is often cited in the literature), we performed two sets of experiments.

First, we investigated the I/Sn ratio in $MASnI_3$ films as a function of excess precursor measured using XRD. By using the CGAVD system as described in Chapter 4, we fabricated four $MASnI_3$ films with varying precursor ratios. As shown in the XRD patterns in Figure 7.7a, two of these films were stoichiometric, one had measurable excess MAI, and one had measurable excess SnI_2.

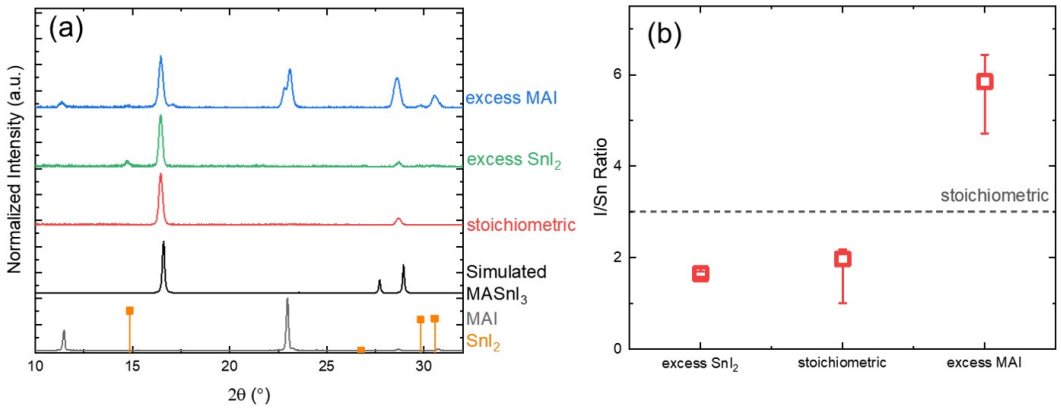

Figure 7.7. Comparison of halogen/metal ratio in $MASnI_3$ films with varying precursor ratios. (a) XRD of four films measured with XPS, including one with excess MAI, one with excess SnI_2, and two with no excess precursor (stoichiometric). X-ray diffraction was collected using a PANalytical X'pert PRO diffractometer with Co Kα radiation (λ=1.7889 Å). (b) Halogen/metal ratios calculated for these four films (stoichiometric datapoint includes two films); error bars indicate minimum and maximum value measured in film during sputtering.

Figure 7.7b shows the measured I/Sn ratios for these films, where error bars indicate minimum and maximum values measured during sputtering (full XPS spectra shown in Figure G.10). Ratios are calculated for only the "film" portion of these spectra as defined by Figure 7.3, except for the excess MAI film, in which the Sn signal dropped off prior to the I signal; for this film the I/Sn ratio was calculated during the first 6 minutes of sputtering. Figure 7.7b demonstrates the ability to observe ratios of halogen/metal that follow an expected trend based on whether there is excess precursor phases measured with XRD. Excess SnI_2 in a film would result in I/Sn ratios <3, whereas we would expect >3 I/Sn ratios for a film with excess MAI. Indeed, these overall trends are shown in Figure 7.7b.

Despite this ability to see expected trends reflected in measured halogen/metal ratios in our XPS depth profiles, this data does not provide proof about the origin of the lower than three value for the case in which there is no excess precursor measured in the film (*i.e.* the stoichiometric case). To explore whether or not the low halogen/metal ratio measured with XPS is reflective of the true ratio in the film or is due to a measurment artifact, we performed XRD, XPS, and Rutherford backscattering (RBS) on identically prepared $MAPbI_3$ films. Details of RBS experiments and fitting can be found in Section G.2.2.

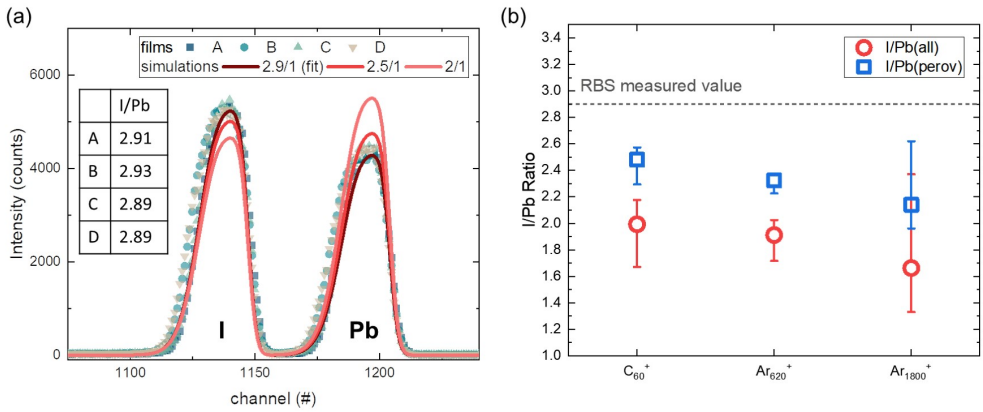

Figure 7.8. Comparison of halogen/metal ratio for $MAPbI_3$ extracted from RBS and XPS measurements. (a) RBS data for four $MAPbI_3$ films that appear stoichiometric in XRD, with fit shown for 2.9/1 ratio and simulations for 2.5/1 and 2/1 ratios. Table inset shows I/Pb ratio calculated for 4 films by peak integration of RBS data. (b) I/Pb ratios measured in XPS using different ion sources, calculated including entire Pb signal (both perovskite and damage Pb peaks), and just perovskite Pb peak. Error bars correspond to max and min ratios.

XRD measurements performed showed no excess precursor peaks (Figure G.3) for four $MAPbI_3$ films. RBS data taken on the same four films is presented in Figure 7.8a, where the four films show nearly idential RBS spectra. I/Pb ratios calculated from peak integration are shown in the inset, with values of I/Pb=2.91$\pm$0.02. Combined with the XRD data, this RBS data confirms that our films have a true I/Pb content close to 3. Subsequent XPS measurements on these films, however, result in halogen/metal ratios substantially lower than 2.9, which is consistant with our previous XPS measurements as well as the literature. Figure 7.8b shows the average I/Pb ratio extracted from XPS measurements for three different sputter sources (C_{60}^+, Ar_{620}^+, and Ar_{1800}^+), which all fall substantially below 2.9. As with our previous measurements on $MASnBr_3$ using different sputtering sources, C_{60}^+ and Ar_{620}^+ perform better than Ar_{1800}^+ in that they have the hightest I/Pb ratio and the smallest error bars. Interestingly, exclusion of the damage Pb peak results in a slightly higher I/Pb ratio (blue squares in Figure 7.8b) compared to that calculated when using the total Pb signal (red circles). While exclusion of the damage peak does not result in a $\sim$3 I/Pb ratio, this result does suggest that part of the low halogen/metal ratio observed in the literature arises from inclusion of the metallic damage signal when calculating atomic percentages in XPS depth profiles. Based on these results, we can conclude

that the lower-than-stoichiometric halogen/metal ratios we observe, and perhaps also those that are commonly observed in the literature, are mainly due to differential sputtering/measurement artifacts arising from ion milling in XPS. This finding motivates further study of the origins of XPS depth profiled artifacts in MHPs as well as the need for careful analysis and interpretation of ion milling techniques when applied to MHP materials.

7.5 XPS depth profiles to probe layered structures

After determining C_{60}^{+} to be the ideal sputtering source to minimize damage and differential sputtering, we apply XPS depth profiling to probe interfaces of multilayer MHP heterojunction films. Two types MHP heterostructures were studied with XPS: $MAPbBr_3$/$MASnBr_3$ (where only the B-site is different between the two layers) and $FAPbBr_3$/$MASnBr_3$ (where both the A- and B-sites vary between the layers). The growth of these heterostructures is described in detail in Chapter 6 and additional details for these XPS experiments can be found in Appendix G.

7.5.1 $MAPbBr_3$/$MASnBr_3$

As described in Chapter 6, no mixing was observed for any $MAPbBr_3$/$MASnBr_3$ heterojunctions. As such, we would expect the Sn and Pb elements to be contained within their respective layers. Probing these structures with depth profiled XPS confirms this expectation as shown in Figure 7.9. As a function of sputter time, Figure 7.9a shows a transition from high Sn 3d photoelectron intensity, originating from the top $MASnBr_3$ layer ($\sim$110 nm thick), to the Pb 4f photoelectrons originating from the bottom $MAPbBr_3$ layer ($\sim$70 nm thick). After 5 minutes of sputtering, the Si 2p signal from the glass substrate is observed. Residual Sn and Pb counts which persist after reaching the substrate are attributed to inefficient removal of metallic species and differences in sputtering rates between organic, metallic, and halogen species, both of which have been discussed in detail in Sections 7.1 and 7.3.

Interestingly, the apparent sharpness of the Sn/Pb interface depends on whether the metallic damage peaks are included when calculating atomic concentration. Figure 7.9b shows the Sn 3d5 and Pb 4f profiles when including total metallic peak area, just the perovskite peak area, and just the damage peak area. As observed in Section 7.3, the area of the damage peak is initially small but increases with sputter time, eventually becoming a significant fraction of the total metal signal for both lead and tin. The result is that including the total metallic peak area results

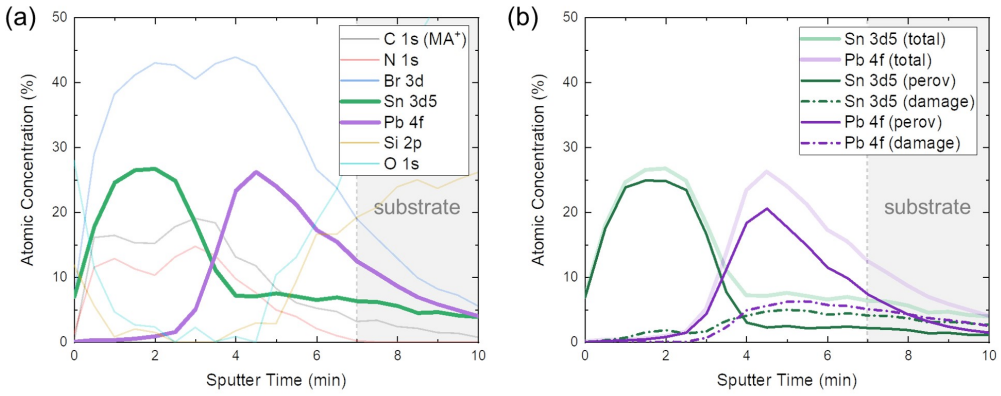

Figure 7.9. XPS depth profiles of $MAPbBr_3/MASnBr_3$ heterojunctions using 20 kv/20 nA C_{60}^+, highlighting separation of Sn and Pb elements in their corresponding layers. Grey area after 7 minutes indicates substrate as defined by Equation 7.2 (a) Atomic concentrations including all metallic signals (perovskite and damage peaks), (b) plot of Sn 3d5 and Pb 4f separated into contributions from perovskite peak and damage peaks.

in Sn and Pb profiles that persist long into the substrate. However when only the perovskite portion of these signals are included, the interface between Sn and Pb appears sharper and the intensity of the tails into the substrate is much lower. Full XPS spectra for Sn and Pb as a function of sputter time are shown in Figure G.25.

In addition to confirming the heterojunction formation for $MAPbBr_3/MASnBr_3$ using depth profiled XPS, we also performed preliminary depth profiled UPS experiments on these samples (for details see Appendix G). For these measurements, the raster area was increased during sputtering as compared to the conditions in Figure 7.9 (6x6 mm instead of 4x4mm) - this resulted in a slower sputtering rate and a greater depth resolution. As shown in Figure 7.10a, the corresponding crossover between the Sn 3d5 and Pb 4f signals occurs at $\sim$12 minutes as opposed to $\sim$3.5 minutes in Figure 7.9. Figure 7.10b shows the UPS profiles as a function of sputter time using this larger raster area. Here, pink traces correspond to the first 12 minutes of sputtering in which the Sn dominates (*i.e.* the $MASnBr_3$ film) and blue traces correspond to timepoints in the $MAPbBr_3$ film. Whereas the low binding energy region (shown in the inset of Figure 7.10b) of the UPS spectra is relatively stable for sputter times corresponding to the $MASnBr_3$ film, upon reaching the $MAPbBr_3$ film the onset of the spectra shifts to higher binding energy. While additional UPS measurements would need to be performed to confirm this result, the difference

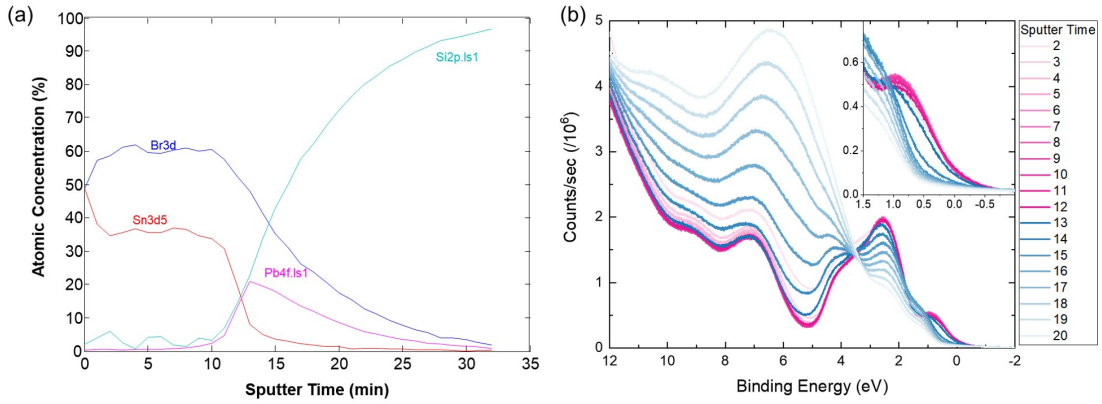

Figure 7.10. XPS and UPS depth profiles of $MAPbBr_3/MASnBr_3$ heterojunction using 20 kv/20 nA C_{60}^+ rastered over 6x6mm. (a) XPS depth profiles at the UPS sputtering conditions to determine the sputtering time required to reach the interface of the $MAPbBr_3$ and $MASnBr_3$ films, in this case, the interface is 12 minutes. (b) UPS spectra as a function of sputter time. Pink traces are spectra that correspond to the $MASnBr_3$ film (2-12 minutes), blue traces correspond to the $MAPbBr_3$ film (>12 minutes). Inset shows close-up of low binding energy region, highlighting the shift in ionization energy of 0.5-1 eV for $MASnBr_3$ and $MAPbBr_3$ films.

in onset appears to be 0.5-1 eV, which is typical of the difference in ionization energies reported for $MAPbBr_3$ and $MASnBr_3$ [330].

7.5.2 $FAPbBr_3/MASnBr_3$

Building off of the results performing depth profiling on $MAPbBr_3/MASnBr_3$ heterojunctions, we then probed slightly more complicated $FAPbBr_3/MASnBr_3$ heterojunctions, where both the A- and B-sites are varying across the interface. Specifically, depth profiled XPS was used in this case to carefully probe which species (A-site or B-site) was responsible for the observed mixing of these heterojunctions (Chapter 6). As such, we performed depth profiles on "unmixed" (measured <100 hrs after deposition) and "mixed" (measured >1500 hrs after deposition) films. Figure 7.11 shows the full XPS depth profiles for these two cases. We can see that the sharpness of the transition between Sn 3d5 and Pb 4f photoelectron intensity profiles appears unchanged for the two cases, indicating minimal diffusion of the B-site cations (Sn^{2+} and Pb^{2+}) across the heterojunction interface. This suggests that the mixing observed in XRD and UVvis measurements is likely due to A-site diffusion.

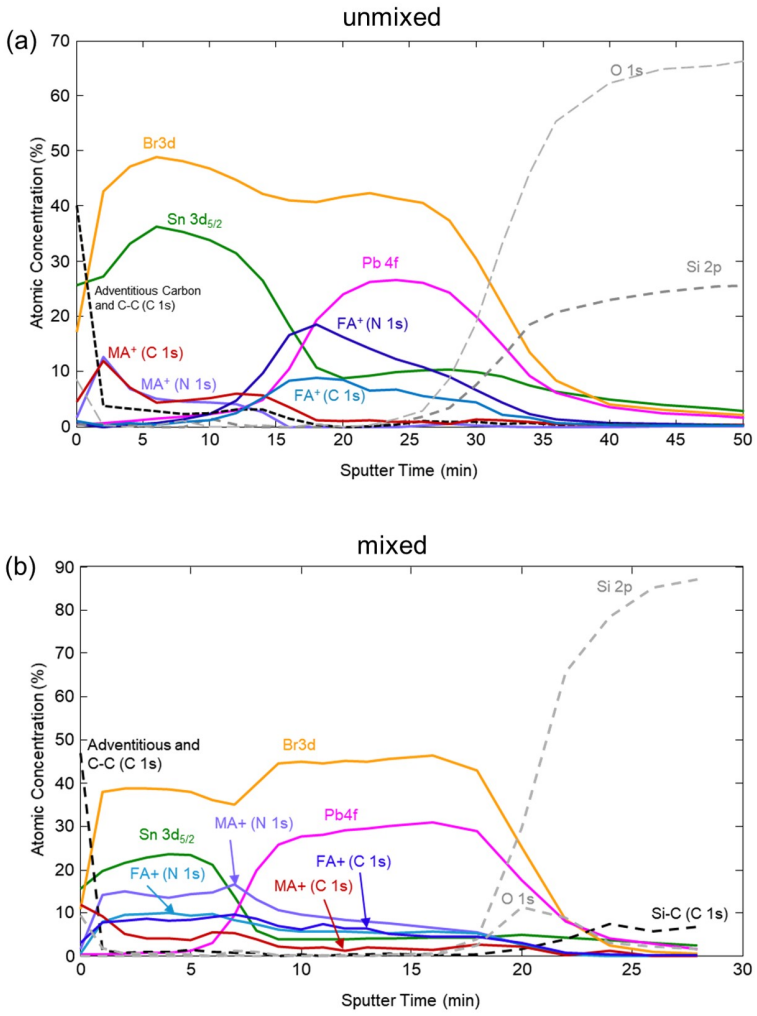

Figure 7.11. XPS depth profiles of unmixed (a) and mixed (b) $FAPbBr_3/MASnBr_3$ heterojunctions. The sharpness of the transition from Sn 3d5 and Pb 4f profiles appears similar for both mixed and unmixed films, indicating minimal diffusion of the B-site. However, the relative intensities of the C 1s and N 1s signals corresponding to MA^+ and FA^+ species differ dramatically for the unmixed and mixed cases: whereas both are present at the surface of the mixed film, the unmixed heterojunction contains regions where only one signal is present.

Fortunately, XPS depth profiling is particularly useful in tracking the organic A-site species in this heterojunction as the different bonding environments for MA^+ (C-N single bond) and FA^+ (C=N double bond) result in resolvable differences in binding energies [308]. Figure 7.12 shows the XPS profiles as a function of sputter time for C 1s and N 1s signals of unmixed

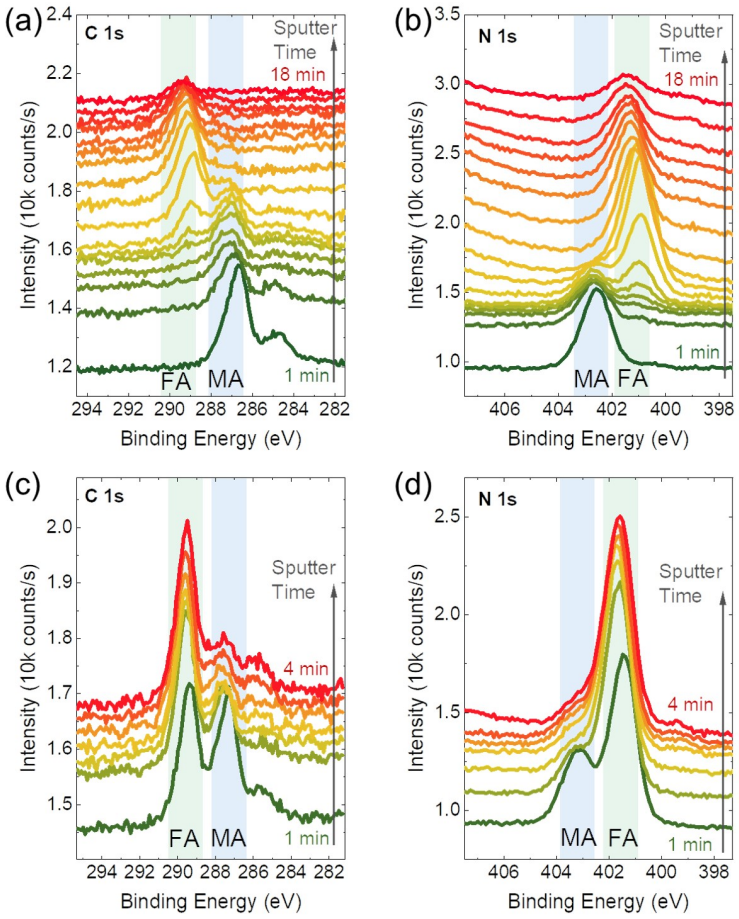

Figure 7.12. C 1s and N 1s XPS profiles of unmixed (a) and (b) and mixed (c) and (d) $FAPbBr_3/MASnBr_3$ Heterojunctions. Signals from both MA^+ and FA^+ are present at the surface for the mixed case, whereas the unmixed case has regions of only MA^+ and only FA^+ signals. Note the low energy C 1s peak in (a) at 284.8 eV is due to adventitious carbon at the surface of the film.

and mixed $FAPbBr_3/MASnBr_3$ heterojunctions. For nitrogen, the N 1s binding energy is $\sim$403 eV in MA^+ and $\sim$401 eV in FA^+. Similarly, the binding energy for carbon C 1s is $\sim$287 eV in MA^+ and $\sim$290 eV in FA^+. For the unmixed cases (7.12 (a) and (b)), both C and N show only contributions from MA^+ in the top layer of the heterojunction corresponding to the $MASnBr_3$ film. As sputtering time increases, a peak corresponding to FA^+ emerges, and there are some sputtering time points (e.g 7 minutes for C 1s and 5 minutes for N 1s) where peaks

corresponding to both FA^+ and MA^+ are present simultaneously. This could be due to some mixing present in this sample and/or beam-induced migration of these species. However, with additional sputtering time, both C 1s and N 1s signals eventually show only an FA^+ peak with no MA^+ contribution. This indicates that there are regions in these heterostructures without substantial A-site mixing.

In contrast, the carbon and nitrogen profiles for the mixed $FAPbBr_3$/$MASnBr_3$ heterojunctions show contributions from both FA^+ and MA^+ at the surface of the film (7.12 (c) and (d)). The presence of the FA^+ species at the surface of the $FAPbBr_3$/$MASnBr_3$ heterojunction confirms the diffusion of the A-site species from the bottom layer through the entirety of the top layer, thus suggesting that A-site diffusion is responsible for the mixing seen in Chapter 6.

7.6 Summary

In summary, we probed the impact of sputtering conditions on MHP XPS depth profiles by using four different sputtering sources (C_{60}^+, Ar_{620}^+, Ar_{2500}^+, and Ar^+) on $MASnBr_3$ MHPs. By quantitatively analyzing sputtering rate, halogen/metal ratios, degree of differential sputtering, and metallic species damage, we conclude that C_{60}^+ performs best for MHPs. Our results provide valuable direction for choosing sputtering conditions for MHP materials, as well as showcasing these results for tin perovskites which had not been reported previously. We also explore in detail the origins of the non-stoichiometric halogen/metal ratio that is ubiquitous for ion-sputtering depth profiling in MHPs. By performing XRD, RBS, ad XPS measurements in tandem, we show that low halogen/metal ratios are predominantly due to measurement artifacts from sputtering and are not inherent to the film chemistry. This definitive conclusion is in contrast to common assumptions made in the literature, and motivates the need to optimize sputtering conditions for MHPs as well as perform careful data analysis and interpretation.

We then employ our best-performing C_{60}^+ source to probe the interfaces and diffusion in all-perovskite heterojunctions. We are able to show successful heterojunction formation for $MAPbBr_3$/$MASnBr_3$ and $FAPbBr_3$/$MASnBr_3$ layered structures, and determine that organic A-site species are migrating across $FAPbBr_3$/$MASnBr_3$ interfaces that show mixing.

Chapter 8

Conclusions and Future Work

8.1 Summary and Conclusions

My dissertation work presented herein has focused on the development and application of a carrier-gas assisted vapor deposition (CGAVD) technique for metal-halide perovskite (MHP) thin films. This CGAVD method is advantageous because it enables substantial tunability in film stoichiometry and morphology, which in turn dictate MHP material properties and device performance, because it allows the deposition of novel multi-layer films typically inaccessible using ubiquitous solution-based techniques, and because it has the potential to be commercially relevant due to its high material utilization efficiency and medium-vacuum requirements. Despite these advantages, CGAVD is nearly unexplored in the vast and quickly growing field of MHPs, perhaps due to the large parameter space afforded by CGAVD and the resulting need for a detailed understanding of how experimental conditions impact deposition. Broadly, my thesis work sought to methodically develop and explore the use of CGAVD for MHP materials in order to showcase the capabilities of this technique and to build a foundation of knowledge such that other researchers may more easily utilize this method going forward.

The substantive portion of my thesis work begins in Chapter 4, which describes the design and validation of the initial prototype and final CGAVD systems. First, a set of design goals/success criteria are defined to guide our design towards the ability to grow MHP films that are relevant for incorporation into optoelectronic devices like solar cells and LEDs. The successful growth of a $MASnI_3$ perovskite using our simple one-source prototype design served as a proof-of-concept and motivated the investment in a more complex 4-source system with a

cooled substrate holder. Details of this final system, including conceptual requirements and operating principles, individual part mechanical designs, finite-element analyses, and experimental verification are described in detail. Importantly, this design has six independently controllable temperatures, pressures, and flow rates that enable a wide parameter space with which to tune deposition conditions. Finally, we present the development and validation of an analytical model to describe material transport in this system for both deposition of individual and multiple MHP precursor species, along with experimental results to confirm this model and measure our system against our success criteria. Throughout this development and validation process, we find that our deposition rate is limited by material convection out of the source and not diffusion across the velocity boundary layer near the substrate, and that our analytical model accurately represents our experimental results when this rate of diffusion $\rightarrow \infty$. Finally, we observe that our CGAVD technique is robust in the sense that, for substrate temperatures above $\sim$25 °C, there is a stoichiometrically self-correcting window of deposition. In this window, the MHP films appear to reject excess precursor in the case of imbalanced precursor fluxes, resulting in a stoichiometric film over a relatively wide range of non-stoichiometric precursor flux rates. This finding not only relaxes the logistical requirement for exactly balanced precursor fluxes, but also allows us to tune film properties while maintaining a nominally stoichiometric film.

Chapter 5 showcases the power of the CGAVD technique to enable the systematic tuning of MHP film stoichiometry and morphology. First, I used the analytical model developed in Chapter 4 to systematically tune MABr:$SnBr_2$ flux ratios and realize a corresponding change in grain size and crystallinity. For $\sim$ 80% molar excess $SnBr_2$, we see small grain size (0.003 μm^2) and low-intensity XRD diffraction peaks. Both of these metrics increase monotonically for increasing MABr fluxes, up to a grain size of over 0.2 μm^2 for $\sim$ 80% molar excess MABr. In addition to this morphological tuning, we also observe a change in electrical properties with changing precursor flux ratios. Collaborating with Bryan Voigt (advised by Profs. Aydil and Leighton) who performed resistivity and Hall effect measurements, we find that we can tune the resistivity, majority carrier density, and mobility of $MASnI_3$ films by at least 1 order of magnitude by tuning their stoichiometry. In order to tune film morphology independently from stoichiometry, we also demonstrate the use of chamber pressure and substrate temperature to control grain size and orientation. Depositing $MASnBr_3$ films from pressures of 0.3 to 10 Torr and substrate temperatures of 30 °C - 70 °C, we observe grain sizes ranging from less than 0.05

μm^2 (low P and T_s) to over 0.7 μm^2 (high P and T_s). The last section of this chapter discusses the results of using CGAVD to deposit MHPs on a variety of substrates. We have found that the morphology of MHP films tends to be less sensitive to substrate (*e.g.* ITO, c-TiO_2, glass) than it is to deposition conditions like pressure, precursor flux rates, and substrate temperature. We note that this ability to deposit films with similar morphologies on different surfaces provides an opportunity to conduct meaningful studies with a variety of electron- and hole-transport layers. Finally, we demonstrate our ability to deposit MHP films on flexible substrates like Kapton, which are promising for the realization of cheap, lightweight, conformal MHP electronics.

The results presented in Chapter 6 are in many ways the crown jewel of my thesis research. Here, we demonstrate the usefulness of vapor deposition techniques to fabricate all-(3D) MHP layered structures which had not been reported previously in the literature. These novel perovskite-perovskite heterojunctions are interesting for several reasons. The first is that these structures are an ideal system to study ion migration in MHPs, and can be a vital method to elucidate which species migrate within a perovskite lattice and how quickly, and how this motion depends on defects, external stimuli, etc. Stable perovskite-perovskite heterojunctions can also be used to improve existing optoelectronic devices like PVs; for instance, perovskite-perovskite heterojunctions could be used to improve light absorption and energy transfer for an HTM-free perovskite PV, as has been shown *via* simulations [273]. Finally, all-perovskite heterojunctions may usher in new applications that take advantage of the substantial optical and electronic tunability of MHP materials, for example by enabling the optimization of energy band alignments for devices that require resonant tunneling or negative differential resistance [274–277]. While some reports of reduced dimensionality MHP heterojunctions exist (*e.g.* $CsPbBr_3$/$CsPbI_3$ nanowires), our work demonstrates the ability to form heterojunctions from a variety of thin film 3D perovskites with a relatively facile technique. We further probe the stability of these heterojunctions, and find two that appear stable $>$1500 hours when stored in N_2: $MAPbBr_3$/$MASnBr_3$ and $CsPbBr_3$/$MASnBr_3$. We also find that, in general, heterojunctions where the halide is varied across the interface mix rapidly, which aligns well with other reports that the halogen ion is the most mobile in the MHP lattice. We also probe the mixing of the $FAPbBr_3$/$MASnBr_3$ heterojunction in detail using absorption, X-ray diffraction, and depth-profiled XPS techniques, and show definitively that the A-site and not the B-site is migrating across this interface. Finally, we tune the diffusion rate of this $FAPbBr_3$/$MASnBr_3$ heterojunction by altering the grain size of the bottom film, thereby providing design rules to improve the

stability of these structures going forward.

In Chapter 7 I present the results of a collaboration with Jennifer Mann *et al.* at Physical Electronics. In this work, we sought to understand and minimize measurement artifacts associated with depth-profiled XPS measurements on MHPs. First, we investigate a variety of ion beams and find that, of the conditions tested, 333 eV/atom C_{60}^{+} minimize differential sputtering and metallic species damage in tin-based MHPs. This result not only guides future experiments using depth-profiled XPS, but establishes these rules for tin MHPs which, to our knowledge, have not been published. We also investigate the origin of the ubiquitous non-stoichiometric halogen/metal ratios (*i.e.* X/B < 3) reported in the literature for depth profiled techniques. We combine XPS with RBS and XRD measurements and show definitively that this low halogen/metal ratio is a measurement artifact and *not* a result of excess metallic species in the film, which has been often hypothesized in the literature. Finally, we apply our optimized sputtering conditions to investigate the all-perovskite MHPs described in Chapter 6, and confirm the formation of $MAPbBr_3$/$MASnBr_3$ and $FAPbBr_3$/$MASnBr_3$ heterojunctions. Further, we take advantage of XPS to differentiate between chemical binding states of carbon and nitrogen to show that only the A-site and not the B-site is diffusing in the $FAPbBr_3$/$MASnBr_3$ structure.

In this Chapter, I conclude this work by describing potential future research directions as well as a general outlook on the field of MHPs for optoelectronics.

8.2 Future Research Directions

8.2.1 Vapor-deposited Pb films for devices and heterojunctions

At the outset of my thesis work, it was unclear whether Sn (or some other element) might become a viable replacement for lead in MHP materials in order to reduce their toxicity. However, over the last 5 years, and as the quantity of research has increased dramatically, the practical and health benefits of using Sn instead of Pb have become less promising. To the first point, the efficiency of Sn-only perovskite PVs is still less than half of that of Pb-based PVs despite substantial research focus on these materials [331, 332]. Second, and perhaps more importantly, it is unclear whether tin-based MHPs would be substantially less toxic/harmful than their lead-based counterparts. While the full life cycle impacts of tin and lead MHPs on humans and other species is not fully understood, preliminary studies show in some cases SnI_2 can be worse for aquatic species than PbI_2 [57, 333]. Furthermore, innovative strategies to prevent

Pb from leaching into the environment in the case of a catastrophic breaking of a solar cell have been investigated, with promising results [160]. Finally, despite potential challenges with permitting and public health, several startups (*e.g.* Oxford PV, Tandem PV) have been created to commercialize Pb-based perovskite PVs. In light of all of these developments, it appears increasingly likely that Pb MHPs will continue to be the technologically and practically most important MHP for the near future.

As such, one major future project could be the application of the CGAVD technique to grow and investigate Pb-perovskite films and devices. The ability of this technique to tune stoichiometry and film morphology can be used to perform detailed investigations of process-property-performance relationships in this material system, which can be challenging to access using common solution based methods. For example, looking at how deposition conditions impact carrier densities and mobilities, and corresponding PV device metrics, would provide valuable tools to inform the optimization of these devices. Furthermore, the application and development of this technique to Pb-MHPs is important to help transition the field to vapor-based techniques, which may allow higher quality films with fewer defects in the long-run. The work for this project has already been started by Wan-Ju Hsu, with promising results for the deposition of PbI_2. Future work will likely include mapping out thermodynamic properties (*i.e.* sublimation enthalpy) of lead precursor materials like PbI_2, investigating how film morphology varies with deposition parameters for lead perovskites, and finally implementing these films in devices to determine their performance vs. these deposition conditions.

In addition to investigating lead films on their own using CGAVD, it would be highly interesting to begin to incorporate the heterojunction films described in Chapter 6 into devices. A first attempt at this could be made either with solution or vapor process Pb-films,[1] and could look at the impact of this heterojunction on PV device performance. Optimization of MHP layer thicknesses, in addition to optimization of the full device stack, could be done with Setfos or similar software to determine the best configuration for carrier generation and transport prior to experimental investigations.

[1] although this would impact whether the devices could be standard and/or inverted as solution processed MHPs cannot be deposited on top of existing MHP layers

8.2.2 Photoluminescence measurements to probe perovskite optical degradation

Despite the progress in utilizing MHPs for light-emitting devices [43, 50–56], there have been no comprehensive investigations of the PL degradation of various MHP materials. Not only would this information provide valuable insight into which MHPs would likely perform the best in devices subject to light soaking, but it could also potentially provide a mechanism to predict EL stability, as has been successful for some OLED devices [334, 335]. Using the robust expertise our group has in probing EL and PL stability for organic materials to study perovskite degradation could add valuable knowledge to the field regarding the stability of MHP optoelectronics.

Initial work done by John Myers-Bangsund (measurement setup) and myself (film synthesis) sought to use optical degradation as a method to perform a preliminary screening of MHPs. Our goal was to determine which materials and processing conditions would be most promising for integration into a stable PeLED device. Our first investigations included building the setup and probing the PL stability of five different spin-coated Pb films: $CsPbBr_3$, $Cs_{0.06}MA_{0.15}FA_{0.79}Pb(Br_{0.4}I_{0.6})_3$, $MA_{0.5}FA_{0.5}PbBr_3$, $MAPbBr_3$, and $FAPbBr_3$. The PL spectra and XRD patterns for these films can be seen in Figure 8.1.

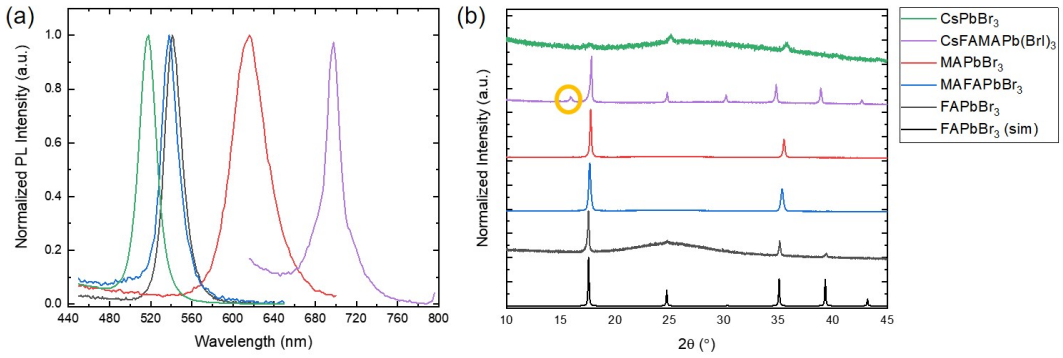

Figure 8.1. (a) PL spectra and (b) XRD patterns for optical stability tests on five spin coated led MHPs. Here, $CsFAMAPb(BrI)_3$ = $Cs_{0.06}MA_{0.15}FA_{0.79}Pb(Br_{0.4}I_{0.6})_3$ and $MAFAPbBr_3$ = $MA_{0.5}FA_{0.5}PbBr_3$. The orange circle in (b) denotes an unknown non-stoichiometric phase present in the $CsFAMAPb(BrI)_3$ film. A simulated XRD pattern for $FAPbBr_3$ is shown for reference. PL spectra were taken with the PTI. X-ray diffraction was collected using a PANalytical X'pert PRO diffractometer with Co Kα radiation (λ=1.7889 Å).

After spin coating, these films were loaded into a testing apparatus, which included a 405 or 473 nm laser source, Arduino-controlled shutter, beam expander, aperture and splitter, and filter wheel [335]. Initial experiments illuminated our MHP films at $\sim$25 W/cm^2, and PL was collected over time. Example spectra are shown in Figure 8.2 for $CsPbBr_3$ and $FAPbBr_3$, with and without a passivating TOPO (trioctylphosphine oxide) treatment. We use these spectra to calculate t_{80}, or the time at which the PL intensity reaches 80% of it's initial value. This is shown in Figure 8.2c. Here, we can see that the PL lifetime of our $CsPbBr_3$ films is substantially better than our $FAPbBr_3$ films. Passivation and a longer annealing time (60 min instead of 10 min at $\sim$100 °C) also improves the PL lifetime substantially for $CsPbBr_3$. Using the conditions here, lifetimes for $MA_{0.5}FA_{0.5}PbBr_3$ and $MAPbBr_3$ were so short that it was difficult to even calculate t_{80}.

Interestingly, the $Cs_{0.06}MA_{0.15}FA_{0.79}Pb(Br_{0.4}I_{0.6})_3$ film showed photobrightening behavior, which has been observed before for these mixed A- and X-site MHPs and may be due to phase segregation in these materials [336]. An example of this effect can be seen in Figure 8.3, where the intensity of the PL signal first drops sharply but then increases with time. In our measurements, this behavior was convoluted with increased scattering over time, which was also observed visually as the films appeared cloudy after our measurements.

Our preliminary results show that current 3D MHPs made *via* spin coating in our lab degrade rapidly under $\sim$25 W/cm^2 473 nm excitation. Among the single A- and B- site MHPs tested, $CsPbBr_3$ performed the best. We also showed that surface passivation (*via* TOPO) and increased

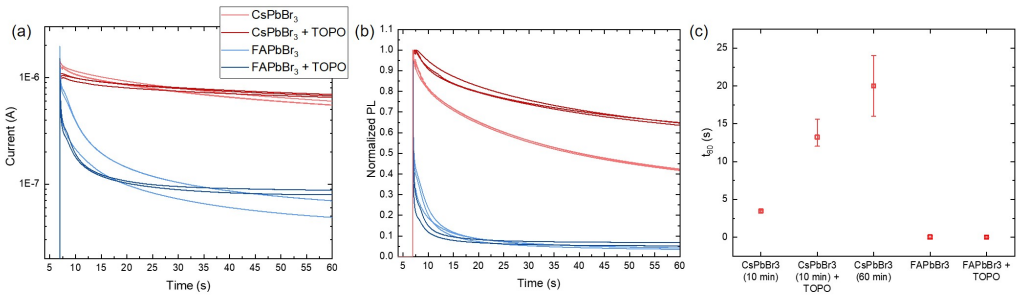

Figure 8.2. (a) Photodetector current, (b) normalized PL spectra, and (c) t_{80} plotted for $CsPbBr_3$ and $FAPbBr_3$ films with and without TOPO treatment. Two annealing conditions for $CsPbBr_3$ are also included. The PL lifetime of $CsPbBr_3$ is substantially longer than for $FAPbBr_3$, and is further increase with TOPO passivation and a longer annealing time.

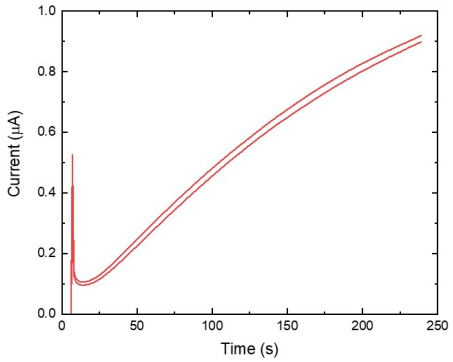

Figure 8.3. Photobrightening behavior of $Cs_{0.06}MA_{0.15}FA_{0.79}Pb(Br_{0.4}I_{0.6})_3$ film, where PL intensity increases over time. This has been observed elsewhere in the literature, and is often attributed to phase segregation [336].

annealing time for $CsPbBr_3$ had a large impact on t_{80}. Future research could include optimization of this setup to improve results (*e.g.* reducing the beam intensity) and further screening of green MHP QDs (purchased from Sigma-Aldrich) and 2D/3D MHPs. After screening for the most promising initial candidates, these could then be incorporated into a PeLED architecture to assess their stability in a functioning device.

8.2.3 Ultrafast Transmission Electron Microscopy

The interaction between phonons and charge carriers in MHPs are likely to influence material properties key to their successful application in optoelectronic devices (*e.g.* non-radiative recombination and carrier scattering processes) [93, 117, 337]. Yet the fundamental mechanisms governing phonon-carrier interactions are not well understood. One of the key open questions in the field of MHPs, for example, is the discrepancy between the observed and expected electron and hole mobilities. Whereas the effective masses of MHPs are low ($\sim$0.2 m_0) and on-par with inorganic semiconductors like Si and GaAs, the mobilities of MHPs are often 1-2 orders of magnitude lower than for inorganics [93]. To make sense of this discrepancy, several common models used to describe carrier mobility due to lattice scattering have been applied, yet all are insufficient to capture both the magnitude ($<$200 cm^2/Vs) and temperature dependence ($T^{-1.5}$) of carrier mobility in MHPs [93, 338]. As such, it appears that the standard canonical models of carrier scattering may be insufficient to describe the behavior in MHPs, potentially due to the mechanically soft, molecularly dynamic, and anharmonic vibratory nature of the MHP lattice [93, 337–339]. A more detailed understanding of the interactions between charge carriers and lattice vibrations is thus required to fully predict the theoretical upper limit of carrier mobility

in MHPs.

Ultrafast transmission electron microscopy, or UEM, is a technique ideally suited to understand the time evolution of phonons, and thus can help address several voids in our collective understanding of fundamental MHP properties. The pump-probe approach of UEM, of which CEMS own Flannigan group is at the forefront, has resulted in the ability to investigate how electron-phonon coupling and phonon-phonon coupling evolve over fs- to ps- time scales in a wide range of materials [340–345]. Because of the scientifically important and functionally relevant questions UEM can elucidate in the field of MHPs, we have recently begun a collaboration with Elisah VandenBussche in the Flannigan group to look at MHP materials in the UEM.

Our initial work up to this point has focused on sample preparation and mitigation of damage from the electron beam in the UEM instrument. Several synthesis techniques were attempted to create phase-pure, $<$100nm thick samples of $MAPbI_3$ required for UEM experiments, including microtoming or FIB-ing single crystals, one-step drop casting of MAI + PbI_2 solutions, PbI_2 platelet growth in solution followed by MAI vapor phase reaction, and one-step spin coating of MAI + PbI_2 solutions onto a TEM grid (see Appendix H for additional synthesis details). Of these methods, one-step spin coating of MAI + PbI_2 solution directly onto a TEM grid provided the most consistently viable $MAPbI_3$ crystals with appropriate thickness.

After optimizing this synthesis technique, Elisah performed several studies to determine how pulsed electron beams could be used to mitigate, and potentially study, the degradation of MHP materials, as discussed in detail elsewhere [346]. Briefly, these initial investigations have shown that the pulsed-beam technique afforded by the UEM can be used to significantly reduce MHP damage caused by the electron beam as compared to traditional thermionic TEM sources, in which the electron emission is random over time. These results are important because they lay a necessary foundation for detailed investigation of MHP materials in the UEM while minimizing material damage. They also provide insight into future research directions to investigate the origins of MHP degradation as they relate to charge-phonon interactions.

Additional questions that could be investigated going forward include how defects impact phonon initiation and propagation and how energy imparted from photoexcited electrons is transferred to the lattice. The latter may be particularly important for understanding the origins of low non-radiative recombination rates in MHPs, as it has been hypothesized that this property may arise from the fact that photogenerated carriers are only (weakly) coupled to low-energy phonons, and therefore energy dissipation *via* phonons is less likely due to the need to

excite multiple phonons simultaneously [93, 117]. Understanding the timescales and modes involved in energy dissipation in these materials using UEM may thus uncover the fundamental mechanisms governing the ideal optoelectronic properties in MHPs.

8.2.4 CGAVD System Improvements

If future research efforts involve substantial use of the CGAVD system, there are several modifications that will help to reduce growth-to-growth variation, improve control of substrate temperature, and increase ease of data collection:

- **Convert sources to active heating.** One of the challenges with the current CGAVD setup is that the source material temperature is controlled by manually positioning the source holders along the temperature gradient established by the furnace. Depending on where in this temperature gradient the sources are, the ampoule itself may see a larger or smaller ΔT from front to back. For example, the MAI source holder may see a nearly 10 °C gradient, whereas the SnI_2 holder will see closer to a 3 °C gradient. This makes it much more challenging to predict deposition rates, especially when sources are used multiple times. Furthermore, it is not clear whether the ampoule geometry is ideal for creating a cavity in which the vapor pressure can come to equilibrium quickly. These issues can lead to substantial variations between growths, which makes consistent experimental results difficult to achieve. To solve both of these issues, and to make the deposition procedure easier, I recommend implementing an active heating element which can be used to heat source material to desired temperatures without relying on the temperature gradient established by the furnace. This can allow much faster heat up and cool down of material, more precise control of temperatures, and uniform temperatures across the entirety of the source material powder volume. A schematic example of this modification is shown in Figure 8.4, which would require adding a flange adapter to the source side of the chamber, individual band heaters for each ampoule, and a temperature controller. Alternatively, the source materials could be heated externally to the chamber altogether, although this would require careful implementation to create a heating scheme that would be safe (would not result in easy burns), and that would minimize heat stress to chamber o-ring and other temperature sensitive components that are currently situated outside of the furnace.

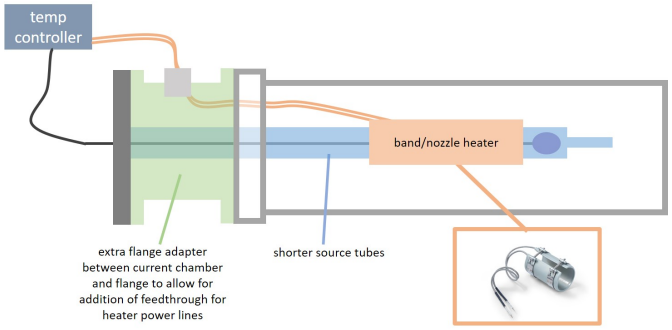

Figure 8.4. Schematic example of actively heated sources. Here, active heating is accomplished through individual band heaters situated around the source ampoules, which are connected to a temperature controller *via* an additional flange adapter on the source side of the chamber.

- **Install chilled water drops to replace ice/H_2O circulator.** Currently, substrate cooling is achieved by a water circulator filled with ice and water. To provide more robust cooling, minimize the hassle of using this system, and enable better temperature control, an improved chilling system could be implemented.

- **Install active thickness monitoring.** The lack of active thickness monitoring makes it challenging to grow films with a desired thickness accurately. The implementation of active thickness monitoring during growth, for example using quartz crystal microbalances (QCMs) or ellipsometry, would mitigate this challenge. However, this would be a substantial effort and would require a redesign of the chamber geometry and several corresponding components. It should be noted that issues observed in VTE systems with accurate thickness monitoring of MAI using QCMs is expected be much less of an issue in CGAVD as the precursor flux rates are controlled by carrier gas flow rate in addition to source material temperature.

- **Enable computer control of temperatures and flow rates.** Currently, many of the components in the CGAVD system are manually controlled, including the temperature and flow-rate of the chilled water, temperature of source material, furnace temperature setpoints, chamber pressure control valve, and dilution gas and purge gas flow rates. Converting these to computer control would enable easier and more precise control and monitoring of these quantities. It would also enable better data logging, especially when integrated with the database (below).

- **Integrate CGAVD data collection with Holmes group database.** Currently, only source material and substrate temperatures are automatically logged during growth. All other

growth conditions (temperatures, pressures, and flow rates) must be recorded manually and input into an excel spreadsheet for reference. Automating as much of this data collection as possible, and integrating this with the Holmes group database would result in better data transparency and reproducibility. Initial efforts could include importing the current excel spreadsheet of experiments into the database and setting up a growth parameter GUI for future growths as has been implemented for OLEDs.

8.3 The Future of MHPs

Given the over 25% power conversion efficiency that has been achieved for MHP photovoltaics in under 10 years of intensive study, it seems very likely that this materials system will continue to be technologically relevant moving forward [19]. Furthermore, the low cost of materials and synthesis methods for MHPs mean that further increases in efficiency are not necessarily required for them to be commercially relevant. Indeed, several start-up companies have already been created in an attempt to commercialize MHP PVs,[2] and some predict that perovskite/silicon tandem solar cells will enter large-scale production in 2021 [347]. However, technological, practical, and political challenges remain before this materials class can be implemented on a widespread scale.

One of the major outstanding issues with MHP commercialization is their instability when exposed to light, heat, oxygen, moisture, and electrical bias, all of which are likely to be applied to devices in operation in the real world [59, 135–137]. In order to compete with Si-based PV devices, it is widely acknowledged that MHP PV modules will need to have an operational lifetime of 20-25 years [348]. While some PVs have succeeded in passing the International Electrotechnical Commission (IEC) accelerated stress tests, it is generally agreed that the field of MHP devices is far from reaching sufficient lifetimes [347]. One review finds that the average degradation rate of MHP PV modules is well over 50%/year, compared to $\sim$0.5%/yr for crystalline Si [59]. A related challenge in the research of MHPs is the lack consistency regarding how and what factors related to stability are tested and reported. Recently, a large number of researchers collaborated to publish a "Consensus Statement" regarding how best to test and report degradation of MHPs in hopes of addressing these inconsistencies [348]. To improve the operating lifetime of MHPs in devices to a suitable level for commercialization will likely

[2] Oxford PV, Solaronix, EPFL, Greatcell Solar, Toshiba, and Microquanta Semiconductor

require a suite of approaches. This may include the implementation of MHPs that have higher intrinsic stability (like all inorganic MHPs or mixed cation and anion MHPs), the minimization of defects that can accelerate degradation mechanisms (surfaces, grain boundaries), surface passivation strategies, and the addition of protective capping and encapsulation layers [59].

The toxicity of all high-performing Pb-perovskites is another major factor impeding the viability of MHPs to be realize commercially, both in terms of the political challenges associated with distributing a lead-containing technologies, and with the real and substantial health impacts that errant lead compounds can cause if not properly contained. The lead contained in high performing MHPs is particularly problematic because of the aforementioned instability of these materials in ambient conditions, where exposure to water can create water-soluble byproducts like PbI_2. As one study that assesses the toxicity of lead-based MHP concludes "there is one strict condition on which the large-scale implementation of this photovoltaic technology hinges: 100% reliable containment of degradation products from modules that lose their structural integrity during their useful life. The perovskite technology can be deployed in a completely safe way (both for human health and the environment) only if modules are fitted with an absolutely fail-safe encapsulation, resistant to extreme conditions" [57]. Interesting approaches to this challenge are already underway, like the development of "on-device" Pb sequestration strategies to retain any potential leakage in the case of catastrophic damage [160]. The discovery of a less toxic, Pb-free (and likely Sn-free) alternative with similar optoelectronic performance would be a boon to this technology, but there currently are no such promising materials. If lead MHPs end up being widely commercialized, extreme care must be taken towards limiting the potential human and ecosystem harm that could arise from Pb-exposure.

In addition to the instability and toxicity of current MHP materials and devices, widespread implementation will require the development and scale-up of industrial scale fabrication techniques that can maintain the integrity and high performance of these thin films. Currently, the vast majority of high-efficiency MHP devices have small active areas, typically less than 1 cm^2. Common techniques that are capable of resulting in large-area films include doctor blading, slot-die coating, printing, soft-cover deposition, spray-deposition, dip coating, and vapor-based deposition [172]. While it remains to be seen which of these techniques will dominate the emerging MHP market, the majority of perovskite startups are using some variation of printing techniques, however doctor-blade coating, soft-cover deposition, and spray coating methods have thus far resulted in the highest efficiencies for devices with active areas over 10 cm^2 [163].

Finally, the next decade of research on MHPs will likely see a burgeoning of applications outside of solar cells. While perovskite materials have already made their way into many types of non-PV devices including photodetectors [40–42], light emitting diodes [43, 56], lasers [44, 45], transistors [46, 47], and resistive memory devices [48, 49], most of these technologies are still in their infancy. It is also possible that we will soon see the emergence of entirely new applications. For example, the advent of all perovskite heterojunctions may enable the realization of devices based on resonant tunneling, negative differential resistance, and quantum confinement.

Bibliography

[1] J. Tsao, N. Lewis, and G. Crabtree. "Solar FAQs". In: *U.S. Department of Energy* (2006), pp. 1–24. DOI: https://www.sandia.gov/~jytsao/SolarFAQs.pdf.

[2] Ren21. *Renewables 2019 global status report*. 2019. DOI: https://www.ren21.net/reports/global-status-report/.

[3] H Topsöe. "Krystallographisch-chemische untersuchungen homologer verbindungen". In: *Zeitschrift für Kristallographie* 8 (1884), pp. 246–296.

[4] D. B. Mitzi, S. Wang, C. A. Feild, C. A. Chess, and A. M. Guloy. "Conducting layered organic-inorganic halides containing (110)-oriented perovskite sheets". In: *Science* 267.5203 (1995), pp. 1473–1476. DOI: 10.1126/science.267.5203.1473.

[5] D. B. Mitzi, C. A. Feild, Z. Schlesinger, and R. B. Laibowitz. "Transport, Optical and Magnetic Properties of the Conducting Halide Perovskite". In: *Journal of Solid State Chemistry* 114 (1995), pp. 159–163. DOI: DOI:10.1006/jssc.1995.1023.

[6] M. A. Green, A. Ho-Baillie, and H. J. Snaith. "The emergence of perovskite solar cells". In: *Nature Photonics* 8.7 (2014), pp. 506–514. DOI: 10.1038/nphoton.2014.134.

[7] M Era, S Morimoto, T Tsutsui, and S Saito. "Organic-inorganic heterostructure electroluminescent device using a layered perovskite semiconductor $(C_6H_5C_2H_4NH_3)_2PbI_4$". In: *Applied Physics Letters* 65.6 (1994), pp. 676–678. DOI: 10.1063/1.112265.

[8] T. Hattori, T. Taira, M. Era, T. Tsutsui, and S. Saito. "Highly efficient electroluminescence from a heterostructure device combined with emissive layered-perovskite and an

electron-transporting organic compound". In: *Chemical Physics Letters* 254.1–2 (1996), pp. 103–108. DOI: 10.1016/0009-2614(96)00310-7.

[9] X Hong, T Ishihara, and A. V. Nurmikko. "Photoconductivity and electroluminescence in lead iodide based natural quantum well structures". In: *Solid State Communications* 84.6 (1992), pp. 657–661. DOI: 10.1016/0038-1098(92)90210-Z.

[10] D. B. Mitzi, C. D. Dimitrakopoulos, and L. L. Kosbar. "Structurally tailored organic-inorganic perovskites: Optical properties and solution-processed channel materials for thin-film transistors". In: *Chemistry of Materials* 13.10 (2001), pp. 3728–3740. DOI: 10.1021/cm010105g.

[11] C. R. Kagan, D. B. Mitzi, and C. D. Dimitrakopoulos. "Organic-Inorganic Hybrid Materials as Semiconducting Channels in Thin-Film Field Effect Transistors". In: *Science Magazine* 286 (1999), pp. 945–947. DOI: 10.1126/science.286.5441.945.

[12] K. Chondroudis and D. B. Mitzi. "Electroluminescence from an organic-inorganic perovskite incorporating a quaterthiophene dye within lead halide perovskite layers". In: *Chemistry of Materials* 11.11 (1999), pp. 3028–3030. DOI: 10.1021/cm990561t.

[13] T. Gebauer and G. Schmid. "Inorganic-organic Hybrid Structured LED's". In: *Zeitschrift für anorganische und allgemeine Chemie* 625.7 (1999), pp. 1124–1128. DOI: 10.1002/(sici)1521-3749(199907)625:7<1124::aid-zaac1124>3.0.co;2-t.

[14] A. Kojima, K. Teshima, T. Miyasaka, and Y. Shirai. "Novel Photoelectrochemical Cell with Mesoscopic Electrodes Sensitized by Lead-halide Compounds (2)". In: *210th ECS Meeting*. 2006. DOI: 10.1149/MA2006-02/7/397.

[15] A. Kojima, K. Teshima, Y. Shirai, and T. Miyasaka. "Organometal halide perovskites as visible-light sensitizers for photovoltaic cells". In: *Journal of the American Chemical Society* 131.17 (2009), pp. 6050–6051. DOI: 10.1021/ja809598r.

[16] J. H. Im, C. R. Lee, J. W. Lee, S. W. Park, and N. G. Park. "6.5% Efficient Perovskite Quantum-Dot-Sensitized Solar Cell". In: *Nanoscale* 3.10 (2011), pp. 4088–4093. DOI: 10.1039/c1nr10867k.

[17] H.-S. Kim et al. “Lead iodide perovskite sensitized all-solid-state submicron thin film mesoscopic solar cell with efficiency exceeding 9%”. In: *Scientific reports* 2.7436 (2012), p. 591. DOI: 110.1038/srep00591.

[18] M. M. Lee, J. Teuscher, T. Miyasaka, T. N. Murakami, and H. J. Snaith. “Efficient Hybrid Solar Cells Based on Meso-Superstructured Organometal Halide Perovskites”. In: *Science* 338 (2012), p. 643. DOI: 10.1126/science.1228604.

[19] National Renewable Energy Laboratory (NREL). *Research-Cell Efficiency Chart*. 2020. DOI: https://www.nrel.gov/pv/cell-efficiency.html.

[20] F. De Angelis. “Celebrating 10 years of perovskite photovoltaics”. In: *ACS Energy Letters* 4.4 (2019), pp. 853–854. DOI: 10.1021/acsenergylett.9b00500.

[21] H. Zhu et al. “Tailored Amphiphilic Molecular Mitigators for Stable Perovskite Solar Cells with 23.5% Efficiency”. In: *Advanced Materials* 32.12 (2020), p. 1907757. DOI: 10.1002/adma.201907757.

[22] G. Xia et al. “Nanoscale Insights into Photovoltaic Hysteresis in Triple-Cation Mixed-Halide Perovskite: Resolving the Role of Polarization and Ionic Migration”. In: *Advanced Materials* (2019), p. 1902870. DOI: 10.1002/adma.201902870.

[23] M. Saliba et al. “Cesium-containing triple cation perovskite solar cells: improved stability, reproducibility and high efficiency”. In: *Energy and Environmental Science* 9 (2016), pp. 1989–1997. DOI: 10.1039/c5ee03874j.

[24] K. Wang et al. “Novel Inorganic Electron Transport Layers for Planar Perovskite Solar Cells: Progress and Prospective”. In: *Nano Energy* 68 (2019), p. 104289. DOI: 10.1016/j.nanoen.2019.104289.

[25] V. Ferguson, S. R. P. Silva, and W. Zhang. “Carbon Materials in Perovskite Solar Cells: Prospects and Future Challenges”. In: *Energy and Environmental Materials* 2 (2019), pp. 107–118. DOI: 10.1002/eem2.12035.

[26] C. M. Wolff, P. Caprioglio, M. Stolterfoht, and D. Neher. “Nonradiative Recombination in Perovskite Solar Cells: The Role of Interfaces”. In: *Advanced Materials* 31 (2019), p. 1902762. DOI: 10.1002/adma.201902762.

[27] P. Vivo, J. K. Salunke, and A. Priimagi. “Hole-Transporting Materials for Printable Perovskite Solar Cells”. In: *Materials* 10.9 (2017), p. 1087. DOI: 10.3390/ma10091087.

[28] C. Zhang, D.-b. Kuang, and W.-q. Wu. “A Review of Diverse Halide Perovskite Morphologies for Efficient Optoelectronic Applications”. In: *Small Methods* 4.2 (2019), p. 1900662. DOI: 10.1002/smtd.201900662.

[29] F. A. Roghabadi et al. “Stability progress of perovskite solar cells dependent on the crystalline structure: From 3D ABX_3 to 2D Ruddlesden-Popper perovskite absorbers”. In: *Journal of Materials Chemistry A* 7 (2019), pp. 5898–5933. DOI: 10.1039/c8ta10444a.

[30] J.-w. Lee, D.-k. Lee, D.-n. Jeong, and N.-g. Park. “Control of Crystal Growth toward Scalable Fabrication of Perovskite Solar Cells”. In: *Advanced Energy Materials* (2018), p. 1807047. DOI: 10.1002/adfm.201807047.

[31] J.-w. Lee et al. “The role of grain boundaries in perovskite solar cells”. In: *Materials Today Energy* 7 (2018), pp. 149–160. DOI: 10.1016/j.mtener.2017.07.014.

[32] M. S. Jamal et al. “Fabrication techniques and morphological analysis of perovskite absorber layer for high-efficiency perovskite solar cell: A review”. In: *Renewable and Sustainable Energy Reviews* 98 (2018), pp. 469–488. DOI: 10.1016/j.rser.2018.09.016.

[33] Z. Wang et al. “27% -Efficiency Four-Terminal Perovskite/Silicon Tandem Solar Cells by Sandwiched Gold Nanomesh”. In: *Advanced Functional Materials* 30.4 (2019), p. 1908298. DOI: 10.1002/adfm.201908298.

[34] A. J. Bett et al. “Two-terminal Perovskite silicon tandem solar cells with a high-Bandgap Perovskite absorber enabling voltages over 1.8 V”. In: *Progress in Photovoltaics: Research and Applications* 28 (2020), pp. 99–110. DOI: 10.1002/pip.3208.

[35] S. Albrecht et al. “Monolithic perovskite/silicon-heterojunction tandem solar cells processed at low temperature”. In: *Energy and Environmental Science* 9 (2016), pp. 81–88. DOI: 10.1039/C5EE02965A.

[36] H. Shen et al. “Monolithic Perovskite / Si Tandem Solar Cells: Pathways to Over 30% Efficiency”. In: *Advanced Electronic Materials* 10.13 (2019), p. 1902840. DOI: 10.1002/aenm.201902840.

[37] R. Lin et al. “Monolithic all-perovskite tandem solar cells with 24.8% efficiency exploiting comproportionation to suppress Sn(II) oxidation in precursor ink”. In: *Nature Energy* 4 (2019), pp. 864–873. DOI: 10.1038/s41560-019-0466-3.

[38] G. E. Eperon et al. “Perovskite-perovskite tandem photovoltaics with optimized band gaps”. In: *Science* 354.6314 (2016), pp. 861–865. DOI: 10.1126/science.aaf9717.

[39] R. Sheng et al. “Monolithic Wide Band Gap Perovskite/Perovskite Tandem Solar Cells with Organic Recombination Layers”. In: *The Journal of Physical Chemistry C* 121.49 (2017), pp. 27256–27262. DOI: 10.1021/acs.jpcc.7b05517.

[40] W. Hu et al. “Germanium / perovskite heterostructure for high-performance and broadband photodetector from visible to infrared telecommunication band”. In: *Light: Science and Applications* 8 (2019), p. 106. DOI: 10.1038/s41377-019-0218-y.

[41] E. López-Fraguas et al. “Visible Light Communication system using an organic emitter and a perovskite photodetector”. In: *Organic Electronics* 73 (2019), pp. 292–298. DOI: 10.1016/j.orgel.2019.06.028.

[42] Y. Yang et al. “All-Perovskite Photodetector with Fast Response”. In: *Nanoscale Research Letters* 14 (2019), p. 291. DOI: 10.1186/s11671-019-3082-z.

[43] K. Lin et al. “Perovskite light-emitting diodes with external quantum efficiency exceeding 20 percent”. In: *Nature* 562 (2018), pp. 245–248. DOI: 10.1038/s41586-018-0575-3.

[44] H. Kim et al. “Optically Pumped Lasing from Hybrid Perovskite Light-Emitting Diodes”. In: *Advanced Optical Materials* 8.1 (2019), p. 1901297. DOI: 10.1002/adom.201901297.

[45] C. Li, Z. Liu, Q. Shang, and Q. Zhang. “Surface-Plasmon-Assisted Metal Halide Perovskite Small Lasers”. In: *Advanced Optical Materials* 7.17 (2019), p. 1900279. DOI: 10.1002/adom.201900279.

[46] W. Yu et al. “Single crystal hybrid perovskite field-effect transistors”. In: *Nature Communications* 9 (2018), p. 5354. DOI: 10.1038/s41467-018-07706-9.

[47] T. Wu, W. Pisula, M. Yusoff, A. Rashid, and P. Gao. “Application of Perovskite-Structured Materials in Field-Effect Transistors”. In: *Advanced Electronic Materials* 5.12 (2019), p. 1900444. DOI: 10.1002/aelm.201900444.

[48] J. Choi et al. “Organolead Halide Perovskites for Low Operating Voltage Multilevel Resistive Switching”. In: *Advanced Materials* 28.31 (2016), pp. 6562–6567. DOI: 10.1002/adma.201600859.

[49] X. Guan et al. “Light-Responsive Ion-Redistribution-Induced Resistive Switching in Hybrid Perovskite Schottky Junctions”. In: *Advanced Functional Materials* 28 (2018), p. 1704665. DOI: 10.1002/adfm.201704665.

[50] S. A. Veldhuis et al. “Perovskite Materials for Light-Emitting Diodes and Lasers”. In: *Advanced Materials* 28 (2016), pp. 6804–6834. DOI: 10.1002/adma.201600669.

[51] S. D. Stranks and H. J. Snaith. “Metal-halide perovskites for photovoltaic and light-emitting devices”. In: *Nature Nanotechnology* 10.5 (2015), pp. 391–402. DOI: 10.1038/nnano.2015.90.

[52] Q. Dong, L. Lei, J. Mendes, and F. So. “Operational stability of perovskite light emitting diodes”. In: *Journal of Physics: Materials* 3 (2020), p. 012002. DOI: 10.1088/2515-7639/ab60c4.

[53] J. Li et al. “High-Throughput Combinatorial Optimizations of Perovskite Light-Emitting Diodes Based on All-Vacuum Deposition”. In: *Advanced Functional Materials* 29.51 (2019), p. 1903607. DOI: 10.1002/adfm.201903607.

[54] C.-h. A. Li, Z. Zhou, P. Vashishtha, and J. E. Halpert. “The future is blue (LEDs): why chemistry is the key to perovskite displays”. In: *Chemistry of Materials* 31.16 (2019), pp. 6003–6032. DOI: 10.1021/acs.chemmater.9b01650.

[55] Q. V. Le, H. W. Jang, and S. Y. Kim. “Recent Advances toward High-Efficiency Halide Perovskite Light-Emitting Diodes : Review and Perspective”. In: *Small Methods* 2 (2018), p. 1700419. DOI: 10.1002/smtd.201700419.

[56] Y. Cao et al. “Perovskite light-emitting diodes based on spontaneously formed submicrometre-scale structures”. In: *Nature* 562 (2018), p. 249. DOI: 10.1038/s41586-018-0576-2.

[57] A. Babayigit, A. Ethirajan, M. Muller, and B. Conings. “Toxicity of organometal halide perovskite solar cells”. In: *Nature Materials* 15.3 (2016), pp. 247–251. DOI: 10.1038/nmat4572.

[58] W. Ke and M. G. Kanatzidis. “Prospects for low-toxicity lead-free perovskite solar cells”. In: *Nature Communications* 10 (2019), p. 965. DOI: 10.1038/s41467-019-08918-3.

[59] S. He, L. Qiu, L. K. Ono, and Y. Qi. “How far are we from attaining 10-year lifetime for metal halide perovskite solar cells?” In: *Materials Science and Engineering* 140 (2020), p. 100545. DOI: 10.1016/j.mser.2020.100545.

[60] C. C. Stoumpos, C. D. Malliakas, and M. G. Kanatzidis. “Semiconducting Tin and Lead Iodide Perovskites with Organic Cations: Phase Transitions, High Mobilities, and Near-Infrared Photoluminescent Properties”. In: *Inorganic Chemistry* 52.15 (2013), pp. 9019–9038. DOI: 10.1021/ic401215x.

[61] C. Ma et al. “2D/3D Perovskite Hybrids as Moisture-Tolerant and Efficient Light Absorbers for Solar Cells”. In: *Nanoscale* 8.43 (2016), pp. 18309–18314. DOI: 10.1039/C6NR04741F.

[62] T. Zhou et al. “Highly Efficient and Stable Solar Cells Based on Crystalline Oriented 2D/3D Hybrid Perovskite”. In: *Advanced Materials* 31.32 (2019), p. 1901242. DOI: 10.1002/adma.201901242.

[63] X. Yang et al. “Efficient green light-emitting diodes based on quasi-two-dimensional composition and phase engineered perovskite with surface passivation”. In: *Nature Communications* 9 (2018), p. 570. DOI: 10.1038/s41467-018-02978-7.

[64] N. Wang et al. “Perovskite light-emitting diodes based on solution-processed self-organized multiple quantum wells”. In: *Nature Photonics* 10 (2016), p. 699. DOI: 10.1038/nphoton.2016.185.

[65] A. H. Proppe et al. “Photochemically Cross-Linked Quantum Well Ligands for 2D/3D Perovskite Photovoltaics with Improved Photovoltage and Stability”. In: *Journal of the American Chemical Society* 141.36 (2019), pp. 14180–14189. DOI: 10.1021/jacs.9b05083.

[66] C. Li et al. “Formability of ABX_3 (X = F, Cl, Br, I) halide perovskites”. In: *Acta Crystallographica Section B: Structural Science* 64.6 (2008), pp. 702–707. DOI: 10.1107/S0108768108032734.

[67] D. Ray et al. “Computational Study of Structural and Electronic Properties of Lead-Free $CsMI_3$ Perovskites (M = Ge, Sn, Pb, Mg, Ca, Sr, Ba)”. In: *The Journal of Physical Chemistry C* 122 (2018), 78387848. DOI: 10.1021/acs.jpcc.8b00226.

[68] A. Poglitsch and D. Weber. “Dynamic disorder in methylammoniumtrihalogenoplumbates (II) observed by millimeter-wave spectroscopy”. In: *The Journal of Chemical Physics* 87.11 (1987), pp. 6373–6378. DOI: 10.1063/1.453467.

[69] P. S. Whitfield et al. “Structures, Phase Transitions and Tricritical Behavior of the Hybrid Perovskite Methyl Ammonium Lead Iodide”. In: *Scientific Reports* 6 (2016), p. 35685. DOI: 10.1038/srep35685.

[70] T. Baikie et al. “Synthesis and crystal chemistry of the hybrid perovskite $(CH_3NH_3)PbI_3$ for solid-state sensitised solar cell applications”. In: *Journal of Materials Chemistry A* 1.18 (2013), p. 5628. DOI: 10.1039/c3ta10518k.

[71] X. Lü et al. “Enhanced Structural Stability and Photo Responsiveness of $CH_3NH_3SnI_3$ Perovskite via Pressure-Induced Amorphization and Recrystallization”. In: *Advanced Materials* (2016), pp. 3–8. DOI: 10.1002/adma.201600771.

[72] C. Ferrara et al. “Wide band-gap tuning in Sn-based hybrid perovskites through cation replacement: The $FA_{1-X}MA_xSnBr_3$ mixed system”. In: *Journal of Materials Chemistry A* 5.19 (2017), pp. 9391–9395. DOI: 10.1039/c7ta01668a.

[73] E. C. Schueller et al. “Crystal Structure Evolution and Notable Thermal Expansion in Hybrid Perovskites Formamidinium Tin Iodide and Formamidinium Lead Bromide”. In: *Inorganic Chemistry* 57.2 (2018), pp. 695–701. DOI: 10.1021/acs.inorgchem.7b02576.

[74] D. H. Fabini et al. “Reentrant Structural and Optical Properties and Large Positive Thermal Expansion in Perovskite Formamidinium Lead Iodide”. In: *Angewandte Chemie - International Edition* 55.49 (2016), pp. 15392–15396. DOI: 10.1002/anie.201609538.

[75] S. Cho and S. H. Yun. “Structure and optical properties of perovskite-embedded dual-phase microcrystals synthesized by sonochemistry”. In: *Communications Chemistry* 3.1 (2020). DOI: 10.1038/s42004-020-0265-6.

[76] A. M. Leguy et al. “The dynamics of methylammonium ions in hybrid organic-inorganic perovskite solar cells”. In: *Nature Communications* 6 (2015), p. 7124. DOI: 10.1038/ncomms8124.

[77] C. Quarti et al. “The raman spectrum of the $CH_3NH_3PbI_3$ hybrid perovskite: Interplay of theory and experiment”. In: *Journal of Physical Chemistry Letters* 5.2 (2014), pp. 279–284. DOI: 10.1021/jz402589q.

[78] S. de Wolf et al. “Organometallic Halide Perovskites: Sharp Optical Absorption Edge and Its Relation to Photovoltaic Performance”. In: *The Journal of Physical Chemistry Letters* 5 (2014), pp. 1035–1039. DOI: 10.1021/jz500279b.

[79] K. Tvingstedt et al. “Radiative efficiency of lead iodide based perovskite solar cells”. In: *Nature Scientific Reports* 4 (2014), pp. 1–7. DOI: 10.1038/srep06071.

[80] D. Shi et al. “Low trap-state density and long carrier diffusion in organolead trihalide perovskite single crystals”. In: *Science* 347.6221 (2015), pp. 519–522. DOI: 10.1126/science.aaa2725.

[81] D. M. Jang et al. “Reversible Halide Exchange Reaction of Organometal Trihalide Perovskite Colloidal Nanocrystals for Full-Range Band Gap Tuning”. In: *Nano Letters* 15.8 (2015), pp. 5191–5199. DOI: 10.1021/acs.nanolett.5b01430.

[82] W. J. Yin, T. Shi, and Y. Yan. “Superior photovoltaic properties of lead halide perovskites: Insights from first-principles theory”. In: *Journal of Physical Chemistry C* 119.10 (2015), pp. 5253–5264. DOI: 10.1021/jp512077m.

[83] Z. Yang et al. “Stable Low-Bandgap Pb-Sn Binary Perovskites for Tandem Solar Cells”. In: *Advanced Materials* 28.40 (2016), pp. 8990–8997. DOI: https://doi.org/10.1002/adma.201602696.

[84] J. H. Noh, S. H. Im, J. H. Heo, T. N. Mandal, and S. I. Seok. “Chemical management for colorful, efficient, and stable inorganic-organic hybrid nanostructured solar cells”. In: *Nano Letters* 13.4 (2013), pp. 1764–1769. DOI: 10.1021/nl400349b.

[85] S. Meloni, G. Palermo, N. Ashari-Astani, M. Grätzel, and U Rothlisberger. “Valence and conduction band tuning in halide perovskites for solar cell applications”. In: *J. Mater. Chem. A* 4 (2016), pp. 15997–16002. DOI: 10.1039/C6TA04949D.

[86] B. Abdollahi Nejand et al. “Vacuum-Assisted Growth of Low-Bandgap Thin Films ($FA_{0.8}MA_{0.2}Sn_{0.5}Pb_{0.5}I_3$) for All-Perovskite Tandem Solar Cells”. In: *Advanced Energy Materials* 10 (2020), p. 1902583. DOI: 10.1002/aenm.201902583.

[87] R. Prasanna et al. “Band Gap Tuning via Lattice Contraction and Octahedral Tilting in Perovskite Materials for Photovoltaics”. In: *Journal of the American Chemical Society* 139.32 (2017), pp. 11117–11124. DOI: 10.1021/jacs.7b04981.

[88] S. Adjokatse, H. H. Fang, and M. A. Loi. “Broadly tunable metal halide perovskites for solid-state light-emission applications”. In: *Materials Today* 20.8 (2017), pp. 413–424. DOI: 10.1016/j.mattod.2017.03.021.

[89] L. N. Quan et al. “Highly Emissive Green Perovskite Nanocrystals in a Solid State Crystalline Matrix”. In: *Advanced Materials* 29.21 (2017), p. 1605945. DOI: 10.1002/adma.201605945.

[90] H Cho et al. “Overcoming the electroluminescence efficiency limitations of perovskite light-emitting diodes”. In: *Science* 350.6265 (2015), pp. 1222–1225. DOI: 10.1126/science.aad1818.

[91] Y. H. Kim et al. “Highly Efficient Light-Emitting Diodes of Colloidal Metal-Halide Perovskite Nanocrystals beyond Quantum Size”. In: *ACS Nano* 11.7 (2017), pp. 6586–6593. DOI: 10.1021/acsnano.6b07617.

[92] X. Gong et al. “Electron-phonon interaction in efficient perovskite blue emitters”. In: *Nature Materials* 17.6 (2018), pp. 550–556. DOI: 10.1038/s41563-018-0081-x.

[93] D. A. Egger et al. “What Remains Unexplained about the Properties of Halide Perovskites?” In: *Advanced Materials* 30.20 (2018), p. 1800691. DOI: 10.1002/adma.201800691.

[94] Z. Yang et al. “Unraveling the Exciton Binding Energy and the Dielectric Constant in Single-Crystal Methylammonium Lead Triiodide Perovskite”. In: *Journal of Physical Chemistry Letters* 8.8 (2017), pp. 1851–1855. DOI: 10.1021/acs.jpclett.7b00524.

[95] M. Sendner et al. “Optical Phonons in Methylammonium Lead Halide Perovskites and Implications for Charge Transport”. In: *Materials Horizons* (2016), pp. 613–620. DOI: 10.1039/C6MH00275G.

[96] M. Saba et al. “Correlated electron-hole plasma in organometal perovskites.” In: *Nature communications* 5 (2014), p. 5049. DOI: 10.1038/ncomms6049.

[97] A. Miyata et al. “Direct measurement of the exciton binding energy and effective masses for charge carriers in organic-inorganic tri-halide perovskites”. In: *Nature Physics* 11.7 (2015), pp. 582–587. DOI: 10.1038/nphys3357.

[98] K. Zheng et al. “Exciton Binding Energy and the Nature of Emissive States in Organometal Halide Perovskites”. In: *The Journal of Physical Chemistry Letters* 6.15 (2015), pp. 2969–2975. DOI: 10.1021/acs.jpclett.5b01252.

[99] N. Wang et al. “Perovskite light-emitting diodes based on solution-processed self-organized multiple quantum wells”. In: *Nature Photonics* 10.11 (2016), pp. 699–704. DOI: 10.1038/nphoton.2016.185.

[100] Y. Tamai, H. Ohkita, H. Benten, and S. Ito. “Exciton Diffusion in Conjugated Polymers: From Fundamental Understanding to Improvement in Photovoltaic Conversion Efficiency”. In: *The Journal of Physical Chemistry Letters* 6.17 (2015), pp. 3417–3428. DOI: 10.1021/acs.jpclett.5b01147.

[101] S. M. Menke and R. J. Holmes. “Exciton diffusion in organic photovoltaic cells”. In: *Energy and Environmental Science* 7.2 (2014), p. 499. DOI: 10.1039/c3ee42444h.

[102] Y. Zou, J. Holst, Y. Zhang, and R. J. Holmes. “7.9based on a simple bulk heterojunction”. In: *Journal of Materials Chemistry A* 2.31 (2014), p. 12397. DOI: 10.1039/C4TA02137A.

[103] I. Mora-Seró. “How Do Perovskite Solar Cells Work?” In: *Joule* 2.4 (2018), pp. 585–587. DOI: 10.1016/j.joule.2018.03.020.

[104] L. Bertoluzzi et al. “Mobile Ion Concentration Measurement and Open-Access Band Diagram Simulation Platform for Halide Perovskite Solar Cells”. In: *Joule* 4.1 (2020), pp. 109–127. DOI: 10.1016/j.joule.2019.10.003.

[105] T. M. Brenner et al. “Are Mobilities in Hybrid Organic-Inorganic Halide Perovskites Actually ”high”?” In: *Journal of Physical Chemistry Letters* 6.23 (2015), pp. 4754–4757. DOI: 10.1021/acs.jpclett.5b02390.

[106] G. Giorgi, J. I. Fujisawa, H. Segawa, and K. Yamashita. “Small photocarrier effective masses featuring ambipolar transport in methylammonium lead iodide perovskite: A density functional analysis”. In: *Journal of Physical Chemistry Letters* 4.24 (2013), pp. 4213–4216. DOI: 10.1021/jz4023865.

[107] J. S. Manser, A Christians, and P. V. Kamat. “Intriguing Optoelectronic Properties of Metal Halide Perovskites”. In: *Chemical Reviews* 116 (2016), pp. 12956–13008. DOI: 10.1021/acs.chemrev.6b00136.

[108] S. D. Stranks et al. “Electron-Hole Diffusion Lengths Exceeding 1 Micrometer in an Organometal Trihalide Perovskite Absorber”. In: *Science Reports* 342 (2013), pp. 341–345. DOI: 10.1126/science.1243982.

[109] C. Wehrenfennig, G. E. Eperon, M. B. Johnston, H. J. Snaith, and L. M. Herz. “High charge carrier mobilities and lifetimes in organolead trihalide perovskites”. In: *Advanced Materials* 26.10 (2014), pp. 1584–1589. DOI: 10.1002/adma.201305172.

[110] Y. Zhai et al. “Individual Electron and Hole Mobilities in Lead-Halide Perovskites Revealed by Noncontact Methods”. In: *ACS Energy Letters* 5.1 (2020), pp. 47–55. DOI: 10.1021/acsenergylett.9b02310.

[111] E. M. Hutter et al. “Vapour-Deposited Cesium Lead Iodide Perovskites: Microsecond Charge Carrier Lifetimes and Enhanced Photovoltaic Performance”. In: *ACS Energy Letters* 2 (2017), pp. 1901–1908. DOI: 10.1021/acsenergylett.7b00591.

[112] A. R. Bowman et al. “Microsecond Carrier Lifetimes, Controlled p-Doping, and Enhanced Air Stability in Low-Bandgap Metal Halide Perovskites”. In: *ACS Energy Letters* 4.9 (2019), pp. 2301–2307. DOI: 10.1021/acsenergylett.9b01446.

[113] Q. Dong et al. “Electron-hole diffusion lengths $>$175 um in solution-grown $CH_3NH_3PbI_3$ single crystals”. In: *Science* 347.6225 (2015), pp. 967–970. DOI: 10.1126/science.aaa5760.

[114] J. Kang and L. W. Wang. "High Defect Tolerance in Lead Halide Perovskite $CsPbBr_3$". In: *Journal of Physical Chemistry Letters* 8.2 (2017), pp. 489–493. DOI: 10.1021/acs.jpclett.6b02800.

[115] W.-J. Yin, T. Shi, and Y. Yan. "Unusual defect physics in $CH_3NH_3PbI_3$ perovskite solar cell absorber". In: *Applied Physics Letters* 104.6 (2014). DOI: 10.1063/1.4864778.

[116] T. Leijtens et al. "Carriers Trapping and Recombination: the Role of Defect Physics in Enhancing the Open Circuit Voltage of Metal Halide Perovskite Solar Cells". In: *Energy Environ. Sci.* 9.11 (2016), pp. 3472–3481. DOI: 10.1039/C6EE01729K.

[117] W. Chu, Q. Zheng, O. V. Prezhdo, J. Zhao, and W. A. Saidi. "Low-frequency lattice phonons in halide perovskites explain high defect tolerance toward electron-hole recombination". In: *Science Advances* 6.7 (2020), eaaw7453. DOI: 10.1126/sciadv.aaw7453.

[118] Q. Wang et al. "Qualifying composition dependent p and n self-doping in $CH_3NH_3PbI_3$". In: *Applied Physics Letters* 105.16 (2014). DOI: 10.1063/1.4899051.

[119] P. Cui et al. "Planar p-n homojunction perovskite solar cells with efficiency exceeding 21.3%". In: *Nature Energy* 4 (2019), pp. 150–159. DOI: 10.1038/s41560-018-0324-8.

[120] K. Wang, W. S. Subhani, Y. Wang, X. Zuo, and H. Wang. "Metal Cations in Efficient Perovskite Solar Cells : Progress and Perspective". In: *Advanced Materials* (2019), p. 1902037. DOI: 10.1002/adma.201902037.

[121] K. Xu and A. Meijerink. "Tuning Exciton-Mn2+ Energy Transfer in Mixed Halide Perovskite Nanocrystals". In: *Chemistry of Materials* (2018). DOI: 10.1021/acs.chemmater.8b02157.

[122] S. Zou et al. "Stabilizing Cesium Lead Halide Perovskite Lattice through Mn (II)-Substitution for Air-Stable Light-Emitting Diodes". In: *Journal of the American Chemical Society* Ii (2017), jacs.7b04000. DOI: 10.1021/jacs.7b04000.

[123] S. P. Senanayak et al. "A general approach for hysteresis-free, operationally stable metal halide perovskite field-effect transistors". In: *Science Advances* 6.15 (2020), eaaz4948. DOI: 10.1126/sciadv.aaz4948.

[124] P. Yadav et al. “The Role of Rubidium in Multiple-Cation-Based High-Efficiency Perovskite Solar Cells”. In: *Advanced Materials* 3 (2017), p. 1701077. DOI: 10.1002/adma.201701077.

[125] H. J. Snaith et al. “Anomalous hysteresis in perovskite solar cells”. In: *Journal of Physical Chemistry Letters* 5.9 (2014), pp. 1511–1515. DOI: 10.1021/jz500113x.

[126] D. Seol et al. “Origin of Hysteresis in $CH_3NH_3PbI_3$ Perovskite Thin Films”. In: *Advanced Functional Materials* 27.37 (2017), p. 1701924. DOI: 10.1002/adfm.201701924.

[127] E. L. Unger et al. “Hysteresis and transient behavior in current-voltage measurements of hybrid-perovskite absorber solar cells”. In: *Energy Environ. Sci.* 7.11 (2014), pp. 3690–3698. DOI: 10.1039/C4EE02465F.

[128] D. Y. Son et al. “Universal Approach toward Hysteresis-Free Perovskite Solar Cell via Defect Engineering”. In: *Journal of the American Chemical Society* 140.4 (2018), pp. 1358–1364. DOI: 10.1021/jacs.7b10430.

[129] C. Li, A. Guerrero, Y. Zhong, and S. Huettner. “Origins and Mechanisms of Hysteresis in Organometal Halide Perovskites”. In: *Journal of Physics: Condensed Matter* 29.19 (2017), p. 193001. DOI: https://doi.org/10.1088/1361-648X/aa626d.

[130] S. Van Reenen, M. Kemerink, and H. J. Snaith. “Modeling Anomalous Hysteresis in Perovskite Solar Cells”. In: *Journal of Physical Chemistry Letters* 6.19 (2015), pp. 3808–3814. DOI: 10.1021/acs.jpclett.5b01645.

[131] M. T. Neukom et al. “Why perovskite solar cells with high efficiency show small IV-curve hysteresis”. In: *Solar Energy Materials and Solar Cells* 169 (2017), pp. 159–166. DOI: 10.1016/j.solmat.2017.05.021.

[132] J.-W. Lee et al. “The Interplay between Trap Density and Hysteresis in Planar Heterojunction Perovskite Solar Cells”. In: *Nano Letters* 17.7 (2017), pp. 4270–4276. DOI: 10.1021/acs.nanolett.7b01211.

[133] S. A. Weber et al. “How the formation of interfacial charge causes hysteresis in perovskite solar cells”. In: *Energy and Environmental Science* 11.9 (2018), pp. 2404–2413. DOI: 10.1039/c8ee01447g.

[134] Y. Zou and R. J. Holmes. “Temperature-Dependent Bias Poling and Hysteresis in Planar Organo-Metal Halide Perovskite Photovoltaic Cells”. In: *Advanced Energy Materials* 6.7 (2016), p. 1501994. DOI: 10.1002/aenm.201501994.

[135] S. P. Dunfield et al. “From Defects to Degradation: A Mechanistic Understanding of Degradation in Perovskite Solar Cell Devices and Modules”. In: *Advanced Energy Materials* 2 (2020), p. 1904054. DOI: 10.1002/aenm.201904054.

[136] K. Domanski, E. A. Alharbi, A. Hagfeldt, M. Grätzel, and W. Tress. “Systematic investigation of the impact of operation conditions on the degradation behaviour of perovskite solar cells”. In: *Nature Energy* 3 (2018), pp. 61–67. DOI: 10.1038/s41560-017-0060-5.

[137] Q. Wali et al. “Advances in stability of perovskite solar cells”. In: *Organic Electronics* 78 (2020), p. 105590. DOI: 10.1016/j.orgel.2019.105590.

[138] J. A. Christians et al. “Tailored interfaces of unencapsulated perovskite solar cells for >1,000 hour operational stability”. In: *Nature Energy* 3 (2018), pp. 68–74. DOI: 10.1038/s41560-017-0067-y.

[139] O. R. Yamilova et al. “Reduction of methylammonium cations as a major electrochemical degradation pathway in $MAPbI_3$ perovskite solar cells”. In: *The Journal of Physical Chemistry Letters* 11.1 (2020), pp. 221–228. DOI: 10.1021/acs.jpclett.9b03161.

[140] F. Hao, C. C. Stoumpos, D. H. Cao, R. P. H. Chang, and M. G. Kanatzidis. “Lead-free solid-state organic–inorganic halide perovskite solar cells”. In: *Nature Photonics* 8.6 (2014), pp. 489–494. DOI: 10.1038/nphoton.2014.82.

[141] E. S. Parrott et al. “Effect of Structural Phase Transition on Charge-Carrier Lifetimes and Defects in CH¡sub¿3¡/sub¿NH¡sub¿3¡/sub¿SnI¡sub¿3¡/sub¿ Perovskite”. In: *Journal of Physical Chemistry Letters* 7 (2016), pp. 1321–1326. DOI: 10.1021/acs.jpclett.6b00322.

[142] F. Hao et al. “Solvent-Mediated Crystallization of $CH_3NH_3SnI_3$ Films for Heterojunction Depleted Perovskite Solar Cells”. In: *Journal of the American Chemical Society* 137.35 (2015), pp. 11445–11452. DOI: 10.1021/jacs.5b06658.

[143] N. K. Noel et al. “Lead-Free Organic-Inorganic Tin Halide Perovskites for Photovoltaic Applications”. In: *Energy and Environmental Science* 7 (2014), pp. 3061–3068. DOI: 10.1039/C4EE01076K.

[144] T. Leijtens, R. Prasanna, A. Gold-Parker, M. F. Toney, and M. D. McGehee. “Mechanism of Tin Oxidation and Stabilization by Lead Substitution in Tin Halide Perovskites”. In: *ACS Energy Letters* 2.9 (2017), pp. 2159–2165. DOI: 10.1021/acsenergylett.7b00636.

[145] S. H. Turren-Cruz, A. Hagfeldt, and M. Saliba. “Methylammonium-free, high- performance, and stable perovskite solar cells on a planar architecture”. In: *Science* 362.6413 (2018), pp. 449–453. DOI: 10.1126/science.aat3583.

[146] Q. Sun et al. “Role of Microstructure in Oxygen Induced Photodegradation of Methylammonium Lead Triiodide Perovskite Films”. In: *Advanced Energy Materials* (2017), p. 1700977. DOI: 10.1002/aenm.201700977.

[147] J. J. Yoo et al. “An interface stabilized perovskite solar cell with high stabilized efficiency and low voltage loss”. In: *Energy and Environmental Science* 12 (2019), pp. 2192–2199. DOI: 10.1039/c9ee00751b.

[148] Z. Huang et al. “Water-Resistant and Flexible Perovskite Solar Cells via a Glued Interfacial Layer”. In: *Advanced Functional Materials* 29.37 (2019), p. 1902629. DOI: 10.1002/adfm.201902629.

[149] Y. Liu et al. “Ultrahydrophobic 3D/2D fluoroarene bilayer-based water-resistant perovskite solar cells with efficiencies exceeding 22%”. In: *Science Advances* 5.6 (2019), eaaw2543. DOI: 10.1126/sciadv.aaw2543.

[150] G Grancini, I Zimmermann, E Mosconi, D Martineau, and S Narbey. “One-Year stable perovskite solar cells by 2D / 3D interface engineering”. In: *Nature communications* 14 (2017), pp. 1–8. DOI: 10.1038/ncomms15684.

[151] A. K. Jena, Y. Numata, M. Ikegami, and T. Miyasaka. “Notorious Role of Spiro-OMeTAD in Performance Deterioration of Perovskite Solar Cells at High Temperature and Reuse of the Perovskite Films to Avoid Pb-waste”. In: *Journal of Materials Chemistry A* 6.5 (2018), pp. 2219–2230. DOI: 10.1039/C7TA07674F.

[152] G.-H. Kim et al. “Fluorine Functionalized Graphene Nano Platelets for Highly Stable Inverted Perovskite Solar Cells”. In: *Nano Letters* 17.10 (2017), pp. 6385–6390. DOI: 10.1021/acs.nanolett.7b03225.

[153] Q. Luo et al. “Carbon Nanotube Based Inverted Flexible Perovskite Solar Cells with All-Inorganic Charge Contacts”. In: *Advanced Functional Materials* 27.42 (2017), p. 1703068. DOI: 10.1002/adfm.201703068.

[154] S. S. Shin, S. J. Lee, and S. I. Seok. “Metal Oxide Charge Transport Layers for Efficient and Stable Perovskite Solar Cells”. In: *Advanced Functional Materials* 29.47 (2019), p. 1900455. DOI: 10.1002/adfm.201900455.

[155] K. Wang, X. Liu, R. Huang, C. Wu, and D. Yang. “Nonionic Sc3N@C80 Dopant for Efficient and Stable Halide Perovskite Photovoltaics”. In: *ACS Energy Letters* 4.8 (2019), pp. 1852–1861. DOI: 10.1021/acsenergylett.9b01042.

[156] K. Schutt et al. “Overcoming Zinc Oxide Interface Instability with a Methylammonium-Free Perovskite for High-Performance Solar Cells”. In: *Advanced Functional Materials* 29.47 (2019), p. 1900466. DOI: 10.1002/adfm.201900466.

[157] X. Jin et al. “$Cu_{2-x}GeS_3$: A New Hole Transporting Material for Stable and Efficient Perovskite Solar Cell”. In: *Journal of Materials Chemistry A* 5.37 (2017), pp. 19884–19891. DOI: 10.1039/C7TA06088B.

[158] H. Back et al. “Achieving long-term stable perovskite solar cells via ion neutralization”. In: *Energy Environ. Sci.* 9.4 (2016), pp. 1258–1263. DOI: 10.1039/C6EE00612D.

[159] Y. Yao et al. “The interface degradation of planar organic–inorganic perovskite solar cell traced by light beam induced current (LBIC)”. In: *RSC Adv.* 7.68 (2017), pp. 42973–42978. DOI: 10.1039/C7RA06423C.

[160] X. Li et al. “On-device lead sequestration for perovskite solar cells”. In: *Nature* 578 (2019), pp. 555–558. DOI: 10.1038/s41586-020-2001-x.

[161] L. Chouhan, S. Ghimire, C. Subrahmanyam, T. Miyasaka, and V. Biju. “Synthesis, optoelectronic properties and applications of halide perovskites”. In: *Chemical Society Reviews* 49.10 (2020), pp. 2869–2885. DOI: 10.1039/c9cs00848a.

[162] J. J. Choi, X. Yang, Z. M. Norman, S. J. L. Billinge, and J. S. Owen. “Structure of methylammonium lead iodide within mesoporous titanium dioxide: Active material in high-performance perovskite solar cells”. In: *Nano Letters* 14.1 (2014), pp. 127–133. DOI: 10.1021/nl403514x.

[163] F. Huang, M. Li, P. Siffalovic, G. Cao, and J. Tian. “From scalable solution fabrication of perovskite films towards commercialization of solar cells”. In: *Energy Environmental Science* (2019). DOI: 10.1039/C8EE03025A.

[164] K. Wojciechowski, M. Saliba, T. Leijtens, A. Abate, and H. J. Snaith. “Sub-150C processed meso-superstructured perovskite solar cells with enhanced efficiency”. In: *Energy Environmental Science* 7.3 (2014), pp. 1142–1147. DOI: 10.1039/C3EE43707H.

[165] W Zhang et al. “Ultrasmooth organic-inorganic perovskite thin-film formation and crystallization for efficient planar heterojunction solar cells”. In: *Nature Communications Commun* 6 (2015), p. 6142. DOI: 10.1038/ncomms7142.

[166] J. Burschka et al. “Sequential deposition as a route to high-performance perovskite-sensitized solar cells”. In: *Nature* 499.7458 (2013), pp. 316–320. DOI: 10.1038/nature12340.

[167] Y.-H. Chiang, H.-M. Cheng, M.-H. Li, T.-F. Guo, and P. Chen. “Low-Pressure Vapor-Assisted Solution Process for Thiocyanate-Based Pseudohalide Perovskite Solar Cells”. In: *ChemSusChem* 9 (2016), p. 2620. DOI: 10.1002/cssc.201600674.

[168] Q. Chen et al. “Planar heterojunction perovskite solar cells via vapor-assisted solution process.” In: *Journal of the American Chemical Society* 136.2 (2014), pp. 622–625. DOI: 10.1021/ja411509g.

[169] A Bahtiar, S Rahmanita, and Y. D. Inayatie. “Pin-Hole Free Perovskite Film for Solar Cells Application Prepared by Controlled Two-Step Spin-Coating Method”. In: *IOP Conference Series: Materials Science and Engineering* 196 (2017), p. 12037. DOI: 10.1088/1757-899X/196/1/012037.

[170] X. Lian et al. “Highly Efficient Sn / Pb Binary Perovskite Solar Cell via Precursor Engineering: A Two-Step Fabrication Process”. In: *Advanced Functional Materials* 1807024 (2019), p. 1807024. DOI: 10.1002/adfm.201807024.

[171] Y. Cui, C. Chen, C. Li, L. Chen, and S. S. Bista. “Correlating Hysteresis and Stability with Organic Cation Composition in the Two-Step Solution-Processed Perovskite Solar Cells”. In: *Applied Materials and Interfaces* 12.9 (2020), pp. 10588–10596. DOI: 10.1021/acsami.9b23374.

[172] L. Qiu, L. K. Ono, and Y. Qi. “Advances and challenges to the commercialization of organic-inorganic halide perovskite solar cell technology”. In: *Materials Today Energy* 7 (2018), pp. 169–189. DOI: 10.1016/j.mtener.2017.09.008.

[173] M. Mateen, Z. Arain, Y. Yang, and X. Liu. “MACl Induced Intermediate Engineering for High- performance Mixed Cation Perovskite Solar Cells”. In: *Applied Materials and Interfaces* 12.9 (2020), pp. 10535–10543. DOI: 10.1021/acsami.9b22719.

[174] M.-j. Choi et al. “Functional additives for high-performance inverted planar perovskite solar cells with exceeding 20% efficiency: selective complexation of organic cations in precursors”. In: *Nano Energy* 71 (2020), p. 104639. DOI: 10.1016/j.nanoen.2020.104639.

[175] M. Xiao et al. “A fast deposition-crystallization procedure for highly efficient lead iodide perovskite thin-film solar cells”. In: *Angewandte Chemie - International Edition* 53.37 (2014), pp. 9898–9903. DOI: 10.1002/anie.201405334.

[176] J. Baker et al. “High throughput fabrication of mesoporous carbon perovskite solar cells”. In: *J. Mater. Chem. A* (2017). DOI: 10.1039/C7TA05674E.

[177] A. Gheno et al. “Toward Highly Efficient Inkjet-Printed Perovskite Solar Cells Fully Processed Under Ambient Conditions and at Low Temperature”. In: *Solar RRL* 2.11 (2018), pp. 1–8. DOI: 10.1002/solr.201800191.

[178] R. Patidar, D. Burkitt, K. Hooper, D. Richards, and T. Watson. “Slot-die coating of perovskite solar cells: An overview”. In: *Materials Today Communications* 22 (2020), p. 100808. DOI: 10.1016/j.mtcomm.2019.100808.

[179] S. Razza et al. “In situ X-ray scattering of perovskite solar cell active layers roll-to-roll coated on flexible substrates”. In: *CrystEngComm* 26.24 (2016), pp. 44034–44040. DOI: 10.1039/C6EE02100J.

[180] F. Guo et al. “A Generalized Crystallization Protocol for Scalable Deposition of High-Quality Perovskite Thin Films for Photovoltaic Applications”. In: *Advanced Science* 6.17 (2019), p. 1901067. DOI: 10.1002/advs.201901067.

[181] S. Tang et al. “Composition Engineering in Doctor-Blading of Perovskite Solar Cells”. In: *Advanced Energy Materials* 7.18 (2017), p. 1700302. DOI: 10.1002/aenm.201700302.

[182] D. K. Mohamad, J. Griffin, C. Bracher, A. T. Barrows, and D. G. Lidzey. “Spray-Cast Multilayer Organometal Perovskite Solar Cells Fabricated in Air”. In: *Advanced Energy Materials* (2016), p. 1600994. DOI: 10.1002/aenm.201600994.

[183] J. E. Bishop, D. K. Mohamad, M. Wong-Stringer, A. Smith, and D. G. Lidzey. “Spray-cast multilayer perovskite solar cells with an active-area of 1.5 cm^2”. In: *Scientific Reports* 7 (2017), p. 7962. DOI: 10.1038/s41598-017-08642-2.

[184] F. Ye et al. “Low-Temperature Soft-Cover Deposition of Uniform Large-Scale Perovskite Films for High-Performance Solar Cells”. In: *Advanced Materials* 1701440 (2017), p. 1701440. DOI: 10.1002/adma.201701440.

[185] M. Adnan and J. K. Lee. “All Sequential Dip-Coating Processed Perovskite Layers from an Aqueous Lead Precursor for High Efficiency Perovskite Solar Cells”. In: *Scientific Reports* 8.1 (2018), pp. 1–10. DOI: 10.1038/s41598-018-20296-2.

[186] M. Adnan and J. K. Lee. “Highly efficient planar heterojunction perovskite solar cells with sequentially dip-coated deposited perovskite layers from a non-halide aqueous lead precursor”. In: *RSC Advances* 10.9 (2020), pp. 5454–5461. DOI: 10.1039/c9ra09607h.

[187] J. Li et al. “Highly Efficient Thermally Co-evaporated Perovskite Solar Cells and Mini-modules”. In: *Joule* 4.5 (2020), pp. 1035–1053. DOI: 10.1016/j.joule.2020.03.005.

[188] C. Gao et al. “Formation of organic-inorganic mixed halide perovskite films by thermal evaporation of $PbCl_2$ and CH_3NH_3I compounds”. In: *RSC Advances* 5 (2015), pp. 26175–26180. DOI: 10.1039/C4RA17316C.

[189] T.-W. Ng, C. Y. Chan, M.-F. Lo, Z. GUAN, and C.-s. Lee. "Formation chemistry of perovskite with mixed iodide/chloride and its implications to charge transport properties". In: *J. Mater. Chem. A* 3 (2015), pp. 9081–9085. DOI: 10.1039/C4TA05819D.

[190] X. Zhu et al. "Superior stability for perovskite solar cells with 20% efficiency using vacuum co-evaporation". In: *Nanoscale* 9.34 (2017), pp. 12316–12323. DOI: 10.1039/C7NR04501H.

[191] C Momblona et al. "Efficient methylammonium lead iodide perovskite solar cells with active layers from 300 to 900 nm". In: *APL Materials* 2.8 (2014), p. 81504. DOI: 10.1063/1.4890056.

[192] L. K. Ono, S. Wang, Y. Kato, S. R. Raga, and Y. Qi. "Fabrication of semi-transparent perovskite films with centimeter-scale superior uniformity by the hybrid deposition method". In: *Energy Environ. Sci.* 7.12 (2014), pp. 3989–3993. DOI: 10.1039/C4EE02539C.

[193] S. Wang et al. "Smooth perovskite thin films and efficient perovskite solar cells prepared by the hybrid deposition method". In: *J. Mater. Chem. A* 3.28 (2015), pp. 14631–14641. DOI: 10.1039/C5TA03593G.

[194] J. Teuscher, A. Ulianov, O. Müntener, M. Grätzel, and N. Tétreault. "Control and Study of the Stoichiometry in Evaporated Perovskite Solar Cells". In: *ChemSusChem* 8.22 (2015), pp. 3847–3852. DOI: 10.1002/cssc.201500972.

[195] D. Zhao et al. "Annealing-free efficient vacuum-deposited planar perovskite solar cells with evaporated fullerenes as electron-selective layers". In: *Nano Energy* 19 (2016), pp. 88–97. DOI: 10.1016/j.nanoen.2015.11.008.

[196] C.-w. Chen et al. "Efficient and Uniform Planar-Type Perovskite Solar Cells by Simple Sequential Vacuum Deposition". In: *Advanced Materials* 26 (2014), pp. 6647–6652. DOI: 10.1002/adma.201402461.

[197] O. Malinkiewicz et al. "Perovskite solar cells employing organic charge-transport layers". In: *Nature Photonics* 8.2 (2013), pp. 128–132. DOI: 10.1038/nphoton.2013.341.

[198] B. S. Kim, T. M. Kim, M. S. Choi, H. S. Shim, and J. J. Kim. "Fully vacuum-processed perovskite solar cells with high open circuit voltage using MoO_3/NPB as hole extraction layers". In: *Organic Electronics* 17 (2015), pp. 102–106. DOI: 10.1016/j.orgel.2014.12.002.

[199] L. E. Polander et al. "Hole-transport material variation in fully vacuum deposited perovskite solar cells". In: *APL Materials* 2.8 (2014), p. 081503. DOI: 10.1063/1.4889843.

[200] A. S. Subbiah et al. "Inorganic hole conducting layers for perovskite-based solar cells". In: *Journal of Physical Chemistry Letters* 5.10 (2014), pp. 1748–1753. DOI: 10.1021/jz500645n.

[201] Q. Lin et al. "Electro-optics of perovskite solar cells". In: *Nature Photonics* 9.2 (2014), pp. 106–112. DOI: 10.1038/nphoton.2014.284.

[202] O. Malinkiewicz et al. "Metal-Oxide-Free Methylammonium Lead Iodide Perovskite-Based Solar Cells: The Influence of Organic Charge Transport Layers". In: *Advanced Energy Materials* 4.15 (2014), p. 1400345. DOI: 10.1002/aenm.201400345.

[203] M. Liu, M. B. Johnston, and H. J. Snaith. "Efficient planar heterojunction perovskite solar cells by vapour deposition". In: *Nature* 501.7467 (2013), pp. 395–398. DOI: 10.1038/nature12509.

[204] J. Ávila, C. Momblona, P. P. Boix, M. Sessolo, and H. J. Bolink. "Vapor-Deposited Perovskites: The Route to High-Performance Solar Cell Production?" In: *Joule* 1.3 (2017), pp. 431–442. DOI: 10.1016/j.joule.2017.07.014.

[205] M. M. Tavakoli, L. Gu, Y. Gao, C. Reckmeier, and J. He. "Fabrication of efficient planar perovskite solar cells using a one-step chemical vapor deposition method". In: *Scientific Reports* 5 (2015), p. 14083. DOI: 10.1038/srep14083.

[206] Y. Jiang et al. "Combination of Hybrid CVD and Cation Exchange for Upscaling Cs-Substituted Mixed Cation Perovskite Solar Cells with High Efficiency and Stability". In: *Advanced Functional Materials* 28.1 (2018), p. 1703835. DOI: 10.1002/adfm.201703835.

[207] B. Wang and T. Chen. "Exceptionally Stable $CH_3NH_3PbI_3$ Films in Moderate Humid Environmental Condition". In: *Advanced Science* 3 (2016), p. 1500262. DOI: 10.1002/advs.201500262.

[208] P. Luo et al. "Uniform, Stable, and Efficient Planar-Heterojunction Perovskite Solar Cells by Facile Low-Pressure Chemical Vapor Deposition under Fully Open-Air Conditions". In: *Applied Materials and Interfaces* 7 (2015), pp. 2708–2714. DOI: 10.1021/am5077588.

[209] M. R. Leyden, M. V. Lee, S. R. Raga, and Y. Qi. "Large formamidinium lead trihalide perovskite solar cells using chemical vapor deposition with high reproducibility and tunable chlorine concentrations". In: *Journal of Materials Chemistry A* 3 (2015), pp. 16097–16103. DOI: 10.1039/C5TA03577E.

[210] M. Tai et al. "Laser induced flash-evaporation printing $CH_3NH_3PbI_3$ thin films for high performance planar solar cells". In: *ACS Applied Materials and Interfaces* 10.31 (2018), pp. 26206–26212. DOI: 10.1021/acsami.8b05918.

[211] H. Hu et al. "Vapour-based processing of hole-conductor-free $CH_3NH_3PbI_3$ perovskite/C60 fullerene planar solar cells". In: *RSC Advances* 4.55 (2014), pp. 28964–28967. DOI: 10.1039/C4RA03820G.

[212] H. A. Abbas et al. "High efficiency sequentially vapor grown n-i-p $CH_3NH_3PbI_3$ perovskite solar cells with undoped P3HT as p-type heterojunction layer". In: *APL Materials* 3.1 (2015), p. 016105. DOI: 10.1063/1.4905932.

[213] D. Yang et al. "Alternating precursor layer deposition for highly stable perovskite films towards efficient solar cells using vacuum deposition". In: *Journal of Materials Chemistry A* 3.18 (2015), pp. 9401–9405. DOI: 10.1039/C5TA01824B.

[214] M.-C. Jung, S. R. Raga, and Y. Qi. "Properties and solar cell applications of Pb-free perovskite films formed by vapor deposition". In: *RSC Advances* 6.4 (2016), pp. 2819–2825. DOI: 10.1039/C5RA21291J.

[215] L. Gil-Escrig et al. "Interface engineering in efficient vacuum deposited perovskite solar cells". In: *Organic Electronics* 37 (2016), pp. 396–401. DOI: 10.1016/j.orgel.2016.07.019.

[216] A. A. Paraecattil, J. D. Jonghe-Risse, V. Pranculis, J. Teuscher, and J.-E. Moser. "Dynamics of Photocarrier Separation in MAPbI 3 Perovskite Multi-Grain Films under Quasi-Static Electric Field". In: *The Journal of Physical Chemistry C* 120.35 (2016), pp. 19595–19602. DOI: 10.1021/acs.jpcc.6b08022.

[217] B. Saparov et al. "Thin-Film Deposition and Characterization of a Sn-Deficient Perovskite Derivative Cs_2SnI_6". In: *Chemistry of Materials* 28.7 (2016), pp. 2315–2322. DOI: 10.1021/acs.chemmater.6b00433.

[218] K. Shum et al. "Synthesis and characterization of $CsSnI_3$ thin films". In: *Applied Physics Letters* 96.22 (2010), p. 221903. DOI: 10.1063/1.3442511.

[219] X. Qiu et al. "From unstable $CsSnI_3$ to air-stable Cs_2SnI_6: A lead-free perovskite solar cell light absorber with bandgap of 1.48 eV and high absorption coefficient". In: *Solar Energy Materials and Solar Cells* 159 (2017), pp. 227–234. DOI: 10.1016/j.solmat.2016.09.022.

[220] D. Moghe et al. "All vapor-deposited lead-free doped $CsSnBr_3$ planar solar cells". In: *Nano Energy* 28 (2016), pp. 469–474. DOI: 10.1016/j.nanoen.2016.09.009.

[221] M. R. Leyden et al. "High performance perovskite solar cells by hybrid chemical vapor deposition". In: *Journal of Materials Chemistry A* 2.44 (2014), pp. 18742–18745. DOI: 10.1039/C4TA04385E.

[222] P. Luo, Z. Liu, W. Xia, C. Yuan, and Y. Lu. "A simple in situ tubular chemical vapor deposition processing of large-scale efficient perovskite solar cells and the research on their novel roll-over phenomenon in J-V curves". In: *Journal of Materials Chemistry A* 3 (2015), pp. 12443–12451. DOI: 10.1039/C5TA02306H.

[223] P. Luo et al. "Chlorine-conducted defect repairment and seed crystal-mediated vapor growth process for controllable preparation of efficient and stable perovskite solar cells". In: *Journal of Materials Chemistry A* 3 (2015), pp. 22949–22959. DOI: 10.1039/C5TA06813D.

[224] Y. Peng, G. Jing, and T. Cui. "A hybrid physical-chemical deposition process at ultra-low temperatures for high-performance perovskite solar cells". In: *Journal of Materials Chemistry A* 3 (2015), pp. 12436–12442. DOI: 10.1039/c5ta01730k.

[225] Y. Peng, G. Jing, and T. Cui. "High-performance perovskite solar cells fabricated by vapor deposition with optimized PbI_2 precursor film". In: *RSC Advances* 5 (2015), pp. 95847–95853. DOI: 10.1039/C5RA19343E.

[226] P. Fan et al. "High-performance perovskite $CH_3NH_3PbI_3$ thin films for solar cells prepared by single-source physical vapour deposition". In: *Scientific Reports* 6 (2016), p. 29910. DOI: 10.1038/srep29910.

[227] C. Momblona et al. "Efficient vacuum deposited p-i-n and n-i-p perovskite solar cells employing doped charge transport layers". In: *Energy and Environmental Science* 9.11 (2016), pp. 3456–3463. DOI: 10.1039/C6EE02100J.

[228] H. Shen et al. "In situ recombination junction between p-Si and TiO_2 enables high-efficiency monolithic perovskite/Si tandem cells". In: *Science advances* 4.12 (2018), eaau9711. DOI: 10.1126/sciadv.aau9711.

[229] D. Pérez-Del-Rey, P. P. Boix, M. Sessolo, A. Hadipour, and H. J. Bolink. "Interfacial Modification for High-Efficiency Vapor-Phase-Deposited Perovskite Solar Cells Based on a Metal Oxide Buffer Layer". In: *Journal of Physical Chemistry Letters* 9.5 (2018), pp. 1041–1046. DOI: 10.1021/acs.jpclett.7b03361.

[230] K. B. Lohmann et al. "Control over crystal size in vapor deposited metal- halide perovskite films". In: *ACS Energy Letters* 5.3 (2020), pp. 710–717. DOI: 10.1021/acsenergylett.0c00183.

[231] J. Borchert et al. "Impurity Tracking Enables Enhanced Control and Reproducibility of Hybrid Perovskite Vapor Deposition". In: *ACS Applied Materials Interfaces* 11.32 (2019), pp. 28851–28857. DOI: 10.1021/acsami.9b07619.

[232] K. Vasseur et al. "A growth and morphology study of organic vapor phase deposited perylene diimide thin films for transistor applications". In: *Journal of Physical Chemistry C* 114.6 (2010), pp. 2730–2737. DOI: 10.1021/jp909242n.

[233] F. Yang, M. Shtein, and S. R. Forrest. "Morphology control and material mixing by high-temperature organic vapor-phase deposition and its application to thin-film solar cells". In: *Journal of Applied Physics* 98 (2005), p. 014906. DOI: 10.1063/1.1941480.

[234] M. Shtein, H. F. Gossenberger, J. B. Benziger, and S. R. Forrest. "Material transport regimes and mechanisms for growth of molecular organic thin films using low pressure organic vapor phase deposition". In: *Journal of Applied Physics* 89.2 (2001), pp. 1470–1476. DOI: 10.1063/1.1332419.

[235] F. Yang, M. Shtein, and S. R. Forrest. "Controlled growth of a molecular bulk heterojunction photovoltaic cell". In: *Nature materials* 4.1 (2005), pp. 37–41. DOI: 10.1038/nmat1285.

[236] M. Shtein, J. Mapel, J. B. Benziger, and S. R. Forrest. "Effects of film morphology and gate dielectric surface preparation on the electrical characteristics of organic-vapor-phase-deposited pentacene thin-film transistors". In: *Applied Physics Letters* 81.2 (2002), pp. 268–270. DOI: 10.1063/1.1491009.

[237] M. Baldo et al. "Organic Vapor Phase Deposition". In: *Advanced Materials* 10.18 (1998), pp. 1505–1514. DOI: 10.1002/(SICI)1521-4095(199812)10:18<1505::AID-ADMA1505>3.0.CO;2-G.

[238] M. R. Leyden, L. K. Ono, S. R. Raga, Y. Kato, and S. Wang. "High performance perovskite solar cells by hybrid chemical vapor deposition". In: *Journal of Materials Chemistry A* 2 (2014), pp. 18742–18745. DOI: 10.1039/C4TA04385E.

[239] M. R. Leyden, M. V. Lee, S. R. Raga, and Y. Qi. "Large formamidinium lead trihalide perovskite solar cells using chemical vapor deposition with high reproducibility and tunable chlorine concentrations". In: *J. Mater. Chem. A* 3.31 (2015), pp. 16097–16103. DOI: 10.1039/C5TA03577E.

[240] L. Qiu et al. "Hybrid chemical vapor deposition enables scalable and stable Cs-FA mixed cation perovskite solar modules with a designated area of 91.8 cm^2 approaching 10% efficiency". In: *Journal of Materials Chemistry A* 7.12 (2019), pp. 6920–6929. DOI: 10.1039/c9ta00239a.

[241] M. R. Leyden, Y. Jiang, and Y. Qi. "Chemical vapor deposition grown formamidinium perovskite solar modules with high steady state power and thermal stability". In: *Journal of Materials Chemistry A* 4.34 (2016), pp. 13125–13132. DOI: https://doi.org/10.1039/C6TA04267H.

[242] M. R. Leyden et al. “Methylammonium Lead Bromide Perovskite Light-Emitting Diodes by Chemical Vapor Deposition”. In: *Journal of Physical Chemistry Letters* 8.14 (2017), pp. 3193–3198. DOI: 10.1021/acs.jpclett.7b01093.

[243] P. Luo et al. “Chemical Vapor Deposition of Perovskites for Photovoltaic Application”. In: *Advanced Materials Interfaces* 4.8 (2017). DOI: 10.1002/admi.201600970.

[244] J. Hirschfelder, C. F. Curtiss, and R. B. Bird. *Molecular Theory of Gases and Liquids*. New York: Wiley, 1954. DOI: 0-471-40065-3.

[245] D. S. Dandy and J. Yun. “Momentum and thermal boundary-layer thickness in a stagnation flow chemical vapor deposition reactor”. In: *Journal of Materials Research* 12.4 (1997), pp. 1112–1121. DOI: 10.1557/JMR.1997.0154.

[246] H. Gamsjager, T. Gajda, S. K. Saxena, J. Sangster, and W. Voigt. *Chemical Thermodynamics of Tin - Volume 12*. OECD, 2012.

[247] A. Dualeh, P. Gao, S. I. Seok, M. K. Nazeeruddin, and M. Graetzel. “Thermal behavior of methylammonium lead-trihalide perovskite photovoltaic light harvesters”. In: *Chemistry of Materials* 26.21 (2014), pp. 6160–6164. DOI: 10.1021/cm502468k.

[248] L. V. Gurvich, I. V. Veyts, and C. B. Alcock, eds. *Thermodynamic Properties Of Individual Substances: Elements And compounds*. 1st ed. CRC Press, 1990.

[249] N. G. Park, M. Grätzel, T. Miyasaka, K. Zhu, and K. Emery. “Towards stable and commercially available perovskite solar cells”. In: *Nature Energy* 1.11 (2016), p. 16152. DOI: 10.1038/nenergy.2016.152.

[250] A. F. Gualdrón-Reyes et al. “Controlling the Phase Segregation in Mixed Halide Perovskites through Nanocrystal Size”. In: *ACS Energy Letters* 4 (2019), pp. 54–62. DOI: 10.1021/acsenergylett.8b02207.

[251] J. H. Heo, D. S. Lee, D. H. Shin, and S. H. Im. “Recent advancement and perspective of flexible hybrid perovskite solar cells”. In: *Journal of Materials Chemistry A* 7 (2018), pp. 888–900. DOI: 10.1039/C8TA09452G.

[252] N. J. Jeon et al. “A fluorene-terminated hole-transporting material for highly efficient and stable perovskite solar cells”. In: *Nature Energy* 3 (2018), pp. 682–689. DOI: 10.1038/s41560-018-0200-6.

[253] Y.-S. Jung et al. “One-step printable perovskite films fabricated under ambient conditions for efficient and reproducible solar cells”. In: *Applied Materials and Interfaces* 9.33 (2017), pp. 27832–27838. DOI: 10.1021/acsami.7b05078.

[254] A. J. Knight et al. “Electronic Traps and Phase Segregation in Lead Mixed-Halide Perovskite”. In: *ACS Energy Letters* 4 (2019), pp. 75–84. DOI: 10.1021/acsenergylett.8b02002.

[255] C. P. Clark, B. Voigt, E. S. Aydil, and R. J. Holmes. “Carrier-gas assisted vapor deposition for highly tunable morphology of halide perovskite thin films”. In: *Sustainable Energy and Fuels* 3.9 (2019), pp. 2447–2455. DOI: 10.1039/c9se00200f.

[256] M. Konstantakou and T. Stergiopoulos. “A critical review on tin halide perovskite solar cells”. In: *Journal of Materials Chemistry A* 5 (2017), pp. 11518–11549. DOI: 10.1039/c7ta00929a.

[257] H. Hasegawa and T. Inabe. “Electrical properties of organic–inorganic hybrid tin bromide cubic perovskites: hole-doping and iodide substitution effects”. In: *New J. Chem.* 40 (2016), pp. 7043–7047. DOI: 10.1039/c6nj00439c.

[258] C. C. Stoumpos et al. “Hybrid germanium iodide perovskite semiconductors: Active lone pairs, structural distortions, direct and indirect energy gaps, and strong nonlinear optical properties”. In: *Journal of the American Chemical Society* 137.21 (2015), pp. 6804–6819. DOI: 10.1021/jacs.5b01025.

[259] P. Xu, S. Chen, H.-J. Xiang, X.-G. Gong, and S.-H. Wei. “Influence of Defects and Synthesis Conditions on the Photovoltaic Performance of Perovskite Semiconductor $CsSnI_3$”. In: *Chemistry of Materials* 26.20 (2014), pp. 6068–6072. DOI: 10.1021/cm503122j.

[260] Y. Wang, W. Tang, and L. Zhang. “Crystalline Size Effects on Texture Coefficient, Electrical and Optical Properties of Sputter-deposited Ga-doped ZnO Thin Films”. In: *Journal of Materials Science and Technology* 31.2 (2015), pp. 175–181. DOI: 10.1016/j.jmst.2014.11.009.

[261] W. Ke, C. C. Stoumpos, and M. G. Kanatzidis. ““Unleaded” Perovskites: Status Quo and Future Prospects of Tin-Based Perovskite Solar Cells”. In: *Advanced Materials* 31.47 (2018), p. 1803230. DOI: 10.1002/adma.201803230.

[262] K. Eom, U. Kwon, S. S. Kalanur, H. J. Park, and H. Seo. “Depth-resolved band alignments of perovskite solar cells with significant interfacial effects”. In: *Journal of Materials Chemistry A* 5.6 (2017), pp. 2563–2571. DOI: 10.1039/C6TA09493G.

[263] D. R. Almalawi, B. Xin, and I. S. Roqan. “Optimized performance III-nitride-perovskite-based heterojunction photodetector via asymmetric electrode con figuration”. In: *RSC Advances* 10 (2020), pp. 6092–6097. DOI: 10.1039/c9ra08823g.

[264] S. D. Stranks, R. L. Hoye, D. Di, R. H. Friend, and F. Deschler. “The Physics of Light Emission in Halide Perovskite Devices”. In: *Advanced Materials* 31.47 (2019). DOI: 10.1002/adma.201803336.

[265] A. Babaei, C. Dreessen, and H. J. Bolink. “High voltage vacuum-processed perovskite solar cells with organic semiconducting interlayers”. In: *RSC Advances* 10 (2020), pp. 6640–6646. DOI: 10.1039/d0ra00214c.

[266] C. Ge et al. “Mechanisms for the enhancement of the lateral photovoltage in perovskite heterostructures”. In: *Solid State Communications* 150 (2010), pp. 2114–2117. DOI: 10.1016/j.ssc.2010.09.016.

[267] J. Zhao, R. Tavakoli, and M. M. Tavakoli. “Synergistic interface and compositional engineering of inverted perovskite solar cells enables highly efficient and stable photovoltaic”. In: *Chemical Communications* 55.62 (2019), pp. 9196–9199. DOI: 10.1039/c9cc04364k.

[268] A. A. Said, J. Xie, and Q. Zhang. “Recent Progress in Organic Electron Transport Materials in Inverted Perovskite Solar Cells”. In: *Small* 15 (2019), p. 1900854. DOI: 10.1002/smll.201900854.

[269] A. K. Jena, M. Ikegami, and T. Miyasaka. “Severe Morphological Deformation of Spiro-OMeTAD in $(CH_3NH_3)PbI_3$ Solar Cells at High Temperature”. In: *ACS Energy Letters* 2 (2017), pp. 1760–1761. DOI: 10.1021/acsenergylett.7b00582.

[270] M. Petrovic et al. “Limitations of a polymer-based hole transporting layer for application in planar inverted perovskite solar cells”. In: *Nanoscale Advances* 1.8 (2019), pp. 3107–3118. DOI: 10.1039/c9na00246d.

[271] N. Shibayama et al. “All-inorganic inverse perovskite solar cells using zinc oxide nanocolloids on spin coated perovskite layer”. In: *Nano Convergence* 4.1 (2017), p. 18. DOI: 10.1186/s40580-017-0113-2.

[272] J. Ryu et al. “Size effects of Graphene Quantum Dots Modified-blocking TiO_2 layer for Efficient Planar Perovskite Solar Cells”. In: *J. Mater. Chem. A* 5.32 (2017), pp. 16834–16842. DOI: 10.1039/C7TA02242E.

[273] Q. Duan et al. “Design of hole-transport-material free $CH_3NH_3PbI_3$/$CsSnI_3$ all-perovskite heterojunction efficient solar cells by device simulation”. In: *Solar Energy* 201 (2020), pp. 555–560. DOI: 10.1016/j.solener.2020.03.037.

[274] W. S. Choi, S. A. Lee, J. H. You, S. Lee, and H. N. Lee. “Resonant tunnelling in a quantum oxide superlattice”. In: *Nature Communications* 6 (2015), p. 7424. DOI: 10.1038/ncomms8424.

[275] M. E. Khan, J. Lee, S. Byeon, and Y. H. Kim. “Semimetallicity and Negative Differential Resistance from Hybrid Halide Perovskite Nanowires”. In: *Advanced Functional Materials* 29.13 (2019), p. 1807620. DOI: 10.1002/adfm.201807620.

[276] L. Dou et al. “Spatially resolved multicolor $CsPbX_3$ nanowire heterojunctions via anion exchange”. In: *Proceedings of the National Academy of Sciences of the United States of America* 114.28 (2017), pp. 7216–7221. DOI: 10.1073/pnas.1703860114.

[277] Y. Fu et al. “Metal halide perovskite nanostructures for optoelectronic applications and the study of physical properties”. In: *Nature Reviews Materials* 4.3 (2019), pp. 169–188. DOI: 10.1038/s41578-019-0080-9.

[278] D. Pan et al. “Visualization and Studies of Ion-Diffusion Kinetics in Cesium Lead Bromide Perovskite Nanowires”. In: *Nano Letters* 18.3 (2018), pp. 1807–1813. DOI: 10.1021/acs.nanolett.7b05023.

[279] D. H. Kang and N. G. Park. “On the Current-Voltage Hysteresis in Perovskite Solar Cells: Dependence on Perovskite Composition and Methods to Remove Hysteresis”. In: *Advanced Materials* 31.34 (2019), p. 1805214. DOI: 10.1002/adma.201805214.

[280] D. W. DeQuilettes et al. “Photo-induced halide redistribution in organic–inorganic perovskite films”. In: *Nature Communications* 7 (2016), p. 11683. DOI: 10.1038/ncomms11683.

[281] H. Li, C. Jia, H. Li, and X. Meng. "$CsPbX_3/Cs_4PbX_6$ core/shell perovskite nanocrystals". In: *Chemical Communications* 54.49 (2018), pp. 6300–6303. DOI: 10.1039/c8cc02802h.

[282] F. Bai et al. "A 0D/3D Heterostructured All-Inorganic Halide Perovskite Solar Cell with High Performance and Enhanced Phase Stability". In: *Advanced Materials* 31.48 (2019), p. 1904735. DOI: 10.1002/adma.201904735.

[283] M. Wang, W. Tian, F. Cao, M. Wang, and L. Li. "Flexible and Self-Powered Lateral Photodetector Based on Inorganic Perovskite $CsPbI_3$-$CsPbBr_3$ Heterojunction Nanowire Array". In: *Advanced Functional Materials* 30.16 (2020), p. 1909771. DOI: 10.1002/adfm.201909771.

[284] A. Krishna, S. Gottis, M. K. Nazeeruddin, and F. Sauvage. "Mixed Dimensional 2D/3D Hybrid Perovskite Absorbers: The Future of Perovskite Solar Cells?" In: *Advanced Functional Materials* 29 (2019), p. 1806482. DOI: 10.1002/adfm.201806482.

[285] L. Zhang, X. Zhang, and G. Lu. "Band Alignment in Two-Dimensional Halide Perovskite Heterostructures: Type I or Type II?" In: *The Journal of Physical Chemistry Letters* 11.8 (2020), pp. 2910–2916. DOI: 10.1021/acs.jpclett.0c00376.

[286] G. Grancini and M. K. Nazeeruddin. "Dimensional tailoring of hybrid perovskites for photovoltaics". In: *Nature Reviews Materials* 4.1 (2019), pp. 4–22. DOI: 10.1038/s41578-018-0065-0.

[287] E. Ruggeri et al. "Controlling the Growth Kinetics and Optoelectronic Properties of 2D/3D Lead-Tin Perovskite Heterojunctions". In: *Advanced Materials* 31 (2019), p. 1905247. DOI: 10.1002/adma.201905247.

[288] B. J. Bohn et al. "Boosting Tunable Blue Luminescence of Halide Perovskite Nanoplatelets through Postsynthetic Surface Trap Repair". In: *Nano Letters* 18.8 (2018), pp. 5231–5238. DOI: 10.1021/acs.nanolett.8b02190.

[289] Y. Chen et al. "2D Ruddlesden–Popper Perovskites for Optoelectronics". In: *Advanced Materials* 30 (2018), p. 1703487. DOI: 10.1002/adma.201703487.

[290] C. Eames et al. "Ionic transport in hybrid lead iodide perovskite solar cells". In: *Nature Communications* 6 (2015), p. 7497. DOI: 10.1038/ncomms8497.

[291] J. Haruyama, K. Sodeyama, L. Han, and Y. Tateyama. “First-Principles Study of Ion Diffusion in Perovskite Solar Cell Sensitizers”. In: *Journal of the American Chemical Society* 137.32 (2015), pp. 10048–10051. DOI: 10.1021/jacs.5b03615.

[292] G. Nedelcu et al. “Fast Anion-Exchange in Highly Luminescent Nanocrystals of Cesium Lead Halide Perovskites ($CsPbX_3$, X = Cl, Br, I)”. In: *Nano Letters* 15.8 (2015), pp. 5635–5640. DOI: 10.1021/acs.nanolett.5b02404.

[293] G. E. Eperon, C. E. Beck, and H. J. Snaith. “Cation exchange for thin film lead iodide perovskite interconversion”. In: *Mater. Horiz.* 3.1 (2016), pp. 63–71. DOI: 10.1039/C5MH00170F.

[294] G. E. Eperon and D. S. Ginger. “B-Site Metal Cation Exchange in Halide Perovskites”. In: *ACS Energy Letters* 2.5 (2017), pp. 1190–1196. DOI: 10.1021/acsenergylett.7b00290.

[295] F. Hao, C. C. Stoumpos, R. P. H. Chang, and M. G. Kanatzidis. “Anomalous band gap behavior in mixed Sn and Pb perovskites enables broadening of absorption spectrum in solar cells”. In: *Journal of the American Chemical Society* 136.22 (2014), pp. 8094–8099. DOI: 10.1021/ja5033259.

[296] D. P. McMeekin et al. “A mixed-cation lead mixed-halide perovskite absorber for tandem solar cells”. In: *Science* 351.6269 (2016), pp. 151–155. DOI: 10.1126/science.aad5845.

[297] N. K. Noel et al. “Interfacial charge-transfer doping of metal halide perovskites for high performance photovoltaics”. In: *Energy and Environmental Science* 12 (2019), pp. 3063–3073. DOI: 10.1039/c9ee01773a.

[298] C.-h. Hou et al. “Validated Analysis of Component Distribution Inside Perovskite Solar Cells and Its Utility in Unveiling Factors of Device Performance and Degradation”. In: *ACS Applied Materials Interfaces* 12.20 (2020), pp. 22730–22740. DOI: 10.1021/acsami.9b22492.

[299] M. L. Lai et al. “Tunable Near-Infrared Luminescence in Tin Halide Perovskite Devices”. In: *Physical Chemistry Letters* 7 (2016), pp. 2653–2658. DOI: 10.1021/acs.jpclett.6b01047.

[300] A. Walsh and S. D. Stranks. "Taking Control of Ion Transport in Halide Perovskite Solar Cells". In: *ACS Energy Letters* 3.8 (2018), pp. 1983–1990. DOI: 10.1021/acsenergylett.8b00764.

[301] A. Oranskaia, J. Yin, O. M. Bakr, J. L. Brédas, and O. F. Mohammed. "Halogen Migration in Hybrid Perovskites: The Organic Cation Matters". In: *Journal of Physical Chemistry Letters* 9.18 (2018), pp. 5474–5480. DOI: 10.1021/acs.jpclett.8b02522.

[302] B. B. Zhang et al. "Defect proliferation in $CsPbBr_3$ crystal induced by ion migration". In: *Applied Physics Letters* 116.6 (2020), p. 063505. DOI: 10.1063/1.5134108.

[303] R. A. John et al. "Ionotronic halide perovskite drift-diffusive synapses for low-power neuromorphic computation". In: *Advanced Materials* 30.51 (2018), p. 1805454. DOI: 10.1002/adma.201805454.

[304] J. Xing et al. "Ultrafast ion migration in hybrid perovskite polycrystalline thin films under light and suppression in single crystals". In: *Phys. Chem. Chem. Phys.* 18 (2016), pp. 30484–30490. DOI: 10.1039/c6cp06496e.

[305] D. Li et al. "Electronic and Ionic Transport Dynamics in Organolead Halide Perovskites". In: *ACS Nano* 10 (2016), 69336941. DOI: 10.1021/acsnano.6b02795.

[306] Y. Shao et al. "Grain boundary dominated ion migration in polycrystalline organic-inorganic halide perovskite films". In: *Energy and Environmental Science* 9 (2016), pp. 1752–1759. DOI: 10.1039/c6ee00413j.

[307] B. Philippe, G. J. Man, and H. Rensmo. "Photoelectron spectroscopy investigations of halide perovskite materials used in solar cells". In: *Characterization Techniques for Perovskite Solar Cell Materials*. 2020. Chap. Photoelect, pp. 109–137. DOI: 10.1016/B978-0-12-814727-6.00005-0.

[308] T. J. Jacobsson et al. "Unreacted PbI_2 as a Double-Edged Sword for Enhancing the Performance of Perovskite Solar Cells". In: *Journal of the American Chemical Society* 138.32 (2016), pp. 10331–10343. DOI: 10.1021/jacs.6b06320.

[309] Frank Müller. *Epitaktisches Wachstum von Graphen und Boronitren auf Übergangsmetallen*. 2014. DOI: https://jacobs.physik.uni-saarland.de/home/

index.php?page=steinbeiss/home_cms_steinbeissdet3-1&navi=service.

[310] Y. Kato et al. “Silver Iodide Formation in Methyl Ammonium Lead Iodide Perovskite Solar Cells with Silver Top Electrodes”. In: *Advanced Materials Interfaces* 2.13 (2015), p. 1500195. DOI: 10.1002/admi.201500195.

[311] E. Bi et al. “Diffusion engineering of ions and charge carriers for stable efficient perovskite solar cells”. In: *Nature Communications* 8 (2017), p. 15330. DOI: 10.1038/ncomms15330.

[312] C. C. Boyd et al. “Barrier Design to Prevent Metal-Induced Degradation and Improve Thermal Stability in Perovskite Solar Cells”. In: *ACS Energy Letters* 3 (2018), pp. 1772–1778. DOI: 10.1021/acsenergylett.8b00926.

[313] S. M. Jain et al. “Vapor phase conversion of PbI_2 to $CH_3NH_3PbI_3$: Spectroscopic evidence for formation of an intermediate phase”. In: *Journal of Materials Chemistry A* 4.7 (2016), pp. 2630–2642. DOI: 10.1039/c5ta08745g.

[314] Z. Ahmad, M. A. Najeeb, R. A. Shakoor, A. Alashraf, and S. A. Al. “Instability in $CH_3NH_3PbI_3$ perovskite solar cells due to elemental migration and chemical composition changes”. In: *Scientific Reports* 7 (2017), p. 15406. DOI: 10.1038/s41598-017-15841-4.

[315] B. W. Park et al. “Chemical engineering of methylammonium lead iodide/bromide perovskites: Tuning of opto-electronic properties and photovoltaic performance”. In: *Journal of Materials Chemistry A* 3.43 (2015), pp. 21760–21771. DOI: 10.1039/c5ta05470b.

[316] D. F. Yancey and C. Reinhardt. “Damage and repair of organic and inorganic surfaces by Ar^+ ion and gas cluster ion beam sputtering”. In: *Journal of Electron Spectroscopy and Related Phenomena* 231 (2019), pp. 104–108. DOI: 10.1016/j.elspec.2018.01.005.

[317] N. C. Erickson, S. N. Raman, J. S. Hammond, and R. J. Holmes. “Depth profiling organic light-emitting devices by gas-cluster ion beam sputtering and X-ray photoelectron spectroscopy”. In: *Organic Electronics* 15 (2014), pp. 2988–2992. DOI: 10.1016/j.orgel.2014.08.039.

[318] Y.-Y. Chen et al. “X-ray Photoelectron Spectrometry Depth Profiling of Organic Thin Films Using C_{60} Sputtering”. In: *Analytical Chemistry* 80.2 (2008), pp. 501–505. DOI: 10.1021/ac701899a.

[319] M. P. Seah, S. J. Spencer, R Havelund, I. S. Gilmore, and A. G. Shard. “Depth resolution at organic interfaces sputtered by argon gas cluster ions: the effect of energy, angle and cluster size”. In: *The Analyst* 140.19 (2015), pp. 6508–6516. DOI: 10.1039/C5AN01473E.

[320] J. Brison, S. Muramoto, and D. G. Castner. “ToF-SIMS depth profiling of organic films: A comparison between single-beam and dual-beam analysis”. In: *Journal of Physical Chemistry C* 114.12 (2010), pp. 5565–5573. DOI: 10.1021/jp9066179.

[321] S. P. Harvey et al. “Mitigating Measurement Artifacts in TOF-SIMS Analysis of Perovskite Solar Cells”. In: *ACS Applied Materials and Interfaces Interfaces* 11 (2019), pp. 30911–30918. DOI: 10.1021/acsami.9b09445.

[322] M. P. Seah. “Universal equation for argon gas cluster sputtering yields”. In: *Journal of Physical Chemistry C* 117.24 (2013), pp. 12622–12632. DOI: 10.1021/jp402684c.

[323] C. Noël and L. Houssiau. “Hybrid Organic / Inorganic Materials Depth Profiling Using Low Energy Cesium Ions”. In: *Journal of The American Society for Mass Spectrometry* 27 (2016), pp. 908–916. DOI: 10.1007/s13361-016-1353-9.

[324] R. Simpson, R. G. White, J. F. Watts, and M. A. Baker. “Applied Surface Science XPS investigation of monatomic and cluster argon ion sputtering of tantalum pentoxide”. In: *Applied Surface Science* 405 (2017), pp. 79–87. DOI: 10.1016/j.apsusc.2017.02.006.

[325] Y. Busby et al. “XPS depth profiles of organo lead halide layers and full perovskite solar cells”. In: *Proc. SPIE 10724, Physical Chemistry of Semiconductor Materials and Interfaces XVII* 1072408 (2018). DOI: 10.1117/12.2320488.

[326] A. L. Palma et al. “Mesoscopic Perovskite Light-Emitting Diodes”. In: *ACS Applied Materials and Interfaces* 8.40 (2016), pp. 26989–26997. DOI: 10.1021/acsami.6b07750.

[327] Y. Busby et al. “Aging effects in interface-engineered perovskite solar cells with 2D nanomaterials: A depth profile analysis”. In: *Materials Today Energy* 9 (2018), pp. 1–10. DOI: 10.1016/j.mtener.2018.04.005.

[328] F. Matteocci et al. “Interface and Composition Analysis on Perovskite Solar Cells”. In: *ACS Applied Materials Interfaces* 7.47 (2015), pp. 26176–26183. DOI: 10.1021/acsami.5b08038.

[329] R. T. Ginting et al. “Degradation mechanism of planar-perovskite solar cells: correlating evolution of iodine distribution and photocurrent hysteresis”. In: *Journal of Materials Chemistry A* 5.9 (2017), pp. 4527–4534. DOI: 10.1039/c6ta09202k.

[330] S. Tao et al. “Absolute energy level positions in tin- and lead-based halide perovskites”. In: *Nature Communications* 10 (2019), p. 2560. DOI: 10.1038/s41467-019-10468-7.

[331] F. Hao, H. Tan, Z. Jin, and L. Ding. “Toward Stable and Efficient Sn-containing Perovskite Solar Cells”. In: *Science Bulletin* 65.10 (2020), pp. 786–790. DOI: 10.1016/j.scib.2020.02.028.

[332] H. Yao et al. “Strategies for Improving the Stability of Tin-Based Perovskite ($ASnX_3$) Solar Cells”. In: *Advanced Sc* 7.10 (2020), p. 1903540. DOI: 10.1002/advs.201903540.

[333] A. Babayigit et al. “Assessing the toxicity of Pb- and Sn-based perovskite solar cells in model organism Danio rerio”. In: *Scientific Reports* 6 (2016), p. 18721. DOI: 10.1038/srep18721.

[334] R. Seifert, S. Scholz, B. Lüssem, and K. Leo. “Comparison of ultraviolet- and charge-induced degradation phenomena in blue fluorescent organic light emitting diodes”. In: *Applied Physics Letters* 97.1 (2010), p. 013308. DOI: 10.1063/1.3460285.

[335] R. Newcomb et al. “Role of host excimer formation in the degradation of organic light-emitting devices”. In: *Applied Physics Letters* 116.6 (2020), p. 063302. DOI: 10.1063/1.5124802.

[336] Z. Andaji-garmaroudi et al. “A Highly Emissive Surface Layer in Mixed-Halide Multication Perovskites”. In: *Advanced Materials* 31 (2019), p. 1902374. DOI: 10.1002/adma.201902374.

[337] A. C. Ferreira et al. “Direct evidence of weakly dispersed and strongly anharmonic optical phonons in hybrid perovskites”. In: *Communications Physics* 3 (2020), p. 48. DOI: 10.1038/s42005-020-0313-7.

[338] M. Sendner et al. “Optical phonons in methylammonium lead halide perovskites and implications for charge transport”. In: *Mater. Horiz.* 3.3 (2016), pp. 613–620. DOI: 10.1039/c6mh00275g.

[339] K. T. Munson, J. R. Swartzfager, and J. B. Asbury. “Lattice Anharmonicity: A Double-Edged Sword for 3D Perovskite-Based Optoelectronics”. In: *ACS Energy Letters* 4.8 (2019), pp. 1888–1897. DOI: 10.1021/acsenergylett.9b01073.

[340] D. J. Flannigan. “Electrons Film Phonon Dynamics in Full”. In: *Physics* 11 (2018), p. 53. DOI: 10.1103/physics.11.53.

[341] M. J. Stern et al. “Mapping momentum-dependent electron-phonon coupling and nonequilibrium phonon dynamics with ultrafast electron diffuse scattering”. In: *Physical Review B* 97.16 (2018), p. 165416. DOI: 10.1103/PhysRevB.97.165416.

[342] D. R. Cremons, D. X. Du, and D. J. Flannigan. “Picosecond phase-velocity dispersion of hypersonic phonons imaged with ultrafast electron microscopy”. In: *Physical Review Materials* 1.7 (2017), p. 073801. DOI: 10.1103/PhysRevMaterials.1.073801.

[343] A. J. McKenna, J. K. Eliason, and D. J. Flannigan. “Spatiotemporal Evolution of Coherent Elastic Strain Waves in a Single MoS_2 Flake”. In: *Nano Letters* 17.6 (2017), pp. 3952–3958. DOI: 10.1021/acs.nanolett.7b01565.

[344] D. R. Cremons, D. A. Plemmons, and D. J. Flannigan. “Defect-mediated phonon dynamics in TaS_2 and WSe_2”. In: *Structural Dynamics* 4.4 (2017), p. 044019. DOI: 10.1063/1.4982817.

[345] D. J. Flannigan and A. M. Lindenberg. “Atomic-scale imaging of ultrafast materials dynamics”. In: *MRS Bulletin* 43.7 (2018), pp. 485–490. DOI: 10.1557/mrs.2018.146.

[346] E. J. VandenBussche, C. P. Clark, R. J. Holmes, and D. J. Flannigan. “Mitigating Damage to Hybrid Perovskites Using Pulsed-Beam TEM”. In: *ChemRxiv. Preprint.* (2020). DOI: 10.26434/chemrxiv.12756461.v1.

[347] "Perovskites take steps to industrialization". In: *Nature Energy* 5.1 (2020). DOI: 10.1038/s41560-020-0552-6.

[348] M. V. Khenkin et al. "Consensus statement for stability assessment and reporting for perovskite photovoltaics based on ISOS procedures". In: *Nature Energy* 5.1 (2020), pp. 35–49. DOI: 10.1038/s41560-019-0529-5.

[349] N. K. McKinnon, D. C. Reeves, and M. H. Akabas. "5-HT3 receptor ion size selectivity is a property of the transmembrane channel, not the cytoplasmic vestibule portals". In: *The Journal of General Physiology* 138.4 (2011), pp. 453–466. DOI: 10.1085/jgp.201110686.

[350] B. N. Cohen, C Labarca, N Davidson, and H. A. Lester. "Mutations in M2 alter the selectivity of the mouse nicotinic acetylcholine receptor for organic and alkali metal cations." In: *The Journal of general physiology* 100.September (1992), pp. 373–400. DOI: 10.1085/jgp.100.3.373.

[351] W. D. Callister Jr. *Materials Science and Engineering, An Introduction.* 7th. John Wiley Sons, 2007.

[352] J. Uribe, D. Ramirez, J. M. Osorio Guillén, J. Osorio, and F. Jaramillo. "$CH_3NH_3CaI_3$ Perovskite: Synthesis, Characterization and First-Principles Studies". In: *Journal of Physical Chemistry C* 120 (2016), pp. 16393–16398. DOI: 10.1021/acs.jpcc.6b04207.

[353] A. Kumar, K. R. Balasubramaniam, J. Kangsabanik, Vikram, and A. Alam. "Crystal structure, stability and optoelectronic properties of the organic-inorganic wide bandgap perovskite CH¡sub¿3¡/sub¿NH¡sub¿3¡/sub¿BaI¡sub¿3¡/sub¿: Candidate for transparent conductor applications". In: *Physical Review B* 94 (2016), p. 180105. arXiv: 1604.08003.

[354] Gary L. McPherson and Katherine Talluto. "Luminescent centers in doped crystals of $CsMgI_3$: Energy storage and thermoluminescence". In: *Solid State Communications* 43.5 (1982), pp. 331–334. DOI: 10.1016/0038-1098(82)90488-4.

[355] U. Shirwadkar et al. "New promising scintillators for gamma-ray spectroscopy: Cs(Ba,Sr)$(Br,I)_3$". In: *2011 IEEE Nuclear Science Symposium Conference Record*. 2011, pp. 1583–1585. DOI: 10.1109/NSSMIC.2011.6154636.

[356] H. Wei, M. Zhuravleva, K. Yang, B. Blalock, and C. L. Melcher. “Effect of Ba substitution in $CsSrI_3$:Eu_2^+”. In: *Journal of Crystal Growth* 384 (2013), pp. 27–32. DOI: 10.1016/j.jcrysgro.2013.09.007.

[357] M. R. Filip and F. Giustino. “Computational Screening of Homovalent Lead Substitution in Organic-Inorganic Halide Perovskites”. In: *The Journal of Physical Chemistry C* 120.1 (2016), pp. 166–173. DOI: 10.1021/acs.jpcc.5b11845.

[358] H. Chen et al. “Spiro-annulated hole-transport material outperforms NPB with higher mobility and stability in organic light-emitting diodes”. In: *Dyes and Pigments* 107 (2014), pp. 15–20. DOI: 10.1016/j.dyepig.2014.03.006.

[359] V. Jankus, C. J. Chiang, F. Dias, and A. P. Monkman. “Deep blue exciplex organic light-emitting diodes with enhanced efficiency; P-type or E-type triplet conversion to singlet excitons?” In: *Advanced Materials* 25.10 (2013), pp. 1455–1459. DOI: 10.1002/adma.201203615.

[360] M. Zhuravleva, B. Blalock, K. Yang, M. Koschan, and C. L. Melcher. “New single crystal scintillators: CsCaCl3:Eu and CsCaI3:Eu”. In: *Journal of Crystal Growth* 352 (2012), pp. 115–119. DOI: 10.1016/j.jcrysgro.2012.02.025.

[361] M. Tyagi, M Zhuravleva, and C. L. Melcher. “Theoretical and experimental characterization of promising new scintillators: Eu¡sup¿2+¡/sup¿doped CsCaCl¡sub¿3¡/sub¿and CsCaI¡sub¿3¡/sub¿”. In: *Journal of Applied Physics* 113 (2013), p. 203504. DOI: 10.1063/1.4807401.

[362] E. Rowe et al. “Double Salts Iodide Scintillators: Cesium Barium Iodide, Cesium Calcium Iodide, and Barium Bromine Iodide”. In: *Crystal Research and Technology* 48.4 (2013), pp. 227–235. DOI: 10.1002/crat.201300010.

[363] H. Cho et al. “High-Efficiency Solution-Processed Inorganic Metal Halide Perovskite Light-Emitting Diodes”. In: *Advanced Materials* 29 (2017), p. 1700579. DOI: 10.1002/adma.201700579.

[364] A. Binek, F. C. Hanusch, P. Docampo, and T. Bein. “Stabilization of the trigonal high-temperature phase of formamidinium lead iodide”. In: *Journal of Physical Chemistry Letters* 6.7 (2015), pp. 1249–1253. DOI: 10.1021/acs.jpclett.5b00380.

[365] D. Li et al. “Size-dependent phase transition in methylammonium lead iodide perovskite microplate crystals”. In: *Nature Communications* 7 (2016), p. 11330. DOI: 10.1038/ncomms11330.

Appendix A

Publications and Presentations

A.1 Publications

6 **C.P. Clark**, J.E. Mann, W.J. Hsu, E.S. Aydil, and R.J. Holmes. "Understanding and mitigating measurement artifacts in XPS sputter depth profiled MHPs". In preparation.

5 E.J. VandenBussche, **C.P. Clark**, R.J. Holmes, and D.J. Flannigan. "Mitigating Damage to Hybrid Perovskites Using Pulsed-Beam TEM. ChemRxiv. Prepr. 2020. DOI: 10.26434/chemrxiv.12756461.v1.

4 **C.P. Clark**, J.E. Mann, J.S. Bangsund, E.S. Aydil, and R.J. Holmes. "Formation of Stable Metal-Halide Perovskite-Perovskite Heterojunctions". Submitted to ACS Energy Letters.

3 **C.P. Clark**, B. Voigt, E.S. Aydil, and R.J. Holmes. "Carrier-gas Assisted Vapor Deposition for Highly Tunable Morphology of Halide Perovskite Thin Films". Sustainable Energy & Fuels 3 (2019), 2447-2455. DOI: 10.1039/c9se00200f.

2 J.S. Bangsund, T.R. Fielitz, T.J. Steiner, K. Shi, J.R. Van Sambeek, **C.P. Clark**, and R.J. Holmes. "Formation of aligned periodic patterns during the crystallization of organic semiconductor thin films". Nature Materials 18 (2019), 725-731. DOI: 10.1038/s41563-019-0379-3.

1 D. Ray, **C.P. Clark**, H.Q. Pham, J. Borycz, R.J. Holmes, E.S. Aydil, and L. Gagliardi. "Computational Study of Structural and Electronic Properties of Lead Free $CsMI_3$ Perovskites (M = Ge, Sn, Pb, Mg, Ca, Sr, Ba)". In: The Journal of Physical Chemistry C

122 (2018), 78387848. DOI: 10.1021/acs.jpcc.8b00226.

A.2 Presentations

6 E.J. VandenBussche, **C.P. Clark**, R.J. Holmes, and D.J. Flannigan. "Pulsed electron beams in TEM for understanding and mitigating damage in hybrid organic-inorganic perovskites". ACS Virtual Meeting, Aug 17-20, 2020.

5 E.J. VandenBussche, **C.P. Clark**, R.J. Holmes, and D.J. Flannigan. "Pulsed Electron Beams for Mitigating Damage in Next-Generation Electronic Materials". Microscopy and Microanalysis Virtual Meeting, Aug 4-7, 2020.

4 **C.P. Clark**, E.S. Aydil, and R.J. Holmes. "Carrier-Gas Assisted Vapor Deposition of Metal Halide Perovskite Thin Films". AVS 66th International Symposium & Exhibition, October 24, 2019.

3 **C.P. Clark**, E.S. Aydil, and R.J. Holmes. "Controlling Stoichiometry and Morphology in Perovskite Films Deposited by Carrier-Gas Assisted Vapor Deposition." iPRIME Conference, University of Minnesota, May 29, 2019.

2 **C.P. Clark**, E.S. Aydil, and R.J. Holmes. "Controlling Stoichiometry and Morphology in Perovskite Films Deposited by Carrier-Gas Assisted Vapor Deposition." Spring MRS Conference, April 25, 2019.

1 **C.P. Clark**, E.S. Aydil, and R.J. Holmes. "Vapor-Deposition for Lead-Free Perovskite Optoelectronics". iPRIME Conference, University of Minnesota, May 30, 2018.

Appendix B

Common Experimental Methods

B.1 Cleaning and Materials

B.1.1 Substrate Cleaning

Glass, Si, and ITO substrates were cleaned via sequential sonication in baths of diluted tergitol, deionized water, and acetone. Substrates were then boiled in isopropanol, dried with N_2, and treated with UV-ozone for 15 minutes.

B.1.2 Materials Used

All materials were used as received: $PbBr_2$ (Sigma Aldrich, 99.999% metals basis), PbI_2 (Sigma Aldrich, 99.999% metals basis), MABr (Sigma Aldrich, >99% purity), FABr (Sigma Aldrich, 98% purity), FAI (Sigma Aldrich, >99% purity), $SnBr_2$ (BTC, 99% purity), MAI (Lumtec, 99.5% purity), SnI_2 (Alfa Aesar, 99.999% purity), CsBr (Sigma Aldrich, 99.9% trace metals basis), N,N-Dimethyl-formamide (anhydrous, 99.8%), Chlorobenzene (anhydrous, 99.8%), Dimethyl sulfoxide (anhydrous, >99.9%).

B.2 Characterization Methods

Film thicknesses were measured using a J.A. Wollam Spectroscopic Ellipsometer and Cauchy model normal fit ($n(\lambda) = A + \frac{B}{\lambda^2} + \frac{C}{\lambda^4}$). Fit was performed at wavelengths corresponding

to the non-absorbing region (*i.e.*, larger energies than the bandgap) of each film which varied depending on the MHP measured.

Absorbance measurements were performed with a CARY 7000 UV-VIS-IR spectrometer.

X-ray diffraction was collected using a PANalytical X'pert PRO (theta-theta) or Bruker D8 (2D) diffractometer with Co Kα radiation (λ=1.7889 Å) unless otherwise specified.

Scanning Electron Microscope (SEM) images were obtained using a JEOL 6500 instrument with 5 kV potential and $\sim$ 30 mA current. Films were affixed to the SEM sample holder with conductive carbon tape, but were not covered with a conductive coating.

Appendix C

Synthesis of Pb and Sn Free MHPs

A substantial portion of my initial research was focused on attempts to synthesize and characterize some potential new Pb- and Sn-free MHPs including $MABaI_3$, $MACaI_3$, and $CsBaI_3$. Several synthesis approaches including solution and solid-state methods were attempted, and the resulting materials were characterized with several techniques including x-ray diffraction (XRD) and UV-visible absorption spectroscopy (UV-vis). As the precursors for the desired perovskite materials are highly hygroscopic, methods for characterization without air exposure were also developed and validated.

We also collaborated with the Gagliardi group to perform density functional calculations on several of these materials ($CsMI_3$ perovskites with M = Ge, Sn, Pb, Mg, Ca, Sr, and Ba) [67]. The outcome of this study, as well as our experimental results, was that Mg and Ba perovskites are unlikely to form because they have positive formation energies. Although Ca and Sr perovskites have negative formation energies with respect to the metal-iodide precursors, they exhibit wide band gaps and high hygroscopicity, making these unlikely candidates for applications in photovoltaic devices. This Chapter is adapted with permission from D. Ray *et al.* "Computational Study of Structural and Electronic Properties of Lead Free $CsMI_3$ Perovskites (M = Ge, Sn, Pb, Mg, Ca, Sr, Ba)". In: The Journal of Physical Chemistry C 122 (2018), 78387848. DOI: 10.1021/acs.jpcc.8b00226. Copyright 2018 American Chemical Society.

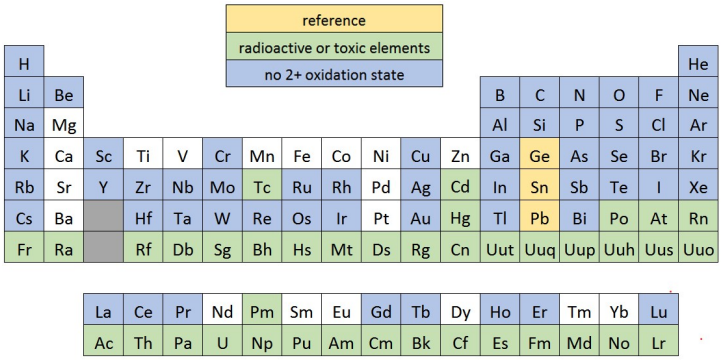

Figure C.1. Elements eliminated as potential replacements for lead based on valence state (blue) and toxicity (green) criteria. 19 elements (white) remain after this elimination.

C.1 Preliminary Work

C.1.1 Identification of Potential B^{2+} Site Cations

Excluding $ASnX_3$, which has known stability issues, no promising Pb-free HPs with ABX_3 stoichiometry had been synthesized at the time of this initial work. With this in mind, we sought to synthesize novel ABX_3 HPs using B-site cations not from column 14 (*i.e.* Ge, Sn, Pb).

Eliminating toxic elements and those that do not have a 2^+ oxidation state (and thus cannot be accommodated in an $A^{1+}B^{2+}X_3^{1-}$ perovskite), reduces the periodic table to the 19 elements shown in white in Figure C.1. Geometric factors were then used to further refine potential replacements for lead. The coordination factor μ (Equation 2.1) and Goldschmidt's tolerance factor t (Equation 2.2), are two metrics that can indicate whether a perovskite will be stable [66]. In both equations, r_A, r_B and r_X are the radii of the ions at sites A, B and X, respectively. For halide perovskites, Li *et al.* find that the vast majority satisfy $0.442 < \mu < 0.895$ and $0.813 < t < 1.107$ [66]. While heuristic, these metrics are a powerful tool to screen for potential HPs.

Accordingly, μ and t were calculated for the 19 elements in Figure C.1 that passed the valence and toxicity filters. Calculations were done for Cl, Br, and I as the X-site halogens, and for three common A-site cations: $CH_3NH_3^+$ (MA^+), $CH_3CH_2NH_3^+$ (EA^+), and Cs^+. Table C.1 lists the ionic radii used in these calculations and Figure C.2 shows the resulting t and μ values for all 171 combinations; combinations highlighted in green with a white background meet both geometric requirements. Considering the scarcity of the lanthanides, Pt, and Pd, the five most attractive replacements for Pb are Ca, Sr, Ba, Ti and V.

To the best of our knowledge, none of the organic halide perovskites in Figure C.2 had been

Ion	Ionic Radii (nm)	Source
MA^+	0.18	[349]
EA^+	0.23	[350]
Cs^+	0.17	[351]
I^-	0.22	[6]
Br^-	0.196	[6]
Cl^-	0.181	[6]

Table C.1: Ionic radii used for geometry calculations.

				halogen = iodine				halogen = bromine				halogen = chlorine			
No	Category	Element	2+ ionic radius (nm)	μ	t			μ	t			μ	t		
				I^-	$I^- + MA^+$	$I^- + EA^+$	$I^- + Cs^+$	Br^-	$Br^- + MA^+$	$Br^- + EA^+$	$Br^- + Cs^+$	Cl^-	$Cl^- + MA^+$	$Cl^- + EA^+$	$Cl^- + Cs^+$
32	*Reference*	*Germanium*	*0.09*	*0.40*	*0.92*	*1.04*	*0.90*	*0.44*	*0.94*	*1.06*	*0.91*	*0.48*	*0.95*	*1.08*	*0.93*
50		*Tin*	*0.11*	*0.50*	*0.86*	*0.96*	*0.84*	*0.56*	*0.87*	*0.98*	*0.85*	*0.61*	*0.88*	*1.00*	*0.85*
82		*Lead*	*0.12*	*0.55*	*0.83*	*0.94*	*0.81*	*0.61*	*0.84*	*0.95*	*0.82*	*0.66*	*0.85*	*0.97*	*0.82*
12	Alkaline Earth	Magnesium	0.07	0.33	0.97	1.09	0.94	0.37	0.99	1.12	0.97	0.40	1.01	1.15	0.98
20		Calcium	0.10	0.45	0.88	0.99	0.86	0.51	0.90	1.02	0.87	0.55	0.91	1.03	0.88
38		Strontium	0.13	0.60	0.80	0.90	0.78	0.67	0.81	0.92	0.79	0.73	0.82	0.93	0.79
56		Barium	0.14	0.62	0.79	0.89	0.77	0.69	0.80	0.91	0.78	0.75	0.81	0.92	0.78
22	Transition Metals	Titanium	0.10	0.45	0.88	0.99	0.86	0.51	0.90	1.02	0.87	0.55	0.91	1.03	0.88
23		Vanadium	0.09	0.42	0.90	1.02	0.88	0.47	0.92	1.04	0.90	0.51	0.93	1.06	0.91
25		Manganese	0.07	0.30	0.99	1.11	0.96	0.34	1.01	1.15	0.98	0.37	1.03	1.17	1.00
26		Iron	0.08	0.35	0.95	1.07	0.93	0.39	0.97	1.10	0.95	0.43	0.99	1.13	0.96
27		Cobalt	0.07	0.33	0.97	1.09	0.94	0.37	0.99	1.12	0.97	0.40	1.01	1.15	0.98
28		Nickel	0.07	0.31	0.98	1.10	0.95	0.35	1.00	1.14	0.98	0.38	1.02	1.16	0.99
46		Palladium	0.10	0.45	0.88	0.99	0.86	0.51	0.90	1.02	0.87	0.55	0.91	1.03	0.88
78		Platinum	0.08	0.36	0.94	1.06	0.92	0.41	0.96	1.09	0.94	0.44	0.98	1.11	0.95
30		Zinc	0.07	0.34	0.96	1.08	0.94	0.38	0.98	1.12	0.96	0.41	1.00	1.14	0.97
60	Lanthanides	Neodymium	0.14	0.65	0.78	0.88	0.76	0.73	0.78	0.89	0.76	0.79	0.79	0.90	0.77
62		Samarium	0.14	0.62	0.79	0.89	0.77	0.69	0.80	0.91	0.78	0.75	0.81	0.92	0.78
63		Europium	0.13	0.60	0.81	0.91	0.79	0.67	0.81	0.92	0.79	0.72	0.82	0.93	0.80
66		Dysprosium	0.12	0.55	0.83	0.93	0.81	0.62	0.84	0.95	0.82	0.67	0.85	0.96	0.82
69		Thulium	0.12	0.53	0.84	0.94	0.82	0.60	0.85	0.96	0.83	0.65	0.86	0.98	0.83
70		Ytterbium	0.12	0.53	0.84	0.95	0.82	0.59	0.85	0.97	0.83	0.64	0.86	0.98	0.84

Figure C.2. Calculated coordination number (μ) and Goldschmidt tolerance factor (t) for potential metal cation replacements for lead in ABX_3 halide perovskites.

synthesized at the time this calculation was completed. Very soon after, a paper claiming to have synthesized $MACaI_3$ was published [352]. Similarly, another paper was found claiming to have synthesized $MABaI_3$ [353]. The tolerance factor calculation does not predict $MABaI_3$ as a stable perovskite: t is 0.79, outside but close to the lower limit (0.813). However, the criteria given by Li *et al.* is not infallible, as their paper also shows six experimentally synthesizable perovskites outside of the defined stability range. Indeed, several papers were found that claim to have synthesized $CsMgI_3$ [354], $CsBaI_3$ [355], and $CsSrI_3$ [356], none of which meet the above $0.442 < \mu < 0.895$ and $0.813 < t < 1.107$ criteria.

However, none of these papers present high-quality XRD data convincingly demonstrating perovskite formation; most include no XRD data at all [352–356]. It was thus thought worthwhile to pursue the synthesis of $MABaI_3$ and $MACaI_3$, with the goal of providing high quality structural and optoelectronic data. The synthesis of $CsBaI_3$ was also attempted as Cs compounds can withstand higher synthesis temperatures. While the bandgaps for $CsBaI_3$ and $MABaI_3$ perovskites are expected to be $>$3 eV, much too large for single-junction PV absorber layers, these materials could be used for tandem cells or transparent conducting contacts [353–357]. It is worth noting that 31 of the calculated compounds in Figure C.2 meet the Li *et al.* criteria. Experimentally screening all of these compounds would be quite time intensive - and supporting DFT calculations by the Gagliardi group were used to further assess the potential for these materials to be stable, as detailed in Section C.3 [67]. In this preliminary work, the strategy has been to select some promising candidates ($MABaI_3$, $MACaI_3$, and $CsBaI_3$) and attempt to synthesize them using solid state and solution methods.

C.1.2 Development of Air-Free Characterization Techniques

The metal halide precursors for the perovskites chosen for synthesis (BaI_2, CaI_2) are very hygroscopic: they will visibly liquefy in air in a matter of hours (see Figure C.3d). Furthermore, it was unknown whether $MABaI_3$, $MACaI_3$, and/or $CsBaI_3$ would be stable in ambient conditions. Thus, a method for conducting XRD and optical measurements without air exposure was required.

Existing methods for encapsulating air-sensitive materials for XRD, including glass capillary tubes and a variety of Kapton and Mylar tapes, were tested. All proved inadequate in their sealing and/or attenuation properties. Therefore, a small vessel was fabricated with a 3.6 μm Mylar window and an o-ring seal, as seen in Figure C.3b. This vessel was used for XRD measurements on all powders and thin films in this chapter unless otherwise stated. Measurements were taken with the Bruker D8 Discover 2D diffractometer (CoKα source, 1.78899 Å). Angles down to 10° 2θ can be reliably measured with this vessel using standard length X-ray collimators.

A sealed vessel for optical measurements was made by adding quartz windows to a KF-flange (Figure C.4). Quartz has low absorption in the UV, which is important for the high-bandgap materials being studied. This vessel was validated in PL and UV-vis setups with a $\sim$400 nm film of NPD (N,N'-Di(1-naphthyl)-N,N'-diphenyl-(1,1'-biphenyl)-4,4'-diamine), an

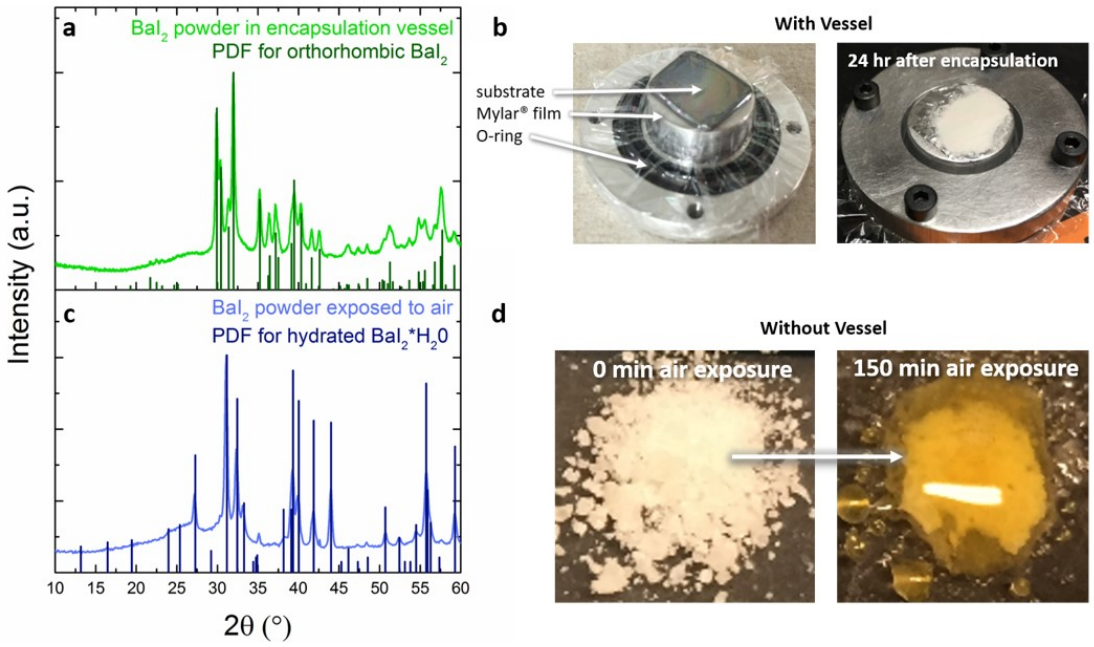

Figure C.3. (a) XRD pattern from BaI_2 powder in vessel after 24 hrs. (b) Vessel for air-free XRD measurements. (c) XRD pattern of air-exposed BaI_2, which matches with the hydrated compound BaI_2*H_20. (d) Visible hydration of air-exposed BaI_2 powder. X-ray diffraction was collected using a Bruker D8 2D diffractometer with Co Kα radiation (λ=1.7889 Å).

HTL used for organic light-emitting devices, which has absorption and luminescence features in the visible and UV [358, 359]. Spectral peak shapes and locations were maintained when using the vessel.

Figure C.4. Sealing vessel for air-free PL and UV-vis measurements, with demonstration of sealing using highly hygroscopic CaI_2.

C.2 Attempted Synthesis of $MABaI_3$, $MACaI_3$ and $CsBaI_3$

C.2.1 Thin Films from Solution

Both one-step and vapor-assisted two-step methods were used in an attempt to synthesize $MABaI_3$ and $MACaI_3$ perovskites. The method for making one-step thin films followed the procedure outlined by Kumar *et al.* [353]. A 1:1 molar ratio of MAI:XI_2 (X = Ba, Ca) powders was dissolved in Dimethlyformamide (DMF) at a concentration equivalent to 40 wt% perovskite. Solutions were kept at 70 °C and stirred at 1000 RPM for 12 hours. At intervals of 7, 14, 21, and 25 days, films were made *via* spin coating at 2000 RPM and were subsequently annealed at 100 °C for 30 minutes.

Films were characterized using 2D XRD. Predicted XRD patterns were simulated based on the unit cell parameters from Kumar *et al.* for $MABaI_3$ (a = 9.299 Å, b = 9.301 Å and c = 13.936 Å) [353] and Uribe *et al.* for $MACaI_3$ (a = 6.2632 Å, b = 6.2780 Å and c = 6.3692 Å) [352]. Predicting exact peak locations for perovskites is difficult due to the subtleties of octahedral tilting. What is important is that regardless of this tilting, perovskites with BaI_6 and CaI_6 octahedra are expected to have planes with d-spacings of $\sim$6.4 to 7.2 Å, which correspond

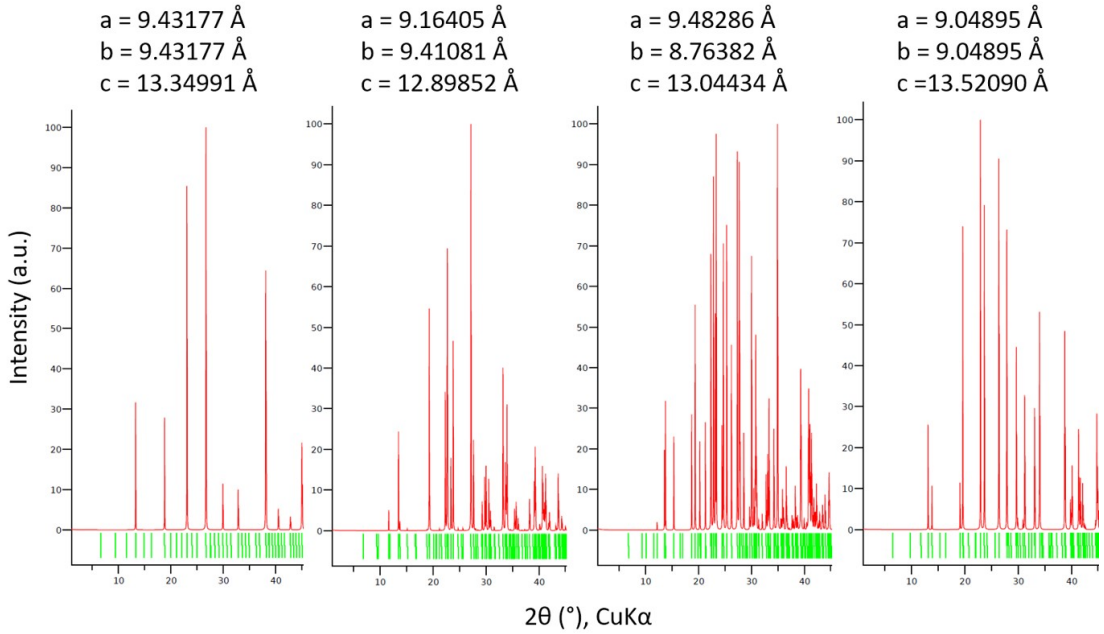

Figure C.5. XRD patterns for several simulated low-energy $CsBaI_3$ crystal structures from the Gagliardi group.

to reflections between 14.3° and 16.1° 2θ (CoKα). This was further verified by simulations on various unit cell geometries performed by the Gagliardi group for $CsBaI_3$, presented in Figure C.5, which show peaks below 15° 2θ for all cases.

Unfortunately, no solution processed films measured with XRD showed any peaks matching the simulated MHP patterns, as shown in Figure C.6. Furthermore, all peaks could be entirely matched by precursor materials, suggesting that a perovskite was not formed in any measureable quantity. As solvent choice has been shown to impact perovskite formation, this procedure was repeated with Dimethyl sulfoxide (DMSO) with the same result (Figure C.6a) [142].

One issue encountered during this process was that the majority of films measured had peaks only corresponding to MAI-they were missing all BaI_2 or CaI_2 peaks. All films that had visible BaI_2 or CaI_2 peaks also had peaks corresponding to hydrated compounds (*e.g.* BaI_2*H_20). We hypothesize that this is due to the extreme air sensitivity of BaI_2 and CaI_2 precursors. Although all synthesis and encapsulation steps were performed in a glovebox, even a trace amount of water in the glovebox or a small leak in the mylar could be sufficient to liquefy a thin film. The issue of creating thin films stable enough for characterization was documented in the literature

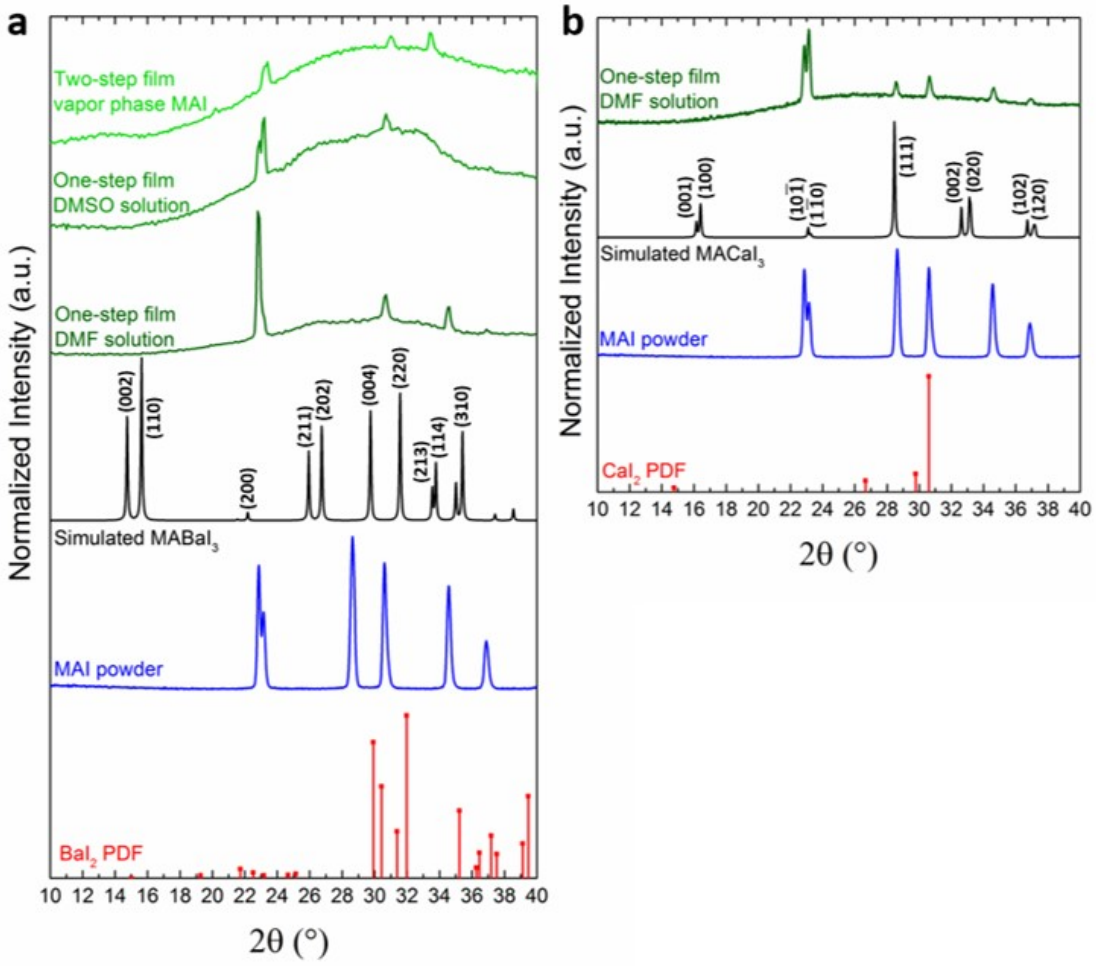

Figure C.6. XRD patterns for air-free solution processed films of (a) MAI and BaI_2 and (b) CaI_2 and MAI. No films showed peaks indicative of perovskite formation. X-ray diffraction was collected using a Bruker D8 2D diffractometer with Co Kα radiation (λ=1.7889 Å).

for $MACaI_3$ [352].

UV-vis absorbance measurements were also recorded for solution processed films. Based on the work of Kumar *et al.*, $MABaI_3$ has a bandgap of ~3.9 eV (~320 nm). All films measured showed a lack of visible peaks above 250 nm, providing further evidence that HPs did not form in any measureable quantity.

A two-step vapor-assisted solution method was also attempted to synthesize $MABaI_3$ and $MACaI_3$. Multiple reaction temperatures and times were tried (e.g., 100 °C for 1 hr, 100 °C

for 24 hr), and each was validated using $MASnI_3$ (Figure C.7). The deposition of MAI onto the substrate was also confirmed visually: upon exposure to MAI, the XI_2 films changed from smooth and transparent to rough and white. An XRD pattern from a representative $MABaI_3$ film is shown in Figure C.6a (lightest green trace), which exhibits peaks only corresponding to MAI.

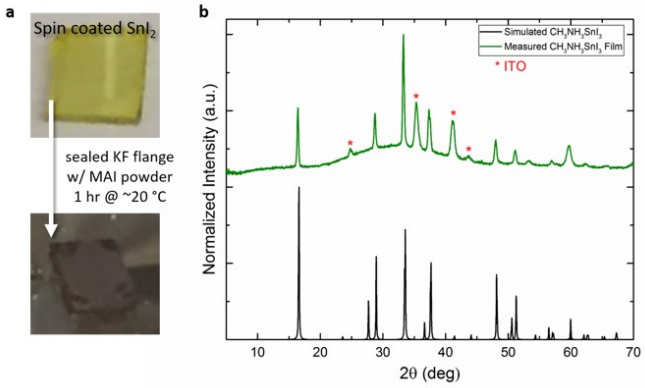

Figure C.7. (a) Appearance of SnI_2 film after spin coating, and then perovskite formation after sitting in a sealed vessel with MAI powder at room temperature for 1 hr. (b) XRD pattern confirming $MASnI_3$ formation for black film. X-ray diffraction was collected using a Bruker D8 2D diffractometer with Co Kα radiation (λ=1.7889 Å).

C.2.2 Solution Aging

During the process of attempting to make thin films from solution, it was observed that some of the solutions yellowed over time. As single-crystal lead-perovskites are often grown in solution [60], it was at first though that this color change could indicate a reaction between MAI and BaI_2, and perhaps even the formation of a perovskite. A reaction occurring in the solution phase is supported by the data presented in Kumar *et al.*: perovskite formation only occurred after the BaI_2 and MAI solution had been aged for 7 or more days [353].

To investigate this possibility, a DMF solution was made with only the BaI_2 precursor (without MAI). When exposed to air, this BaI_2 only solution also yellowed. A series of UV-Vis absorbance measurements were recorded for both BaI_2 + MAI and BaI_2 only solutions as a function of air exposure time. These data are shown in Figure C.8. The solutions had the same absorbance trends over time, suggesting that the yellowing was not due to a reaction between MAI and BaI_2, and thus was not due to perovskite formation. Additionally, thin films made *via*

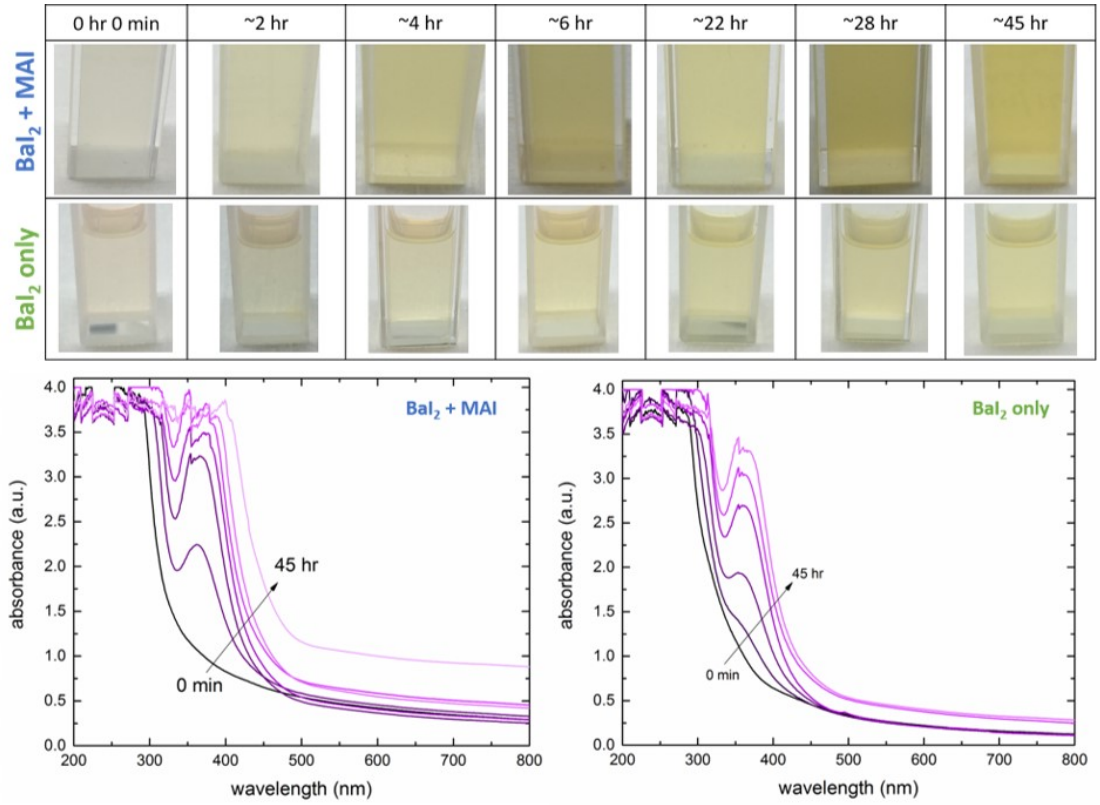

Figure C.8. Solutions of BaI_2 and BaI_2 + MAI in DMF, yellowing with air exposure, and corresponding UV-vis scans.

spin coating from yellowed and non-yellowed BaI_2 and MAI solutions showed no differentiating features in UV-vis measurements.

Yellowing upon exposure to air could be due to the hygroscopic nature of the BaI_2 compounds. However, water added to the solution in an N_2 glovebox produced no visible color change. This suggests exposure to water alone is not responsible for the yellowing. Nonetheless, this has no impact on the conclusion that the yellowing is not due to perovskite formation.

C.2.3 Solid State Precursor Methods

Several difficulties were encountered during solution-based synthesis, including dewetting during film formation, poor film morphologies, and extreme air-sensitivity of films and solutions. This motivated the use of a more robust, solution-free process for $MABaI_3$, $MACaI_3$, and

$CsBaI_3$. "Solid state precursor" methods have been successfully used in the literature to synthesize HP materials, and involve the heating of well-mixed solid precursors (e.g. BaI_2 + MAI) [60]. While typically resulting in a less phase-pure perovskite, this method is more robust and provides a much larger sample volume for characterization.

The most direct way to observe perovskite formation is to perform measurements during the heating process. To that end, *in-situ* heated XRD and differential scanning calorimetry (DSC) measurements were done on mixed precursor samples as a function of temperature. Using the *in situ* heating capabilities of the D8 Advance XRD, we attempted to follow the solid-state reactions as mixtures of XI_2 and MAI powders are heated while collecting XRD. The D8 Advance relies on a highly flat powdered sample for alignment and measurement. Unfortunately, it was observed that MAI powder grows 3D crystals out of the plane when it is heated for >1hr (Figure C.9). This behavior makes in situ heated XRD an ineffective characterization technique for solid-state perovskite synthesis involving MAI.

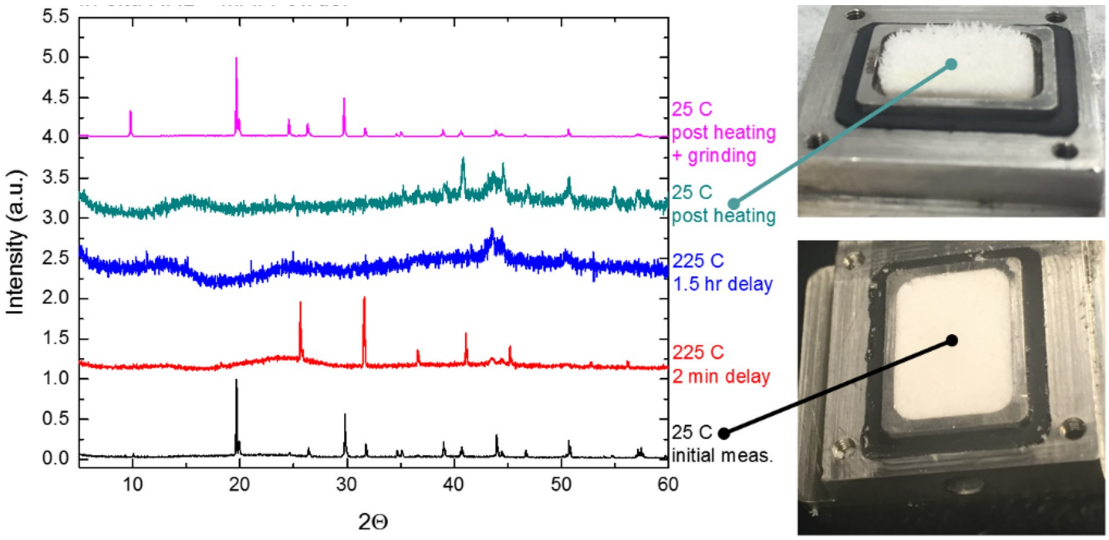

Figure C.9. In-situ heated XRD on MAI powder sample. Upon heating, an initially flat sample results in 3D crystal growth, which renders the measurement impossible. XRD was collected using a Bruker D8 Advance diffractometer with Cu Kα radiation (λ=1.541 Å).

Differential scanning calorimetry (DSC) is another method that can probe if a reaction between two heated powders occurs at various temperatures. DSC measurements were taken on finely ground (~5 mg) powders of individual precursors (BaI_2, CaI_2, or MAI) and mixed precursors (BaI_2 with MAI, CaI_2 with MAI). All samples were loaded into hermetically sealed

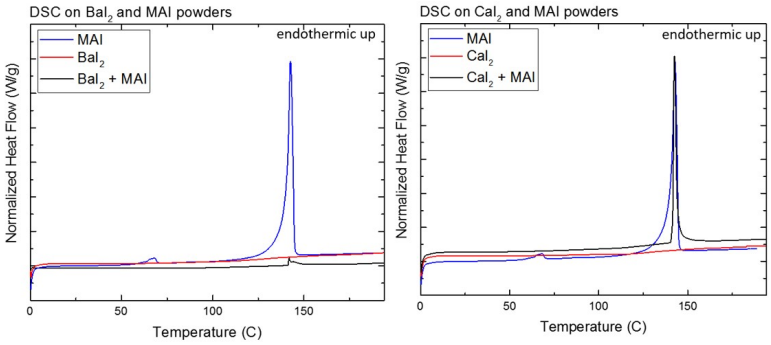

Figure C.10. DSC data for individual precursor powders and mixed powders. The only distinct feature is the phase change of MAI near 140 °C.

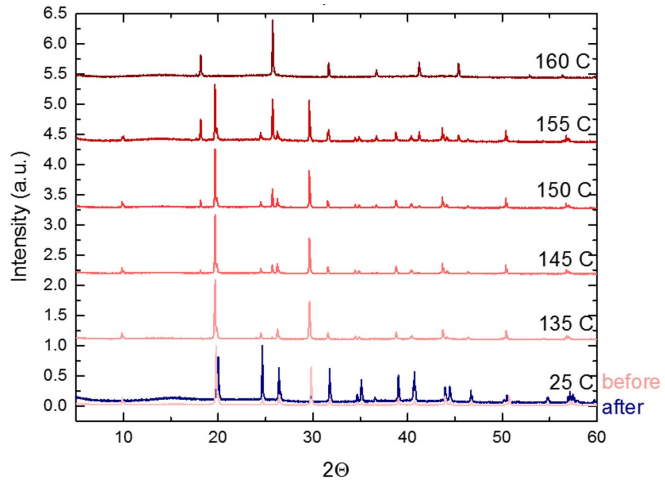

Figure C.11. X-ray diffraction patterns showing methylammonium iodide (MAI) phase change. The phase change from tetragonal to cubic crystal structures begins to occur at ∼145 °C, and is visibly until 155 °C in this data. XRD was collected using a Bruker D8 Advance diffractometer with Cu Kα radiation (λ=1.541 Å).

DSC pans in an N_2 glovebox. Samples were heated at a rate of 1° C/min, up to 200 °C (below the decomposition temperature of MAI). Figure C.10 shows DSC traces for BaI_2 and CaI_2 measurements. The only distinct feature in the mixed precursor powders is due to the phase change of MAI near 140 °C, which was also confirmed *via* XRD (Figure C.11). There was no indication of a reaction between the precursor powders at these temperatures and heating rate. Higher temperatures are inaccessible due to the decomposition of MAI (Figure C.12), but longer time at the highest temperature may enable a reaction if the reaction is kinetically limited.

Because in-situ heated XRD and DSC proved inconclusive, we attempted solid-state synthesis by heating mixed precursor powders in ampoules for long reaction times. In a glovebox, finely ground powders (mixed by co-grinding) were loaded into a 0.5" OD quartz ampoule, which was evacuated overnight to ∼3 mTorr. Ampoules were then flame-sealed and heated in a furnace at the desired temperature (see Figure C.13a). After heating, the resulting powders/ingots were ground and characterized using 2D XRD. This procedure was carried out for

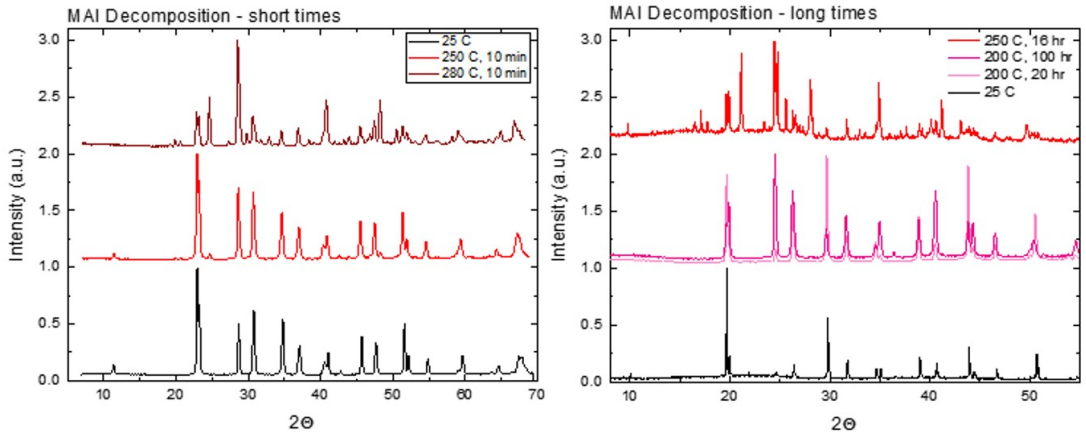

Figure C.12. Decomposition of MAI. All samples are MAI powder heated in sealed quartz ampoules (∼3 mTorr N_2). XRD was collected using a Bruker D8 2D diffractometer with Co Kα radiation (λ=1.7889 Å).

a

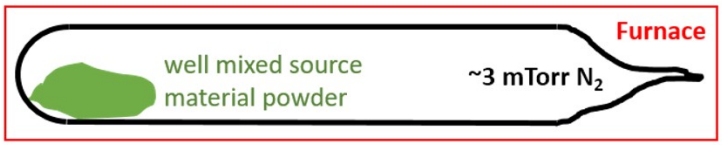

b

Precursor Powders	Furnace Temperatures	Precursor Ratios (XI_2:AI)
BaI_2 + MAI	44 hr at 150 °C 100 hr at 200 °C	1:1 1:3, 1:1, 3:1
BaI_2 + CsI	12 hr at 750 °C	1:6, 1:3, 1:1, 3:1
CaI_2 + MAI	44 hr at 150 °C	1:1

Figure C.13. (a) Schematic of solid-state precursor reaction method. (b) Solid-state synthesis parameters tested.

a variety of stoichiometries and temperatures, as summarized in Figure C.13b. The MAI compounds could not be heated above 200 °C, because MAI starts to decompose above this temperature (see Figure C.12). The Cs and BaI_2 compounds, however, can be heated above their melting temperatures. This "Bridgman Technique" is common for growing $CsBX_3$ (B=Ba, Sr, Ca, X=Halogen) crystals for scintillators [355, 356, 360, 361]. All tests were also done on neat precursor powders (BaI_2, CaI_2, MAI, CsI) as a control.

None of the solid-state trials resulted in measurable perovskite formation, as determined from the absence of XRD peaks below 20° 2θ. Figure C.14 shows representative XRD data from these experiments. Ca compounds are not included due to issues with sample hydration. The MAI and BaI_2 compound shown in Figure C.14a has peaks that correspond only to MAI.

As with the thin films, trials that had visible BaI_2 peaks also showed hydrated BaI_2 compounds.

XRD patterns for the BaI_2 and CsI precursors are shown in Figure C.14b. The 3:1 BaI_2:CsI stoichiometry formed the known "double-salt iodide" material $CsBa_2I_5$ [362]. Increasing the molar ratio of CsI resulted in the disappearance of the $CsBa_2I_5$ phase, appearance of significant CsI precursor peaks, and also the appearance of two peaks near 30° 2θ (marked with question marks). While the exact identity of these peaks were not identifiable, our hypothesis is that they are shifted BaI_2 peaks due to the incorporation of Cs interstitial or substitutional defects. At the 1:1 ratio, the unknown peak is shifted left of the nominal BaI_2 peaks by 0.16° 2θ. At 1:3 and 1:6 CsI:BaI_2 ratios, the measured peaks are shifted by 0.3° 2θ. The increase in peak shift could be due to an increase in Cs^+ incorporation into the lattice, which appears to saturate above the 1:3 ratio. Peaks shifted to a lower angle would reflect the larger size of Cs^+ compared to Ba^{2+}. Regardless of the identity of these two peaks, the powder XRD patterns in Figure C.14b lack any peaks below 20° 2θ, indicating that no measureable amount of perovskite was formed. Unlike the synthesis of $MABaI_3$, where all precursors stayed in the solid phase, melting the precursors means that kinetic barriers are an unlikely cause of lack of perovskite formation. This is confirmed with the measured formation of the $CsBa_2I_5$ phase.

The results presented here provide significant evidence that $MABaI_3$, $MACaI_3$, and $CsBaI_3$ perovskites were not synthesized in measurable quantities using a variety of techniques. While this does not conclusively prove that these perovskites cannot be made, it does suggest that they would have high kinetic barriers to reaction and/or exist in metastable states.

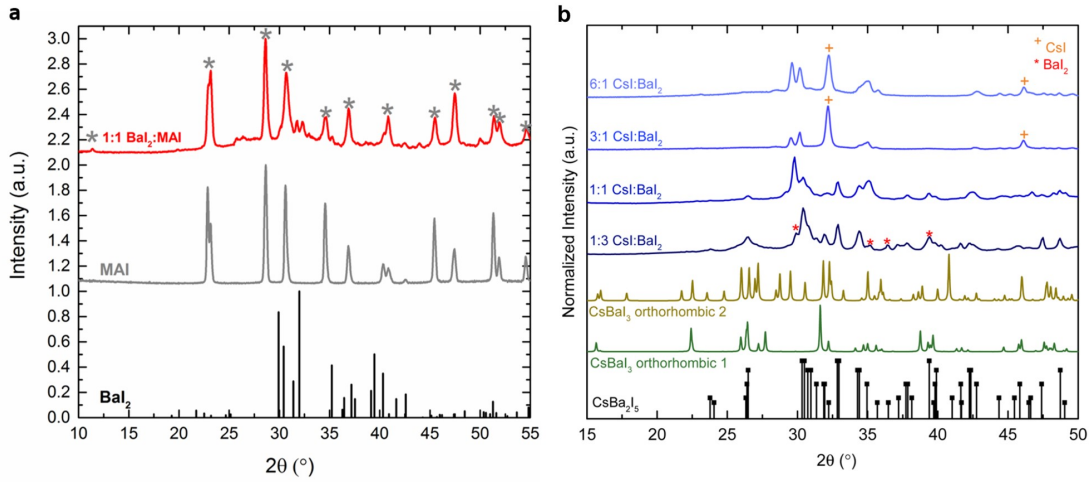

Figure C.14. (a) XRD pattern for 1:1 molar ratio of BaI_2:MAI heated for 100 hr at 200 °C, showing no appreciable formation of $MABaI_3$ perovskite. (b) XRD patterns for different stoichiometries of CsI and BaI_2 precursors used in an attempt to synthesize $CsBaI_3$. The 1:3 CsI:BaI_2 ratio (darkest blue trace) formed the known $CsBa_2I_5$ double-salt iodide (black sticks) with the residual BaI_2 precursor (red asterisks). Increasing the molar ratio of CsI resulted in the disappearance of the $CsBa_2I_5$ phase and the appearance of significant CsI precursor peaks (orange crosses). Two unknown peaks near 2θ =30°, hypothesized to be shifted BaI_2 peaks due to the incorporation of Cs interstitial or substitutional defects, are evident in the 3:1 and 6:1 CsI:BaI_2 traces. Notably, no peaks match the simulated $CsBaI_3$ patterns (green and yellow traces), which suggests that the $CsBaI_3$ perovskite was not formed in a measurable quantity. XRD was collected using a Bruker D8 2D diffractometer with Co Kα radiation (λ=1.7889 Å).

C.3 Collaboration with the Gagliardi Group

To support a collaboration with the Gagliardi group, we also attempted the synthesis of $CsSrBr_3$ and $CsCaI_3$ [67]. As with $MACaI_3$, the attempted synthesis of $CsCaI_3$ was similarly unsuccessful, likely due to the extreme hygroscopicity of CaI_2. All XRD patterns measured showed peaks that could be entirely matched by CsI, CaI_2, or hydrated versions of CaI_2 such as CaI_2*H_2O.

By contrast, $CsSrBr_3$ was readily synthesized using the solid-state technique shown in Figure C.13a. Figure C.15 shows the XRD patterns for 1:2, 1:1, and 2:1 molar ratios of CsBr and $SrBr_2$ precursors, all of which resulted in significant formation of $CsSrBr_3$, with some residual precursor in the 1:2 and 2:1 ratios. Absorption measurements were performed on $CsSrBr_3$ powder suspended in silicone oil (Figure C.16). No appreciable absorption was detected in this suspension down to a wavelength of 200 nm, suggesting a band gap greater than 6.2 eV. This

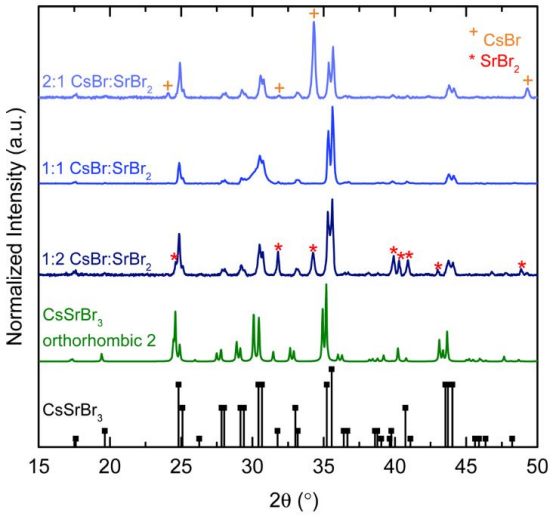

Figure C.15. XRD patterns for different stoichiometries of CsBr and $SrBr_2$ precursors used to synthesize $CsSrBr_3$. All three ratios (blue traces) show the formation of the $CsSrBr_3$ perovskite (black sticks). As expected, the 1:2 ratio also contains excess $SrBr_2$ (red asterisks), and the 2:1 ratio contains excess CsBr (orange crosses). XRD was collected using a Bruker D8 2D diffractometer with Co Kα radiation (λ=1.7889 Å).

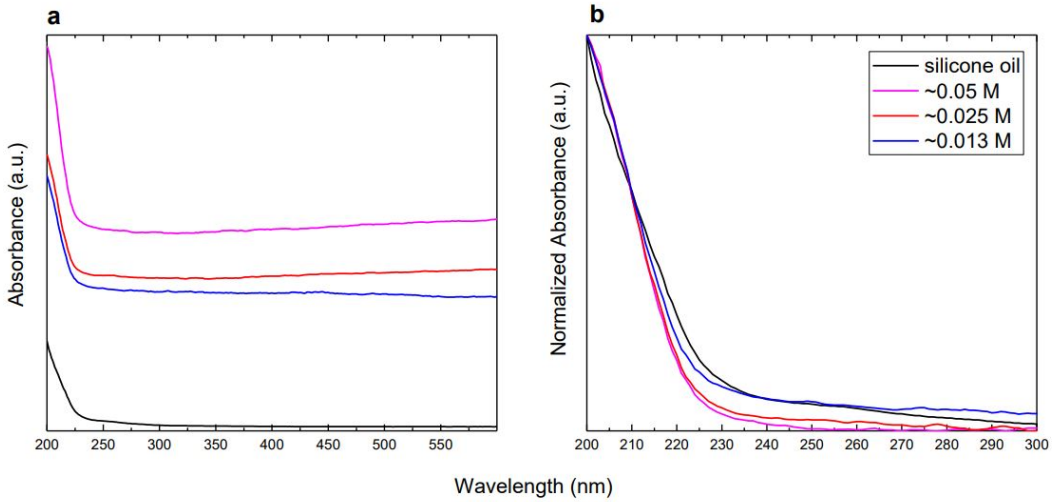

Figure C.16. Absorption data for several concentrations of $CsSrBr_3$ suspended in silicone oil. (a) Raw absorbance data, which shows significant scattering at long wavelengths for large concentrations. (b) Normalized absorbance data, which shows there is no significant absorption above the background silicone oil signal down to 200 nm (instrument limit). This indicates that the optical bandgap of $CsSrBr_3$ could be $>$6.2 eV.

large bandgap was supported by a calculated band gap of 5.7 eV using the HSE06 functional [67].

In parallel with our experimental work, the Gagliardi group performed electronic structure

calculations of $CsMI_3$ perovskites with M = Ge, Sn, Pb, Mg, Ca, Sr, and Ba. The goal was to identify which, if any, alkaline earth metal species would be a viable replacement for lead in ABX_3 MHPs. Using several different density functional theory (DFT) functionals, the formation energy of different perovskite phases, their relative stability, and structural and electronic properties were explored. The outcome of this study wass that Mg and Ba perovskites are unlikely to form in the cubic, tetragonal, or orthorhombic phases because they have positive formation energies. Ca and Sr perovskites had negative formation energies (with respect to the metal-iodide precursors), however they exhibit wide band gaps and high hygroscopicity, making these unlikely candidates for applications in photovoltaic devices. These DFT results supported our experimental findings, and motivated purusing other types of perovskites going forward. Details of the DFT calculations and results can be found in ref [67].

Appendix D

Appendix for Chapter 4

D.1 Custom Metal Parts

The following section contains drawings that were provided to the CSE shop for making the custom metal parts for the CGAVD system.

Component 1
All dimensions in inches

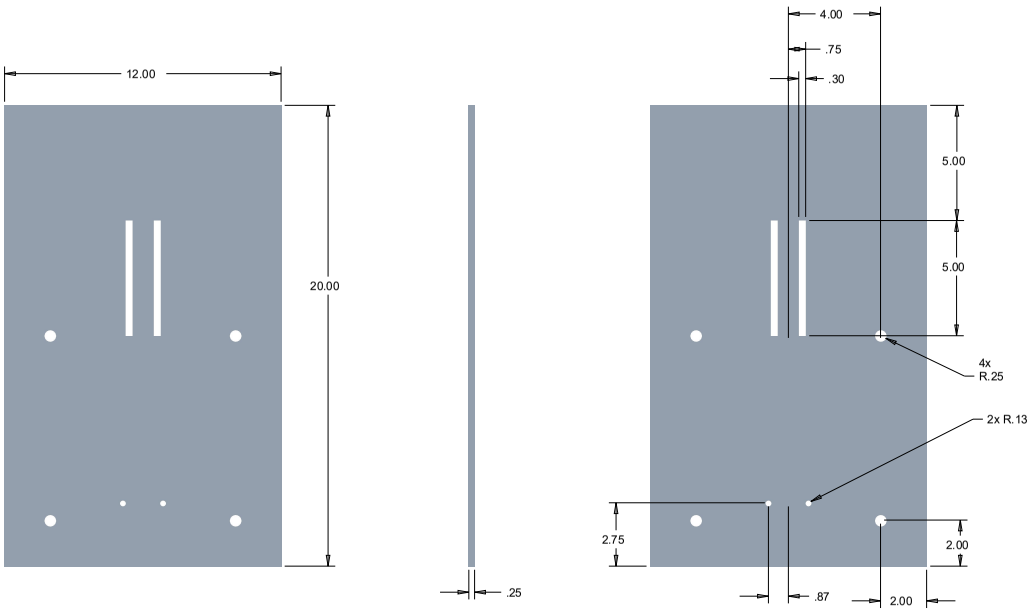

Component 3
All dimensions in inches
Made of stainless steel

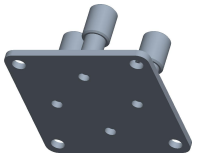

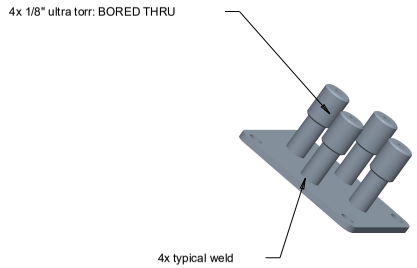

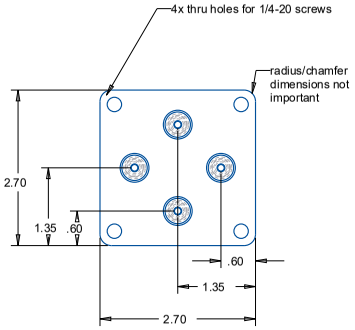

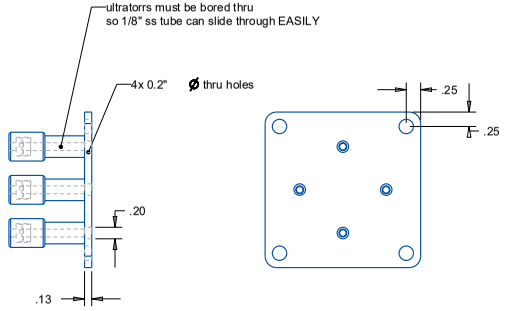

Component 4
All dimensions in inches
Block can be made out of Al and connected to SS components via epoxy

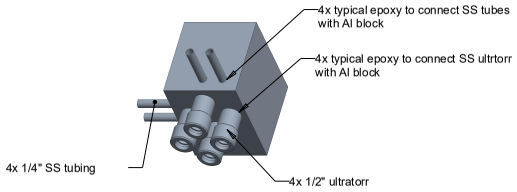

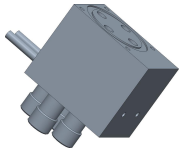

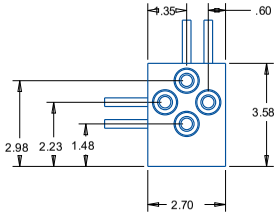

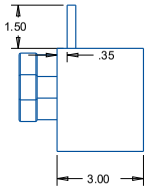

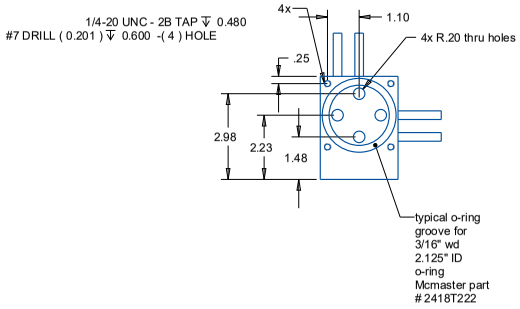

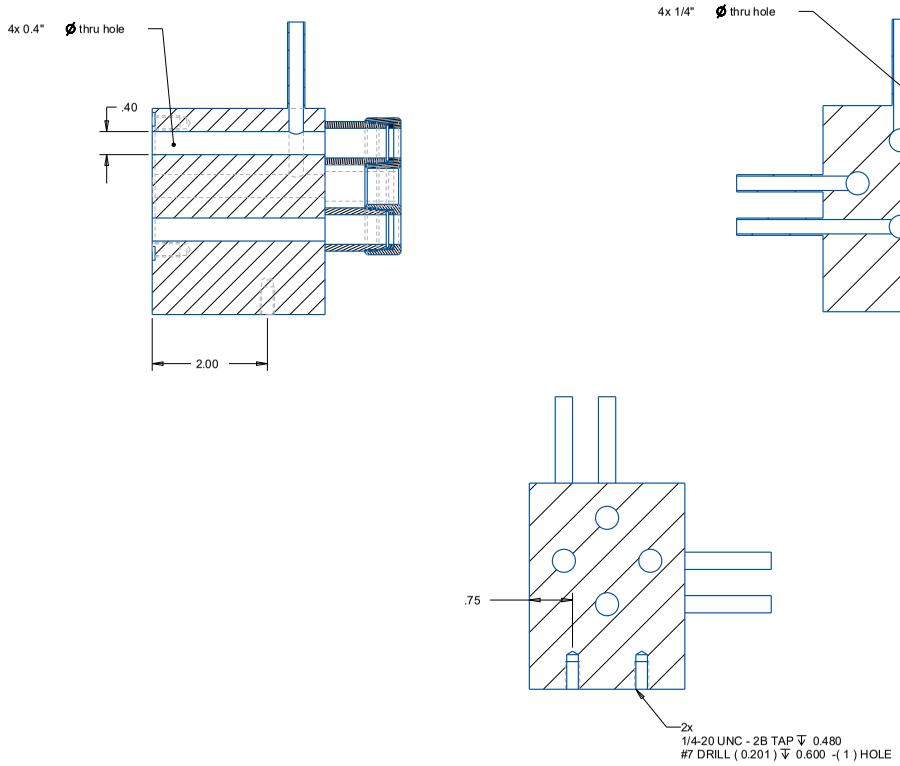
4x 0.4" Ø thru hole
.40
2.00
4x 1/4" Ø thru hole
.75
2x
1/4-20 UNC - 2B TAP ↧ 0.480
#7 DRILL (0.201) ↧ 0.600 -(1) HOLE

Component 5
All dimensions in inches

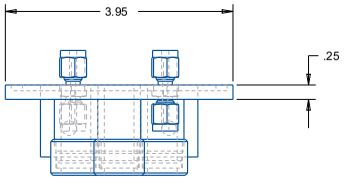

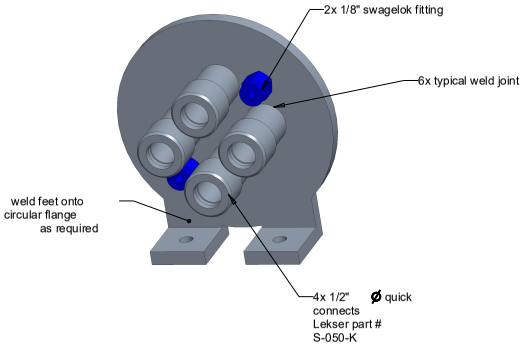

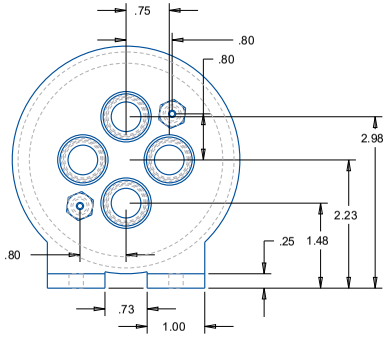

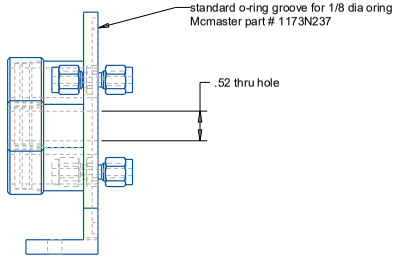

Component 6: Showerhead

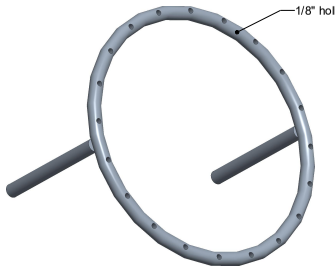

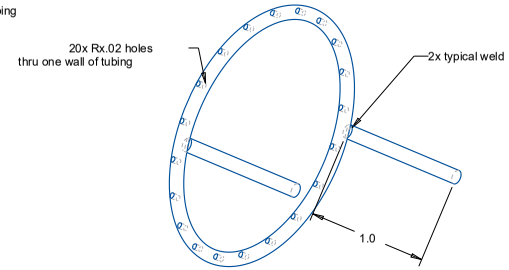

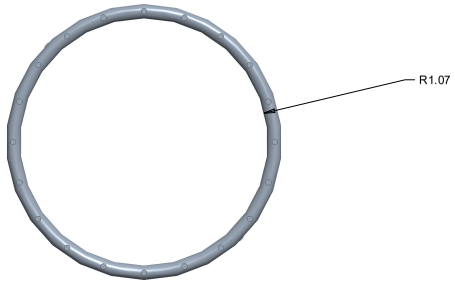

COOLED_CHUCK_ASSYM

Component 3: Cooled Chuck
fabricated from 316 SS and OFE Cu

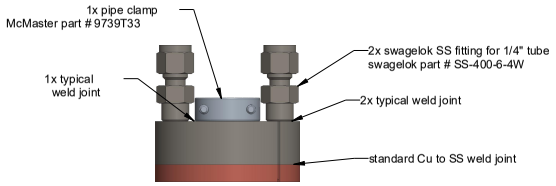

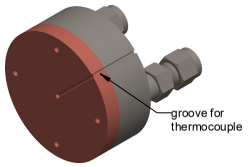

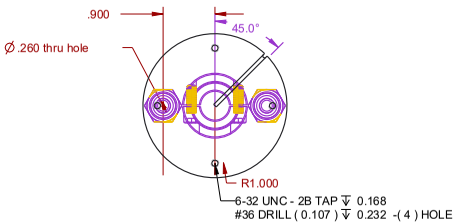

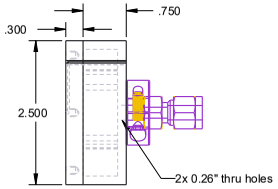

		DRAWN BY	DATE
		CHECKED BY	DATE
		APPROVED BY	DATE
	SCALE 1:1		SHEET 1 OF1
UNLESS OTHERWISE SPECIFIED ALL DIMENSIONS ARE IN INCHES. TOLERANCES ARE: X.XX = ± 0.1 X.XXX = ± 0.01 X.XXX = ± 0.01 ANG = ± 1 °	TITLE		
DO NOT SCALE	PROJECT	MODEL NAME: COOLED_CHUCK_ASSYM	ISSUE

ASME STANDARD INCH

MODEL NAME: COOLED_CHUCK_ASSYM

TITLE

detailed view of cooling channels inside SS component

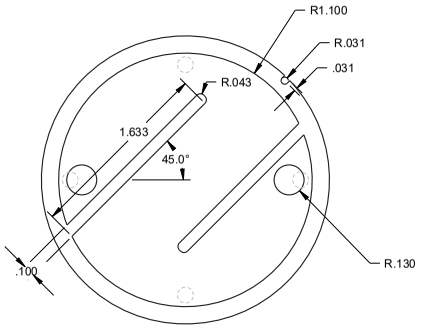

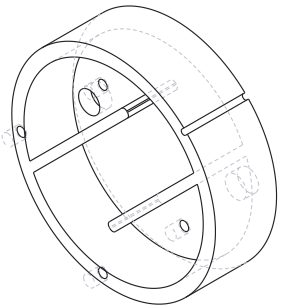

		DRAWN BY	DATE
		CHECKED BY	DATE
		APPROVED BY	DATE
	THIS DOCUMENT IS SUPPLIED IN CONFIDENCE AGREEING NOT TO DISCLOSE ITS CONTENTS TO ANY THIRD PARTY WITHOUT THE WRITTEN PERMISSION OF MTI BASED WITH OUT THE COPYRIGHT OR MEMORY PRIOR OR	SCALE 2:1	SHEET 1 OF1
UNLESS OTHERWISE SPECIFIED ALL DIMENSIONS ARE IN INCHES TOLERANCES ARE: X.XX = ± 0.01 X.XXX = ± 0.005 ANG +/- 1 °	TITLE		
DO NOT SCALE	PROJECT	MODEL NAME: COOLED_CHUCK_ASSYM	ISSUE

SUBSTRATE_HOLDER_PLATE

Component 2: Substrate Holder
fabricated from OFE copper

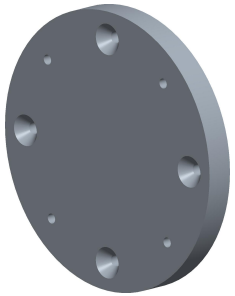

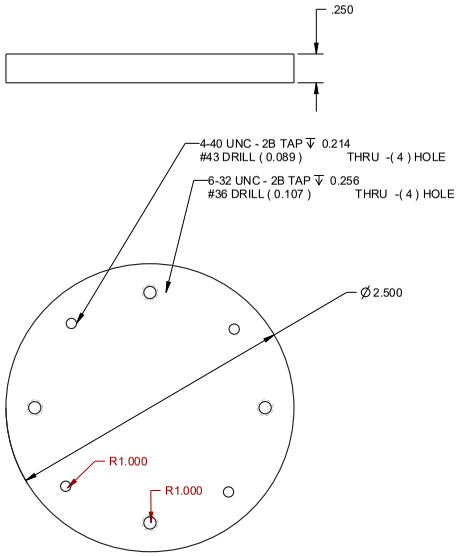

		DRAWN BY	DATE
		CHECKED BY	DATE
		APPROVED BY	DATE
		SCALE 2:1	SHEET 1 OF1

UNLESS OTHERWISE SPECIFIED ALL DIMENSIONS ARE IN INCHES
TOLERANCES ARE:
X ± 0.1
XXX ± 0.01
XXXX ± 0.001
ANG +/- 1 °

DO NOT SCALE

TITLE

PROJECT

MODEL NAME: SUBSTRATE_HOLDER_PLA

ISSUE

ASME STANDARD(INCH)

MODEL NAME
SUPPORT_ROD

TITLE

Component 4: Support Rod
fabricated from 316 SS
I would like 2 rods - one solid and one
hollow (a standard wall thickness is fine)

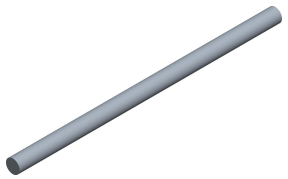

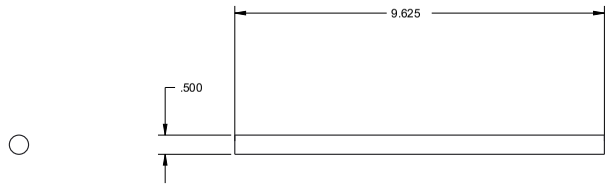

		DRAWN BY	DATE
		CHECKED BY	DATE
		APPROVED BY	DATE
THIS DOCUMENT IS SUPPLIED IN CONFIDENCE AGREEMENT BUT TOK OF ANY KIND WHATSOEVER AND NO LIABILITY IS ACCEPTED FOR ANY ACTION IN MATTERS MADE WITH OUT THE EXPRESS CONSENT OF MEYER ENGINEERING		SCALE 2:3	SHEET 1 OF1
UNLESS OTHERWISE SPECIFIED ALL DIMENSIONS ARE IN INCHES TOLERANCES ARE: X.XX = ± 0.1 X.XXX = ± 0.01 X.XXX = ± 0.001 ANG = ± 1 °	TITLE		
DO NOT SCALE	PROJECT	MODEL NAME SUPPORT_ROD	ISSUE

ASME STANDARD INCH

SUBSTRATE_FLANGE_ASSYM

Component 5: Substrate Flange fabricated from 316 SS

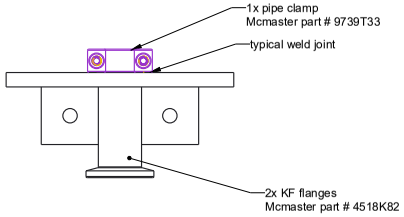

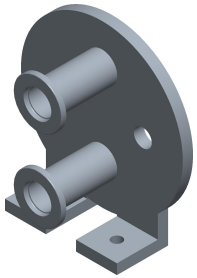

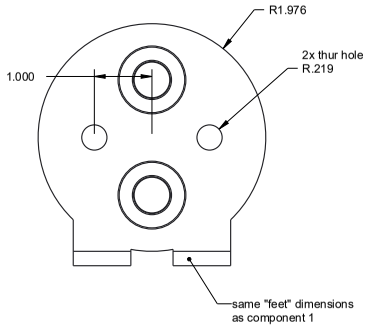

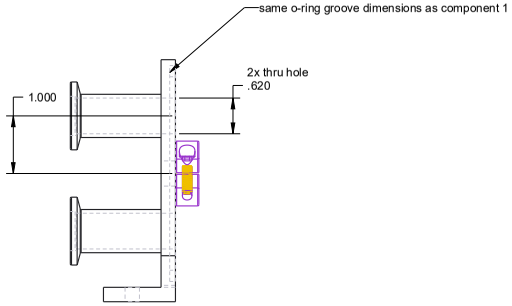

	DRAWN BY		DATE
	CHECKED BY		DATE
	APPROVED BY		DATE
THIS DOCUMENT IS SUPPLIED IN CONFIDENCE AGREEMENT BUT IS NOT TO BE REPRODUCED OR DISCLOSED TO ANY OTHER PERSON WITHOUT THE WRITTEN CONSENT OF MIT MEMS WITH WHOM THE COPYRIGHT OR MEMS PROTECTION RIGHTS OR	SCALE 1:1		SHEET 1 OF1
UNLESS OTHERWISE SPECIFIED ALL DIMENSIONS ARE IN INCHES TOLERANCES ARE: X.XX = ± 0.01 X.XXX = ± 0.005 ANG +/- 1 ° DO NOT SCALE	TITLE		
	PROJECT	MODEL NAME	ISSUE
		SUBSTRATE_FLANGE_ASS	

ASME STANDARD(INCH)

D.2 Custom Quartz

The following section contains drawings that were provided for making the custom quartz parts for the CGAVD system.

General Description

Double-flanged quartz tube

Tube is 75 mm (2.953 in) ID, 80 mm (3.150 in) OD

Flanges are 0.5" thickness and 0.5" width

Total length of tube and flanges is 41"

See drawing below for dimensions and tolerances

All dimensions are in inches

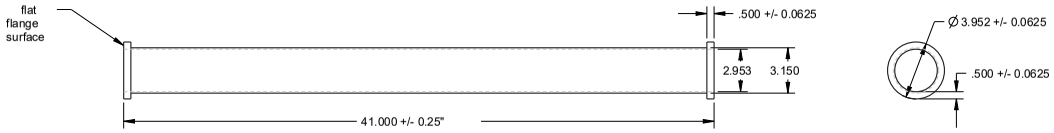

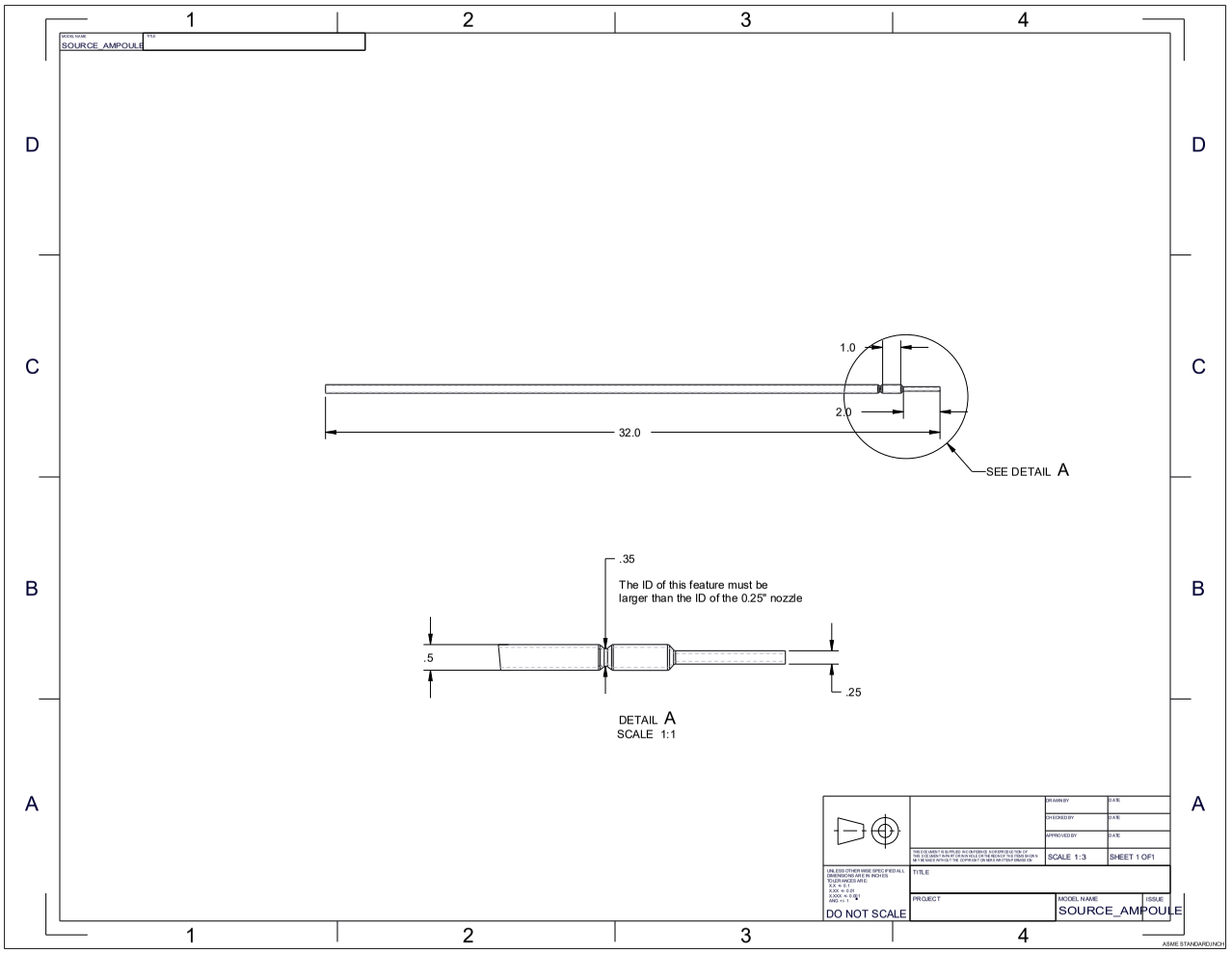
1
2
3
4
A
B
C
D
MODEL NAME
SOURCE_AMPOULE
TITLE
1.0
2.0
32.0
SEE DETAIL A
.35
The ID of this feature must be
larger than the ID of the 0.25" nozzle
.5
.25
DETAIL A
SCALE 1:1
DRAWN BY
DATE
CHECKED BY
DATE
APPROVED BY
DATE
SCALE 1:3
SHEET 1 OF1
TITLE
PROJECT
MODEL NAME
SOURCE_AMPOULE
ISSUE
DO NOT SCALE
ASME STANDARD INCH

MODEL NAME
SOURCE_AMPOULE

TITLE

	DRAWN BY	DATE
	CHECKED BY	DATE
	APPROVED BY	DATE
THIS DOCUMENT IS SUPPLIED IN CONFIDENCE. A CONFIDENTIALITY AGREEMENT MUST BE IN PLACE BEFORE ANY INFORMATION IN IT IS USED WITH OUT THE COPYRIGHT OWNERS WRITTEN PERMISSION.	SCALE 1:3	SHEET 1 OF1

UNLESS OTHERWISE SPECIFIED ALL DIMENSIONS ARE IN INCHES
TOLERANCES ARE:
X.X = ± 0.1
X.XX = ± 0.01
X.XXX = ± 0.001
ANG +/- 1 °

DO NOT SCALE

TITLE

PROJECT

MODEL NAME
SOURCE_AMPOULE

ISSUE

New source material holder

All material is quartz
Drawing not to scale
All units in milimeters

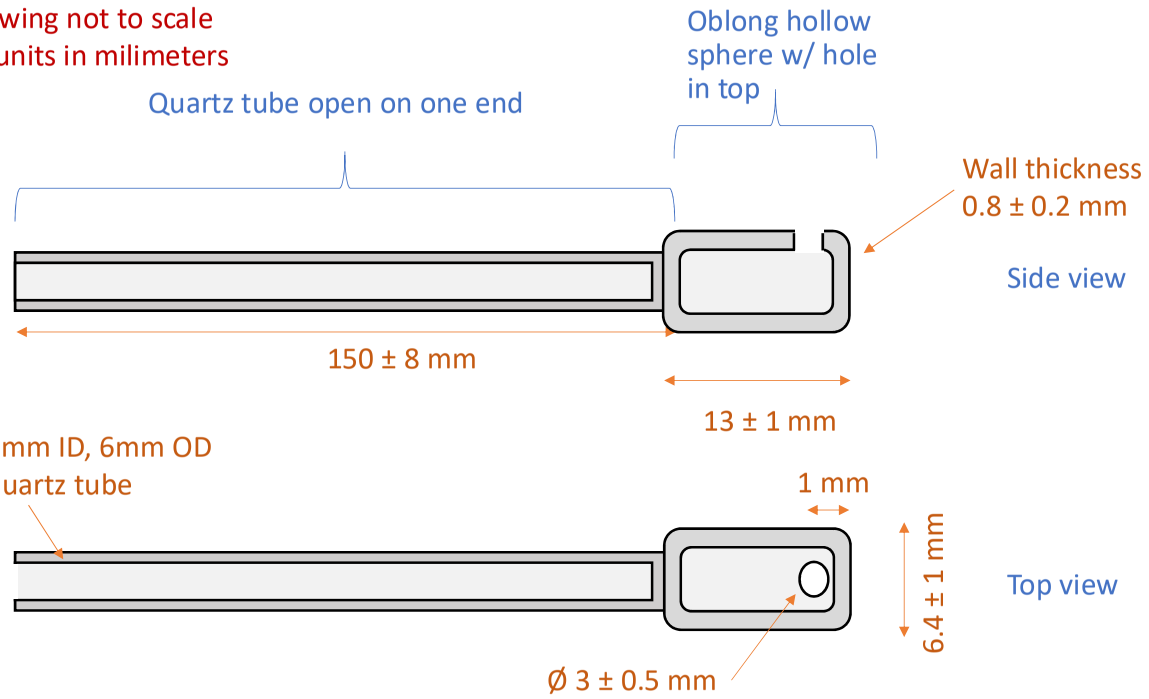

D.3 Custom Acrylic for Enclosure

The following section contains drawings that were provided for making the custom acrylic parts for the CGAVD system enclosure.

2x machined acrylic panels w/ door and ports for gloves

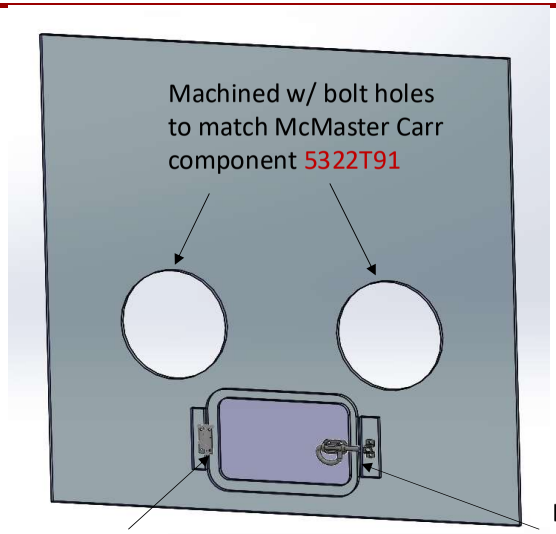

hinge is McMaster Carr component 15205A24

All units in inches

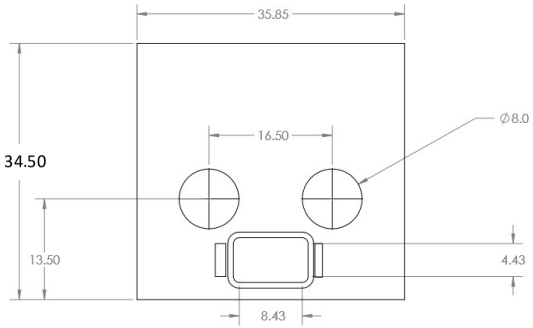

Latch is McMaster Carr component 1754A21

- Need 2 identical panels
- ¼" thick clear translucent acrylic panel
- Overall dimensions are ¼" x 35.85" x 34.5"
- Circular ports are for gloves, need to have bolt holes machined to match McMaster Carr component 5322T91
- Exact door dimensions (filet radius, etc.) not critical

D.4 Supporting Data

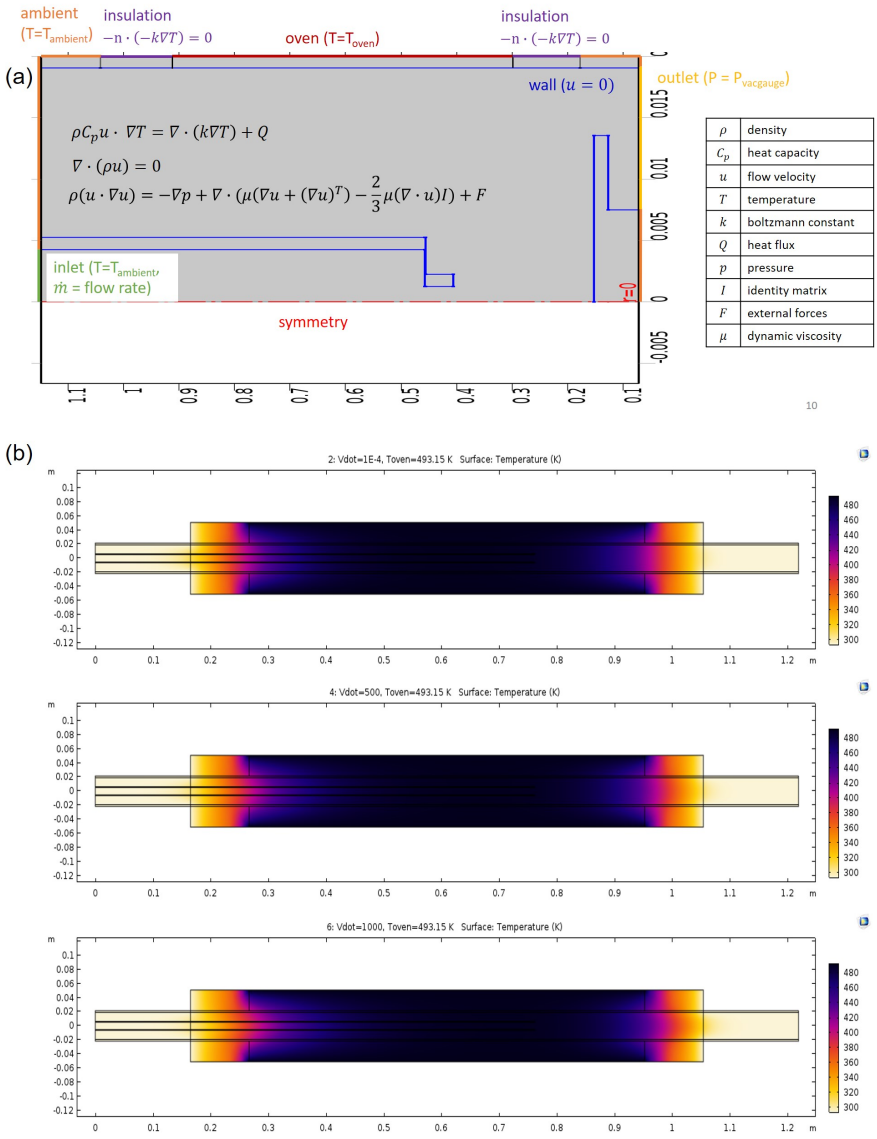

Figure D.1. FEA simulations in COMSOL to model thermal profile in prototype CGAVD system. (a) Geometry, boundary conditions, and partial differential equations solved in this simulation. (b) Simulated temperature profiles at a three different carrier gas flow rates: 0 sccm, 500 sccm, and 1000 sccm. These results are used to construct the axial temperature profiles in Figure 4.2.

Reynolds # Estimation

$$Re = \frac{\rho v L}{\mu}$$

ρ = fluid density [kg/m^3]
v = fluid velocity [m/s]
L = characteristic linear dimension [m]
μ = dynamic viscosity [kg/m·s]

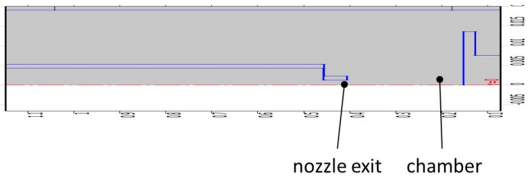

	nozzle		chamber		Comments
ṁ [sccm]	200	1000	200	1000	
ρ [kg/m^3]	0.0017	0.0124	0.0017	0.0124	ideal gas
v [m/s]	0.67 / 2.2	3.4 / 9.49	0.002 / 0.007	0.02 / 0.05	hand calcs / COMSOL model
L [m]	0.00125		0.0381		diameter
μ [kg/m·s]	$1.75*10^{-5}$				N_2 viscosity at 400 K
Re	1	6	0.04	0.2	

Figure D.2. Reynolds number calculations for a variety of carrier gas flow rates, based both on hand calculations and COMSOL calculations of gas flow velocities. Re stays well in the laminar flow region for this system.

	(a)		(b)		(c)		(d)		(e)		(f)	
	MABr	**$SnBr_2$**	**MABr**	**$SnBr_2$**	**MABr**	**$SnBr_2$**	**MABr**	**$SnBr_2$**	**MABr**	**$SnBr_2$**	**MABr**	**$SnBr_2$**
$\dot{V}_{CG,i}$ (sccm)	4	3	4	3.5	4	3.3	3.3	5	3.3	5.4	3.3	5.4
T_i (°C)	151	249	154	250	151	249	147	246	148	247	148	252
$\dot{V}_{DIL}$ (sccm)	193		192		193		192		191		191	
T_g (°C)	280		280		280		280		280		280	
T_s (°C)	15		15		15		15		15		15	
P (Torr)	2.6		2.6		2.6		2.6		2.6		2.6	

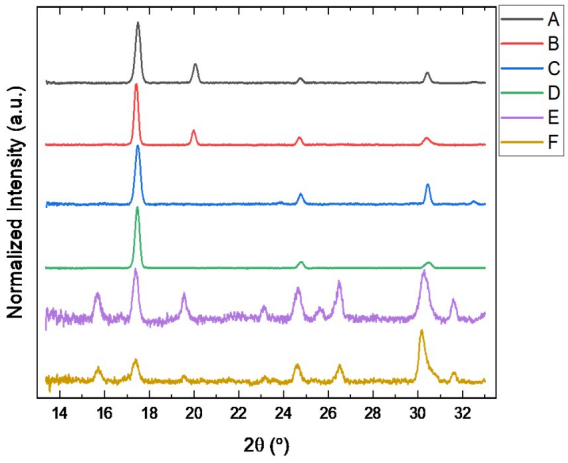

Figure D.3. Deposition parameters and XRD patterns corresponding to low-temperature films in Figure 4.17. XRD was collected using a Bruker D8 2D diffractometer with Co Kα radiation (λ=1.7889 Å).

Appendix E

Appendix for Chapter 5

E.1 Experimental Methods

For electronic measurements, films were deposited onto Ag, Au, or ITO contacts in a van der Pauw geometry. Four terminal resistance and Hall effect measurements were measured DC with a Keithley 2400 or a combination of a Keithley 220 current source and a Keithley 2002 voltmeter at 280 K in a Quantum Design Physical Property Measurement System (PPMS) equipped with a 9 T superconducting magnet. Checks were made for ohmicity, contact resistance, and Joule heating. All electronic measurements and analysis were performed by Bryan Voigt.

E.2 Supporting Data

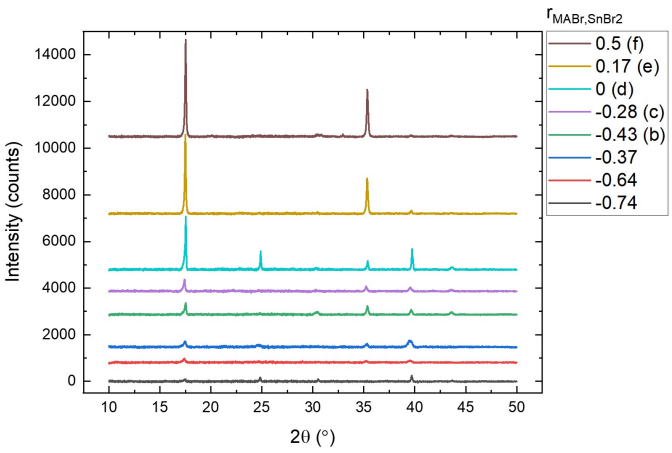

Figure E.1. X-ray diffraction patterns corresponding to XRD peak heights reported in Figure 5.3. XRD was collected using a Bruker D8 2D diffractometer with Co Kα radiation (λ=1.7889 Å).

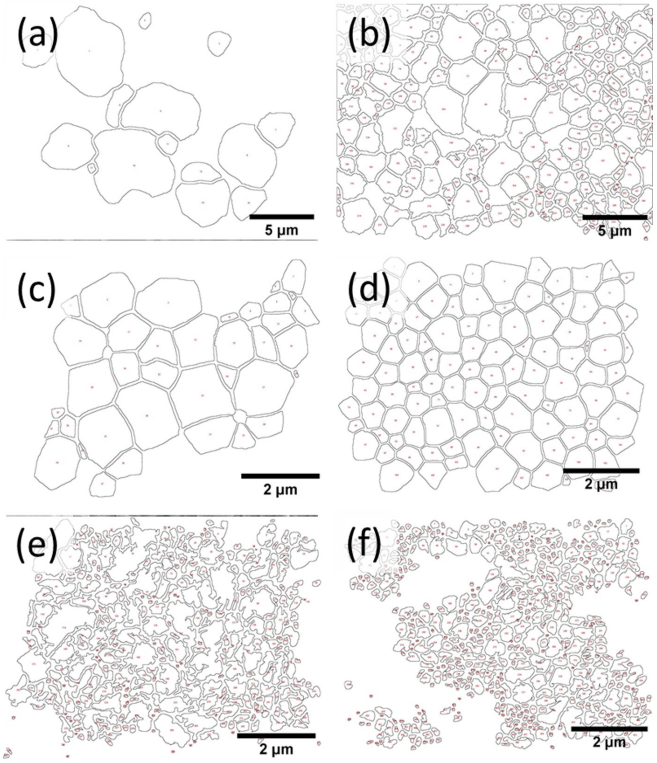

Figure E.2. Images used for grain size determination that were prepared using the Weka trainable segmentation tool in ImageJ on the SEM images in Figure 5.2.

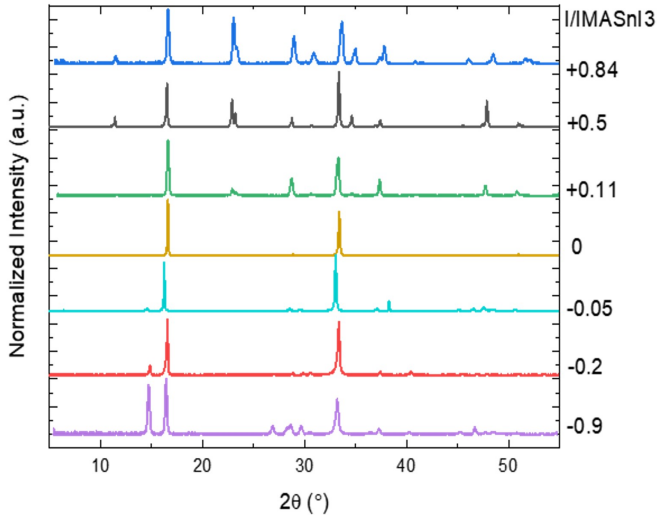

Figure E.3. X-ray diffraction patterns corresponding to films in Figure 5.4. Normalized excess precursor ratios (I_{MAI}/I_{MASnI_3} or I_{SnI_2}/I_{MASnI_3}) are listed to the right of the graph, with positive numbers indicating excess MAI and negative numbers indicating excess SnI_2. XRD was collected using a Bruker D8 2D diffractometer with Co Kα radiation (λ=1.7889 Å).

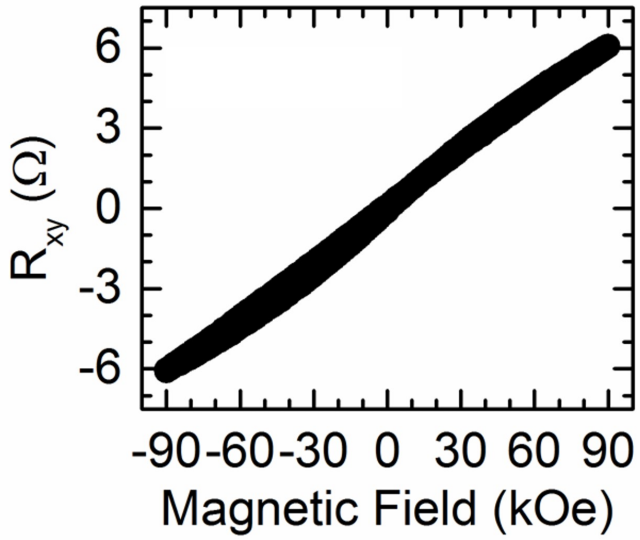

Figure E.4. The magnetic field dependence of the transverse (Hall) resistance (Rxy) for a stoichiometric $MASnI_3$ film (normalized excess precursor = 0 in Figure 5.4) at 280 K. The positive slope indicates p-type majority carriers, with the slope inversely proportional to hole concentration.

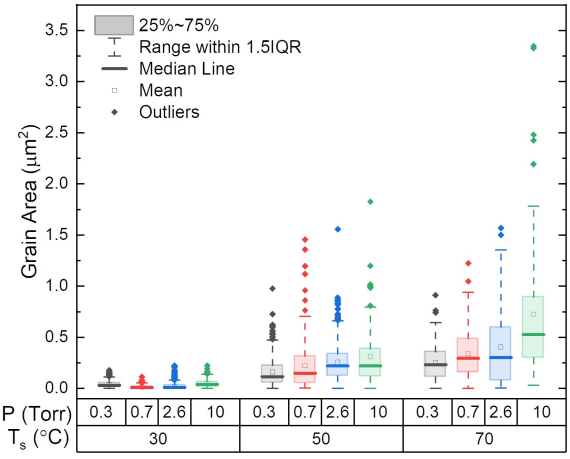

Figure E.5. Grain area distributions *vs.* P and T_s corresponding to films in Figure 5.5. IQR corresponds to the interquartile range. Each distribution contains between 200 and 300 grains, taken from several SEM images from different areas on each substrate.

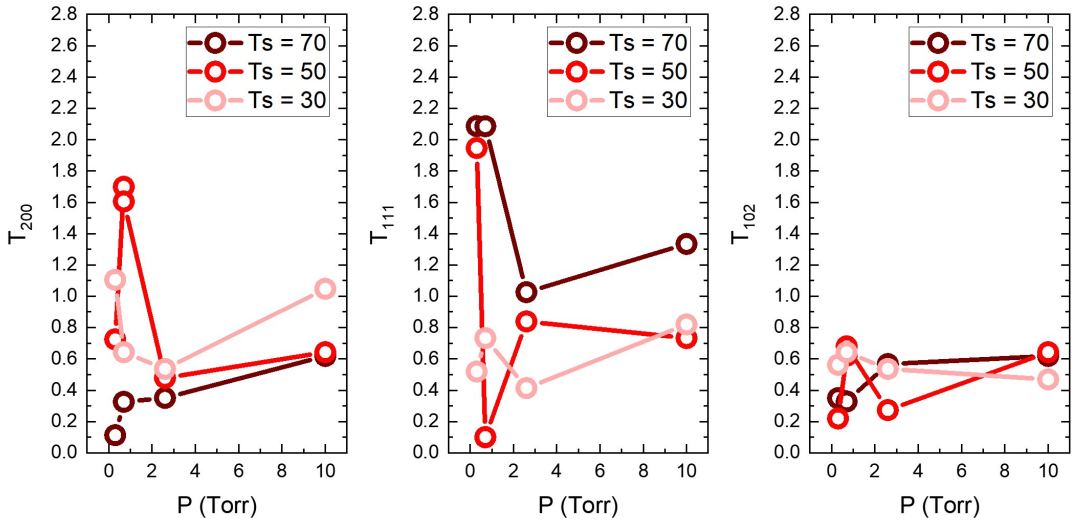

Figure E.6. Texture coefficient $TC_{h_i k_i l_i}$ as a function of P and T_s for additional peaks corresponding to Figure 5.5.

Appendix F

Appendix for Chapter 6

F.1 Experimental Methods

Substrate cleaning procedures, materials used, and additional characterization methods can be found in Appendix B.

F.1.1 Perovskite Film Synthesis

$MAPbBr_3$ & $FAPbBr_3$: $MAPbBr_3$ & $FAPbBr_3$ films were synthesized using a 1-step spin coating process inside of an N_2 glovebox. 1M or 0.6M $MAPbBr_3$ solutions (depending on desired film thickness) with 15% excess MABr were made by dissolving 1:1.15 molar ratios of $PbBr_2$:MABr in a 4:1 volume ratio of DMF:DMSO. 0.6M $FAPbBr_3$ solutions were made by dissolving 1:1.10 molar ratio of $PbBr_2$:FABr in a 4:1 volume ratio of DMF:DMSO. Solutions were stirred at 1000 rpm until dissolved and filtered with a 0.2 μm PTFE filter. Films were then static spin coated at 3000 rpm for 2 minutes, with 200 μL of chlorobenzene dropped between 10s and 45s into the spin cycle. Films were then annealed at 95 °C for 60 minutes.

$CsPbBr_3$: $CsPbBr_3$ films were synthesized using a 1-step spin coating process inside an N_2 glovebox following Cho *et al.* [363]. A 10.4 wt% $CsPbBr_3$ with 10% molar excess CsBr solution was made by dissolving $PbBr_2$ and CsBr in DMSO. Solutions were stirred at 60 °C and 1000 rpm until dissolved and filtered with a 0.2 μm PTFE filter. Films were then static spin coated at 3000 rpm for 2 minutes and then annealed at 95 °C for 60 minutes.

$MAPbI_3$: $MAPbI_3$ films were synthesized using a 1-step spin coating process inside an N_2

glovebox. 0.3M $MAPbI_3$ solutions were made by dissolving 1:1.10 molar ratios of PbI_2:MAI in a 4:1 volume ratio of DMF:DMSO. Solutions were stirred at 1000 rpm until dissolved and filtered with a 0.2 μm PTFE filter. Films were then static spin coated at 3000 rpm for 2 minutes and then annealed at 95 °C for 60 minutes.

$FAPbI_3$: $FAPbI_3$ films were synthesized using a 2-step process inside an N_2 glovebox following Binek *et al.* [364]. A 1M PbI_2 solution was made my dissolving PbI_2 in DMF, stirring at 1000 rpm and heating at 60 °C until dissolved. The PbI_2 solution was then filtered with a 0.2 μm PTFE filter. A 20 mM of organic halide solution was then made with 85% FAI and 15% MAI in IPA and stirred at 1000 rpm until dissolved. Both solutions were kept at 60 °C during film synthesis. First, a PbI_2 film was deposited *via* dynamic spin coating 80 μL PbI_2 solution at 3000 rpm for 15 seconds. Immediately after spin coating, the films were gently immersed in the FAI/MAI/IPA solution for 4-5 minutes, at which point they were spin coated at 3000 rpm for 5s to remove remaining solution.

$MASnBr_3$ & $MASnI_3$: Deposition of Sn films using CGAVD followed the procedure outlined in Chapters 4 and 5. The deposition parameters for $MASnBr_3$ & $MASnI_3$ films reported herein are as follows:

	$MASnBr_3$		**$MASnI_3$**	
	MABr	**$SnBr_2$**	**MAI**	**SnI_2**
Carrier gas flow rate	3 sccm		3 – 4 sccm	
Dilution gas flow rate	~50 sccm			
Source temperature	140 – 145 °C	230 – 235 °C	140 – 150 °C	260 – 270 °C
Substrate temperature	10 – 15 °C			
Chamber Temperature	280 °C			
Chamber Pressure	0.5 Torr		0.5 – 0.6 Torr	

Figure F.1. Carrier-gas assisted vapor deposition parameters for $MASnBr_3$ & $MASnI_3$ films.

F.2 Additional Supporting Data

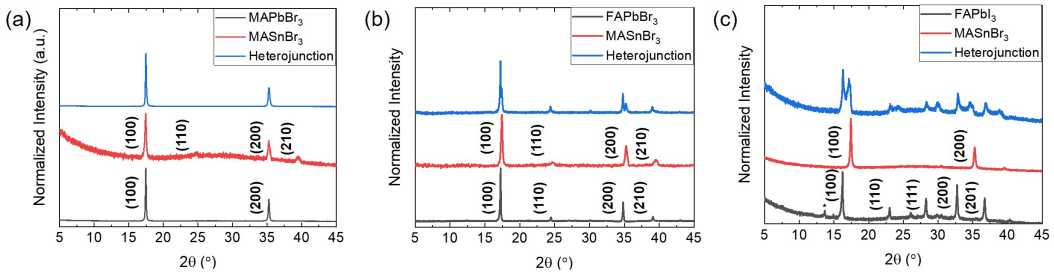

Figure F.2. XRD patterns (a) – (c) corresponding to films in Figure 6.5d – f. The asterisk in (f) corresponds to excess PbI_2 phase. XRD was collected using a PANalytical X'pert PRO diffractometer with Co Kα radiation (λ=1.7889 Å).

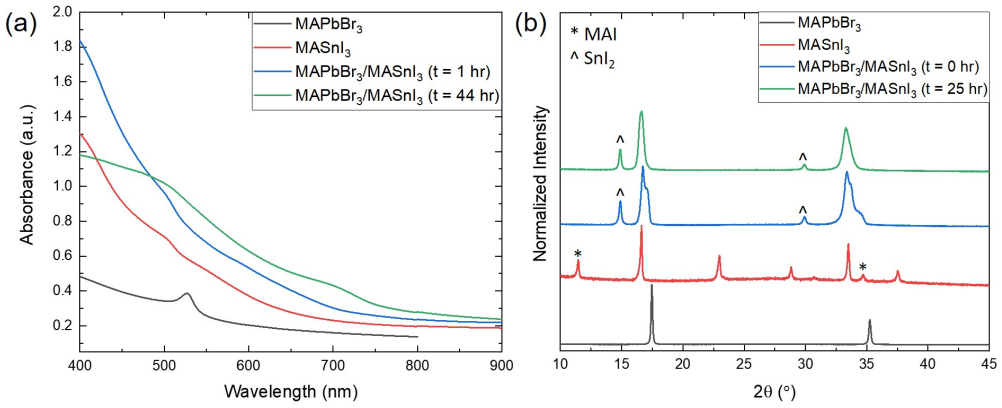

Figure F.3. Representative absorbance spectra (a) and XRD patterns (b) of a $MAPbBr_3$/$MASnI_3$ heterojunction. All samples measured showed substantial mixing for the initial measurements, indicated by the lack of absorption onsets and XRD peaks corresponding to the individual film layers. Whereas substantial MAI excess was observable in the neat $MASnI_3$ film (*) via XRD, the heterojunction had substantial SnI_2 excess (^). It is possible that these non-stoichiometries could have contributed to faster mixing *via* altering the defect distribution. XRD was collected using a PANalytical X'pert PRO diffractometer with Co Kα radiation (λ=1.7889 Å).

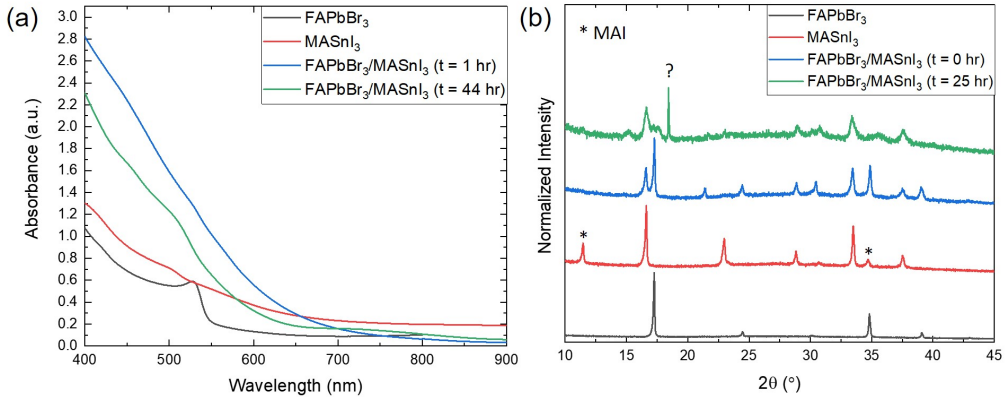

Figure F.4. Representative absorbance spectra (a) and XRD patterns (b) of a $FAPbBr_3/MASnI_3$ heterojunction, where t = 0 hr XRD measurements shows peaks corresponding to both constituent layers. MAI (*) is visible in the neat $MASnI_3$ film but not in the heterojunction, it is possible that these non-stoichiometries could have contributed to faster mixing *via* altering the defect distribution. XRD spectra at t = 25 hr shows substantial mixing alongside potential degradation, as sharp peak at $2\theta = 16.5°$ does not correspond to either constituent MHP. XRD was collected using a PANalytical X'pert PRO diffractometer with Co Kα radiation (λ=1.7889 Å).

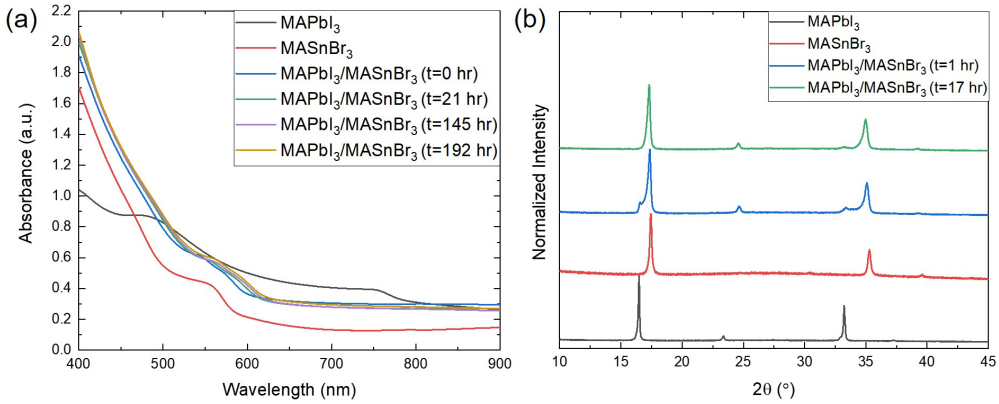

Figure F.5. Representative absorbance spectra (a) and XRD patterns (b) of a $MAPbI_3/MASnBr_3$ heterojunction. While initial absorption (t = 0 hr) measurements show evidence for substantial mixing and lack onsets and features at wavelengths corresponding to constituent films ($\lambda \sim 785$ nm for $MAPbI_3$ and $\lambda \sim 580$ nm for $MASnBr_3$), there is a small peak visible in the t = 1 hr XRD measurements that corresponds to the $MAPbI_3$ (100) peak at $2\theta = 16.5°$; *i.e.*, at 1 hour there is mixing but it is not complete. Measurements at later times for XRD indicate only one phase is present. XRD was collected using a PANalytical X'pert PRO diffractometer with Co Kα radiation (λ=1.7889 Å).

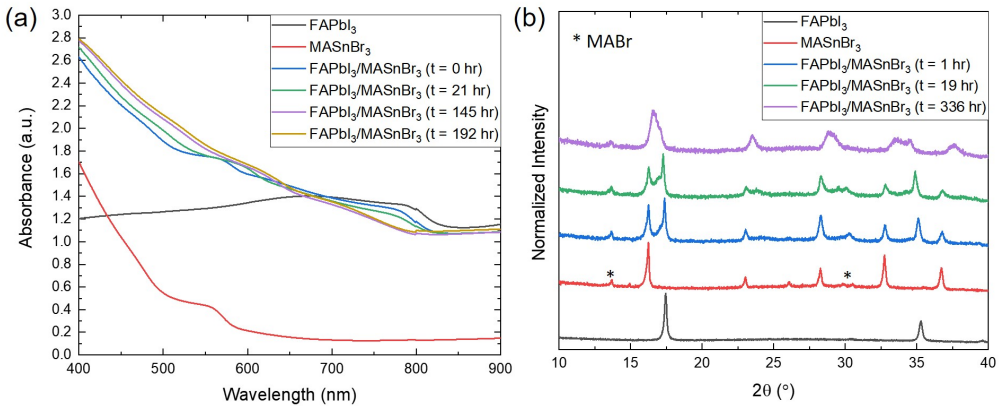

Figure F.6. Representative absorbance spectra (a) and XRD patterns (b) of a $FAPbI_3/MASnBr_3$ heterojunction. Absorbance spectra for films containing $FAPbI_3$ have a large background due to scattering from the films; all films appeared dull to the eye. XRD patterns of both $MASnBr_3$ and heterojunctions show a small peak due to excess MABr at $2\theta = 14°$, it is possible that these non-stoichiometries could have contributed to faster mixing via altering the defect distribution. XRD measurements show peaks corresponding to both constituent layers at t = 0 hr, and evidence of substantial mixing at t = 336 hr. XRD was collected using a PANalytical X'pert PRO diffractometer with Co Kα radiation (λ=1.7889 Å).

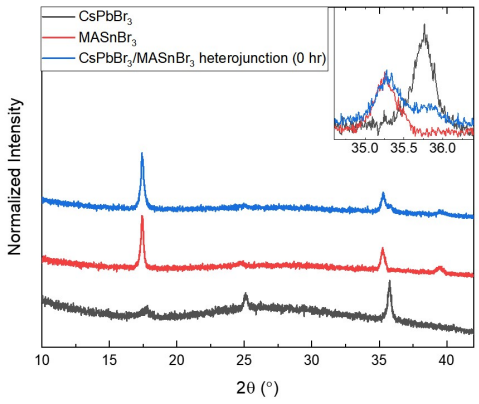

Figure F.7. Representative XRD patterns of a $CsPbBr_3/MASnBr_3$ heterojunction. XRD was collected using a PANalytical X'pert PRO diffractometer with Co Kα radiation (λ=1.7889 Å).

(a) F(x) = a1*exp(-((x-b1)/c1)^2) + a2*exp(-((x-b2)/c2)^2) + a3*exp(-((x-b3)/c3)^2)

Parameter	**a1, a2, a3**	**b1**	**b2**	**b3**	**c1, c2, c3**
Initial guess	0.5	34.8	35.0	35.3	0.1
Lower Bound	0	34.75	34.95	35.25	0
Upper Bound	1	34.85	35.05	35.35	1

(b)

	2 hr	189 hr	356 hr	434 hr	506 hr	677 hr
Small grained film						
area peak 1	0.17	0.10		0.05	0.03	
area peak 2	0.01	0.23		0.23	0.20	
area peak 3	0.11	0.06		0.03	0.02	
area 2/ (area 1+ area 3)	0.05	1.46		2.93	4.55	
Large island film						
area peak 1	0.20	0.21	0.21	0.21	0.17	0.19
area peak 2	0.02	0.04	0.07	0.07	0.09	0.09
area peak 3	0.21	0.20	0.21	0.22	0.17	0.20
area 2/ (area 1+ area 3)	0.04	0.10	0.18	0.17	0.28	0.23

Figure F.8. Fitting parameters (a) for the $FAPbBr_3$/$MASnBr_3$ heterojunctions shown in Figure 6.14a. (b) Results of fitting and calculation of Figure 6.14b y-axis values for small and large grained films.

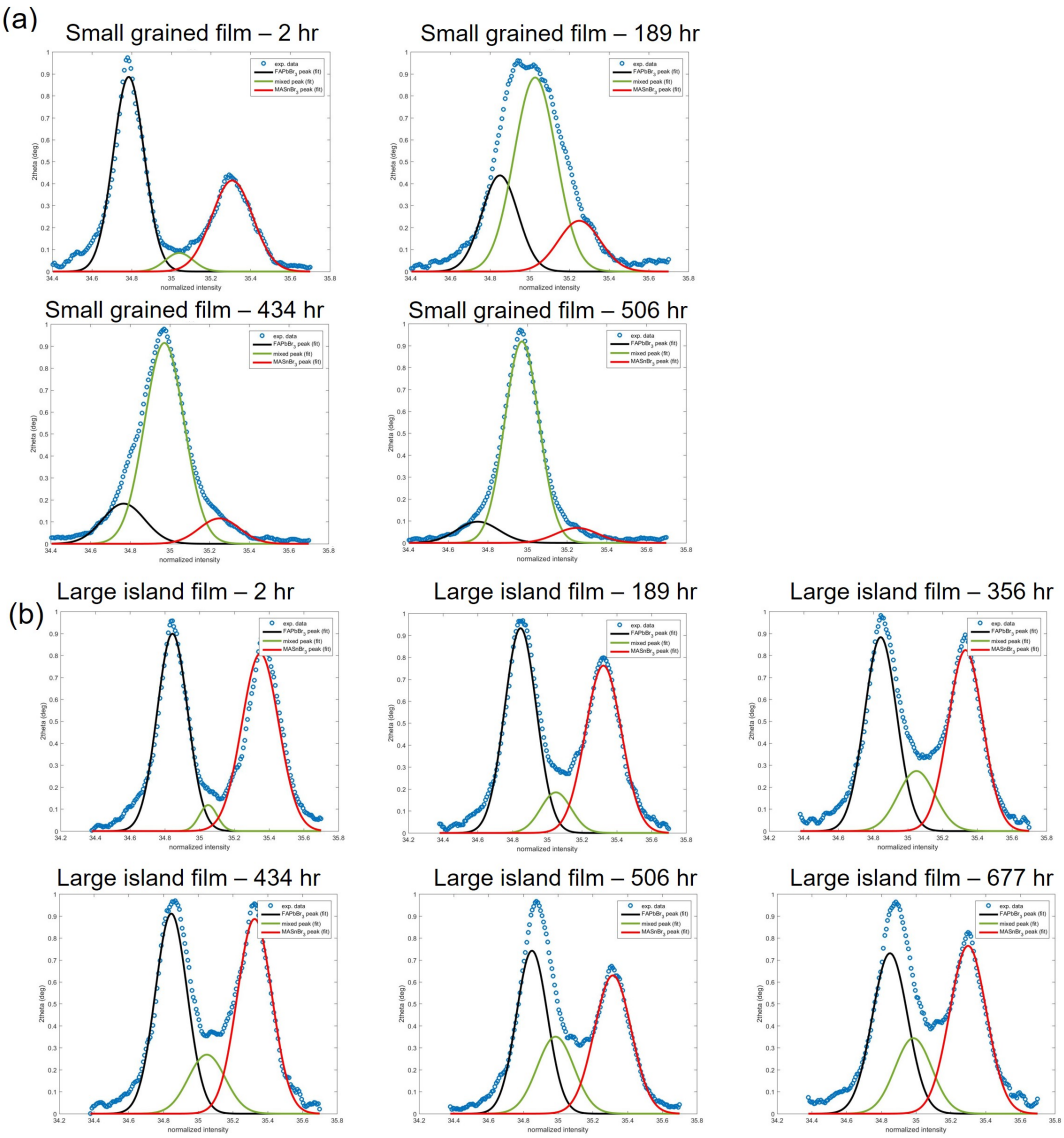

Figure F.9. Results of fitting using the parameters in Figure F.8 for one small-grained and one large-island $FAPbBr_3/MASnBr_3$ heterojunction shown in Figure 6.14b.

(a,b) $MASnBr_3$

	MABr	$SnBr_2$
$\dot{V}_{CG,i}$ (sccm)	3.5	5
T_i (°C)	147	246
$\dot{V}_{DIL}$ (sccm)	192	
T_g (°C)	280	
T_s (°C)	20	
P (Torr)	2.6	
Film Thickness (nm)	450	

(a,b) $MASnBr_{1.5}I_{1.5}$

	MABr	$SnBr_2$	MAI	SnI_2
	Deposition 1 ($MASnBr_3$)		Deposition 2 ($MASnI_3$)	
$\dot{V}_{CG,i}$ (sccm)	50	50	50	50
T_i (°C)	138	240	140	285
$\dot{V}_{DIL}$ (sccm)	0		0	
T_g (°C)	250		250	
T_s (°C)	15		15	
P (Torr)	1.3		1.3	
Film Thickness (nm)	160		151	

(a,b) $MASnBr_2I_1$

	MABr	$SnBr_2$	MAI	SnI_2
	Deposition 1 ($MASnBr_3$)		Deposition 2 ($MASnI_3$)	
$\dot{V}_{CG,i}$ (sccm)	5	17	5	12
T_i (°C)	136	246	150	287
$\dot{V}_{DIL}$ (sccm)	177		175	
T_g (°C)	280		280	
T_s (°C)	15		15	
P (Torr)	10		10	
Film Thickness (nm)	91		49	

(a,b) $MASnI_3$

	MAI	SnI_2
$\dot{V}_{CG,i}$ (sccm)	5	12
T_i (°C)	149	287
$\dot{V}_{DIL}$ (sccm)	183	
T_g (°C)	280	
T_s (°C)	15	
P (Torr)	2.6	
Film Thickness (nm)	410	

(c) $MASnBr_3$

	MABr	$SnBr_2$
$\dot{V}_{CG,i}$ (sccm)	4	5
T_i (°C)	139	221
$\dot{V}_{DIL}$ (sccm)	90	
T_g (°C)	280	
T_s (°C)	45	
P (Torr)	0.7	
Film Thickness (nm)	125	

Figure F.10. Deposition conditions for rapidly mixing $MASnBr_3$/$MASnI_3$ films in Figure 6.11

Appendix G

Appendix for Chapter 7

G.1 Summary of All Experiments

XPS experiments were performed in several sets spanning from June 2018 - July 2020. A brief description of the purpose of these experiments is as follows, with more experimental details outlined in Table G.1:

June 2018: This was the first set of experiments performed using depth-profiled XPS. The goal was to test different sputtering sources on $MASnBr_3$ films to see which performed the best for future experiments.

November 2018: Fine-tune etching parameters for C_{60}^+ and Ar_{620}^+ sources based off of Jun 2018 experiments, test on thicker $MASnBr_3$ films.

May 2019: Investigate differences in halogen/metal ratio for films with measurable excess precursors in XRD.

October 2019: Compare results from XPS, XRD, and and RBS to determine cause of non-stoichiometric halogen to metal ratio.

December 2019: Investigate behavior and potential differential etching rates in all-inorganic MHP $CsPbBr_3$.

February 2020: Perform XPS experiments on $MAPbBr_3$/$MASnBr_3$ heterojunctions to verify stability of this layer structure and/or see evidence of B-site mixing.

March 2020: Perform XPS experiments on $FAPbBr_3$/$MASnBr_3$ heterojunctions of various ages to probe extent of A-site and/or B-site mixing.

June 2020: Repeat of June 2018 experiments to vary sputter source, but this time on

$MAPbI_3$ films in order to get redundancy on this measurement and see how Sn and Pb films compare in relation to sputter source behavior. Unfortunately, these films had substrate signal (Si, O) the whole way throughout the depth profile, and thus were unusable. Our hypothesis is that th e$MAPbI_3$ films were not fully covering the substrate.

date	film	sample	sub.	film thick. (nm)	ion gun	ion energy (eV)	ion current (nA)	zalar rotation	raster (mm x mm)	Pass energies
June 2018	$MASnBr_3$	stoichiometric	glass	100	Ar	500	500	Yes	2x2	55 eV (Sn, Br, O, C), 112 (Si)
					C_{60}	20	20		4x4	69 eV (Sn, Br, C, N), 112 eV (Si, O)
					Ar_{620}	20	10		2x2	112 eV (all)
					Ar_{2500}	20	40	No	3x3	
Nov 2018	$MASnBr_3$	stoichiometric	glass	200	Ar_{620}	20	12.5	no	3x3	112 eV (all)
				160	C_{60}	20	20	no	4x4	
				100						
May 2019	$MASnI_3$	excess SnI_2	glass	250	C_{60}	20	20	no	4x4	140 eV (Si,O)
		stoichiometric								
		excess MAI								
		stoichiometric								
Oct 2019	$MAPbI_3$	stoichiometric	glass	200	C_{60}	20	20	yes	4x4	140 eV (O, Si)
					Ar_{620}				3x3	
					Ar_{1800}	10		no		
Dec 2019	$CsPbBr_3$	stoichiometric	glass	?	C_{60}	20	20	no	4x4	140 eV (O, Si)
					Ar_{1800}	10	20	no	3x3	69 eV (all)
Feb 2020	$MAPbBr_3$/ $MASnBr_3$	stoichiometric	glass	70/110	C_{60}	20	20	no	4x4	112 eV (Si, N, O)
March 2020	$FAPbBr_3$/ $MASnBr_3$	stoichiometric	glass	180/110 or 190	C_{60}	20	20	yes	4x4	112 eV (O, Si)
	$MAPbBr_3$/ $MASnBr_3$		Si							55 eV (C, N), 112 eV (O, Si)

Table G.1: Summary of film and measurement parameters for all XPS experiments performed. Pass energies are 69 eV unless noted otherwise.

G.2 Experimental Methods

G.2.1 UPS Experimental Methods

UPS experiments were performed by Jennifer Mann in Feb 2020 on the same instrument as described in Section 7.2. In this case, a Helium photon source (He I, 21.2eV, 57 W) was used and the X-ray spot size was 4-6mm. The sputtering source was 20 kV/20 nA C_{60}^{+}, rastered over 6x6mm. Takeoff angle was 75 degrees and a pass energy was 1.3 eV.

G.2.2 RBS Experimental Methods

RBS experiments were performed by Greg Haugstad at Charfac using a MAS 1700 pelletron tandem ion accelerator (5SDH) equipped with charge exchange RF plasma source by National Electrostatics Corporation (NEC). Analytical endstation (RBS 400) by Charles Evans and Associates. The ion beam used was H^{++} at 40 μC and energies between 3.5 and 4.3 MeV. RBS data was fit using SIMNRA software, with samples comprised of two layers (Si for substrate and $CH_3NH_3PbI_3$ for MHP film). Result of fitting shown below, where I/Pb ratio is 2.90.

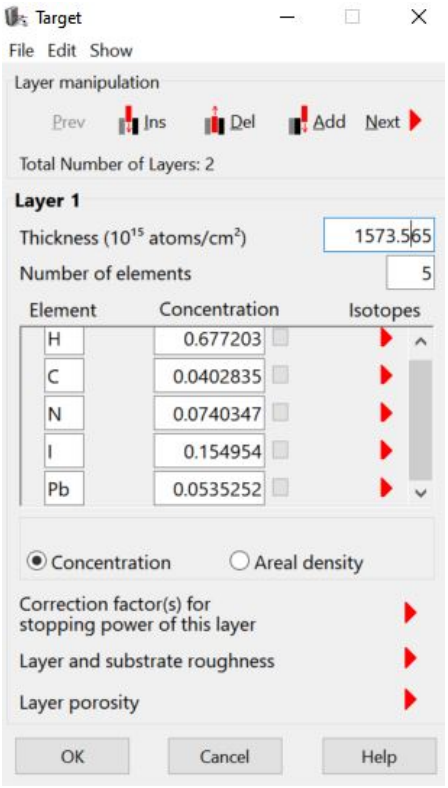

Figure G.1. Result of data fit for RBS using SIMNRA software. Here, the I/Pb ratio is 2.9.

G.3 Supplemental Data for XPS Experiments

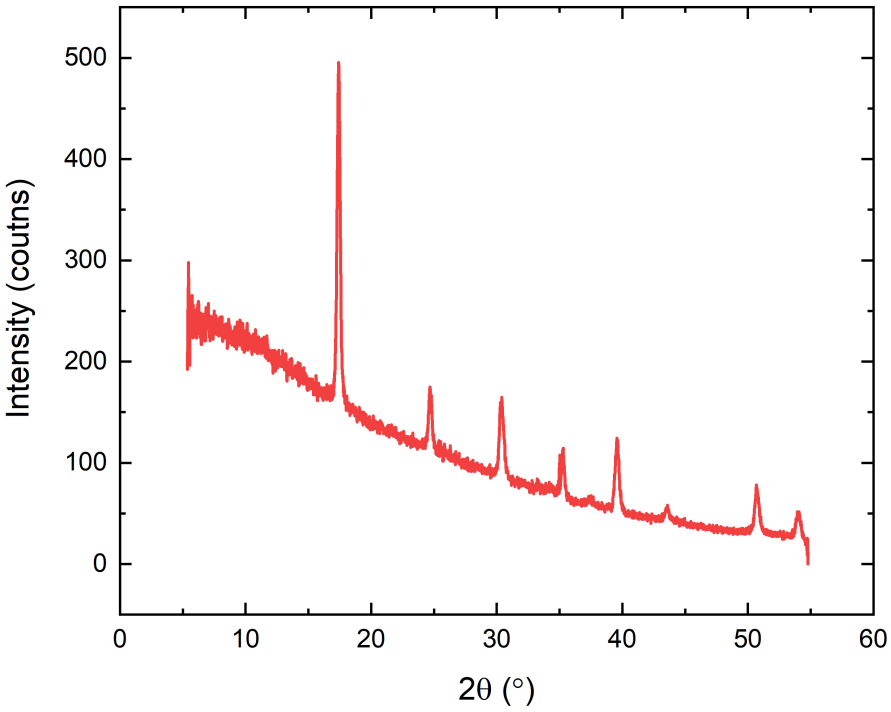

Figure G.2. XRD taken on $MASnBr_3$ films used in June 2018 XPS experiments, showing no observed crystalline precursor peaks. XRD was collected using a Bruker D8 2D diffractometer with Co Kα radiation (λ=1.7889 Å).

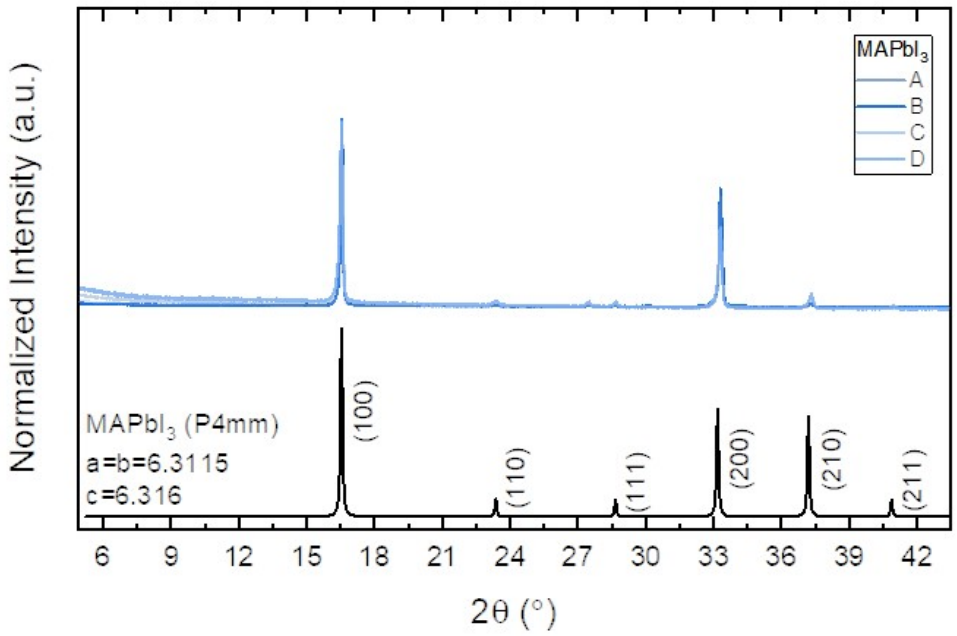

Figure G.3. XRD taken on $MAPbI_3$ films used in Oct 2019 XPS and RBS experiments, showing no observed crystalline precursor peaks. XRD was collected using a PANalytical X'pert PRO diffractometer with Co Kα radiation (λ=1.7889 Å).

G.4 Additional XPS Data

This section contains additional XPS data that was not included in Chapter 7, organized by experiment date.

G.4.1 November 2018

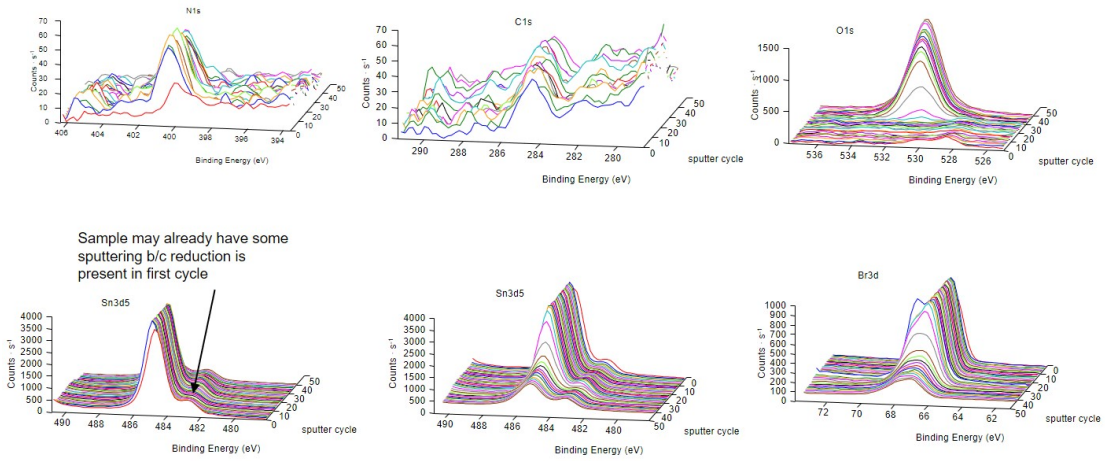

Figure G.4. XPS depth profile montage plots for $MASnBr_3$ films taken in November 2018 with the Ar^+_{620} sputtering source.

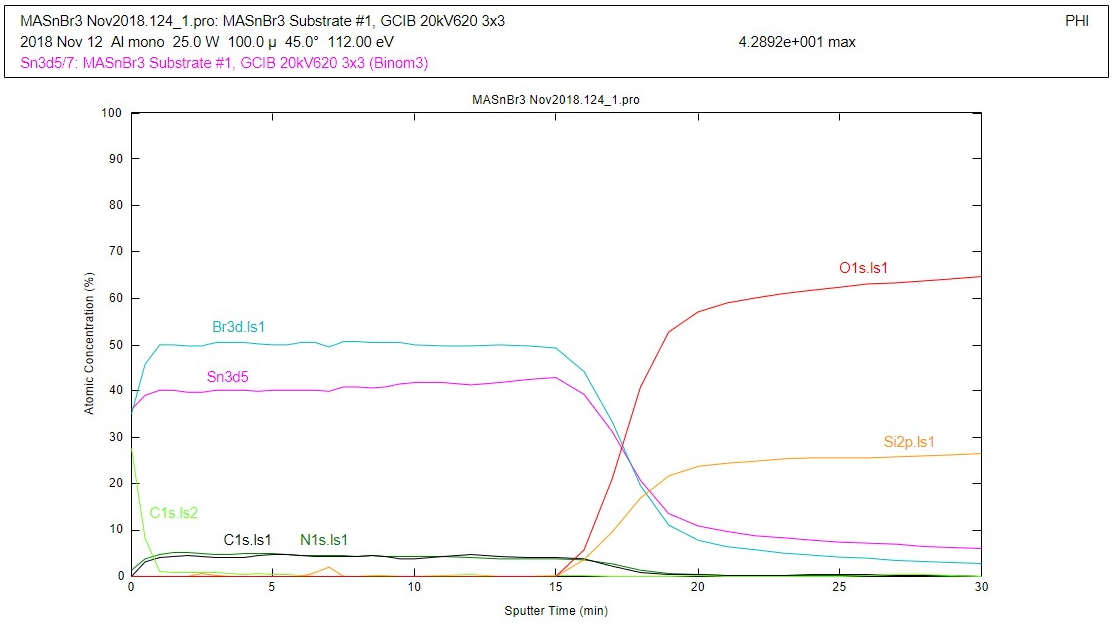

Figure G.5. XPS depth profiles for $MASnBr_3$ films taken in November 2018 with the Ar^+_{620} sputtering source, created by integrating the montage plots in Figure G.4.

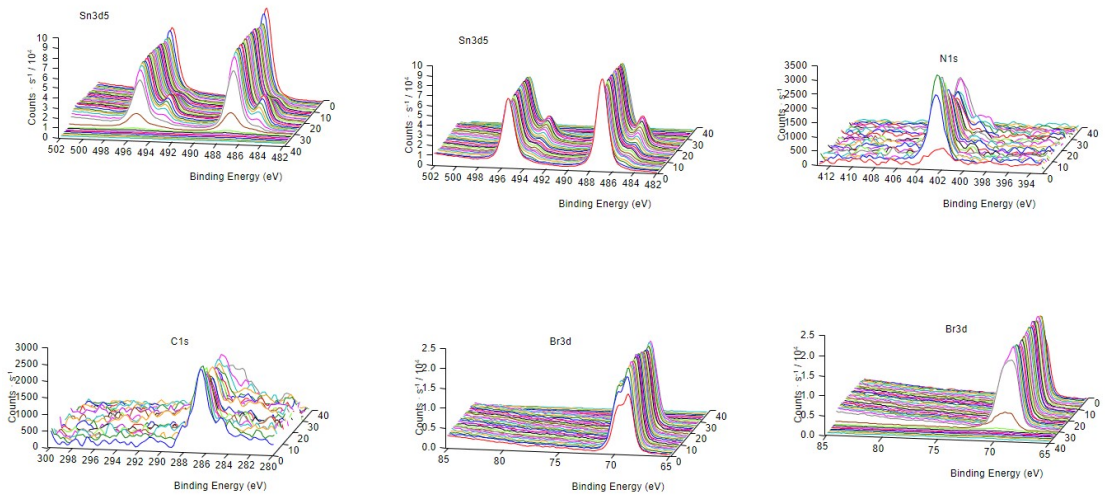

Figure G.6. XPS depth profile montage plots for 160nm thick $MASnBr_3$ films taken in November 2018 with the C^+_{60} sputtering source.

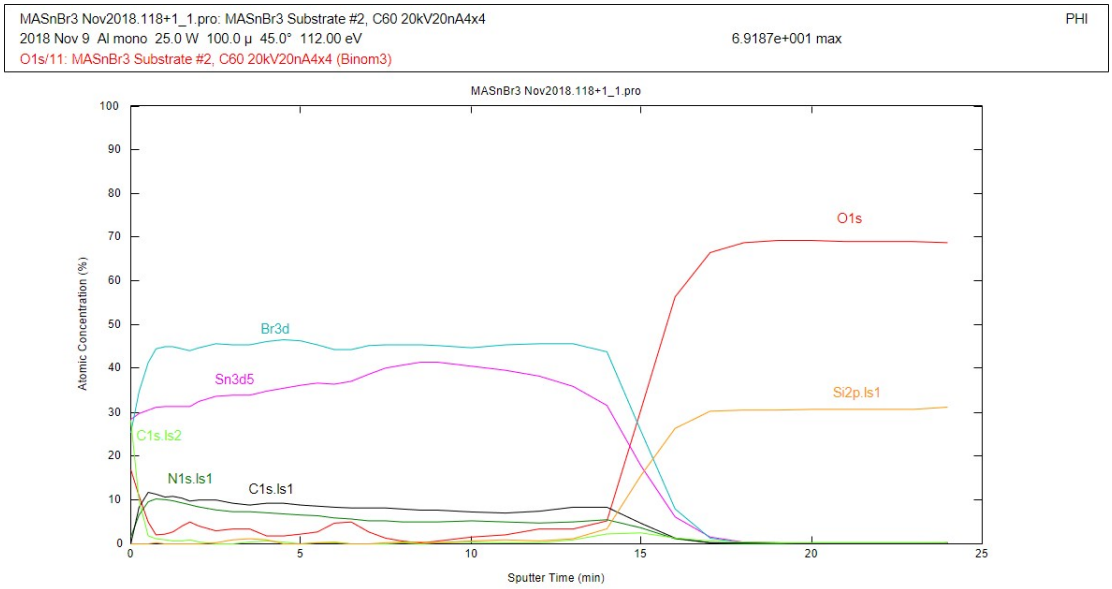

Figure G.7. XPS depth profiles for 160nm thick $MASnBr_3$ films taken in November 2018 with the C_{60}^{+} sputtering source, created by integrating the montage plots in Figure G.6.

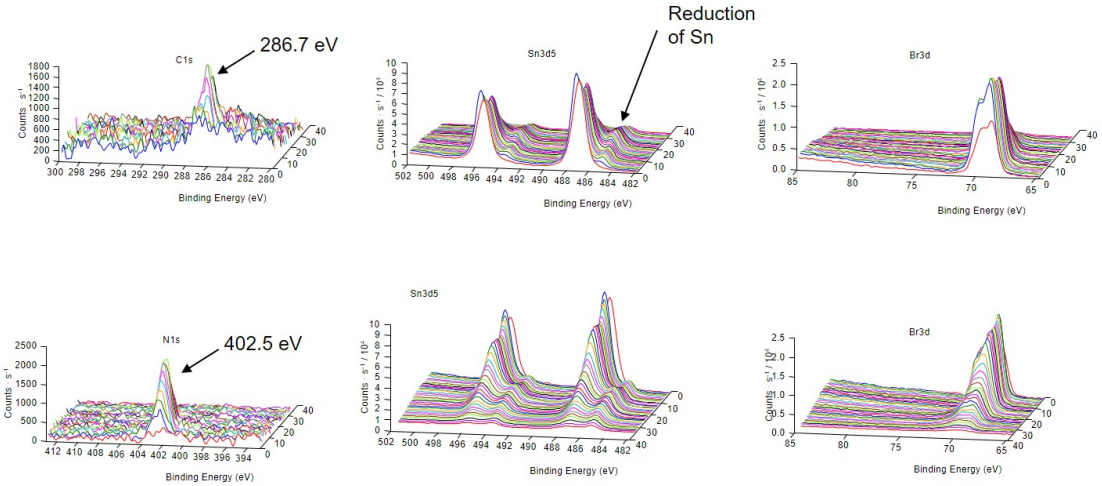

Figure G.8. XPS depth profile montage plots for 100nm thick $MASnBr_3$ films taken in November 2018 with the C_{60}^{+} sputtering source.

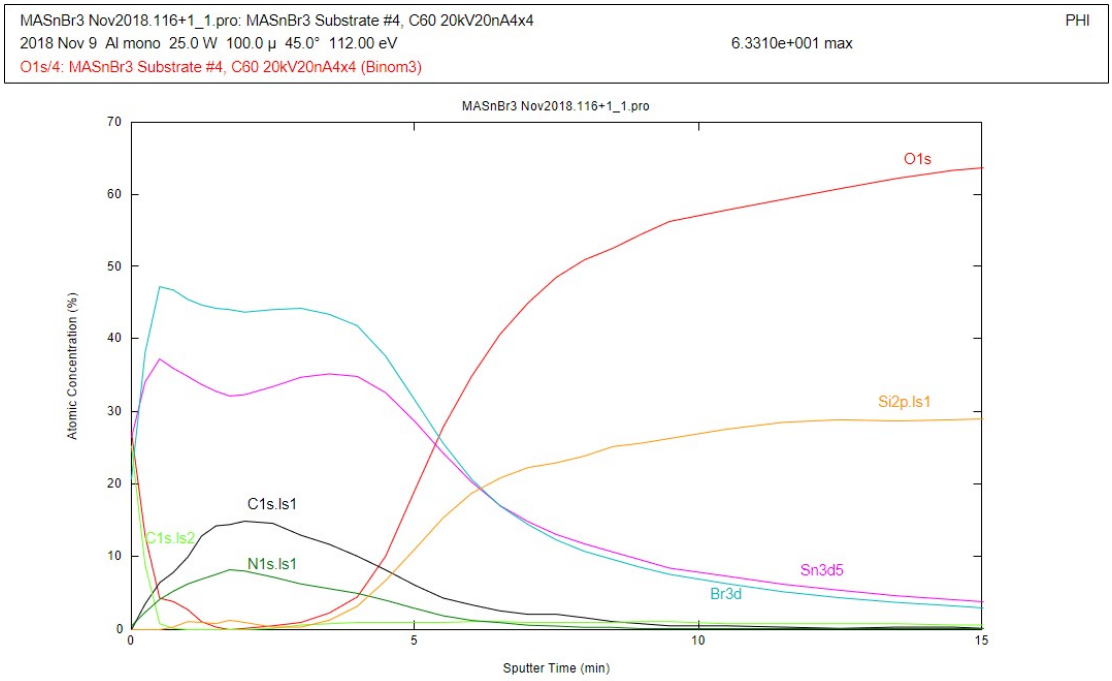

Figure G.9. XPS depth profiles for 100nm thick $MASnBr_3$ films taken in November 2018 with the C_{60}^{+} sputtering source, created by integrating the montage plots in Figure G.8.

G.4.2 May 2019

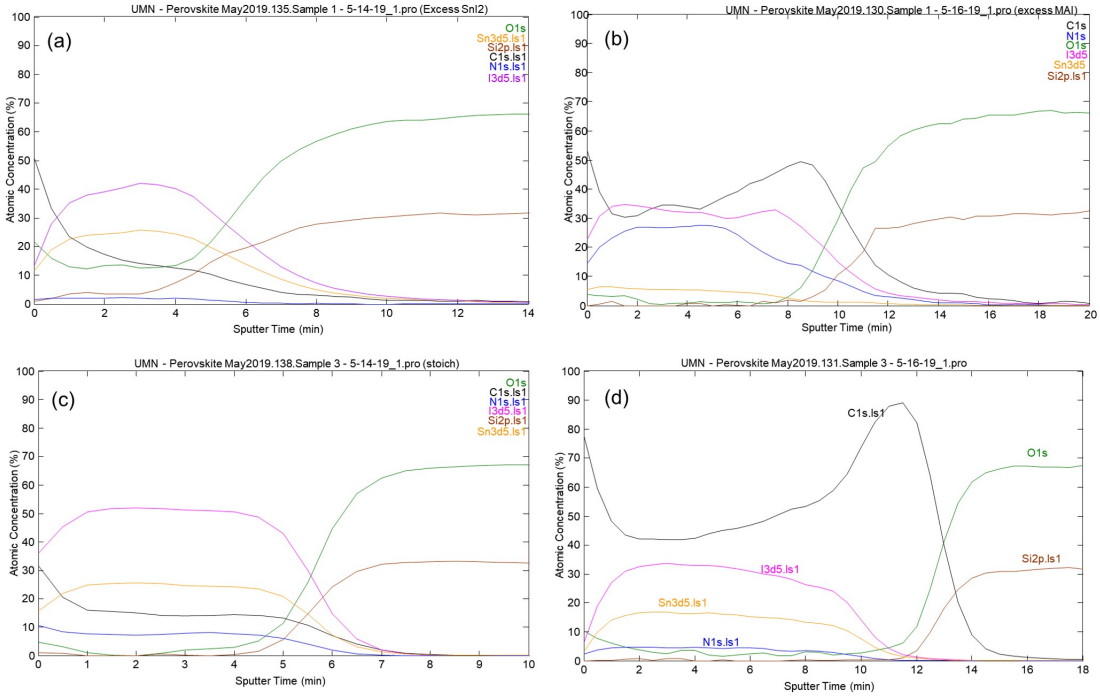

Figure G.10. Full XPS Spectra for $MASnI_3$ films from May 2019 Experiments.

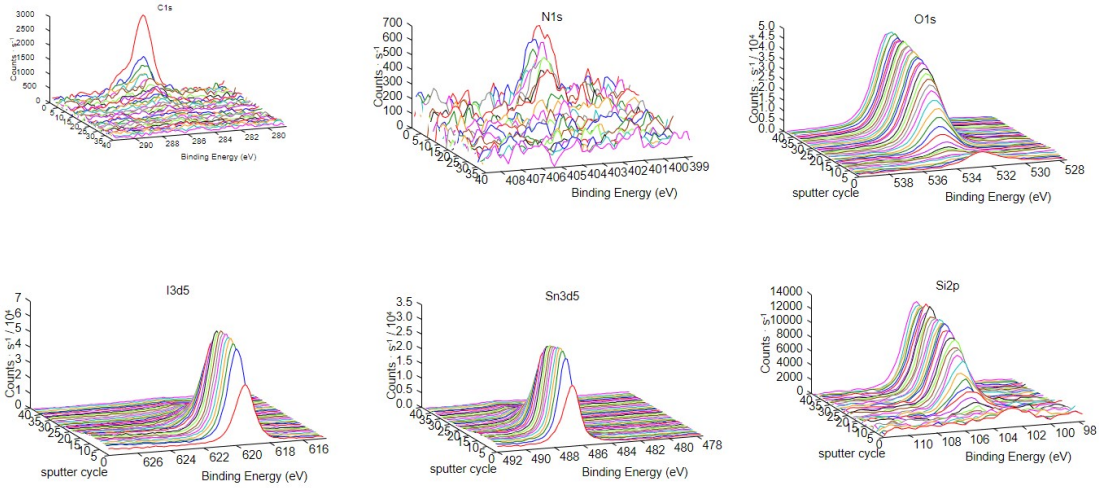

Figure G.11. XPS montage plots for $MASnI_3$ films with excess SnI_2 from May 2019 Experiments.

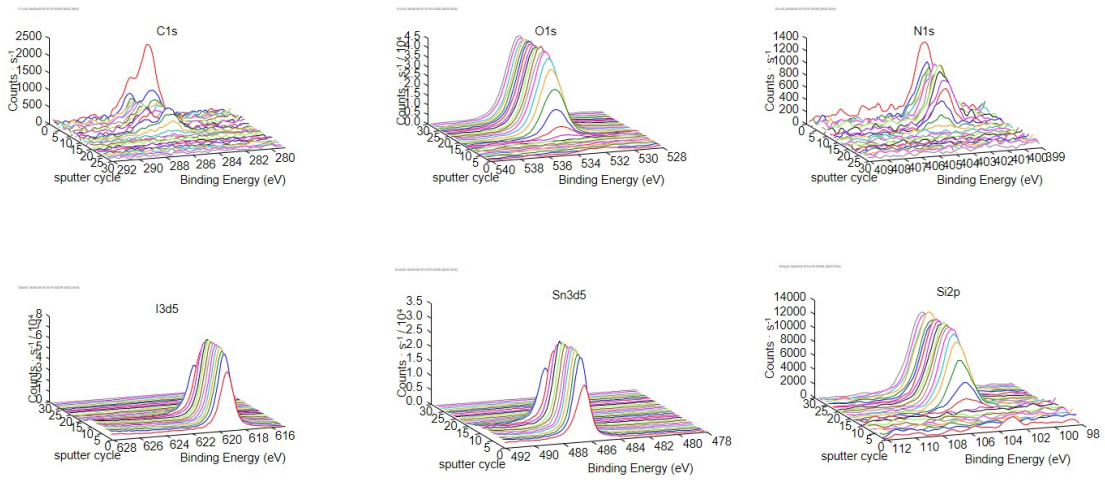

Figure G.12. XPS montage plots for stoichiometric $MASnI_3$ film from May 2019 Experiments.

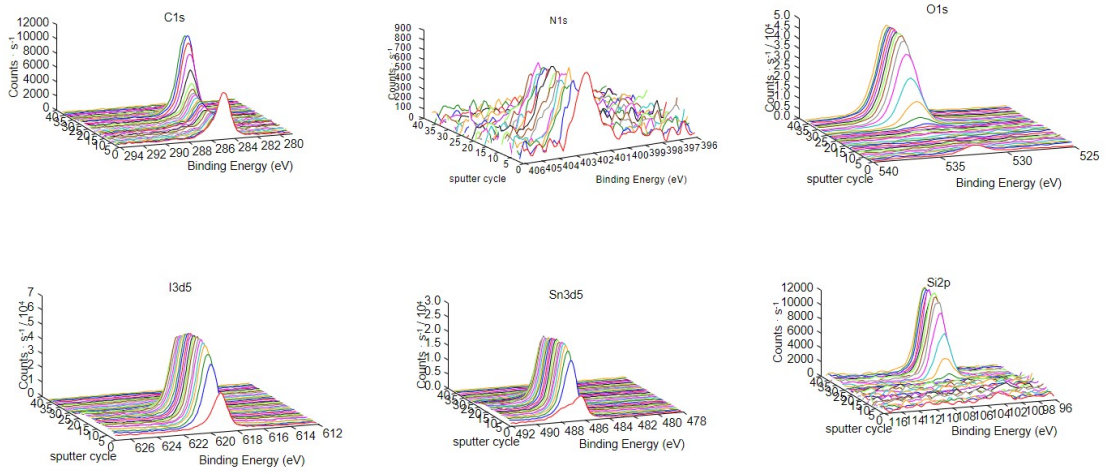

Figure G.13. XPS montage plots for stoichiometric $MASnI_3$ film from May 2019 Experiments.

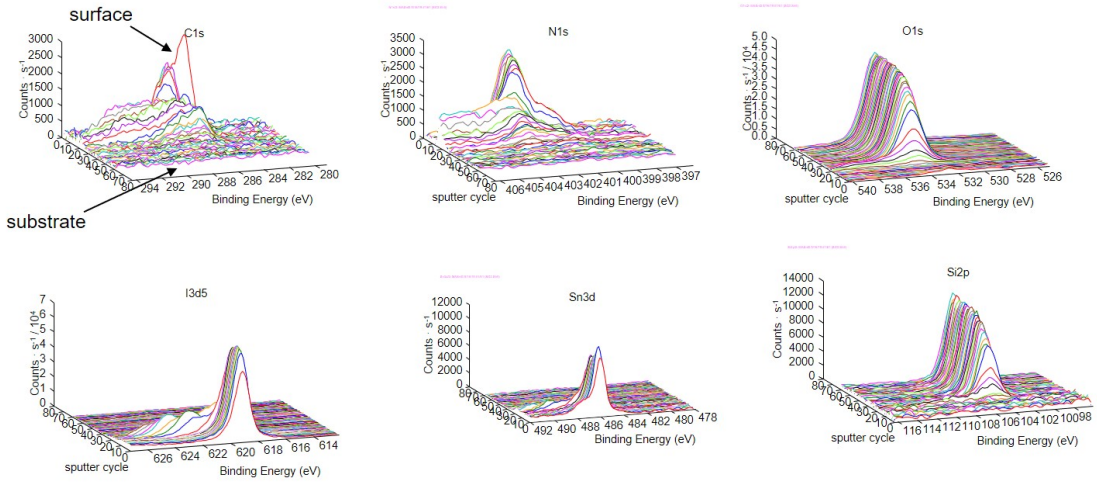

Figure G.14. XPS montage plots for $MASnI_3$ films with excess MAI from May 2019 Experiments.

G.4.3 October 2019

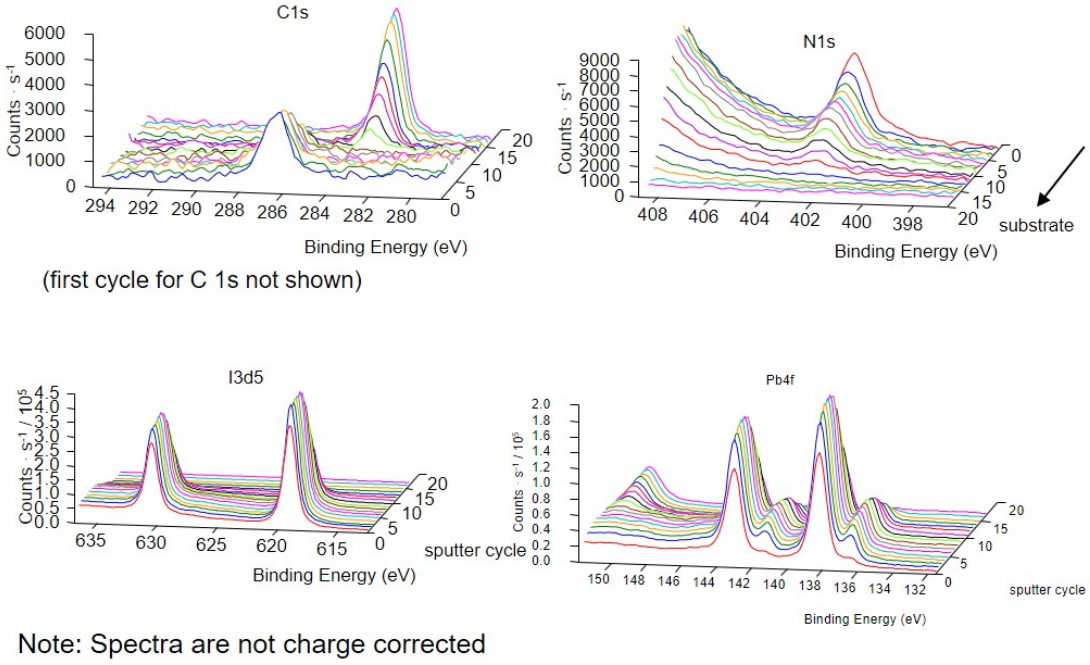

Figure G.15. XPS montage plots for $MAPbI_3$ films from October 2019 experiments using a C_{60}^{+} source.

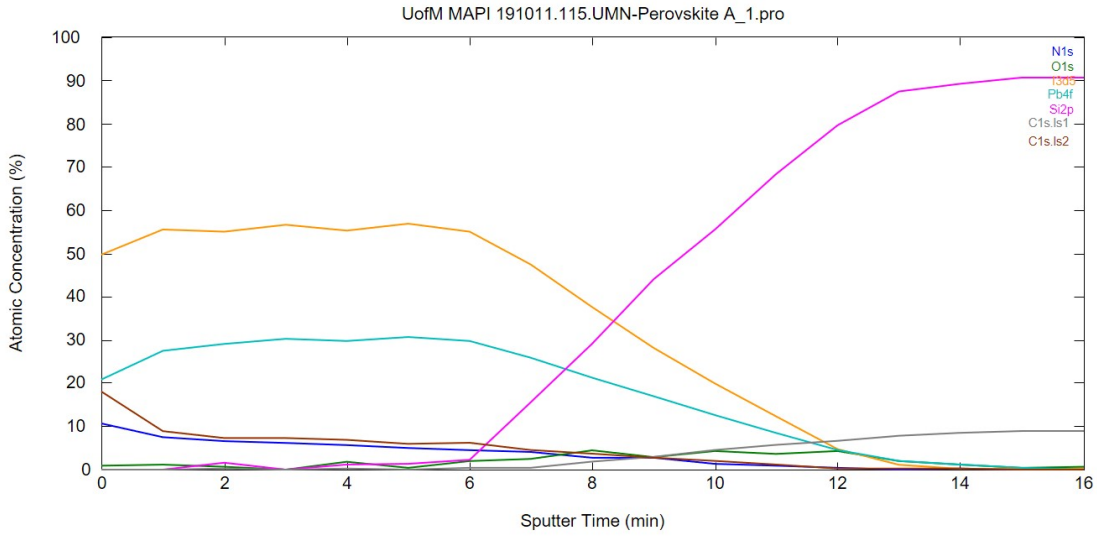

Figure G.16. XPS depth profiles for $MAPbI_3$ films from October 2019 experiments using a C_{60}^+ source.

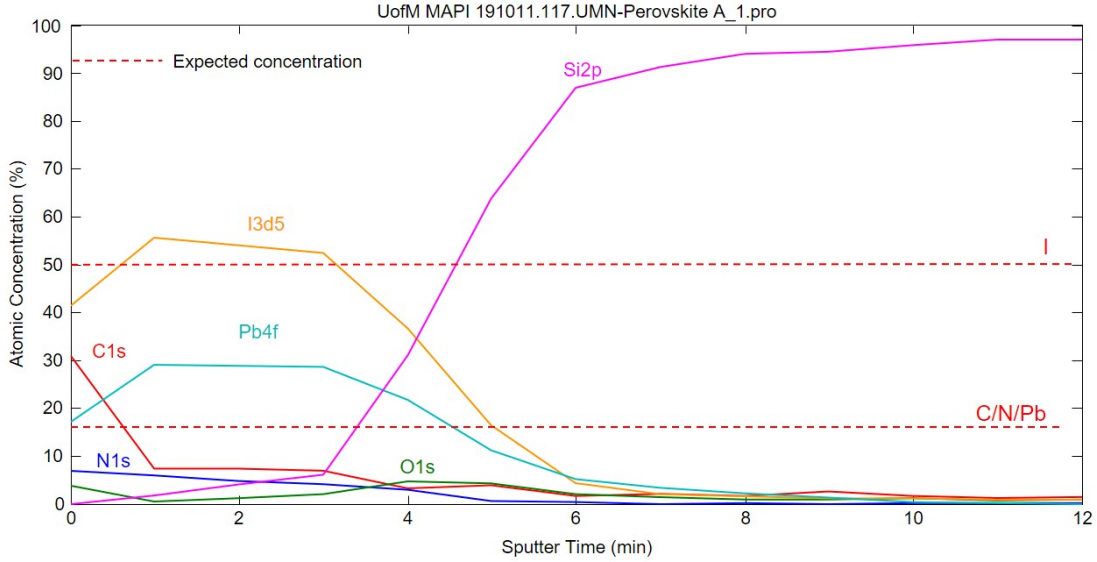

Figure G.17. XPS depth profiles for $MAPbI_3$ films from October 2019 experiments using a Ar_{620}^+ source.

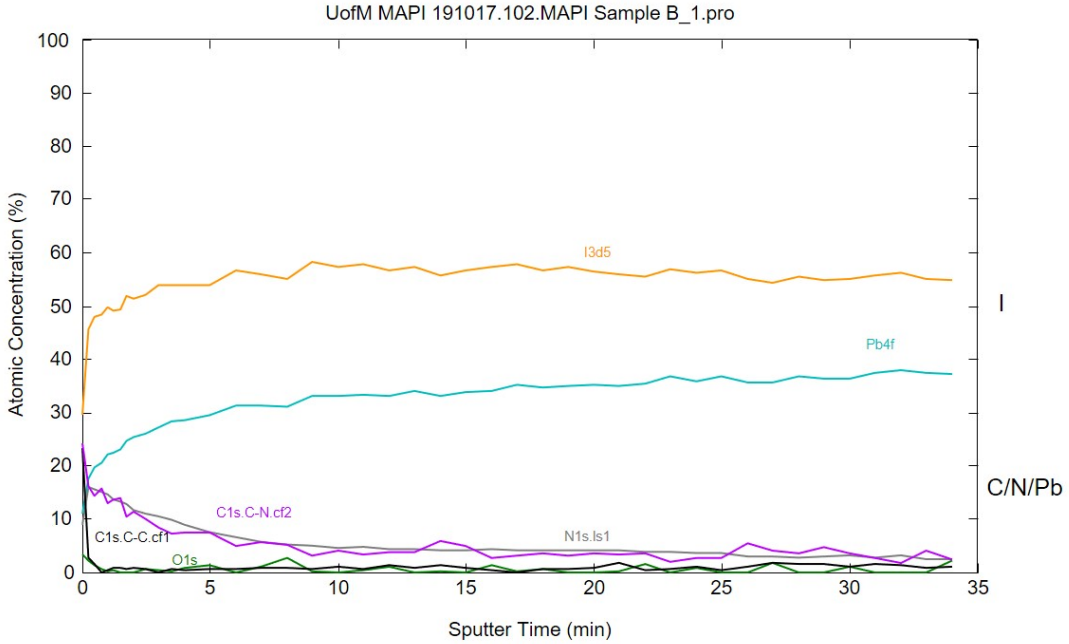

Figure G.18. XPS depth profiles for $MAPbI_3$ films from October 2019 experiments using a Ar^{+}_{1800} source.

G.4.4 December 2019

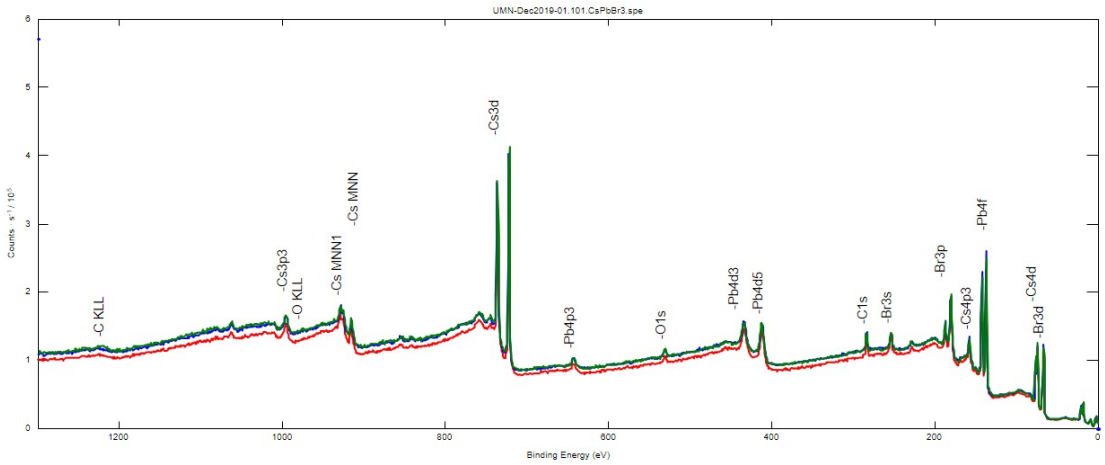

Figure G.19. Survey scan of as received $CsPbBr_3$ used in December 2019 experiments prior to sputtering.

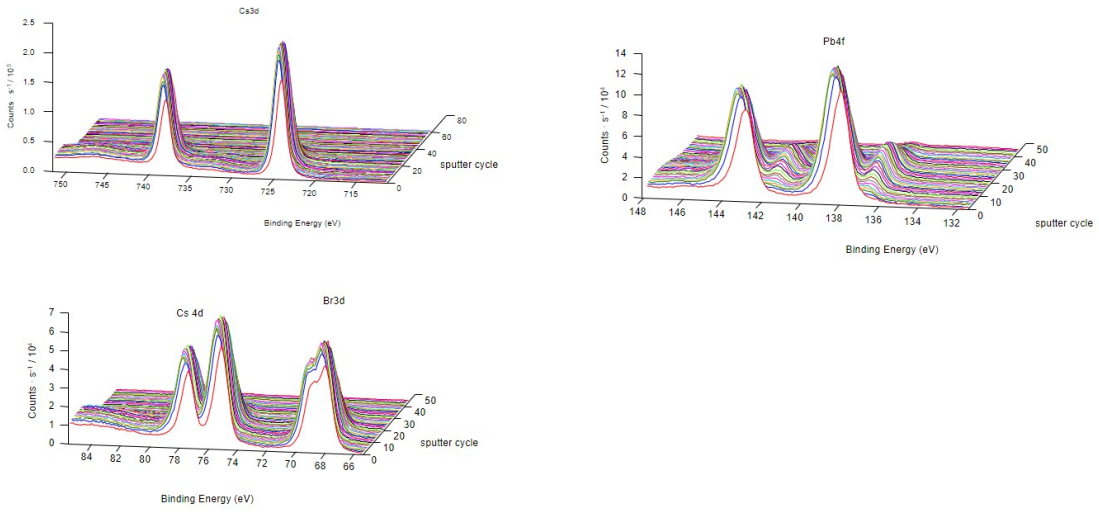

Figure G.20. XPS montage plots for $CsPbBr_3$ films from December 2019 experiments using a C_{60}^{+} source.

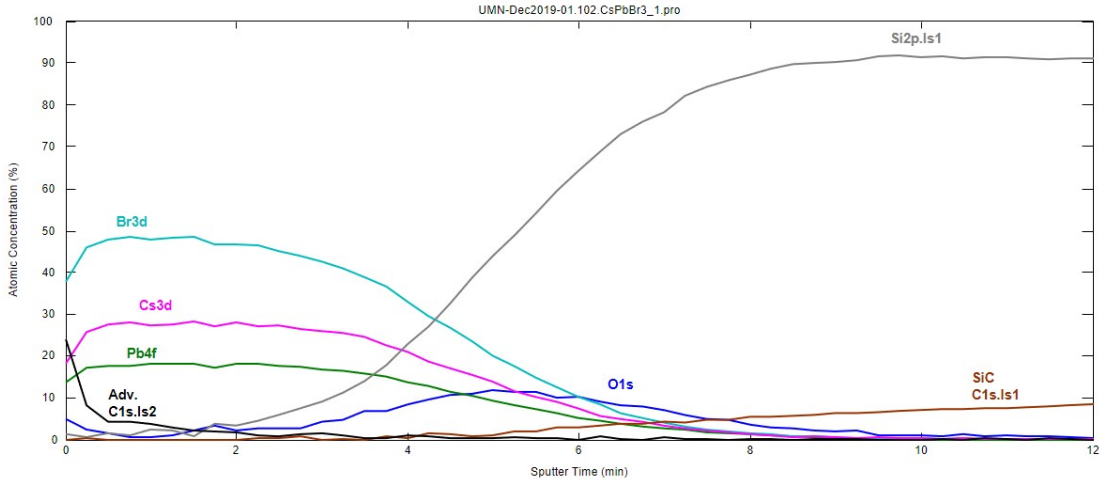

Figure G.21. XPS depth profiles for $CsPbBr_3$ films from December 2019 experiments using a C_{60}^+ source.

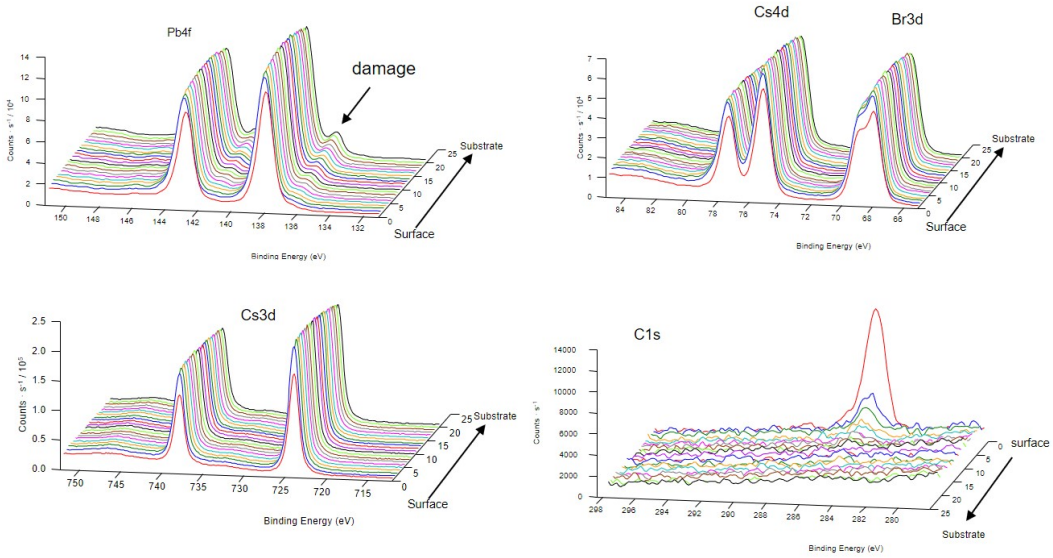

Figure G.22. XPS montage plots for $CsPbBr_3$ films from December 2019 experiments using a Ar^+_{1800} source.

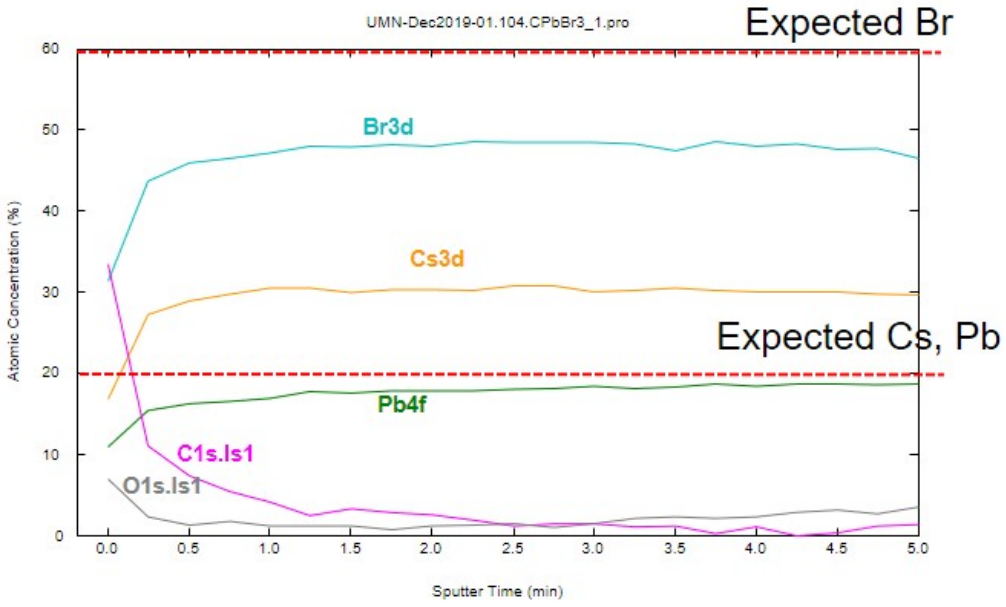

Figure G.23. XPS depth profiles for $CsPbBr_3$ films from December 2019 experiments using a Ar^+_{1800} source.

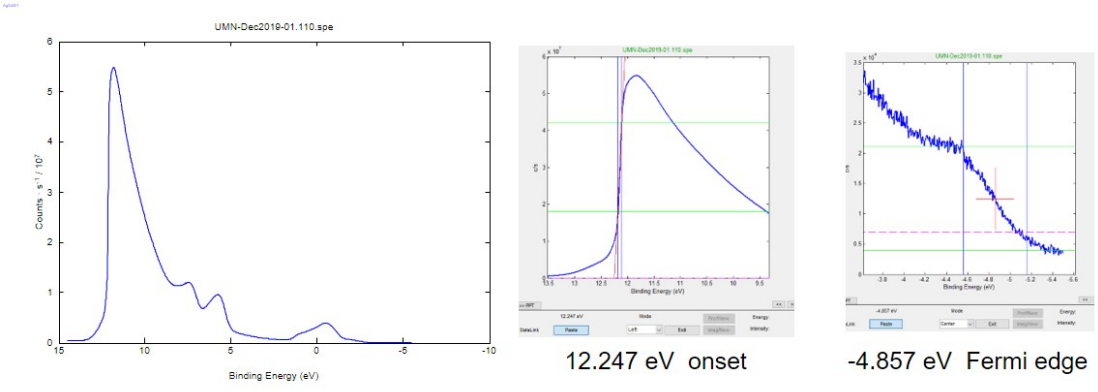

Figure G.24. $CsPbBr_3$ work function measurement using UPS, with 10 kV/20 nA Ar^+_{1800} source rastered over 6x6mm.

G.4.5 February 2020

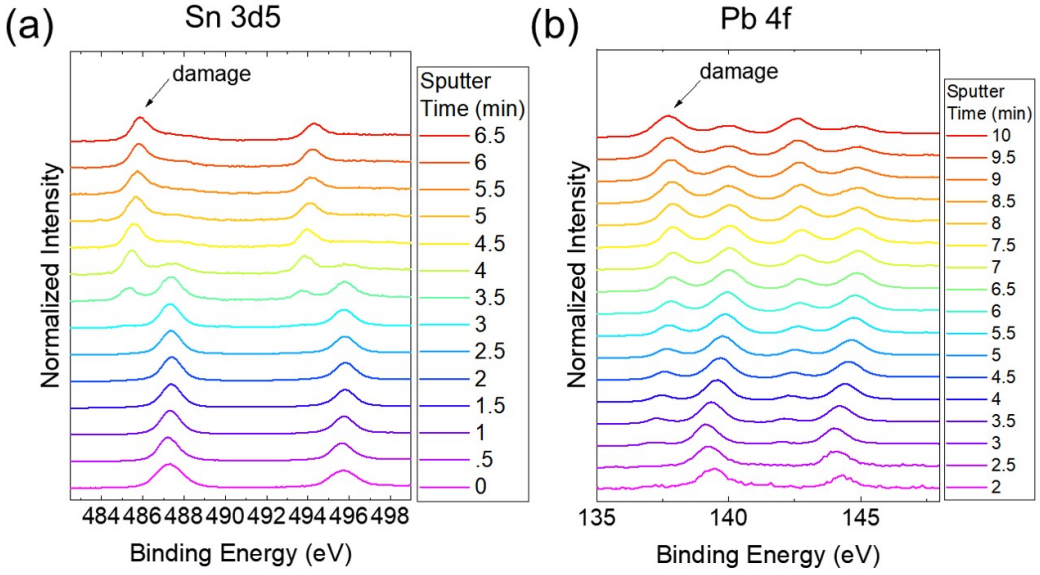

Figure G.25. Sn and Pb XPS spectra vs. sputter time for $MAPbBr_3/MASnBr_3$ heterojunction measured in February 2020.

Appendix H

Appendix for UEM Experiments

H.1 Optimized Experimental Methods

Of the various synthesis methods attempted to make $MAPbI_3$ flakes for UEM, a single step spin-coating process directly onto the TEM grid was the most consistant and produced the highest quality samples. The optimized procedure is as follows: Make 0.3M solution of $MAPbI_3$ w/ 10% molar excess MAI in DMSO (*i.e.* dissolve powders in DMSO). Place grid on Si wafer w/ a drop of toluene, evaporate toluene to get the grid to stick to the Si wafer. Dynamic spin coat 200 μL of 0.3M solution @ 3000rpm for 90s. Anneal grid on Si wafter at 100 °C for 60 min.

H.2 Other Attempted Synthesis Methods

H.2.1 One-step drop casting of MAI + PbI_2 solutions

My first attempt to synthesize $MAPbI_3$ on TEM grids was *via* drop-casting a solution of MAI + PbI_2 in DMSO, followed by a 1 hour annealing of the grid at 100 °C. Unfortunately, this resulted in significant impurities (i.e. not phase pure $MAPbI_3$) and crystallites that were much too thick to be electron beam transparent. As such, this method was quickly abandoned.

H.2.2 Microtoming or FIB-ing single crystals

Single crystal growth was performed by dissolving 1M MAI + PbI_2 in γ-Butyrolactone. This solution was heated at 60 °C for three days, and then filtered with a 0.2 μm filter. Crystal

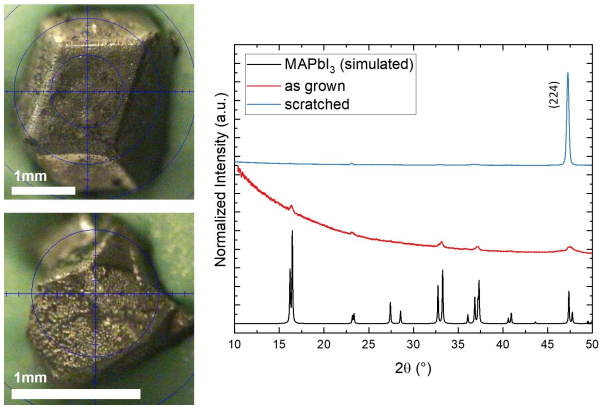

Figure H.1. Typical $MAPbI_3$ single crystals (left) and XRD patterns (right). Note that many crystals grown using this method appear to be decorated with smaller crystallites on the surface, as scratching the surface resulted in significant change in XRD intensity. XRD was collected using a Bruker D8 2D diffractometer with Co Kα radiation (λ=1.7889 Å).

growth was initiated *via* reverse temperature crystalization by heating this filtered solution at 110 °C in an oil bath for 3+ hours. This method was highly successful at growing macroscopic and phase-pure crystals of $MAPbI_3$, as seen in Figure H.1. Unfortunately, common methods to create sufficiently thin layers of $MAPbI_3$ from these large single crystals proved untenable. Ion milling (FIB) was attempted, but this caused substantial degradation of the MHP material, such that it was too damaged to be used in UEM experiments. Similarly, microtoming was attempted, but this resulted in a crumbling of the MHP instead of clean slices. Therefore, this method was not pursued further.

H.2.3 PbI_2 platelet growth in solution + vapor phase MAI

PbI_2 microplatelets were synthesized in solution following the procedure outlined by Li *et al.* [365]. Then, TEM grids were dipped in this suspension, dried on a hotplate, and then sealed in a KF flange with MAI powder. The flange was then heated to 110 °C - 120 °C) for ∼24 hours to sublime MAI vapor such that it would react with the PbI_2 platelets. While this method produced nice platelets, it was difficult to get monodispersed and thus consistently stoichiometry platelets. Furthermore, once reacted with MAI, the platelets were typically too thick to be electron transparent.